

**REAL-TIME SIGNAL PROCESSING FOR FLYING HEIGHT  
MEASUREMENT AND CONTROL IN HARD DRIVES SUBJECT TO SHOCK  
AND VIBRATION**

by

**AMEI LI**

A thesis submitted to the University of Plymouth  
in partial fulfilment for the degree of

**DOCTOR OF PHILOSOPHY**

School of Computing Communication and Electronics  
Faculty of Technology

**March 2008**

	University of Plymouth Library
Item No.	900 793025X
Shelfmark	THESIS 621.3822 L1

# **REAL-TIME SIGNAL PROCESSING FOR FLYING HEIGHT MEASUREMENT AND CONTROL IN HARD DRIVES SUBJECT TO SHOCK AND VIBRATION**

**AMEI LI**

## **ABSTRACT**

Three readback signal detection methods are investigated for real-time flying height or head disk spacing variation measurement under vibration conditions. This is carried out by theoretical analysis, numerical simulation, and experimental study. The first method (amplitude detection) provides a simple way to study the head disk spacing change. The second method ( $PW_{50}$  parameter estimation) can be used effectively for real-time spacing variation measurement in normally operated hard disk drives, primarily in low frequency spacing variation conditions. The third method (thermal signal detection), on the other hand, is more effective and suitable for high frequency spacing variation measurement. By combining the  $PW_{50}$  estimation and thermal signal detection methods, a novel spacing variation detection method for the whole frequency range is constructed. This combined signal detection method not only has been used to study the head disk spacing variation itself, but also has the potential of being used for real time flying height control.

Analytical models are developed for head disk assembly and head position servo control mechanisms to analyse the operation failure of hard disk drives under vibration conditions. Theoretical analysis and numerical simulation show their good agreement with experimental results.

A novel active flying height control method is proposed to suppress the flying height or head-disk spacing variation in hard disk drives under vibration conditions. Simulation results show that this active flying height control can effectively suppress the head-disk spacing variation, therefore the performance and reliability of HDDs can be well improved when working in vibration conditions. The method has a good potential to be applied to future ruggedized hard disk drives.

# TABLE OF CONTENTS

REAL-TIME SIGNAL PROCESSING FOR FLYING HEIGHT MEASUREMENT AND CONTROL IN HARD DRIVES SUBJECT TO SHOCK AND VIBRATION .....	III
ABSTRACT.....	III
TABLE OF CONTENTS .....	IV
LIST OF FIGURES.....	VIII
ACKNOWLEDGEMENTS .....	XIII
ABBREVIATIONS.....	XIV
AUTHOR'S DECLARATION .....	XV
PUBLICATIONS .....	XVI
Chapter 1 Introduction.....	1
1.1 Overview .....	1
1.2 Advances in HDD industry .....	3
1.3 Physics of Magnetic Recording.....	8
1.3.1 Basic principles.....	8
1.3.2 Overview of magnetic hard disk drives .....	11
1.4 Flying Height and Recording Density.....	15
1.5 Hard Disk Drive Head Disk Interface .....	18
1.6 The Vibration Problem in Hard Disk Drives.....	21
1.6.1 Limitations of hard disk drive operation.....	21
1.6.2 Hard disk drive operation failure .....	23
Chapter 2 Head Disk Spacing Measurement Review.....	26
2.1 Traditional Optical Interferometry .....	27
2.2 Modern Intensity Interferometry .....	33



2.3	Oblique Polarisation Interferometry.....	35
2.4	Dual-Beam Normal Incidence Polarisation Interferometry Method .....	40
2.4.1	Dual-beam normal incidence polarisation interferometry .....	40
2.4.2	Relative displacement measuring method .....	44
2.5	Laser Doppler interferometry .....	45
2.6	Capacitance Technique.....	46
2.7	Summary.....	48
Chapter 3	Real Time Head Disk Spacing Measurement Methods.....	50
3.1	Analysis of Amplitude of Readback Signal Measurement Method .....	50
3.2	PW <sub>50</sub> of Readback Signal Measurement Method .....	52
3.3	PW <sub>50</sub> Parameter Estimation Method for Flying Height Determination .....	56
3.4	Thermal Signal Detection Method .....	61
Chapter 4	Hard Disk Drive Operation Failure and Head Disk Spacing Variation Suppression .....	64
4.1	Analysis of Hard Disk Drive Operation Failure under Vibration Conditions...	64
4.1.1	Related research within the Lab.....	64
4.1.2	Analysis on head-disk spacing variation .....	65
4.1.3	Head position servo control mechanism.....	70
4.1.4	Summary.....	72
4.2	Head Disk Spacing Variation Suppression via Active Flying Height Control .	72
4.2.1	Introduction.....	72
4.2.2	Research on micro actuators within the Lab.....	73
4.2.2.1	Bonded piezoelectric actuators .....	74
4.2.2.2	Embedded piezoelectric actuators.....	74
4.2.2.3	Composite piezoelectric arms .....	75
4.2.3	Real time active flying height variation control .....	75

4.2.4	Summary.....	79
Chapter 5	Experimental Study.....	80
5.1	Experimental Equipment.....	80
5.1.1	Electrodynamic shaker.....	80
5.1.2	Shaker control system.....	81
5.1.3	Digital storage oscilloscopes .....	83
5.1.4	FIR filter .....	83
5.2	Real Time Head Disk Spacing Measurement.....	84
5.2.1	Amplitude of readback signal measurement method.....	84
5.2.2	PW50 of readback signal measurement method.....	90
5.2.3	PW50 parameter estimation method for flying height determination .....	90
5.2.3.1	Estimation using isotropic (1, -1) recorded sequences .....	91
5.2.3.2	Estimation using random bits recorded sequences .....	93
5.2.3.3	Convergence and tracking properties of the parameter estimation method .....	95
5.2.3.4	PW50 estimation using readback signals of real hard disk drives.....	101
5.2.3.5	Summary .....	102
5.2.4	Thermal signal detection method.....	103
5.3	Analysis of Hard Disk Drive Operation Failure under Vibration Conditions.	105
5.4	Active Flying Height Variation Control.....	109
Chapter 6	Conclusions and Future Work .....	117
6.1	Conclusions .....	117
6.1.1	Real time head disk spacing measurement .....	117
6.1.2	Analysis of hard disk drive operation failure under vibration conditions	118
6.1.3	Real time active flying height control.....	118
6.2	Future Work.....	119

Chapter 7	Appendices.....	120
7.1	Software Developed During This Research .....	120
7.1.1	Magnetic recording channel modelling and readback simulation software ... .....	120
7.1.1.1	Readback from an isotropic (1,-1) recoded bit sequence.....	120
7.1.1.2	Readback from a random bits recorded sequence.....	124
7.1.2	Hard disk drive vibration analysis software .....	127
7.1.2.1	Analysis of head-disk spacing variation .....	127
7.1.2.2	Head position servo control .....	130
7.1.3	Readback signal processing software .....	133
7.1.4	Thermal signal simulation and processing software.....	135
7.1.5	PW50 parameter estimation software .....	137
7.1.5.1	Estimation using an isotropic (1, -1) recorded sequence .....	137
7.1.5.2	Estimation using a random bits recorded sequence .....	139
7.1.5.3	Tracking property of the parameter estimation method.....	141
7.1.5.4	PW50 estimation using readback signal of real hard disk drives.....	143
7.1.6	Flying height control simulation software .....	148
7.2	Readback Signals and Under Different Vibration Frequencies .....	153
References	.....	171

# **LIST OF FIGURES**

Figure 1-1 Flying height history for the leading-edge products of the magnetic recording industry..... 1

Figure 1-2 Leading-edge magnetic hard disk drive areal density vs. year of production introduction (including prediction) [Wang & Taratorin, 1999]. The line is for visual guidance only. .... 4

Figure 1-3 Schematic principle of magnetic recording ..... 8

Figure 1-4 Longitudinal recording (Courtesy of Hitachi Global Storage Technologies). 9

Figure 1-5 Perpendicular recording (Courtesy of Hitachi Global Storage Technologies) ..... 10

Figure 1-6 A photograph of a hard disk drive (Courtesy of IBM Corporation) ..... 12

Figure 1-7 Another photograph of a hard disk drive (Courtesy of Western Digital Corporation) ..... 13

Figure 1-8 Schematic diagram of hard-disk assembly: (a) top view, (b) side view, (c) magnified view of slider..... 14

Figure 1-9 Read process in longitudinal magnetic recording ..... 15

Figure 1-10 Readback voltage output pulse from a single transition ..... 17

Figure 1-11 A schematic of the head gimbal assembly ..... 18

Figure 1-12 Physical model of a head slider flying above a rigid disk surface. Flexure damping coefficients ( $C_z, C_\alpha, C_\beta$ ) are not shown [White, 1984]..... 19

Figure 1-13 Diagram showing track mis-registration..... 24

Figure 1-14 Readback from randomly recorded bit sequence, with and without random peak position jitter..... 25

Figure 1-15 Readback from recorded high density isotropic (1,-1) bit sequence, with and without random peak position jitter..... 25

Figure 2-1 Parallel plate optical interferometry.....	28
Figure 2-2 D.C. output of the photo-detector as a function of flying height.....	32
Figure 2-3 Schematic of single or three-wavelength monochromatic interferometer ....	34
Figure 2-4 Light beam at disk slider interface.....	34
Figure 2-5 Polarisation interferometer for flying height testing.....	36
Figure 2-6 Reflected intensity as a function of flying height .....	39
Figure 2-7 Phase difference between the two polarisation components as a function of flying height .....	39
Figure 2-8 Dual-beam normal incidence polarisation interferometer .....	41
Figure 2-9 Flying height measurement (single layer reflections).....	42
Figure 2-10 Intensity and phase difference as functions of head-disk spacing. ....	44
Figure 2-11 Relative displacement measuring method.....	45
Figure 2-12 Schematic diagram of (a) the optical and (b) electronic systems of the Laser Doppler Vibrometer [Bogy & Talke, 1985].....	46
Figure 3-1 Definition of $PW_x$ , the pulse width at a slicing level of $x\%$ $(-100 \leq x \leq +100)$ .....	53
Figure 3-2 $PW_{50}$ estimation model .....	58
Figure 4-1 Head suspension and disk assembly in a hard disk drive. ....	66
Figure 4-2 Frequency response of the amplitude of head disk spacing variation.....	70
Figure 4-3 Block diagram of head position servo loop. ....	71
Figure 4-4 Frequency response of the sensitivity function.....	71
Figure 4-5 Head assembly in HDDs with bonded piezo film on the suspension arm. ....	76
Figure 4-6 Flying height variation suppression mechanism.....	77
Figure 4-7 Block diagram of closed-loop control system.....	77
Figure 5-1 Block diagram of the electrodynamic shaker and its control system.....	80
Figure 5-2 Mounting plate of the electrodynamic shaker.....	81

Figure 5-3 Readback signal at a vibration frequency of 5.8 kHz .....	86
Figure 5-4 Fullwave rectified signal of the readback shown in Figure 5-3 .....	87
Figure 5-5 Extracted envelope of the readback signal under 5800 Hz vibration by a 60- order lowpass FIR filter .....	88
Figure 5-6 Extracted envelope of the readback signal under 5800 Hz vibration by a 500- order lowpass FIR filter .....	89
Figure 5-7 Readback signal with no added noise .....	91
Figure 5-8 Estimation of $PW_{50}$ from readback signal with no noise.....	92
Figure 5-9 Readback signal with added noises.....	92
Figure 5-10 Estimation of $PW_{50}$ from readback signal with noises .....	93
Figure 5-11 Readback signal with no added noise .....	94
Figure 5-12 Estimation of $PW_{50}$ from readback signal with no noise.....	94
Figure 5-13 Readback signal with noises .....	95
Figure 5-14 Estimation of $PW_{50}$ from readback signal with noises .....	95
Figure 5-15 PW50 estimation convergence and tracking process with $\beta = 0.2$ .....	96
Figure 5-16 PW50 estimation convergence and tracking process with $\beta = 0.5$ .....	97
Figure 5-17 PW50 estimation convergence and tracking process with $\beta = 0.7$ .....	97
Figure 5-18 PW50 estimation convergence process with $\beta = 1.0$ .....	98
Figure 5-19 PW50 estimation convergence and tracking process with $\beta = 0.2$ .....	99
Figure 5-20 PW50 estimation convergence and tracking process with $\beta = 0.5$ .....	99
Figure 5-21 PW50 estimation convergence and tracking process with $\beta = 0.7$ .....	100
Figure 5-22 PW50 estimation convergence and tracking process with $\beta = 1.0$ .....	100
Figure 5-23 Part of readback signal from a real hard disk drive .....	101
Figure 5-24 Estimation of $PW_{50}$ using readback signals from a real hard disk. ....	102

Figure 5-25 Readback signal of a disk drive with MR heads at a vibration frequency of 5.8kHz.....	104
Figure 5-26 Extracted thermal signal by using signal processing .....	105
Figure 5-27 Readback signal under 4500Hz vibration .....	106
Figure 5-28 Extracted envelope of the readback signal under 4500Hz vibration .....	107
Figure 5-29 Frequency response of the effective head-disk spacing variation to the vibration amplitude of the disk .....	109
Figure 5-30 Open loop frequency response of the compensated servo control system. ....	110
Figure 5-31 Step response of the servo control system. ....	111
Figure 5-32 500Hz unit-amplitude sinusoidal disturbance input, and the resulted head-disk spacing variation.....	112
Figure 5-33 1000Hz unit-amplitude sinusoidal disturbance input, and the resulted head-disk spacing variation.....	113
Figure 5-34 2000Hz unit-amplitude sinusoidal disturbance input, and the resulted head-disk spacing variation.....	114
Figure 5-35 35000Hz unit-amplitude sinusoidal disturbance input, and the resulted head-disk spacing variation.....	115
Figure 7-1 Readback signal under 10300Hz vibration. ....	153
Figure 7-2 Readback signal under 9800Hz vibration .....	154
Figure 7-3 Readback signal under 8030Hz vibration .....	155
Figure 7-4 Readback signal under 5800Hz vibration .....	156
Figure 7-5 Readback signal under 5300Hz vibration .....	157
Figure 7-6 Readback signal under 3900Hz vibration .....	158
Figure 7-7 Readback signal under 3440Hz vibration .....	159
Figure 7-8 Readback signal under 1300Hz vibration .....	160

Figure 7-9 Readback signal under 1180Hz vibration .....	161
Figure 7-10 Readback signal under 523Hz vibration .....	162
Figure 7-11 Readback signal under 160Hz vibration .....	163
Figure 7-12 Readback signal under 45Hz vibration .....	164
Figure 7-13 Extracted envelope of the readback signal under 10300Hz vibration .....	165
Figure 7-14 Extracted envelope of the readback signal under 9800Hz vibration .....	165
Figure 7-15 Extracted envelope of the readback signal under 8030Hz vibration .....	166
Figure 7-16 Extracted envelope of the readback signal under 5800Hz vibration .....	166
Figure 7-17 Extracted envelope of the readback signal under 3900Hz vibration .....	167
Figure 7-18 Extracted envelope of the readback signal under 3440Hz vibration .....	167
Figure 7-19 Extracted envelope of the readback signal under 2400Hz vibration .....	168
Figure 7-20 Extracted envelope of the readback signal under 1180Hz vibration .....	168
Figure 7-21 Extracted envelope of the readback signal under 523Hz vibration .....	169
Figure 7-22 Extracted envelope of the readback signal under 160Hz vibration .....	169
Figure 7-23 Extracted envelope of the readback signal under 45Hz vibration .....	170



## **ACKNOWLEDGEMENTS**

This work has been conducted under the supervision of Dr David Jenkins, Professor Warwick Clegg, and Dr Paul Davey. I would like to express my great thanks for their tremendous support, encouragement and guidance from the beginning till the end.

I would like to express my gratitude to all those people who have been associated with this project especially the following.

Both academic members and technical staff at the Centre for Research in Information Storage Technology and SCCE for their support.

Chibesa Chilumbu, James Windmill, Glen Tunstall, and Robert Windmill for their humour and friendship.

Last but by no means least, I would like to thank my husband, my sons, and my own and my husband's family. Without their continuous encouragement, support, love and understanding, this thesis would not have been finished.

## ABBREVIATIONS

AEM	Arm-mounted electronic module
AWG	Additive White Gaussian
b	Bit
B	Byte
BER	Bit error rate
DC	Direct Current
FIR	Finite Impulse Response
HDD	Hard Disk Drive
HGA	Head gimbal assembly
IIR	Infinite Impulse Response
ML	Maximum likelihood
MMSE	Minimum mean square error
MR	Magnetoresistive
PES	Position error signal
PI	Proportional and integral
PID	Proportional integral and differential
PRBS	Pseudo random binary sequences
PRML	Partial response maximum likelihood
PW <sub>50</sub>	Pulse width at 50% of the peak value
TMR	Track mis-registration

## **AUTHOR'S DECLARATION**

At no time during the registration for the degree of Doctor of Philosophy has the author been registered for any other University award without prior agreement of the Graduate Committee.

This study was financed with the aid of the Faculty of Technology, University of Plymouth. The author is extremely grateful for the support.

Twelve papers from this work have been presented at international conferences, three of which are published in the relevant journals. Copies of some of the published papers are included in the Selected Publications section of this thesis.

The author also attended the IEEE/AIP 8th Joint MMM-Intermag Conference, San Antonio, Texas, January 7-11, 2001, funded partly by the Student Travel Award from IEEE and the Instrument Science and Technology Group (ISAT) of the IOP.

## PUBLICATIONS

1. Amei Li, Xinqun Liu, Warwick Clegg, David Jenkins, and Donnelly T., "Real Time Method to Measure Head Disk Spacing Variation under Vibration Conditions", IEEE Transactions on Instrumentation and Measurement, vol. 52, no.3, pp.916-920, June, 2003.
2. Xinqun Liu; Amei Li; Warwick Clegg, David Jenkins, and Paul Davey; "Head-disk spacing variation suppression via active flying height control", ", IEEE Transactions on Instrumentation and Measurement, vol. 51 no.5, pp.897-901, Oct., 2002.
3. Warwick Clegg, Xinqun Liu, Bo Liu, and Amei Li, "Normal incidence polarization interferometry flying height testing," IEEE Transactions on Magnetics, vol. 37, no. 4I, pp.1941-1943, 2001.
4. Glen Tunstall, David Jenkins, Warwick Clegg, Amei Li; Paul Davey; "CD-ROM optics for flying height measurement in hard disk drives" Proc. SPIE Vol. 4442, pp.126-134, Dec., 2001.
5. Glen Tunstall, Warwick Clegg, David Jenkins, Paul Davey, and Amei Li, "Observing hard disk drive suspension arm and disk vibrations," 12th Annual Symposium on Information Storage and Processing Systems, Santa Clara, USA, June, 2001.
6. Amei Li, Xinqun Liu, Warwick Clegg, David Jenkins, "Real Time Methods to Measure Head Disk Spacing under Vibration Conditions," presented at *IEEE Instrumentation and Measurement Technology Conference*, Budapest, Hungary, May, 2001. Proceedings of the 18th IEEE IMTC, vol. 2, pp.945-949, 2001.
7. Xinqun Liu, Amei Li, Warwick Clegg, David Jenkins, and Paul Davey, "Head Disk Spacing Vibration Suppression via Active Flying Height Control," presented at *IEEE Instrumentation and Measurement Technology Conference*, Budapest, Hungary, May, 2001. Proceedings of the 18th IEEE IMTC, vol. 2, pp.888-891, 2001.
8. Amei Li, Xinqun Liu, David Jenkins, Warwick Clegg, and Paul Davey, "Parameter estimation method for real time flying height detection of hard disk drives," presented at the *IEEE/AIP 8th Joint MMM-Intermag Conference*, San Antonio, Texas, January 7-11, 2001.
9. Amei Li, Xinqun Liu, Warwick Clegg, Glen Tunstall, and Paul Davey, "Analysis of hard disk drive operation failure under vibration conditions," presented at the *IEEE/AIP 8th Joint MMM-Intermag Conference*, San Antonio, Texas, January 7-11, 2001.

10. Warwick Clegg, Xinqun Liu, Bo Liu, and Amei Li, "Normal incidence polarization interferometry flying height testing," presented at the *IEEE/AIP 8th Joint MMM-Intermag Conference*, San Antonio, Texas, January 7-11, 2001.
11. Amei Li, Xinqun Liu, Warwick Clegg, David Jenkins, and Paul Davey, "Real Time Flying Height Measurement under Vibration Conditions" presented at CMMP2000.
12. D F L Jenkins, W W Clegg, L He, J Windmill, G Tunstall, X Liu, C Chilumbu and A Li. Sensors For Dynamic Characterisation Of Magnetic Storage Systems. Invited paper- Sensor Review Journal, Vol. 20, No.4, 307-315, 2000.

Word count of main body of thesis: 42,000

Signed..... Amei Li .....

Date..... 29.04.2008 .....

# Chapter 1 Introduction

## 1.1 Overview

The need for ever-greater storage capacity has resulted in the data-storage recording densities of magnetic hard disk drives growing at a rate of about 60% every year in the past one and a half decades. In order to support these developments, work has been undertaken in parallel to improve the heads, media, channel, and electronics. However, one of the most critical and effective parameters in increasing areal density is the flying height or spacing between the read-write head and the recording disk medium. Since 1990, the flying height has been reduced from above 140nm to under 10nm for the leading-edge products of the magnetic recording industry, which is illustrated in Figure 1-1.

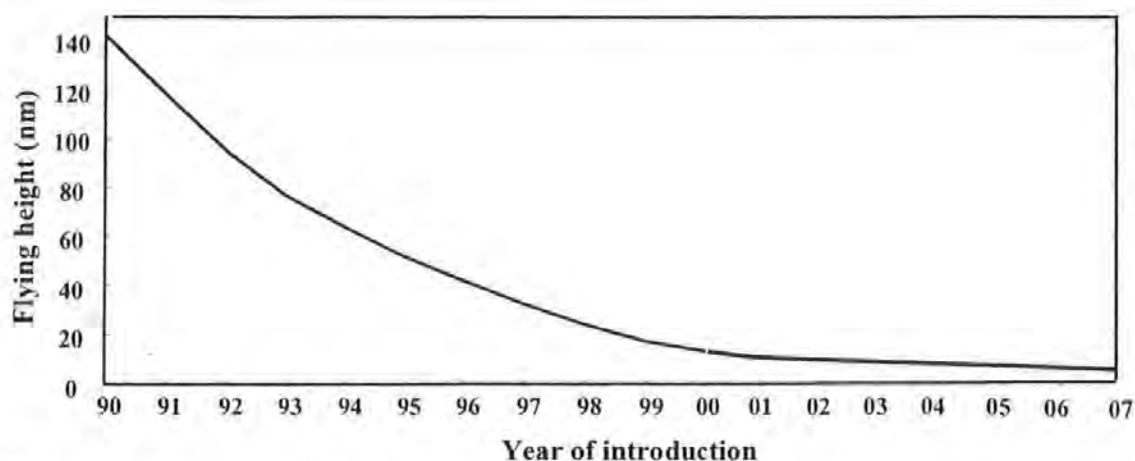


Figure 1-1 Flying height history for the leading-edge products of the magnetic recording industry

The current state of the art head-disk spacing of high-density hard disk drives has reached the level of around 5 nm.

Although it is very desirable to reduce the head-disk spacing or flying height to increase the recording areal density, head disk contact is undesirable during disk operation since that will deteriorate the tribological performance of the head disk interface and its reliability. Hence high accuracy head-disk spacing measurement and characterisation becomes more and more important and necessary. Especially when hard disk drives are operated in vibration conditions, the chance of head disk contact is getting high and this may be one of the main reasons for disk read/write failure. Therefore, it also becomes very important to make high accuracy real-time head-disk spacing measurements, which can then be used for real-time head-disk spacing control to prevent the head disk contact. This project was proposed from such a background to meet this technical challenge. The thesis is outlined in the following.

In Chapter Chapter 1, the background of this research work and an overview of the development of magnetic hard disk drives are given.

In Chapter 2, head disk spacing measurement methods are reviewed

In Chapter Chapter 3, three readback signal detection methods are presented for real-time head disk spacing variation measurement under vibration conditions, which are amplitude of readback signal detection method,  $PW_{50}$  (pulse width at 50% of the peak value) of readback signal measurement method, and thermal signal detection method. A special  $PW_{50}$  measurement method, the  $PW_{50}$  parameter estimation method, is particularly presented.

In Chapter 4, theoretical analysis is given to hard disk drive operation failure under vibration conditions. This is carried out from two aspects, first from the mechanics of the head suspension arm, the rotating disk, and the aerodynamics of the head-slider's air-bearing, second from the characteristics of the head position servo control mechanism. Analytical models are developed for head disk assembly and head position servo loop.

Also in Chapter Chapter 4, a novel active flying height control method is presented for the suppression of head-disk spacing variation in hard disk drives under shock or vibration conditions. Thermal signal detection method is used for real-time derivation of spacing variation signal for feedback control. Design details of the servo control system are given.

In Chapter Chapter 5, experimental studies are carried out to verify the presented methods and theoretical analyses through out the thesis. Simulation results, experimental results, and discussion are detailed.

Chapter Chapter 6 draws conclusions and provides recommendations for further research.

In Appendices (Chapter 7), modelling and simulation software developed throughout this research project are presented. Plots of more readback signals under different vibration frequencies are also provided here.

## **1.2 Advances in HDD industry**

Since the invention of the hard disk drive, it has undergone both evolutionary and revolutionary changes at a tremendous pace. The progress of areal data density is shown in Figure 1-2, which indicates an annual compound growth rate of about 30% in the 1970s and 1980s, but an even more astonishing rate of about 60% in the 1990s due to the introduction of magnetoresistive (MR) heads and partial-response maximum likelihood (PRML) detection channels.



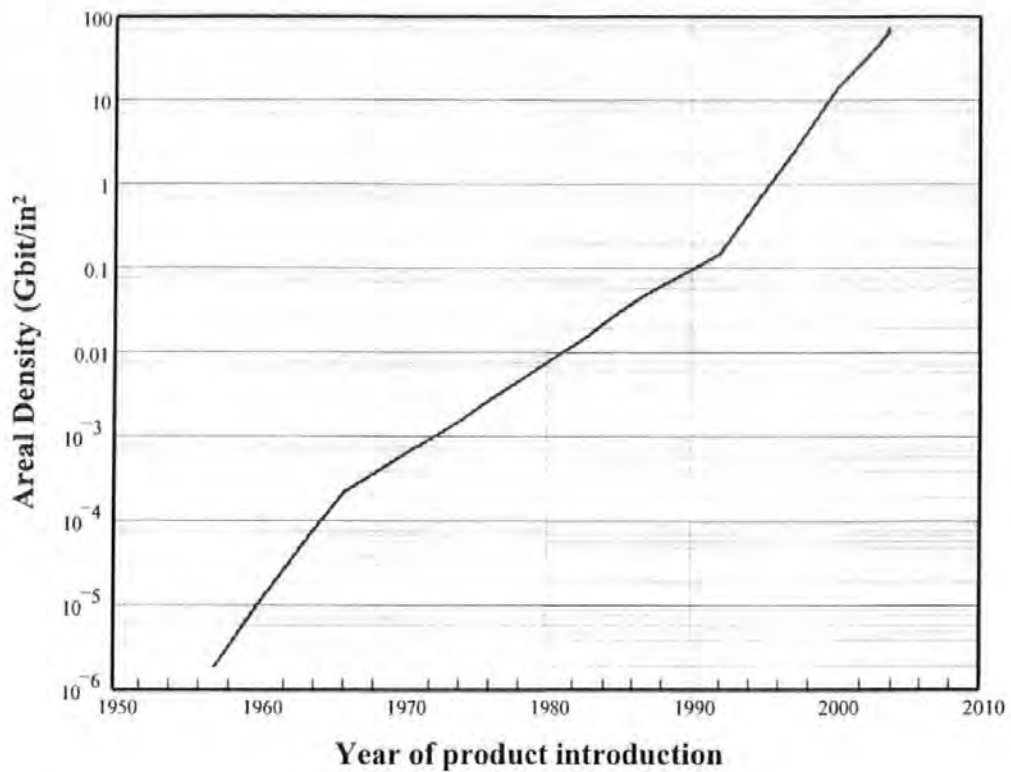


Figure 1-2 Leading-edge magnetic hard disk drive areal density vs. year of production introduction (including prediction) [Wang & Taratorin, 1999]. The line is for visual guidance only.

Hard disk drives, also called rigid disk files, were first developed by IBM, San Jose, California in the late 1950s. The very first hard disk drive was introduced in 1956, which contained 50 disks each with a diameter of 24 in., provided a data capacity of 5 MB and a data rate of 70.4 Kb/s. The areal density was about 2 Kb/in<sup>2</sup>. In 1973, a generation of hard disk drive, the IBM 3340, also named Winchester was introduced, which contained two or four disks with a diameter of 14 in., providing a data capacity of 35 or 70 MB, a data rate of 6.4 Mb/s, and an areal density of 1.69 Mb/in<sup>2</sup>. Around two decades on in 1997, the highest areal density of any hard disk drive reached 2.6 Gb/in<sup>2</sup>, which was found in the IBM Travelstar 4GT. It had a data capacity of 4 GB and a data rate of 83.2 MB/s, and contained four disks with a diameter of 2.5 in. The following are news releases from the HDD industry:

In March 1998, IBM announced the highest capacity hard disk drive for notebook computers, Travelstar 6GT. It had a capacity of 6.4 GB and an areal density of 4.1 Gb/in<sup>2</sup>.

In October 1998, IBM announced the highest capacity hard disk drive for premium notebook computers, the Travelstar 14GS. It had a capacity of 14.1 GB and an areal density of 5.0 Gb/in<sup>2</sup>. Its Travelstar 10GT and travelstar 6GN had a capacity of 10.0 GB and 6.4 GB and an areal density of 5.6 Gb/in<sup>2</sup> and 5.7 Gb/in<sup>2</sup> respectively.

In November 1998, IBM announced its highest capacity desktop PC hard disk drive in the world, IBM Deskstar 25GP, the areal density of which was 3.74 Gb/in<sup>2</sup>. It had a capacity of 25 GB, a data rate of 195.6 Mb/s, and contained 5 or 4 disk platters.

In June 1999, IBM announced the world's highest capacity hard disk drive for desktop PCs, Deskstar 37GP. It had a capacity of 37.5 GB, a data rate of 248 Mb/s, and an areal density of 5.3 Gb/in<sup>2</sup>.

In October 1999, IBM announced the world's highest capacity server hard disk drive, Ultrastar 72ZX, which contained 11 disk platters, and had a capacity of 73.4 GB and areal density of 7.04 Gb/in<sup>2</sup>.

In March 2000, IBM announced the highest capacity hard disk in the world drive for desktop computers, the Deskstar 75GXP. It contained 5 glass disk platters, and had a capacity of 75 GB, a data rate of 444 Mb/s, and an areal density of 11.2 Gb/in<sup>2</sup>. Its Deskstar 40GV had an areal density of 14.3 Gb/in<sup>2</sup>.

In April 2000, IBM announced its world's highest capacity notebook computer hard disk drive, the Travelstar 32GH, which contained 4 glass disk platters and had a capacity of 32 GB and an areal density of 14 Gb/in<sup>2</sup>. Both its Travelstar 30 GT and Travelstar 20 GN had an areal density of 17.1 Gb/in<sup>2</sup>.

In January 2003, Hitachi introduced its high-end enterprise hard disk drive, the Hitachi Ultrastar 15K73 which had an areal density of 31 Gb/in<sup>2</sup>.

In May 2003, Fujitsu bolstered its mobile hard disk drive market growth by introducing its new 80GB, 5400RPM MHT-AH mobile drive in a 2.5" 9.5mm form factor, with an areal density of up to 69 Gb/in<sup>2</sup>.

In August 2004, Toshiba added 30GB and 60GB models to its 1.8in hard drive line-up, which were used in iPod. The two models featured one and two 30GB platters respectively. Both offered an areal density of 93.5 Gb/in<sup>2</sup>.

In December 2004, Toshiba paved the way for 80GB iPods when it said it would ship an 80GB 1.8in hard drive in Q3 2005 - a year after it introduced the 60GB version that was found inside the iPod Photo. Toshiba claimed the drives marked the first ever use of a perpendicular recording system with an areal density of 133 Gb/in<sup>2</sup>. By this time, almost all the other HDD manufacturers were pursuing perpendicular technology as the next stage in the evolution of magnetic storage.

In June 2005, Seagate pledged to be the first hard disk maker to bring to market 2.5in HDDs with perpendicular recording technology. Seagate said it was to implement the technology in a 2.5in notebook drive running at 5400rpm but offering a capacity of 160GB and 138 Gb/in<sup>2</sup>.

In January 2006, Seagate began shipping its first laptop sized, 2.5 inch hard drive using perpendicular recording technology, the Seagate Momentus 5400.3.

In April 2006, Seagate began shipping the world's first 3.5 inch perpendicular recording hard drive, the Cheetah 15K.5, which provides up to 300GB storage. Seagate also announced the availability of Barracuda 7200.10, a series of 3.5 inch HDDs utilizing perpendicular recording with a maximum capacity of 750 GB.

In June 2006, Toshiba announced a 2.5-inch hard drive of 200-GB capacity with mass production starting in August.

In August 2006, Fujitsu extended its 2.5-inch lineup to include SATA models utilizing perpendicular recording, offering up to 160GB capacity with an areal density of 138 Gb/in<sup>2</sup>.

In December 2006, Toshiba said its new 100GB two-platter HDD was based on perpendicular magnetic recording and was designed in the "short" 1.8-inch form factor. This new drive offered a footprint that was 10 percent smaller than first-generation 1.8-inch drives. With an areal density of 155.3 Gb/in<sup>2</sup>, the drive was specially designed for thin and light mobile computers. In addition, Toshiba's new 1.8-inch capacity leader featured the same tunnel magneto-resistive (TMR) head technology combined with perpendicular recording that delivered the company's world-leading 200GB capacity in the 2.5-inch HDD class with an areal density of 178.8 Gb/in<sup>2</sup>.

Also in December 2006, Fujitsu announced the global launch of its MHX2300BT series of 2.5-inch hard disk drives, with capacities of 250 and 300 GB.

In January 2007, Hitachi announced the first 1 Terabyte Hard Drive using the technology, and started shipping since May.

Let us now consider attainments in research: In February of 1999, Seagate set a new data-storage density mark of 16.3 Gb/in<sup>2</sup>. In May, IBM demonstrated an even higher data-storage density of 20 Gb/in<sup>2</sup>. Five months later, IBM revealed their state-of-the-art hard disk drive with a data-storage density of 35.3 Gb/in<sup>2</sup>. In March 2000, Seagate announced that they have demonstrated the world's highest areal density of 45 Gb/in<sup>2</sup>.

In 2002, by using perpendicular recording technology, Seagate demonstrated an areal density of 100 Gb/in<sup>2</sup>. In April 2005, Hitachi demonstrated an areal density of 230Gb/in<sup>2</sup> on perpendicular recording technology. In September 2006, Hitachi demonstrated an areal density of 345 Gb/in<sup>2</sup>.

In order to achieve such a high data-storage density, the corresponding head flying height has to be lower than 10 nm.

## 1.3 Physics of Magnetic Recording

### 1.3.1 Basic principles

Magnetic hard disk drives, floppy disk drives, and tape drives are all based on the same fundamental principle of magnetic recording which involves an inductive recording head (magnetoresistive (MR) read heads are being used nowadays) and a recording medium, as shown in Figure 1-3. [Wang & Taratorin, 1999]

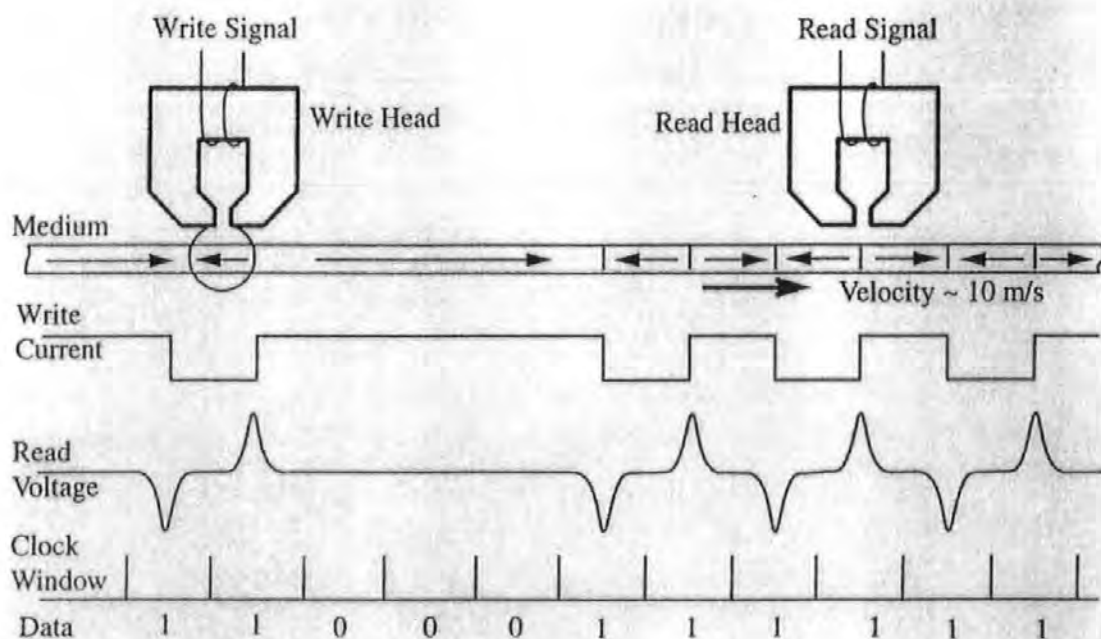


Figure 1-3 Schematic principle of magnetic recording

The inductive recording head is a transducer essentially consisting of some coils wound around a horseshoe-shaped soft magnetic material (with a low coercivity and high permeability) which has an air gap (called the head gap). The recording medium is made of a hard magnetic material with a large coercivity.

There are three possible modes of magnetic recording. One is the *longitudinal recording*, in which the medium magnetisation is parallel to the disk plane, as shown in Figure 1-3 and Figure 1-4.

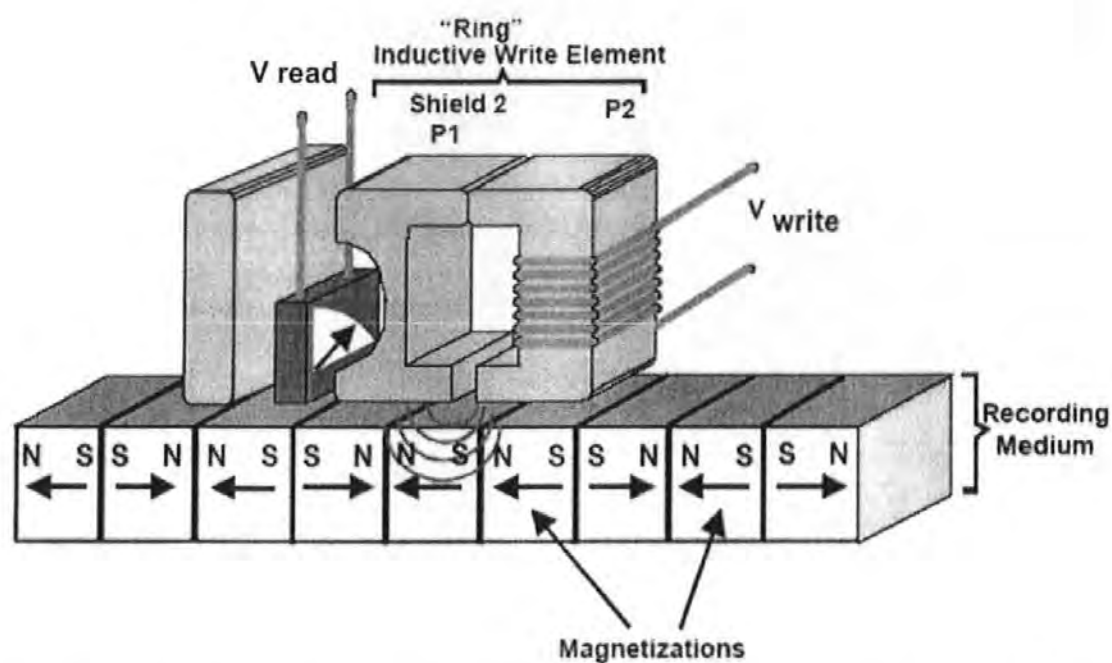


Figure 1-4 Longitudinal recording (Courtesy of Hitachi Global Storage Technologies)

The second mode is *perpendicular recording*, in which the medium magnetisation is normal to the disk plane, as shown in Figure 1-5.

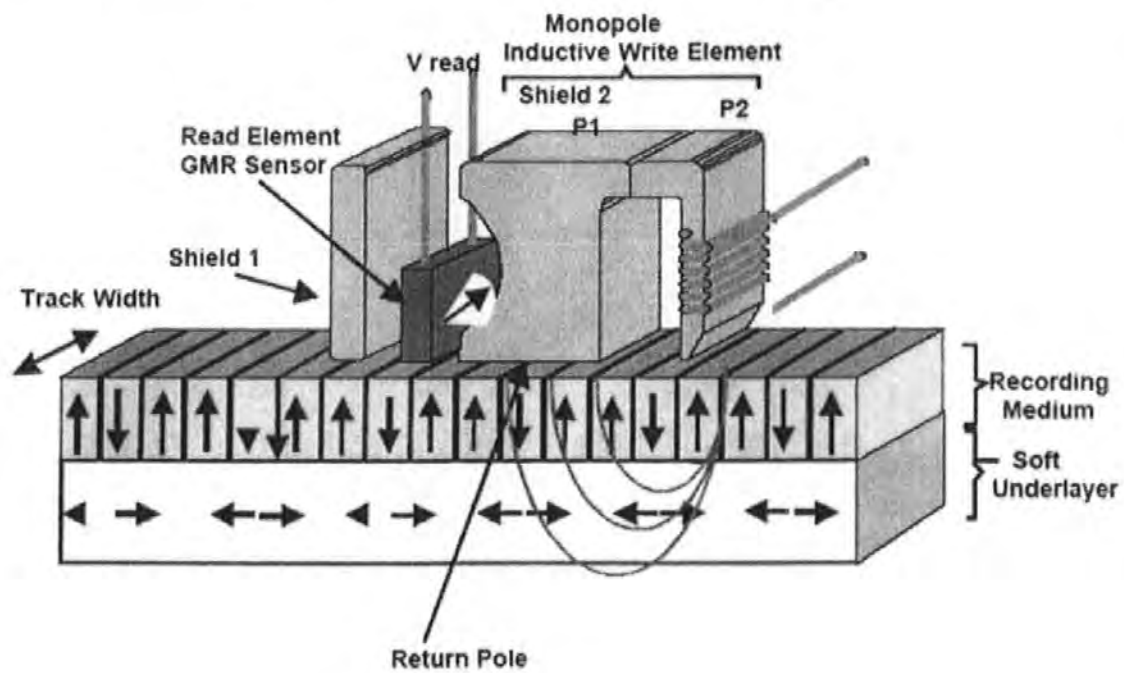


Figure 1-5 Perpendicular recording (Courtesy of Hitachi Global Storage Technologies)

The third mode is *transverse recording*, where the medium magnetisation is normal to the page. Before 2004, *longitudinal recording* was adopted in all commercial magnetic recording systems. Since 2005, *perpendicular recording* has been used in the high end HDD products. *Transverse recording* is not being actively pursued due to various technical constraints.

During the write process, a write current is passed through the head coils to produce a magnetic write field in the medium near the head gap. The write field must be larger than the medium coercivity to magnetise the medium along the field direction. By switching the direction of the write current, magnetisation transitions can be written in the medium. In reality, the magnetic transition length is finite, but it is shown to be zero in Figure 1-3 for simplicity.

During the read process, the medium with written transitions is passed underneath the head gap, as shown in Figure 1-3. The relative motion between the head and the magnetostatic stray field produced by the magnetic transitions generates induced voltage pulses in the coils due to Faraday's law. Each transition corresponds to a voltage pulse that has finite amplitude and a finite half-amplitude pulse width  $PW_{50}$ , which limits how close the voltage pulses can be spaced and still be resolved.

In a simple coding scheme of digital magnetic recording called non-return-to-zero modified (NRZI) coding, the presence of a transition or a voltage pulse in a given clock window (timing window) represents a "1", while the absence of a transition or pulse represents a "0". Therefore, the linear data density is fundamentally limited by the value of  $PW_{50}$ .

### 1.3.2 Overview of magnetic hard disk drives

Among the magnetic storage systems, magnetic hard disk drive is the dominant mass storage device for computers because of its storage capacity, low cost per megabyte, reasonably fast access time, and a mature manufacturing infrastructure.

A magnetic disk drive is mainly composed of the following four parts:

1. *Magnetic read/write heads and magnetic disks (platters)*. Each write/read head, which is too small to be visible to the eye, is located on the trailing edge of a *slider* (or called *head-slider*). The slider is mounted on the end of a stainless steel gimbal-suspension, forming the so-called *head-gimbal assembly* (HGA). The write/read head and a recording disk surface are often called a *head-disk assembly*.
2. *Data detection electronics and write circuit*, which are mostly located on a printed circuit board with many very-large-scale integrated (VLSI) chips.
3. *Mechanical servo and control system*, including spindles, actuators, suspensions, and control chips.
4. *Interface* to microprocessor, located at one edge of the printed circuit board, through which the microprocessor input information from or output information to the disk drives.

Photographs of hard disk drives are shown in Figure 1-6 and Figure 1-7.



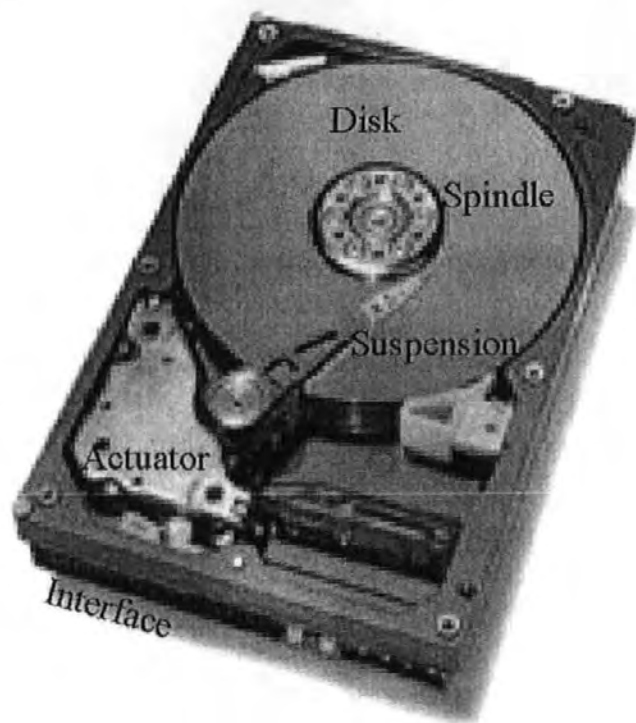


Figure 1-6 A photograph of a hard disk drive (Courtesy of IBM Corporation)

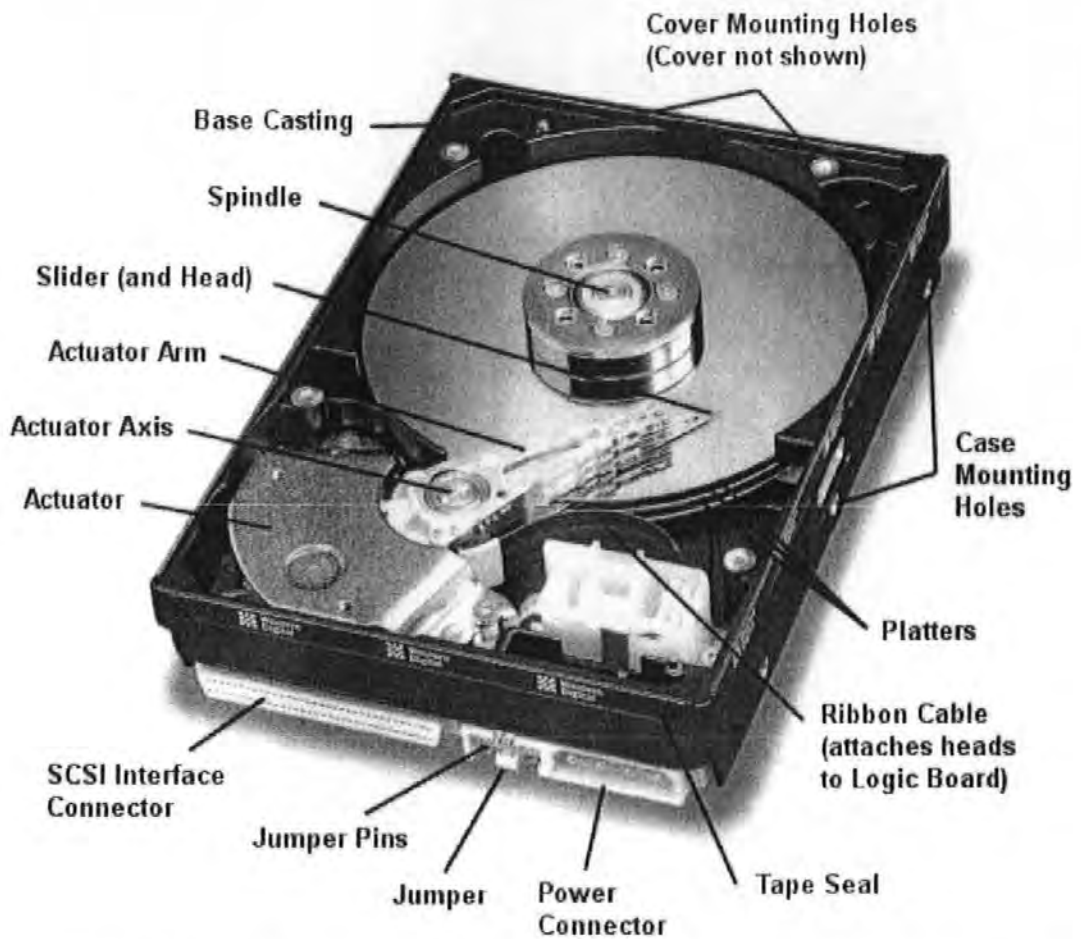


Figure 1-7 Another photograph of a hard disk drive (Courtesy of Western Digital Corporation)

The operation of the head-disk assembly is based on a self-pressured air bearing between the slider and the spinning disk. This air bearing maintains a constant separation called flying height between them, as shown in Figure 1-8. By positioning the head-slider along the radial direction, different data tracks can be written on the disk. Each data track is divided into many data sectors. The state-of-the-art flying height is of the order of 10nm, while the relative speed between slider and disk is extremely high (about 10 m/s or higher).

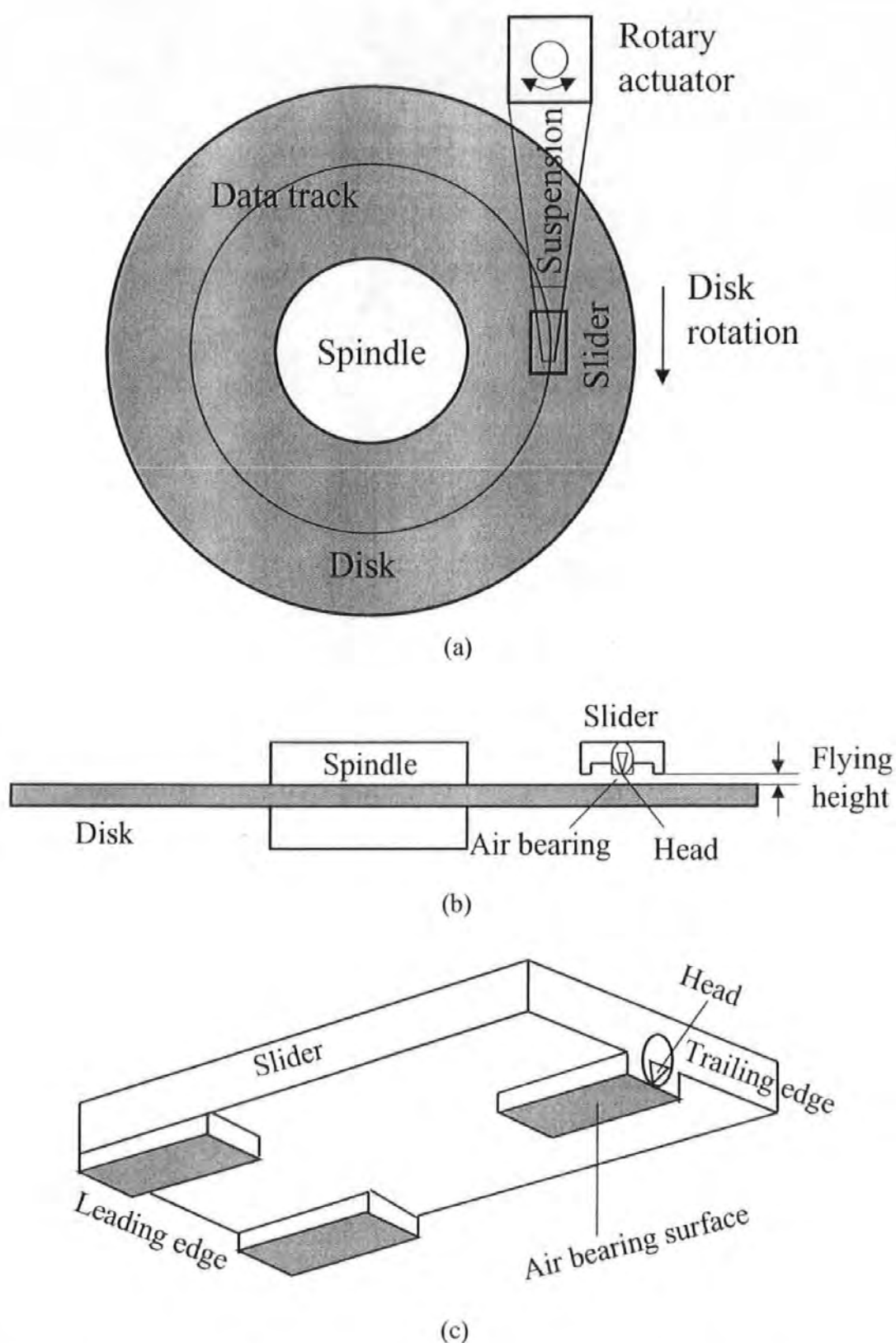


Figure 1-8 Schematic diagram of hard-disk assembly: (a) top view, (b) side view, (c) magnified view of slider.

## 1.4 Flying Height and Recording Density

This section will illustrate that flying height is an important parameter of increasing the areal recording density. The read process in longitudinal magnetic recording will be analysed to demonstrate the relationship between the flying height and areal density, which is shown in Figure 1-9.

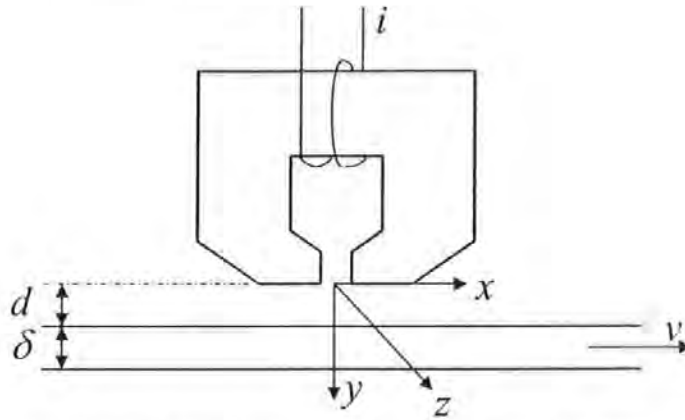


Figure 1-9 Read process in longitudinal magnetic recording

**Reciprocity formula.** When a magnetic recording medium with written magnetic transitions passes underneath an inductive recording head, the magnetic flux produced by each transition is picked up by the head. The variation of the magnetic flux produces an induced voltage in the head coil, that is, a readback signal. Assume that the head produces a field  $H_x(x, y, z)$  in the  $x$  direction. Then, for a medium with magnetisation of  $M_x$ , the corresponding output voltage  $V_x$  at time  $t$  can be derived using the principle of reciprocity as below [Mee & Daniel, 1995]:

$$V_x(\bar{x}) = -\mu_0 v \int_{-w/2}^{w/2} dz \int_d^{d+\delta} dy \int_{-\infty}^{\infty} \frac{dM_x(x - \bar{x})}{dx} \frac{H_x(x, y, z)}{i} dx \quad (1.1)$$

where  $\bar{x} = vt$

$\mu_0$  = permeability of free space

$v$  = medium velocity

$w$  = track width

$d$  = spacing from head to medium

$\delta$  = thickness of medium

$i$  = current in head coil which produces above-mentioned field

Equation (1.1) can be simplified when the track width  $w$  is much larger than other dimensions in the system, hence it may be assumed that there is no variation of magnetisation with the  $z$  dimension.

Thus the above formula can be simplified to

$$V_x(\bar{x}) = -\mu_0 v w \int_d^{d+\delta} dy \int_{-\infty}^{\infty} \frac{dM_x(x-\bar{x})}{d\bar{x}} \frac{H_x(x,y)}{i} dx \quad (1.2)$$

This equation forms the basis for the study of the reproduce or read process and is often referred to simply as the reciprocity formula.

**Readback from single transition.** The real magnetic transition is not an infinitely sharp step transition, but rather a finite width transition, which is often approximated by an arctangent function:

$$M_x(x-\bar{x}) = \frac{2}{\pi} M_0 \tan^{-1}\left(\frac{x-\bar{x}}{a}\right) \quad (1.3)$$

where  $a$  is the transition parameter. It can be observed that the arctangent transition becomes a step transition if  $a = 0$ .

From the reciprocity formula, and Karlqvist equation for the head field expression, the readback voltage output produced in a short gap (almost zero gap-length) read head can be obtained [Mee & Daniel, 1995]:

$$V_x(\bar{x}) = \frac{-\mu_0 \gamma w M_0 H_g g}{\pi i} \ln \frac{(a+d+\delta)^2 + \bar{x}^2}{(a+d)^2 + \bar{x}^2} \quad (1.4)$$

where  $H_g$  is the field in the gap, and  $g$  is the gap length.

The amplitude of this voltage output pulse is obtained by putting  $\bar{x} = 0$  in the above equation, while pulse width is another important parameter as shown in Figure 1-10.

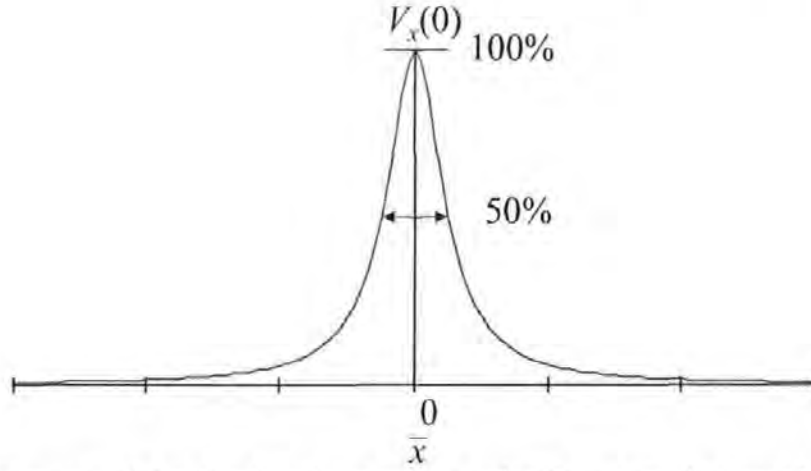


Figure 1-10 Readback voltage output pulse from a single transition

The pulse width at 50 percent of peak amplitude ( $PW_{50}$ ) can be derived by solving the equation  $V_x(0)/2 = V_x(\bar{x})$  to give:

$$PW_{50} = 2\sqrt{(d+a)(d+\delta+a)} \quad (1.5)$$

When the reproduce gap length is not negligible, a suitable general case approximation for  $PW_{50}$  is given below:

$$PW_{50} = 2\sqrt{(d+a)(d+\delta+a) + g^2/4} \quad (1.6)$$

For thin media, equations (1.5) and (1.6) reduce to the following form:

$$PW_{50} = 2(d+a) \quad (1.7)$$

From equation (1.5)–(1.7), it is clearly seen that to increase the recording density, or to achieve a narrow readback voltage pulse, one of the most effective ways is to decrease

the head-disk spacing or the flying height, assuming other parameters can not be changed. A similar result can also be obtained in the reproduce process using MR read heads [Wang & Taratorin, 1999]. These are the reasons why the flying height of the hard disk drive is getting lower and lower.

## 1.5 Hard Disk Drive Head Disk Interface

A schematic of the head gimbal assembly (HGA) of the hard disk drive is shown as in Figure 1-11.

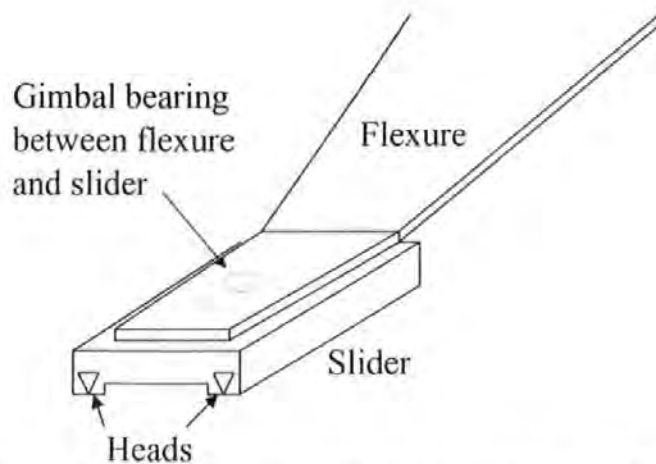


Figure 1-11 A schematic of the head gimbal assembly

The disk head slider is attached to a thin leaf spring (referred to as load beam and/or flexure) suspension, which supports the slider over the disk surface in an attitude that in part determines its flying characteristics. The suspension design allows the head slider to move freely around the load point and permits freedom of motion in the vertical direction as well as rotational motions about the pitch and roll axes—pitch and roll. The flying attitude of the air-bearing slider is usually described by three important parameters: the trailing-edge air film thickness or flying height, pitch angle, and roll

angle. Lower air film thickness or flying height are achieved by changing one or more of the many slider parameters in a way that reduces the load bearing capacity of the slider.

The governing equations and analysis for a particular kind of slider can be found in the literature [White, 1984; Hu & Bogoy, 1997]. For a conventional two-rail taper-flat slider (e.g. IBM 337-type), from a theoretical point of view, the flying height and the pitch and roll angles can be determined by a number of equations. To show this, the relevant parameters are shown in Figure 1-12.

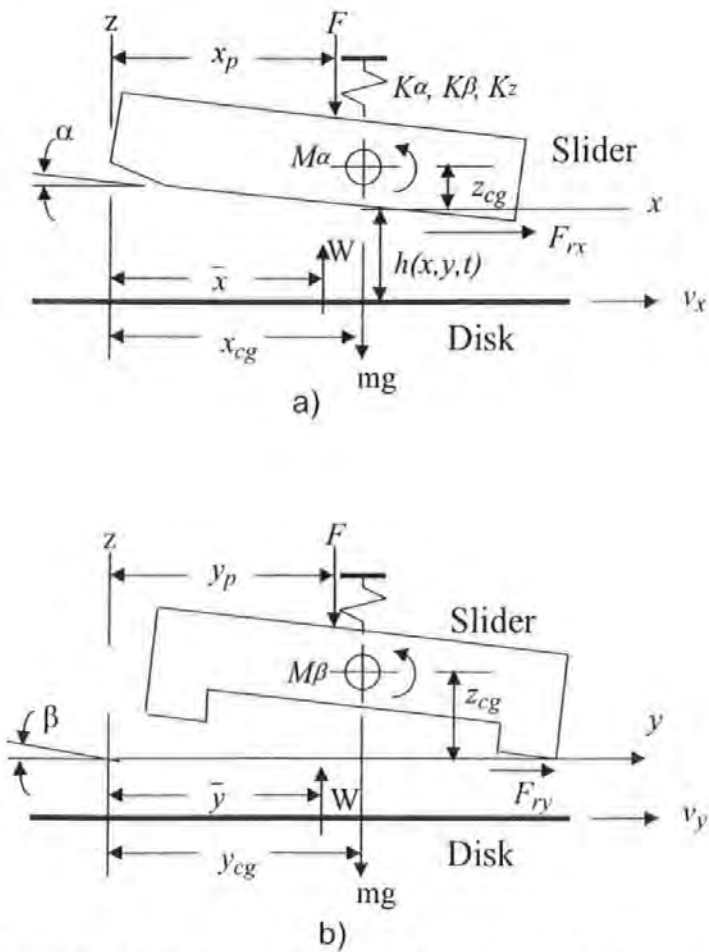


Figure 1-12 Physical model of a head slider flying above a rigid disk surface. Flexure damping coefficients ( $C_z, C_\alpha, C_\beta$ ) are not shown [White, 1984].

The air-bearing film will be determined by the following modified Reynolds equation [Bhushan, 1996]:



$$\begin{aligned} & \frac{\partial}{\partial x} \left[ ph^3 \left( 1 + \frac{6aMp_a h_m}{ph} \right) \frac{\partial p}{\partial x} \right] + \frac{\partial}{\partial y} \left[ ph^3 \left( 1 + \frac{6aMp_a h_m}{ph} \right) \frac{\partial p}{\partial y} \right] \\ & = 6\eta_a \left[ \frac{\partial}{\partial x} (v_x ph) + \frac{\partial}{\partial y} (v_y ph) \right] + 12\eta_a \frac{\partial}{\partial t} (ph) \end{aligned} \quad (1.8)$$

where  $x$  and  $y$  are the spatial coordinates,  $t$  is the time,  $a$  is the surface correction coefficient,  $M$  is the Knudsen number at ambient conditions,  $p_a$  is the ambient pressure,  $h_m$  is a reference film thickness,  $\eta_a$  is the viscosity at ambient conditions,  $v_x$  and  $v_y$  are the disk velocity components in  $x$  and  $y$  directions (if the skew angle of the head slider is zero,  $v_y$  will be zero.),  $p$  is the local pressure of the air, and  $h$  is the local air film thickness or flying height.

The rigid body motion equations for the head slider attached to the flexure that provides three degrees of freedom are given by:

$$m \frac{d^2 z}{dt^2} + C_z \frac{dz}{dt} + K_z z + mg + F = W(t) \quad (1.9a)$$

$$I_\alpha \frac{d^2 \alpha}{dt^2} + C_\alpha \frac{d\alpha}{dt} + K_\alpha \alpha + M_\alpha + (F + K_z z)(x_{cg} - x_p) + F_{rx} z_{cg} = (x_{cg} - \bar{x})W(t) \quad (1.9b)$$

and

$$I_\beta \frac{d^2 \beta}{dt^2} + C_\beta \frac{d\beta}{dt} + K_\beta \beta + M_\beta + (F + K_z z)(y_{cg} - y_p) + F_{ry} z_{cg} = (y_{cg} - \bar{y})W(t) \quad (1.9c)$$

where the bearing load is:

$$W(t) = \int_0^B \int_0^L (p - p_a) dx dy \quad (1.9d)$$

the load point location (air-film centre of pressure) can be determined from:

$$\bar{x}(t) = \frac{1}{W(t)} \int_0^B \int_0^L x(p - p_a) dx dy \quad (1.9e)$$

and

$$\bar{y}(t) = \frac{1}{W(t)} \int_0^B \int_0^L y(p - p_a) dx dy \quad (1.9f)$$

and the resultant fluid friction forces in the  $x$  and  $y$  direction are given by:

$$F_{rx} = \int_0^B \int_0^L \left\{ \frac{\eta_a v_x}{h[1 + (2aMp_a h_m / ph)]} + \frac{h}{2} \frac{\partial p}{\partial x} \right\} dx dy \quad (1.9g)$$

and

$$F_{ry} = \int_0^B \int_0^L \left\{ \frac{\eta_a v_y}{h[1 + (2aMp_a h_m / ph)]} + \frac{h}{2} \frac{\partial p}{\partial y} \right\} dx dy \quad (1.9h)$$

where  $B$  and  $L$  are the bearing breadth and length of the slider,  $C_z, C_\alpha$  and  $C_\beta$  are the flexure's damping coefficients,  $K_z, K_\alpha$  and  $K_\beta$  are the flexure's stiffness coefficients,  $F$  is the applied force at the pivot location  $x_p$  and  $y_p$ ,  $I_\alpha$  and  $I_\beta$  are the slider's moments of inertia,  $M_\alpha$  and  $M_\beta$  are the static moments,  $m$  is the slider's mass,  $x_{cg}, y_{cg}$  and  $z_{cg}$  are the coordinates of the slider's mass centre,  $\alpha$  is the pitch angle, and  $\beta$  is the roll angle. Full analysis of the slider dynamics requires a simultaneous solution of equation (1.7) and (1.8), which can be found in the literature [White & Nigam, 1980; White, 1984; Aruga et al., 1986; Hendriks, 1988; Bhushan, 1996], though it is very complicated.

## 1.6 The Vibration Problem in Hard Disk Drives

### 1.6.1 Limitations of hard disk drive operation

Conventional hard disk drives are very reliable under normal operating conditions. However, they can suffer from data read/write failure when operated in hostile

conditions [Tunstall et al., 2000]. In areas where vibrations exist, hard disk drives can fail catastrophically and reading or writing data can no longer be successful. At least the data transfer rate becomes very slow.

In addition to typical mobile environments, environments such as military and aerospace are featured with large shocks and vibrations. Ocean going craft can also have difficulties with hard drives as the engine and waves transmit vibrations through hull. Dennis [Dennis, 1997] evaluated many proposed solutions, mainly employing large vibration isolation cages and mountings that passively damped the vibrations. However, additional isolation mountings are not the ideal solution. The extra space and weight needed precludes this method from many key areas. Passive dampers, which are only effective over a limited bandwidth, are all that is used in the 'ruggedised' laptops.

Another approach to passively damp the hard disk drive was to develop laminate disks constructed from three sections [McAllister, 1997; Heo & Shen, 1999; and Kuo et al., 2000], two normal disks with a damping sandwich layer in between. However, passive damping bandwidth limitations still exist and the disks thickness increases, thus again increasing the disk drive's physical size.

Hard disk drive manufacturers have invested a large amount of research in how and why drives can become damaged in non-operation. This is primarily not to provide the end user with more robust and reliable drives but to reduce failure costs. Drives can experience large shocks during transportation which may cause severe damage and failure during initial usage [Ishimaru, 1996; Jiang, 1992; Kumar et al., 1994; Schrek, 1994; Kouhei, 1995]. This is costly for the manufacturer as the drive has to be replaced, and inconvenient for the end user as well.

## **1.6.2 Hard disk drive operation failure**

It is important to understand precisely what happens within the disk drive, and which parts and areas fails under shock and vibration conditions. When mechanical components are vibrated they bend and distort, and this is further compounded when vibrated at resonant frequencies.

There are two major mechanical components that, when excited at resonance, can result in data transfer failure. One is the suspension arm (i.e., the actuator arm and loading beam) that pre-tensions the head against the disk to counterbalance its aerodynamic lift. This is designed to control the disk head flying height during normal operating conditions. The other is the hard disk (i.e., the data storage medium) itself. In vibration conditions, air bearing resonance will be produced. This resonance is very important since it causes a few kinds of vibrations in the head-disk interface [Harrison et al., 1999]. First, it will cause head disk spacing (i.e., flying height) fluctuation which modulates the amplitude of the read-back signal. This resonance is also important from a tribological point of view since it can cause interface contact force fluctuation. Second, it will cause transversal vibration of the head (i.e. vibration in the direction orthogonal to the data tracks) which will result in position error variation of the head servo control system, i.e. track mis-registration (TMR), introducing off-track interference noises to the signal read back, and amplitude modulation of the read back signal. Figure 1-13 shows the track mis-registration.

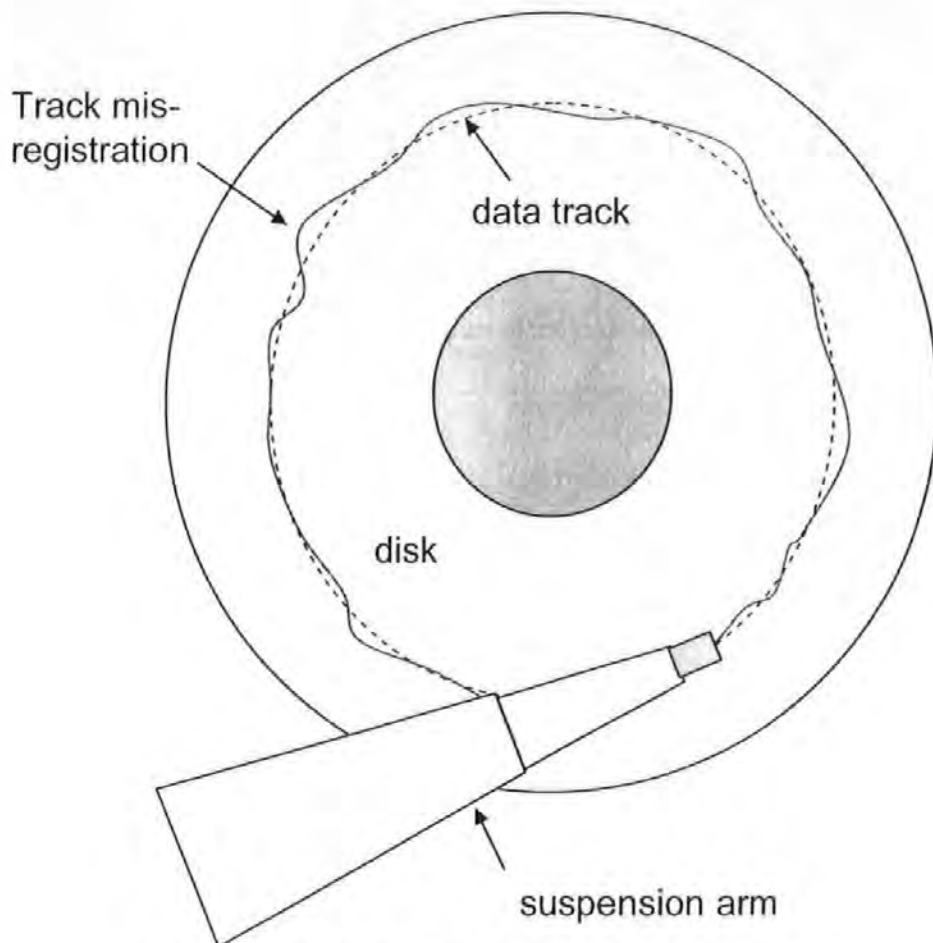


Figure 1-13 Diagram showing track mis-registration

Last, this resonance may cause longitudinal vibration of the head, i.e. vibration in the direction along the data tracks, which will cause frequency modulation of the signal read back by the head, and this will in fact introduce peak position jitter noise which will deteriorate every kind of detector's performance and increase the Bit Error Rate. Figure 1-14 and Figure 1-15 show the readback signals with and without the existence of jitter noise. The solid line is the readback signal without jitter noise, while the dotted line is the readback signal with jitter noise. The curves are obtained by simulation with no other noise added.

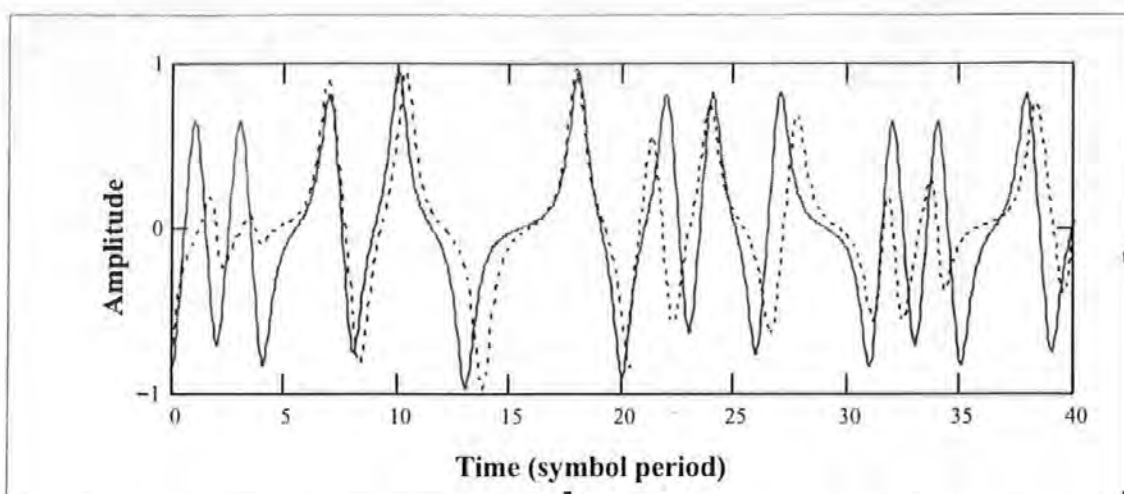


Figure 1-14 Readback from randomly recorded bit sequence, with and without random peak position jitter

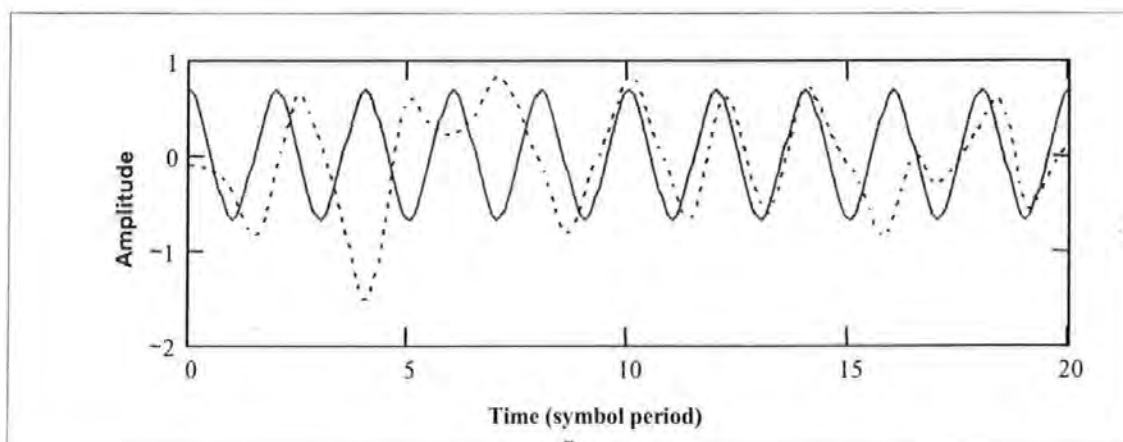


Figure 1-15 Readback from recorded high density isotropic (1,-1) bit sequence, with and without random peak position jitter

In Chapter Chapter 4, theoretical analysis will be given to analyse the reasons of disk operation failure under vibration conditions. Experimental investigation will be given in Chapter 6.

## **Chapter 2 Head Disk Spacing Measurement Review**

Because of its importance, many contributions have been made to the development of methods for the measurement and characterisation of the flying height or the spacing between the head slider and the disk medium. Over the past few decades, a variety of methods have been developed and used to measure this parameter. The methods can be classified into two general categories: optical methods and electrical methods. Optical interferometry is a well established technique to measure film thickness. As early as 1919, interference colours were utilised to measure the thickness of lubricating films on glass. The extension of its application to the measurement of lubrication film for rolling element bearing was made by Archard and Kirk (1963) and later by Cameron and Gohar (1966) and Foord et al (1969–1970). Since then, this optical technique has been extensively used for various tribological applications, including the head-medium interface. A number of optical interferometry methods have been used for the measurement of the head disk spacing. A classical method is the intensity-based interferometry technique, in which monochromatic light or white light is used for the light source. Modern electronics and computational techniques have made the testing accuracy of this intensity interferometry method much higher than before. Polarisation interferometry is another popular method in which both intensity and phase information are utilised to determine the flying height. The main advantage of this method is that it is able to overcome the loss of sensitivity of the intensity interferometry method when the flying height is near-contact. The above two methods were called direct spacing measuring (DSM) methods in which a special transparent glass disk is used in place of

the real magnetic disk, and the flying height is determined by analysing the interference phenomena between the slider and the rotating glass disk [Ohkubo & Kishigami, 1988; Lacey et al., 1992; de Groot, 1998a; Clegg et al., 2001; Liu et al., 2005]. Other optical methods include Laser Doppler Interferometry (LDI), Phase Demodulated Laser Interferometry (PDLI), etc., in which the head-disk spacing is determined by measuring the relative motion between the head-slider and the disk by using dual-beam interferometry [Briggs & Talke, 1989; McMillan & Talke, 1994; Lee & Wu, 1995; Staudenmann, 1998; Liu et al., 2000]. These methods were called relative displacement measuring (RDM) methods, in which a real magnetic disk and head-slider assembly can be employed. The DSM method has the advantage that the absolute head-disk spacing can be directly measured, while the RDM method has the advantage of using a real magnetic disk. Typical electrical methods are the capacitance probe technique [Sonnenfield, 1993] and the readback transducer method [Shi et al., 1987]. The electrical resistance or acoustic emission measurement techniques are other electrical methods for the measurement of frequency and intensity of contact between the asperities of the surfaces of the head slider and disk.

In the following sections, a detailed review and analysis is given of several important head disk spacing measurement techniques.

## **2.1 Traditional Optical Interferometry**

A typical situation where interference occurs is shown in Figure 2-1. A thin parallel film



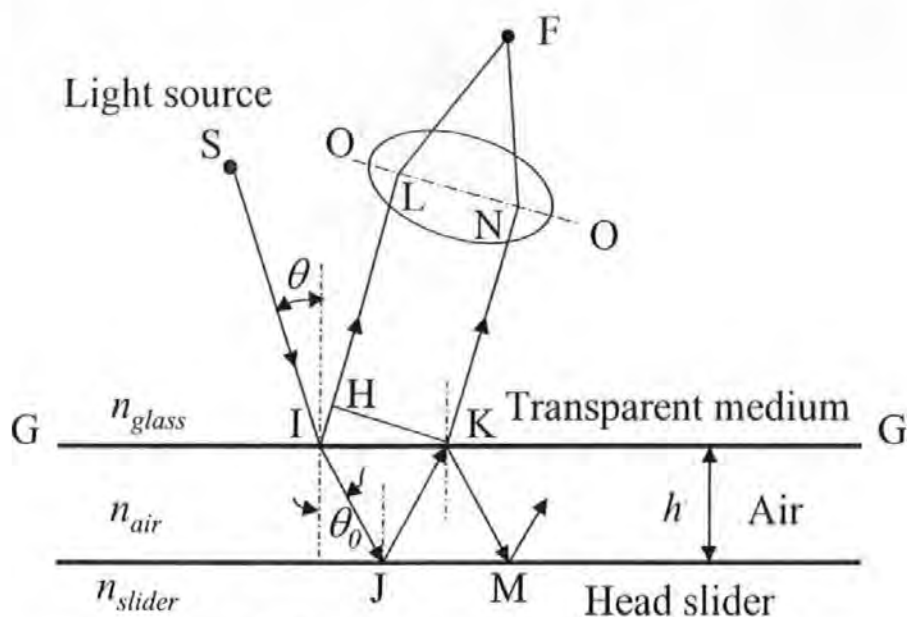


Figure 2-1 Parallel plate optical interferometry

of air is bounded on one side by the transparent medium (e.g. glass disk) and the other side by the air-bearing surface of the head slider. The refractive indices of the glass and air are  $n_{glass}$  and  $n_{air}$  respectively and it is known that  $n_{glass} > n_{air}$ . Monochromatic light of wavelength  $\lambda$  originated from the source S is divided into a transmitted ray IJ and a reflected ray IL at the glass-air interface AA. IJ is reflected at J and emerges along KN parallel to IL. To simplify the explanation, we neglect the reflected ray KM, although multiple reflections should be accounted for to get maximum accuracy. After superposition at F, the two parallel rays IL and KN give rise to interference phenomena due to their path difference. Referring to Figure 2-1, the optical path difference  $\delta$  is obtained as:

$$\delta = 2n_{air} IJ - IH + del \quad (2.1)$$

where  $del$  is the additional delay caused by the advance in the phase produced by the reflection at the air slider interface at J. Using Snell's law of refraction, it follows from equation (2.1) that

$$\delta = 2n_{air}h \cos \theta_0 + del \quad (2.2)$$

where  $\theta_0$  is the angle of incidence of the beam in the air film. It is common knowledge that if the two rays are in phase after superposition, maximum reinforcement occurs. On the other hand, if the path-length difference leads to a phase difference of  $180^\circ$ , maximum cancellation occurs. So the resulting beam is of maximum intensity if the path difference  $\delta$  is a multiple of wavelength  $\lambda$ , that is

$$\delta = m\lambda, \quad m=1,2,3, \dots \quad (2.3a)$$

On the other hand, the minimum intensity occurs if

$$\delta = \frac{2m+1}{2}\lambda, \quad m=1,2,3, \dots \quad (2.3b)$$

In the case of the head slider being a dielectric material, the phase change on reflection from the air-slider interface will be  $180^\circ$ , that is,  $del = \lambda/2$ . Since the refractive index of air is 1, for normal incidence, the bright fringes are located at the film thickness corresponding to

$$h = \frac{2m+1}{4}\lambda, \quad m = 0, 1, 2, 3, \dots \quad (2.3c)$$

while the dark fringes are located at

$$h = m\frac{\lambda}{2}, \quad m = 0, 1, 2, 3, \dots \quad (2.3d)$$

If the light source is white rather than monochromatic, the interference pattern from a thin film will consist of continuous colour fringes instead of alternating bright and dark fringes of the monochromatic light. Each wavelength of the white light forms its own interference pattern. Hence the colour of the interference pattern at any point is due to the superposition of those colours whose wavelength intensities are strengthened through constructive interference, and the absence of those colours the wavelength intensities of which are weakened because of destructive interference at that particular

film thickness. From Newton's colour chart, it is known that the colour is a function of the film thickness. The zero spacing corresponds to a very dark (almost black) fringe. As the spacing increases, a sequence of well-defined colours appears beginning with grey, followed consecutively by white, yellow, orange, red, violet, indigo, blue, green, etc. At spacing larger than  $1\text{ }\mu\text{m}$ , the contrast becomes weaker, and at a distance over  $1.5\text{ }\mu\text{m}$ , only alternating green and red colours remain.

For visual measurement of air-film thickness of less than  $1.5\text{ }\mu\text{m}$ , this white light interferometry is normally used. In white light interferometry, for a film thickness from  $0$  to  $0.5\text{ }\mu\text{m}$ , only one single wavelength in the visible spectrum gains maximum intensity. The colours are quite pure and distinct, except from  $0$  to  $0.15\text{ }\mu\text{m}$ , where the wavelengths in the visible spectrum reach their first intensity maximum so close together that the combined interference pattern appears as one fringe, changing from black at zero through grey to white at  $0.125\text{ }\mu\text{m}$  before the first yellow occurs at  $0.175\text{ }\mu\text{m}$ . From  $0.5$  to  $1.0\text{ }\mu\text{m}$ , there are two wavelengths in the visible spectrum that reach a maximum intensity at any given film thickness. From  $1.1$  to  $1.5\text{ }\mu\text{m}$ , there are three such wavelengths, and so on. As the number of wavelengths that reach their maxima simultaneously increases, the colour of the interference fringe appears less distinct, until the superposition is such that the result is practically white illumination. By comparison of the colour of the fringes with the Newton's fringe chart (called the calibration chart), a minimum film thickness of about  $0.05\text{ }\mu\text{m}$  can be readily detected. The accuracy and resolution are about  $0.025\text{ }\mu\text{m}$  for film thickness between  $0.05$  and  $0.5\text{ }\mu\text{m}$ . This resolution decreases to about  $0.10\text{ }\mu\text{m}$  at a film thickness of about  $1.5\text{ }\mu\text{m}$ . It is clear that the most useful operating range for this white light interferometry method lies within the spacing range from  $0.05\text{ }\mu\text{m}$  to  $1.0\text{ }\mu\text{m}$  [Lin & Sullivan, 1972; Tanaka et al., 1984; Mitsuya & Ohkubo, 1987].

The drawback of the white light interferometry method discussed above is apparent: the resolution is too low and the measurement speed is too slow. This problem can be overcome by using a monochromatic light and a solid state photodiode detector [Fleischer & Lin, 1974; Nigam, 1982; Mizoshita et al., 1985; Best et al., 1986; Yamada et al., 1986]. The intensity of the monochromatic interference fringe is converted into electronic signals by a photo-detector. Referring to Figure 2-1 again, as the head medium spacing changes, the intensity at the detector positioned at F is given to be

$$I = I_1 + I_2 + 2\sqrt{I_1 I_2} \cos\left(\frac{2\pi}{\lambda} \delta\right) \quad (2.4a)$$

where  $I_1$  is the intensity of light reflected from the glass disk surface (IL) and  $I_2$  is the intensity of light reflected from the slider's air bearing surface (KN).

The maximum intensity occurs when  $\cos(2\pi\delta / \lambda) = 1$ , and the minimum intensity occurs when  $\cos(2\pi\delta / \lambda) = -1$ . Therefore,

$$\begin{aligned} I_{\max} &= I_1 + I_2 + 2\sqrt{I_1 I_2} \\ I_{\min} &= I_1 + I_2 - 2\sqrt{I_1 I_2} \end{aligned} \quad (2.4b)$$

The clarity of fringes is usually described by their visibility:

$$\gamma = \frac{I_{\max} - I_{\min}}{I_{\max} + I_{\min}} = \frac{2\sqrt{I_1 I_2}}{I_1 + I_2} \quad (2.5)$$

which has a maximum of one when  $I_1 = I_2$ . Although high reflectivities of the surfaces are not a necessary requirement for this two-beam interferometry to achieve a good visibility, they are important to make an efficient use of the total light input, and obtain sharpened fringes of good visibility.

If the phase shift on reflection from the air slider interface is known ( $\delta_{el} = \lambda/2$  for the head slider being dielectric material), the average film thickness can be calculated from (2.4a) using the d.c. part of the intensity signal. The ac intensity fluctuations are caused

by the dynamic vibrations of the slider [Best et al., 1986]. If the values of  $I_{\max}$  and  $I_{\min}$  of the d.c. intensities are known, dynamic measurement can be calibrated in peak-to-peak height without the knowledge of  $\Delta h$ . Figure 2-2 shows the simulation result of the d.c. output of the photo-detector as a function of flying height.

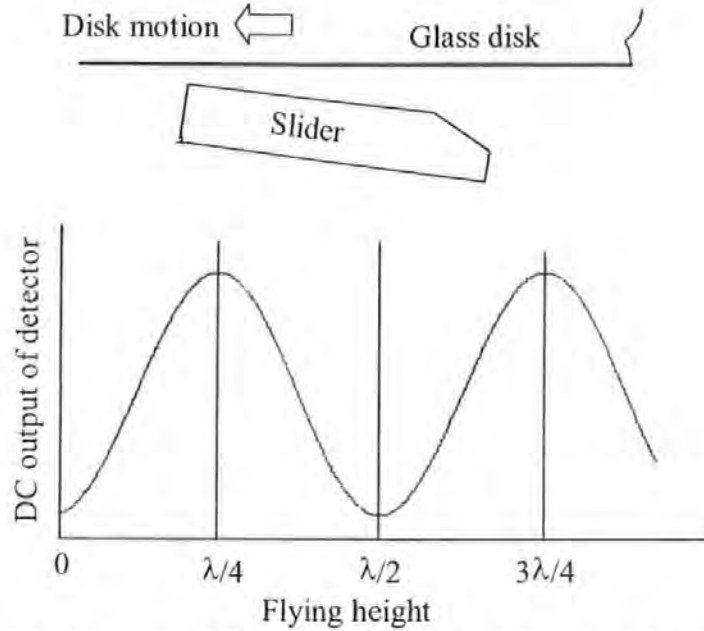


Figure 2-2 D.C. output of the photo-detector as a function of flying height

From [Best et al., 1986], the flying height variation  $\Delta h$ , causing an observed intensity fluctuation  $\Delta I$  around an average intensity  $\bar{I}$ , is given to first order by

$$\Delta I = \pm 4\pi \cos \theta \frac{\sqrt{4I_1 I_2 - (\bar{I} - I_1 - I_2)^2}}{\lambda} \Delta h \quad (2.6)$$

where  $\theta$  is the angle of incidence. The sign of this equation depends on which quadrant the data are taken in. The maximum  $\Delta I$  for a given  $\Delta h$  occurs when  $\bar{I} = I_1 + I_2$  (i.e. the mid value points between  $I_{\max}$  and  $I_{\min}$  of the d.c. intensity curve). Second order effects become important when the dynamic data are taken near the maximum or minimum of the dc intensity curve.

## 2.2 Modern Intensity Interferometry

Intensity Interferometry is one of the popular methods used by the majority of the industry to determine the absolute flying height. Its popularity is based on its accuracy, with no modification to the slider, and ability to view the complete air-bearing surface. The operating principle of this technique is straightforward: A mechanism loads the slider onto a rotating glass disk, the light source illuminates a measurement point on the slider, and the thin film of the air bearing modulates the reflected light over portions of the modulation curve. The flying height is determined by measuring the reflected intensity. Single-wavelength testers are limited by the periodicity of the interference, which introduces ambiguities and a severe loss of measurement sensitivity near the extrema of the curve. To overcome this problem, Phase Metrics Corporation introduced a three-wavelength design for high speed single point measurement [Lacey et al., 1992]. In the meantime, considerations were made and incorporated to compensate the Phase Change on Reflection Phenomenon (PCOR) [Lacey et al, 1993; Lue & Lacey, 1994; Li, 1996; Li & Menon, 1996; Li, 1997], which requires an entirely separate ellipsometric analysis to determine the PCOR for each of the three wavelengths.

Figure 2-3 shows the schematic of a modern intensity interferometry flying-height tester.

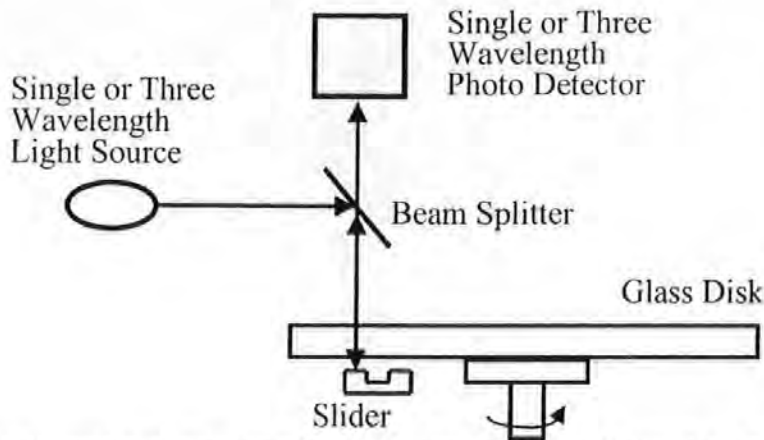


Figure 2-3 Schematic of single or three-wavelength monochromatic interferometer

A beam of light  $E_i$  emitted from the light source passes into the glass disk, as illustrated conceptually in Figure 2-4. At the glass air interface,  $E_{r1}$ , a portion of  $E_i$ , is reflected back into the glass disk. The remaining light  $E_{t1}$  transmits through the air spacing between the glass disk and the slider air-bearing surface. Similar to that at the

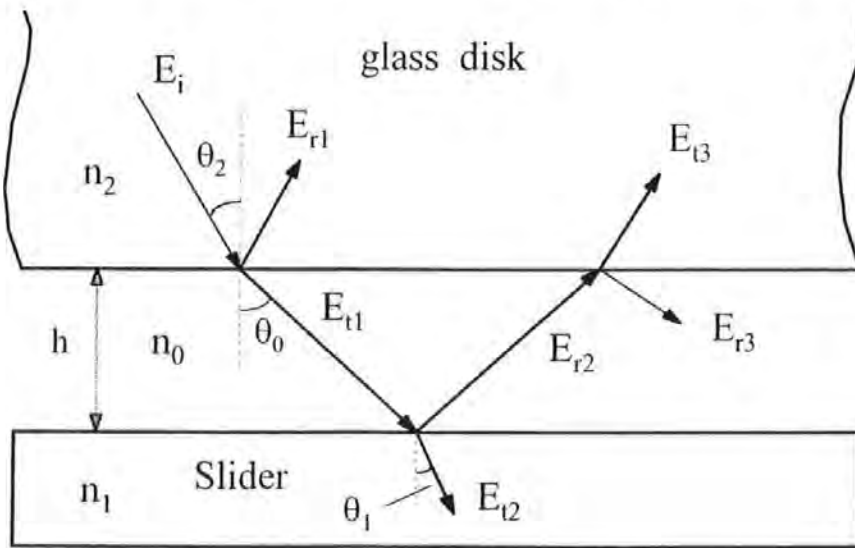


Figure 2-4 Light beam at disk slider interface

glass air interface, a portion of  $E_{t1}$ , labelled as  $E_{r2}$ , is reflected off at the air slider interface.  $E_{t3}$  of this reflected light transmits into the glass disk, and interferes with

$E_{r1}$ . For such a single reflection at normal incidence, the intensity of the interfered light beam is

$$I_s = I_{r1} + I_{t3} + 2\sqrt{I_{r1}I_{t3}} \cos\left(\frac{4\pi}{\lambda}h + \phi_s\right) \quad (2.7)$$

where  $I = \langle E^2 \rangle \equiv$  time average of the electric field squared,  $I_s$  is the intensity of the interfered light beam,  $\lambda$  is the wavelength of the light,  $h$  is the head disk spacing or flying height, and  $\phi_s$  is the phase shift of light when it is reflected off the slider air-bearing surface. This phase shift can be calculated from

$$\phi_s = \pi - \tan^{-1}\left(\frac{2n_0k_1}{n_0^2 - n_1^2 - k_1^2}\right) \quad (2.8)$$

where  $n_0$  is the real index of the air above the slider and  $(n_1 + ik_1)$  is the complex index of the slider material [Born & Wolf, 1989]. If the slider is made of a dielectric material, this phase shift will be  $\pi$  ( $180^\circ$ ). Because the popularly-used slider material ( $\text{Al}_2\text{O}_3/\text{T}_i\text{C}$  ceramic) is not completely dielectric ( $k_1 \neq 0$ ), equation (2.8) does not yield a value of  $\pi$  for  $\phi_s$ . A typical flying height tester using this single reflection theory is the Phase Metrics Dynamic Flying Height Tester (DFHT) [Lacey et al., 1992; McMillan & Talke, 1994].

## 2.3 Oblique Polarisation Interferometry

As stated by de Groot (1996b), a fundamental difficulty of Intensity Interferometry relates to the loss of measurement sensitivity near contact. The intensity modulation for all wavelengths has a vanishing derivative at low flying height. It became evident to many researchers that simply measuring the reflected intensity from the slider-glass



interface is not adequate for production testing of the next generation of disk drives in which head-sliders fly very near to contact, i.e., in the 5 to 20nm height range, even in the presence of substantial PCOR. A polarisation interferometry method was proposed by de Groot (1996a, 1996b), which includes both phase detection and intensity detection. Figure 2-5 shows the basic optical geometry of this polarisation interferometry flying height testing configuration.

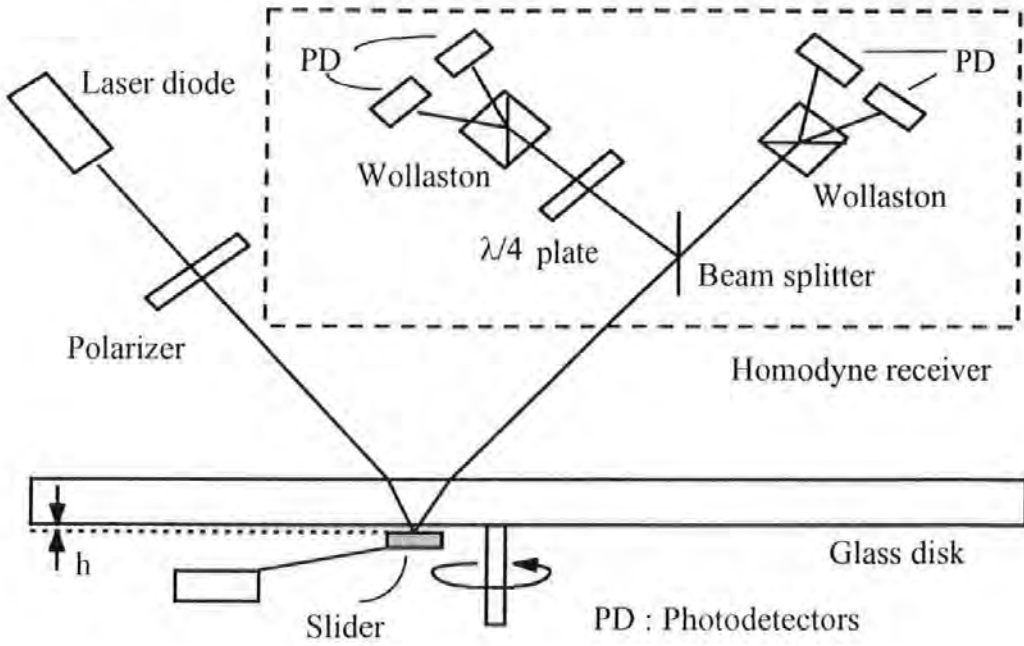


Figure 2-5 Polarisation interferometer for flying height testing

The oblique beam incidence defines two orthogonal polarisation components 's' and 'p', where 'p' polarisation is parallel to the plane of incidence. By using Jones' vectors [Azzam & Bashara, 1987; Born & Wolf, 1989], the electric field of the incident beam can be written as

$$\mathbf{E} = \begin{pmatrix} \mathbf{E}_s \\ \mathbf{E}_p \end{pmatrix} \quad (2.9)$$

For example, if the incident beam is linearly polarised with equal  $s$  and  $p$  components, then  $|\mathbf{E}_s| = |\mathbf{E}_p| = 1/\sqrt{2}|\mathbf{E}|$ . The electric field components  $\mathbf{E}_s$  and  $\mathbf{E}_p$  are complex

numbers, so that any relative phase shift between the two polarisation components can be represented as a complex phase angle. The combined reflections from the slider surface and the surface of the glass disk modify the polarisation state of the beam. The electric field of the reflected beam is given by

$$\mathbf{E}' = \mathbf{S}\mathbf{E} \quad (2.10)$$

where

$$\mathbf{S} = \begin{pmatrix} r_s & 0 \\ 0 & r_p \end{pmatrix} \quad (2.11)$$

and  $r_s$ ,  $r_p$  are the effective reflectivities of the slider-glass combination (interface), which can be represented by the standard thin-film equations for layered media and are given by [Born & Wolf, 1989]

$$r_s(\beta) = \frac{r_{1s} + r_{2s} \exp(i\beta)}{1 + r_{1s} r_{2s} \exp(i\beta)} \quad (2.12a)$$

$$r_p(\beta) = \frac{r_{1p} + r_{2p} \exp(i\beta)}{1 + r_{1p} r_{2p} \exp(i\beta)} \quad (2.12b)$$

where the phase term  $\beta$  is given by

$$\beta = 2kh \cos(\theta) \quad (2.13)$$

The reflection coefficients  $r_{1s}$  and  $r_{1p}$  are for the glass-air boundary, and  $r_{2s}$  and  $r_{2p}$  for the air-slider boundary. The phase  $\beta$  depends on the wave number  $k = 2\pi / \lambda$ , the angle of incidence  $\theta$ , and the flying height  $h$ . The normalised intensity of the reflected beam is

$$I(\beta) = I_s(\beta) + I_p(\beta) \quad (2.14)$$

where

$$I_s(\beta) = |r_s(\beta)|^2 \quad (2.15a)$$

$$I_p(\beta) = |r_p(\beta)|^2 \quad (2.15b)$$

The phase difference between the two polarisation components of the reflected beam is

$$\phi(\beta) = \arg[r_s(\beta)] - \arg[r_p(\beta)] \quad (2.16)$$

The intensity  $I(\beta)$  and the phase difference  $\phi(\beta)$  are measured with a homodyne interferometric receiver, which basically consists of a polariser, a beam splitter, two Wollaston prisms, one  $\lambda/4$  plate and four photodetectors as shown in Figure 2-5. The components of this homodyne receiver are selected and arranged so that the four intensities  $I_1, I_2, I_3, I_4$  detected by the four photodetectors correspond to a sequence of four interference signals separated in phase by exactly  $\pi/2$  radians and are given by

$$I_1 = \alpha \left( I_s + I_p + 2\sqrt{I_s I_p} \cos \phi \right) \quad (2.17a)$$

$$I_2 = \alpha \left( I_s + I_p - 2\sqrt{I_s I_p} \cos \phi \right) \quad (2.17b)$$

$$I_3 = \alpha \left( I_s + I_p + 2\sqrt{I_s I_p} \sin \phi \right) \quad (2.17c)$$

$$I_4 = \alpha \left( I_s + I_p - 2\sqrt{I_s I_p} \sin \phi \right) \quad (2.17d)$$

where  $\alpha$  is a constant coefficient. Then the phase difference between the  $s$  and  $p$  polarisation components can be extracted by means of the formula

$$\phi = \tan^{-1} \left( \frac{I_3 - I_4}{I_1 - I_2} \right) \quad (2.18)$$

Figure 2-6 and Figure 2-7 show the plots of the intensity  $I(\beta)$  and the phase  $\phi(\beta)$  as functions of flying height.

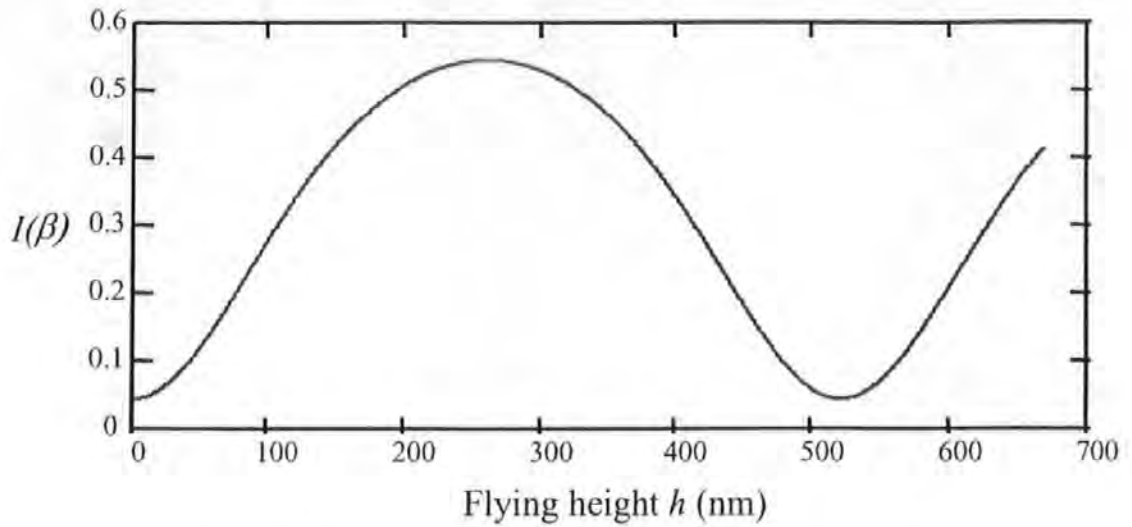


Figure 2-6 Reflected intensity as a function of flying height

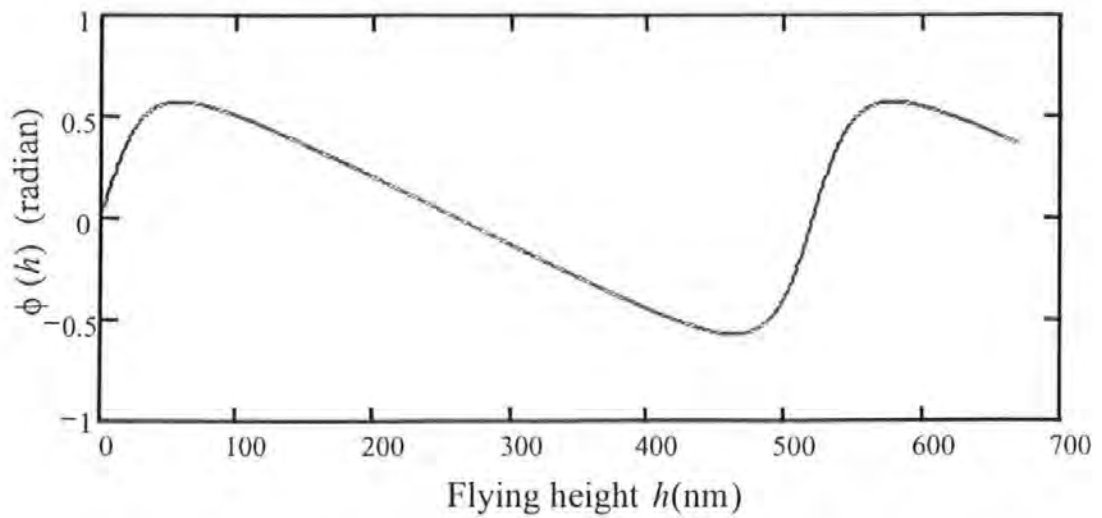


Figure 2-7 Phase difference between the two polarisation components as a function of flying height

The importance of the intensity and phase curves of this polarisation interferometer is that they are complementary. When the intensity curve has a steep slope, the phase is fairly constant; when the intensity is nearly constant, the phase is changing rapidly. Using both curves together means that there is always a way to measure flying height with good sensitivity. Of particular importance is the region near to zero flying height, where the intensity  $I(\beta)$  varies slowly and is therefore a poor measure of flying height,

whereas the phase  $\theta(\beta)$  varies rapidly in this region, with maximum sensitivity at contact (if neglecting the phase change on reflection effect).

## **2.4 Dual-Beam Normal Incidence Polarisation Interferometry Method**

This is the flying height measurement method developed in our laboratory. In the *oblique incidence polarisation interferometry* method described in the last section, intensity information and phase information are used together to determine the flying height down to contact. However, since the light beam is obliquely incident on the glass disk, the sensitivity of its intensity channel is reduced by a factor of  $1/\cos\theta$  ( $\theta \approx 50^\circ$ ) compared with that of the normal incidence. Besides, because all the above mentioned interferometry methods can only perform one point measurement at a time, they cannot measure head slider's pitch and roll, which is also important for the study of head-slider dynamics. In addition, when a real head and magnetic disk assembly needs to be tested for the flying height, they become unsuitable because a specially-made transparent glass disk has to be employed in place of the real magnetic disk. The normal incidence polarisation interferometry method described here can overcome these problems [Liu et al., 2000; Liu et al., 2005].

### **2.4.1 Dual-beam normal incidence polarisation interferometry**

The schematic diagram of the dual-beam normal incidence polarisation interferometer is shown in Figure 2-8. The main part of the interferometer utilises a polarising beam

splitter  $PBS_1$ , two quarter-wave plates  $QW_1$  and  $QW_2$ , two mirrors  $M_1$  and  $M_2$ , and a non-polarising beam splitter  $NPBS_1$  as both a beam splitter and phase shifter.

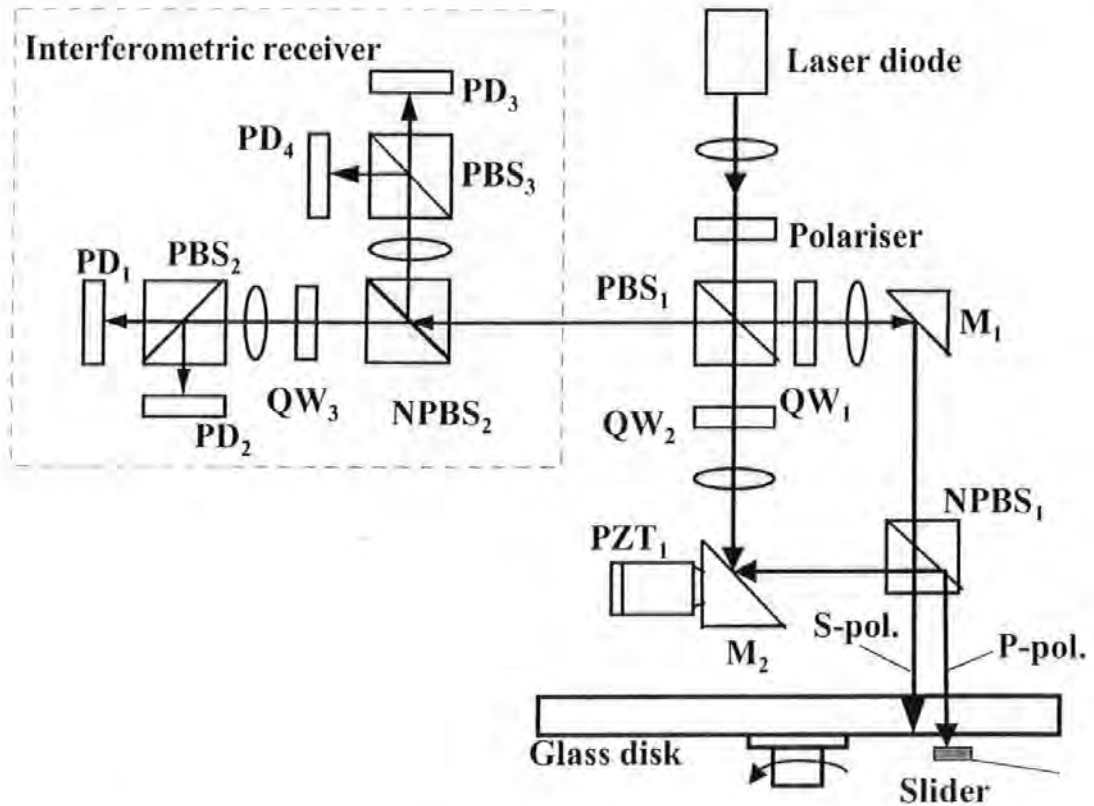


Figure 2-8 Dual-beam normal incidence polarisation interferometer

Mirror  $M_2$  is driven by a piezoelectric translator  $PZT_1$ , which can be used to perform system calibration.  $M_2$  can also be micro-positioned manually to adjust the spacing of the two measurement beams. A laser diode is used as the light source. The p-polarised object beam is focused onto the slider's air-bearing surface and then reflected to the interferometric receiver. The s-polarised reference beam is focused onto an adjacent point on the glass disk and then also reflected on to the interferometric receiver. The interferometric receiver is used to measure the intensity of the returned interfered beam and the phase difference between the two polarised beams. It consists of a non-polarising beam splitter  $NPBS_2$ , two polarising beam splitters  $PBS_2$  and  $PBS_3$ , a quarter-wave plate  $QW_3$ , and four photo-detectors.

For the glass disk being used, anti-reflection coatings are applied to the top surface as shown in Figure 2-9 where  $h$  represents the head-disk spacing to be measured.

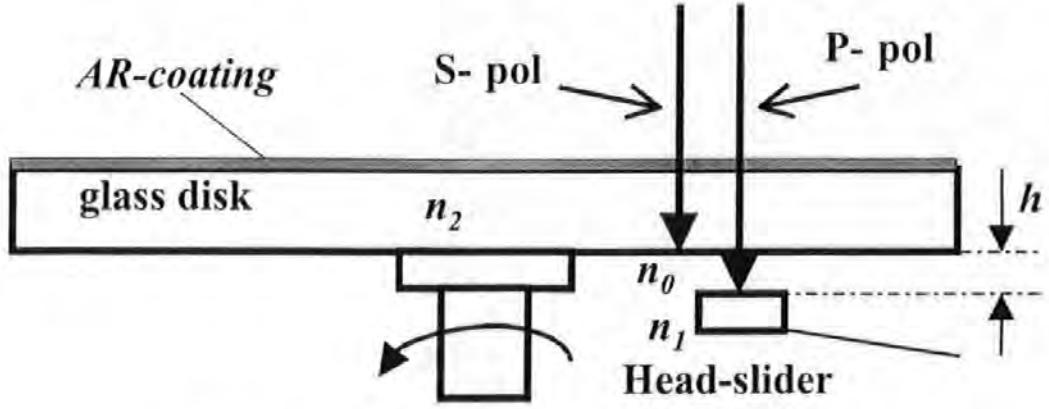


Figure 2-9 Flying height measurement (single layer reflections)

According to the standard thin-film equation [Born & Wolf, 1989], the reflection coefficient of the p-polarised beam is

$$r_p = \frac{r_{p20} + r_{p01} \exp(i\beta_p)}{1 + r_{p20} r_{p01} \exp(i\beta_p)} \quad (2.19)$$

where  $r_{p20} = \frac{n_2 - n_0}{n_2 + n_0}$ ,  $r_{p01} = \frac{n_0 - (n_1 + ik_1)}{n_0 + (n_1 + ik_1)}$ ,  $\beta_p = \frac{4\pi}{\lambda} n_0 h$ ,  $\lambda$  is the wavelength,  $h$  is the

head-disk spacing, and  $n_2$ ,  $n_0$  and  $(n_1 + ik_1)$  are the refractive indices of the glass disk, air, and slider material respectively. So the intensity and phase change of the reflected p-polarised light are

$$I_p = I_{p0} |r_p|^2 \quad (2.20)$$

and

$$\phi_p = \arg(r_p) \quad (2.21)$$

respectively, where  $I_{p0}$  is the intensity of the incident p-pol beam.

The intensity and phase change of the reflected s-pol beam are

$$I_s = I_{s0} |r_{s20}|^2 \quad (2.22)$$

$$\phi_s = \arg(r_{s20}) \quad (2.23)$$

where  $r_{s20} = \frac{n_2 - n_0}{n_2 + n_0}$ ,  $I_{s0}$  is the intensity of the incident s-pol beam.

Therefore, the intensity  $I$  and the phase difference  $\phi$  between the two polarisation components of the return beamed are:

$$I = I_{p0} \left| \frac{r_{p20} + r_{p01} \exp(i\beta_p)}{1 + r_{p20} r_{p01} \exp(i\beta_p)} \right|^2 + I_{s0} |r_{s20}|^2 \quad (2.24)$$

$$\phi = \arg(r_{s20}) - \arg\left(\frac{r_{p20} + r_{p01} \exp(i\beta_p)}{1 + r_{p20} r_{p01} \exp(i\beta_p)}\right) + \theta_0 \quad (2.25)$$

where  $\theta_0$  is the initial phase difference between the two beams. The intensity  $I$  and phase difference  $\phi$  can be detected by the interferometric receiver to be:

$$I = I_s + I_p \quad (2.26)$$

$$\phi = \tan^{-1} \left( \frac{I_2 - I_1}{I_3 - I_4} \right) \quad (2.27)$$

where  $I_1$ ,  $I_2$ ,  $I_3$  and  $I_4$  are the intensities detected by the four photo-detectors respectively.

From (2.24) and (2.25), the intensity  $I$  and the phase difference  $\theta = (\phi - \theta_0)$  as a function of the head-disk spacing  $h$  are plotted in Figure 2-10, where the refractive index of glass disk is 1.5, the index of head-slider is  $n_1 + ik_1 = 2.2 + 0.4i$ , the wavelength of light source (e.g. laser diode) is 670 nm, and  $I_0 = I_{p0} = I_{s0}$  is assumed.



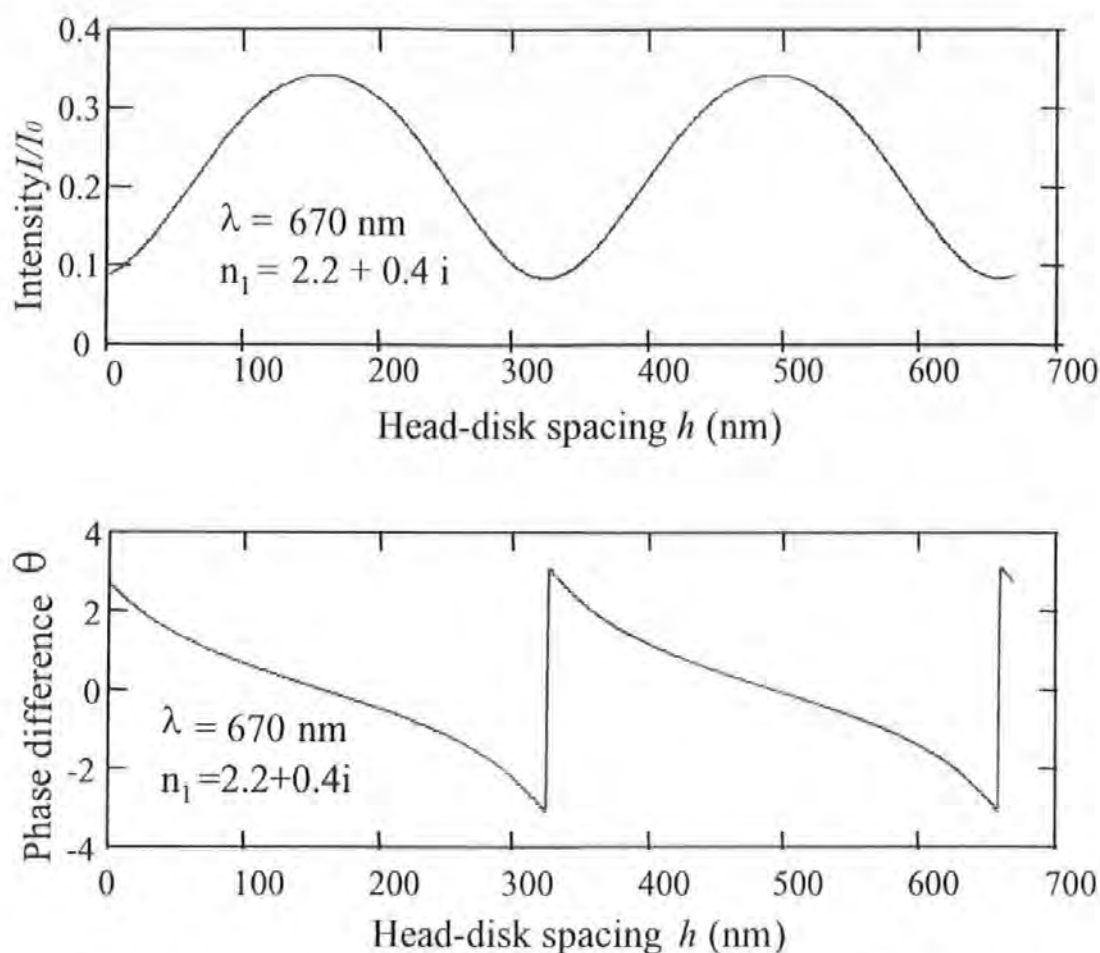


Figure 2-10 Intensity and phase difference as functions of head-disk spacing.

From the intensity curve and phase-difference curve in Figure 2-10, it can be seen that with the measured intensity and phase information, the head-disk spacing can be determined.

## 2.4.2 Relative displacement measuring method

With this dual-beam polarisation interferometry method, when a real magnetic disk is used, the head-disk spacing can be measured as the relative displacement between the head-slider and the disk. In this case, the measurement beam is focused on the back

surface of the head-slider and the reference beam is focused on an adjacent point on the disk, which is shown in Figure 2-11.

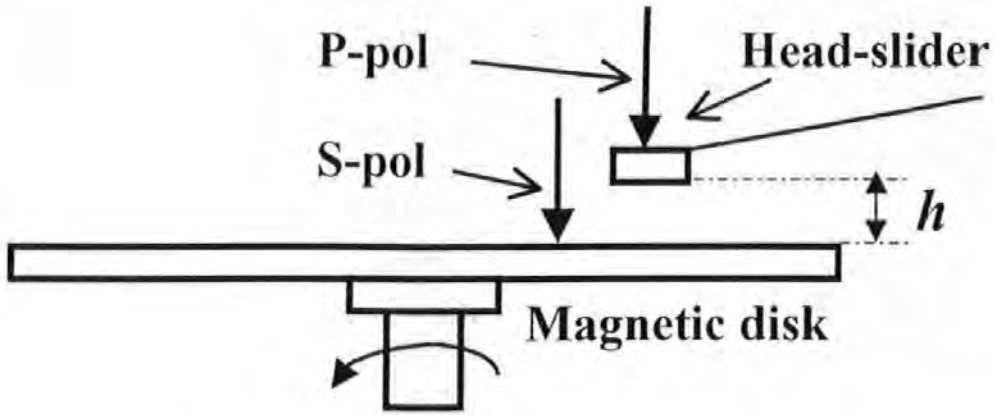


Figure 2-11 Relative displacement measuring method

The head-disk spacing  $h$  has a simple relationship with the phase difference  $\phi$  detected by the interferometric receiver:

$$4\pi h / \lambda + \theta_0 = \phi \quad (2.28)$$

where  $\lambda$  is the wavelength of the laser and  $\theta_0$  is the initial phase difference between the two beams.

## 2.5 Laser Doppler interferometry

Laser Doppler interferometry was also used to measure the dynamics of the head slider in a hard disk drive [Miu et al., 1984; Bogy & Talke, 1985; Miu & Bogy, 1986; Riener & Talke, 1988; Riener et al., 1988; Briggs & Talke, 1989]. Laser Doppler vibrometry (LDV) is used to measure the out-of-plane velocities of the four corners from which the out-of-plane velocity of the geometric centre as well as the pitch and roll of the slider can be calculated. LDV is based on the fact that an acousto-optically modulated light

beam, when reflected from a moving surface, is frequency modulated by the motion of the surface. Such a phenomenon is a particular case of the well-known Doppler effect. The frequency modulation is proportional to the velocity component of the moving surface parallel to the direction of the light beam, which is normally incident on the surface. The resolution limit of the LDV is a function of the resolution capability of the frequency demodulator. Figure 2-12 shows a schematic diagram of the optical and electronic systems of the LDV [Miu & Bogy, 1986]. The output of this instrument is proportional to the normal velocity of the measured surface.

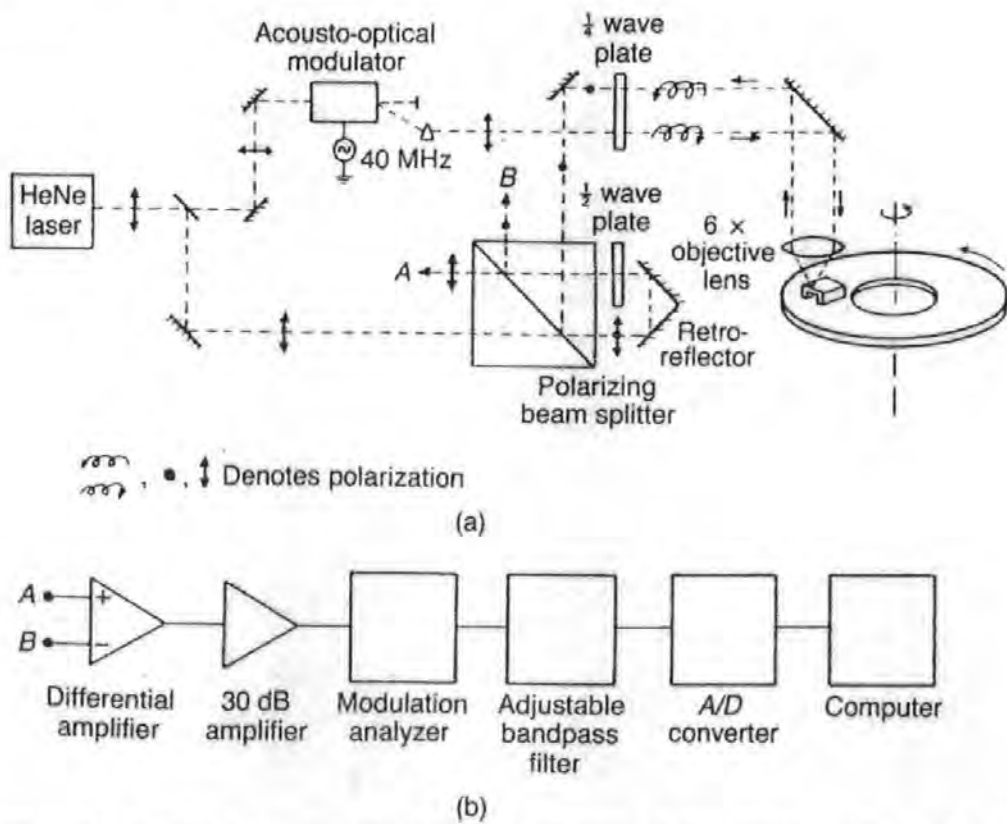


Figure 2-12 Schematic diagram of (a) the optical and (b) electronic systems of the Laser Doppler Vibrometer [Bogy & Talke, 1985]

## 2.6 Capacitance Technique

The measurement of capacitance between two sliding surfaces was extensively used to measure film thickness. Crook (1958, 1961) used the capacitance technique to measure

the film thickness in the contact zone between oil lubricated rollers. Archard and Kirk (1961) also used this technique to measure the film thickness between oil lubricated crossed cylinders. Licht (1968) used the capacitance technique to measure dynamic air film thickness in self-acting foil bearings. This technique has also been used in head medium interfaces.

Neglecting edge effects, the capacitance between the two parallel flat plats of area  $A$  and spacing  $h$  is given by

$$C = \epsilon_0 A / h \quad (2.29)$$

Regardless of edge effects, the capacitance  $C$  of a plate oriented with arbitrary pitch angle  $\alpha$  and roll angle  $\beta$  relative to the disk (see Figure 1-12) can be written as [Millman et al., 1986]

$$C = \epsilon_0 \int_0^L \int_0^B \frac{dxdy}{h_m + x \tan \alpha - y \tan \beta} \quad (2.30)$$

where  $\epsilon_0$  is the dielectric constant of the ambient air and  $L$  and  $B$  are the length and width of the rail. The minimum film thickness  $h_m$  is related to the effective minimum film thickness  $h_m'$  by the following relation:

$$h_m' = h_m + \frac{t_l}{\epsilon_l} + \frac{t_c}{\epsilon_c} \quad (2.31)$$

so that the lubricant and magnetic coating thickness ( $t_l, t_c$ ) can be included with their corresponding dielectric constants  $\epsilon_l$  and  $\epsilon_c$ . Millman et al. (1986) derived the following expression from equation (3.30):

$$\begin{aligned}
C = \frac{\varepsilon_0}{\tan \theta} & \left\{ \left[ B + \frac{\tan \alpha}{\tan \beta} \left( L + \frac{h_m^1}{\tan \alpha} \right) \right] \left[ \ln \left( \frac{B \tan \beta}{\tan \alpha} \left( L + \frac{h_m^1}{\tan \alpha} \right) \right) \right] \right. \\
& - \left( B + \frac{h_m^1}{\tan \beta} \right) \left[ \ln \left( \frac{B \tan \beta}{\tan \alpha} + \frac{h_m^1}{\tan \alpha} \right) \right] \\
& \left. - \left[ \frac{\tan \alpha}{\tan \beta} \left( L + \frac{h_m^1}{\tan \alpha} \right) \right] \left[ \ln \left( L + \frac{h_m^1}{\tan \alpha} \right) \right] + \left( \frac{h_m^1}{\tan \beta} \right) \left[ \ln \left( \frac{h_m^1}{\tan \alpha} \right) \right] \right\}
\end{aligned} \tag{2.32}$$

This equation has three unknowns ( $h_m^1$ ,  $\tan \alpha$ , and  $\tan \beta$ ) and can be solved numerically if the capacitance is known at three different locations. At each location, the film thickness variation,  $h_m$ , causing an observed capacitance fluctuation,  $\Delta C$ , is given by [Best, 1987]

$$\Delta C = \frac{\varepsilon_0 LB}{h_m^1 (h_m^1 + \alpha L + \beta B)} \Delta h \tag{2.33}$$

## 2.7 Summary

The major disk head flying height measurement methods that have been used in hard disk drive industry are reviewed in this chapter. Almost all of them employ optical interferometry technology. The features of these methods are summarised in Table 2-1.

Method	Light source	Testing disk	Measurement resolution	Pitch and roll measurement
Traditional optical interferometry	White light or monochromatic light	Glass disk	Low	No
Modern intensity interferometry	Laser	Glass disk	high	No
Oblique polarisation interferometry	Laser	Glass disk	high	No
Dual-beam normal incidence polarisation interferometry	Laser	Glass disk or real disk	high	Yes
Laser doppler interferometry	Laser	Real disk	medium	Yes
Capacitance technique	Not required	Specially modified head slider and disk	low	No

Table 2-1 Features of hard disk head flying height measurement methods

# **Chapter 3 Real Time Head Disk Spacing Measurement Methods**

The readback transducer method is a non-invasive flying height measurement method by which the flying height or head-disk spacing variation can be determined from the readback signal. Three methods are described here, including amplitude of the readback signal measurement method,  $PW_{50}$  (pulse width at 50% of the peak value) of readback signal measurement method, and thermal signal detection method. A special  $PW_{50}$  measurement method, the  $PW_{50}$  parameter estimation method, is particularly presented and described in detail. Experimental study and result analysis are performed in Section 5.2.

## **3.1 Analysis of Amplitude of Readback Signal Measurement Method**

This method is used to measure the head-disk spacing change by detecting the variation of the readback signal amplitude [Shi et al., 1987; Eaton & Baldwinson, 1997; Schardt, 1998; Novotny & Hsiao, 1998]. The magnitude of the readback signal depends on many parameters. Assuming longitudinal magnetisation and unit permeability of the recording medium, Wallace (1951) derived the following equation for the readback voltage of a sinusoidally recorded signal:

$$e(t) = 4\pi(10^{-8})N\alpha W \left( \frac{\mu}{1+\mu} \right) Mv \left[ 1 - \exp\left(-\frac{2\pi\delta}{\lambda}\right) \right] G(\lambda) \exp\left(-\frac{2\pi\delta}{\lambda}\right) \cos\left(\frac{2\pi vt}{\lambda}\right) \quad (3.1)$$

where

$e(t)$  voltage of readback signal (V)

$t$  time (s)

$N$  number of turns of the readback coil

$\alpha$  head efficiency

$W$  head width (cm)

$\mu$  core permeability

$M$  peak remanent magnetisation of the recording medium (EMU/cc)

$v$  tangential velocity (cm/s)

$\delta$  medium thickness (cm)

$\lambda$  wavelength of recorded signal (cm)

$G(\lambda)$  gap factor

$d$  spacing between the head and medium (cm)

For a given disk file operating at a given track, the quantities  $N$ ,  $\alpha$ ,  $\mu$ ,  $v$ ,  $\lambda$  are constants.

Let  $E$  denote the amplitude of  $e(t)$ , then from (3.1)

$$E = f(M, \delta) \exp(-2\pi d / \lambda) \quad (3.2)$$

where  $f(M, \delta)$  is a function deducible from (3.1). Since  $f(M, \delta)$  is non-negative, it can be further written as

$$f(M, \delta) = C \exp[-2\pi s(M, \delta) / \lambda] \quad (3.3)$$

where  $C$  is a positive constant.

Thus,

$$E = C \exp[-2\pi(d + s) / \lambda] \quad (3.4)$$



Here we may view  $s(M, \delta)$  as a “virtual spacing variation” introduced by the non-uniform  $M$  and  $\delta$ , and we note that  $d$  and  $s$  are linearly superimposed. We will neglect  $s$  in the following further discussion.

Now let  $d_0$  denote an arbitrary reference spacing (not necessarily the steady flying height),  $\Delta d$  the spacing variation, and  $A$  the amplitude modulation of the readback signal resulting from the spacing variation defined by

$$d = d_0 + \Delta d \quad (3.5)$$

and

$$A = [E(d) - E(d_0)] / E(d_0) \quad (3.6)$$

then it follows from (3.4)~(3.5) that

$$\Delta d = -\frac{\lambda}{2\pi} \ln(1 + A) = -\frac{\lambda}{2\pi} \ln \frac{E(d)}{E(d_0)} = -\frac{v}{2\pi f} \ln \frac{E(d)}{E(d_0)} \quad (3.7)$$

where  $f$  is the recording frequency,  $E(d_0)$  and  $E(d)$  are amplitudes of the readback signal at spacing of  $d_0$  and  $d$  respectively.

From (3.7), it is seen that the head-disk spacing change can be determined by measuring the amplitude of the readback signal before and after the change. It should be stressed that equation (3.7) is not accurate for modern disk drives because of the assumptions being made in its derivation process. Therefore this method is suitable to be used for qualitative evaluation of the head disk spacing variation.

## 3.2 PW<sub>50</sub> of Readback Signal Measurement Method

The PW<sub>50</sub> of readback signal measurement method is based on the detection of the pulse width of the read-back signal. Since the head disk spacing variation provides a

proportional change in pulse width by measuring the pulse width change, flying height variation can be determined [Klaassen & van Peppen, 1994]. In Chapter Chapter 1, from equation (1.7), it has been shown that under some conditions, the  $PW_{50}$  has a linear relationship with head disk spacing or flying height. Another rational derivation of the relationship between the flying height change and the pulse width variation is given below.

A readback signal is shown in Figure 3-1, which is supposed to be read from a series of

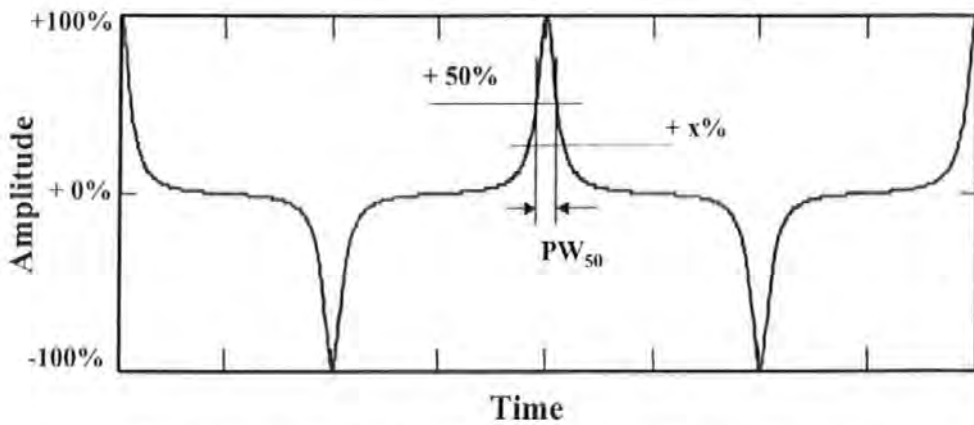


Figure 3-1 Definition of  $PW_x$ , the pulse width at a slicing level of  $x\%$  ( $-100 \leq x \leq +100$ ).

isolated transitions written on the disk. The shape of this waveform will be characterised by its pulse width  $PW_x$  at  $x$  percent ( $-100 \leq x \leq +100$ ) of the peak to base-line amplitude. The pulse length at  $x$  percent is represented by  $PL_x$  which is the length of the pulse projected along the track. For a disk travelling at velocity  $v$  with respect to the head,  $PL_x = vPW_x$ . Wallace (1951) demonstrated that the magnetic spacing loss can be represented by a non-causal (no phase shift) low-pass filter, whose cutoff frequency decreases with increasing flying height. For an increase  $\Delta d$  in the flying height  $d$ , this “spacing loss filter” has a transfer function  $H(\omega)$  given by:

$$H(\omega) = \exp(-\Delta d |\omega| / v) = \exp(-2\pi \Delta d / \lambda) \quad (3.8)$$

where  $\lambda$  is the wavelength along the track of a sinusoidal signal at an angular frequency  $\omega$ . This filter is applied to the readback signal at flying height  $d$  to arrive at the signal at flying height  $d + \Delta d$ .

For pulses with Lorentzian shape (which is usually the close approximation of the readback signal shape), we can easily calculate what happens to the pulse width for a varying flying height. A Lorentzian readback pulse shape is given by:

$$e(t) = \frac{e(0)}{1 + \left( \frac{2t}{PW_{50}} \right)^2} \quad (3.9)$$

where  $e(0)$  is the peak amplitude, and  $PW_{50}$  is the pulse width at half maximum value.

The Fourier transform of this Lorentzian pulse is:

$$F_i(\omega) = \frac{\pi}{2} e(0) PW_{50} \exp(-|\omega| PW_{50} / 2) \quad (3.10)$$

Filtering the Lorentzian pulse of (3.9) by the spacing loss filter of (3.8) produces an output pulse whose Fourier transform  $F_o(\omega)$  is equal to the product of  $F_i(\omega)$  and  $H(\omega)$ :

$$F_o(\omega) = \frac{\pi}{2} e(0) PW_{50} \exp \left[ - \left( \frac{PW_{50}}{2} + \frac{\Delta d}{v} \right) |\omega| \right] \quad (3.11)$$

Transforming  $F_o(\omega)$  back to the time domain gives out the Wallace spacing loss weighted pulse:

$$e'(t) = \frac{e'(0)}{1 + \left( \frac{2t}{PW'_{50}} \right)^2} \quad (3.12)$$

which, again, has a Lorentzian shape. A Lorentzian pulse is obviously shape invariant under the Wallace head medium spacing loss.

The pulse width at half maximum value is now:

$$PW'_{50} = PW_{50} + 2 \frac{\Delta d}{v} = \frac{PL_{50} + 2\Delta d}{v} \quad (3.13)$$

From (3.13) we can conclude that (for Lorentzian pulses) pulse width measurement yields an incremental measurement of flying height  $d$ . If we conduct a difference measurement before and after a change of  $\Delta d$  in the flying height  $d$ , the increment in pulse width is:

$$\Delta PW_{50} = PW'_{50} - PW_{50} = S_{50} \frac{\Delta d}{v} \quad (3.14)$$

where the measurement sensitivity factor  $S_{50}$  is defined as:

$$S_{50} = \frac{\Delta PL_{50}}{\Delta d} \quad (3.15)$$

For a Lorentzian pulse obviously  $S_{50} = 2$ . More generally, for a slicing level of  $x$  percent, it can be shown that for Lorentzian pulse:

$$\Delta PW'_x = PW'_x - PW_x = 2 \frac{\Delta d}{v} \sqrt{\frac{100 - |x|}{|x|}} \quad (3.16)$$

and therefore, the sensitivity factor at slicing level  $x$  is given by:

$$S_x = \frac{\Delta PL_x}{\Delta d} = 2 \sqrt{\frac{100 - |x|}{|x|}} \quad (3.17)$$

It looks from equation (3.17) that the sensitivity  $S_x$  increases when lowering the slicing level  $x$ . However, the uncertainty in the measurement will also increase due to baseline noise and the more shallow slope of the readback pulse towards its base (see Figure 2.1). Klaassen and van Peppen (1994) provided a method and circuitry, which can directly measure the pulse width from isolated read-back pulse signals. Some advanced Digital Storage Oscilloscopes/Disk Drive Analyzers (e.g. products of Lecroy and Tektronix) provide as well the function of measuring the  $PW_{50}$  from isolated read-back pulse signals. Zhu et al. (1998) also tried to provide a digital sampling technique to measure

the  $PW_{50}$  of isolated readback pulse signals. It was claimed the method could be used under relatively low sampling rates. In section 3.3, a parameter estimation method will be presented, which can be used to determine the  $PW_{50}$  without the restriction of the readback pulse signals being isolated.

### 3.3 $PW_{50}$ Parameter Estimation Method for Flying Height Determination

It has been mentioned in section 3.2 that the  $PW_{50}$  measuring method is one of the non-invasive readback transducer flying height testing methods. The methods developed by researchers so far provided ways which can only be used to measure or determine the  $PW_{50}$  from isolated readback pulse signals. A good question is thus, is it possible to measure or determine the pulse width from a normal readback signal from a hard disk drive? In this section, we propose a parameter estimation method that can be used to measure the  $PW_{50}$  so as to determine the flying height. Different from other  $PW_{50}$  measurement methods, this method is not restricted by the isolated readback pulse signal requirement. So it has the potential of being able to be used to measure the flying height variation in real time in a normally operated hard disk drive, thus may further provide a possibility for the measured flying height variation to be used for real time flying height control. The theoretical basis of this method is presented in the following discussion.

The write/read process in digital magnetic recording is generally modelled as a pulse amplitude modulation system of the form

$$s(t) = \sum_k a_k p(t - KT) + n(t) \quad (3.18)$$

where  $a_k \in \{-1, 1\}$  is the input sequence,  $P(t)$  is the effective channel impulse response (or dibit response),  $T$  is the symbol period, and  $n(t)$  is the additive noise [Moon & Carley, 1990; Immink, 1989]. Equivalently, the readback signal can be written as

$$s(t) = \sum_k b_k h(t - KT) + n(t) \quad (3.19)$$

where  $h(t)$  is the transition response and  $b_k$  is the transition sequence given by

$$b_k = a_k - a_{k-1}, \quad b_k \in \{-2, 0, 2\} \quad (3.20)$$

The effective channel impulse response and transition responses are therefore related by

$$p(t) = h(t) - h(t - T) \quad (3.21)$$

The transition response is generally approximated using a Lorentzian function given by

$$h(t) = \frac{A_h}{PW_{50}} \frac{1}{1 + \left( \frac{2t}{PW_{50}} \right)^2} \quad (3.22)$$

For a given head-disk assembly,  $A_h$  is a constant, which must be known in order to use this estimation method. In real application or in calibration process, this constant can be determined from isolated readback signal pulses. In simulation, it can be selected as a reasonable value, and here we set it to 1. An equivalent discrete time model of the storage channel can be obtained by passing the readback signal through a matched-filter and a symbol-rate sampler. The schematic diagram for the resulting discrete time system is shown in Figure 3-2, where the readback sample  $r_k$  is given by  $r_k = y_k + n_k$ ,  $y_k$  and  $n_k$  denote signal and noise samples respectively [Shafiee & Moon, 1996].

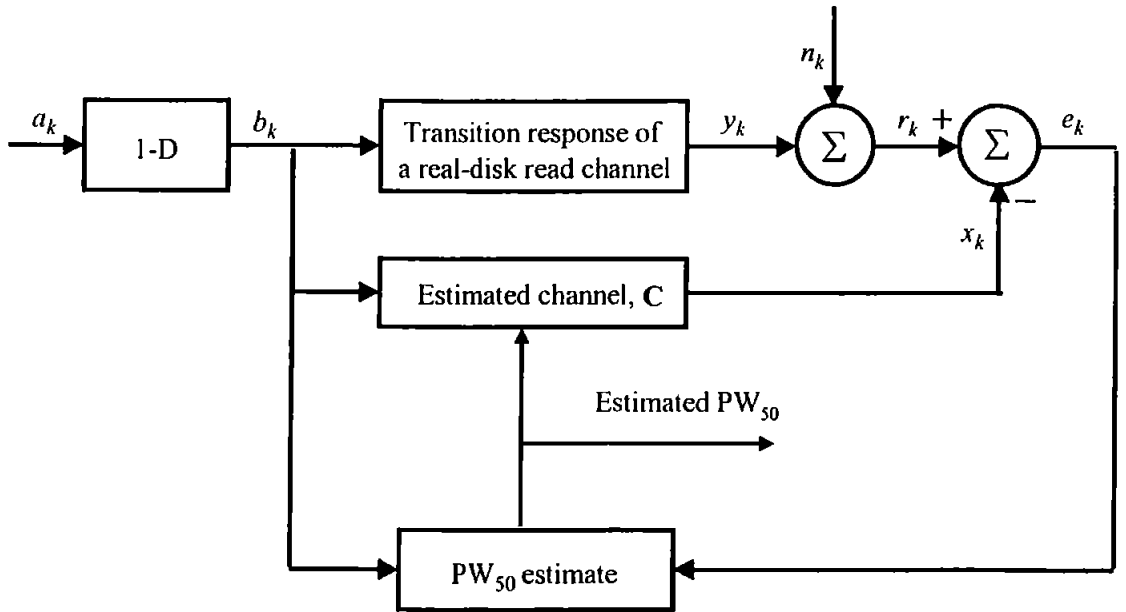


Figure 3-2 PW50 estimation model

The problem now in fact becomes a channel identification problem. As in all channel identification methods, it is assumed that linear superposition holds for the channel to be estimated. For Lorentzian transition response, since it is a function of only one parameter, channel identification reduces to estimation of the  $PW_{50}$  parameter, which is just what we need. With the same method as that used by Shafiee and Moon (1996), our approach is to minimise the mean square error between  $r_k$  and the predicted channel output  $x_k$ , with respect to the desired channel parameter  $PW_{50}$ .

$x_k$  is given by

$$x_k = \sum_{m=-L}^L b(k-m)c(m) = C^T B_k \quad (3.23)$$

where  $L$  is an integer that should be selected large enough so that  $c(k)|_{|k|>L}$  are small enough to be neglected,  $B_k$  is a vector of length  $2L+1$  containing transition sequence,  $C$  is a vector of length  $2L+1$  containing estimated transition response coefficients, which is given by

$$c(m) = \frac{1}{PW_{50}} \frac{1}{1 + \left( \frac{2m}{PW_{50}} \right)^2} \quad (3.24)$$

With  $PW_{50}$  as the only parameter to be estimated, the mean square error (MSE) can be written as

$$E\{e_k^2\} = E\{(r_k - C^T B_k)^2\} \quad (3.25)$$

To find the minimum mean square error (MMSE) estimate of  $PW_{50}$ , taking the derivative of the MSE function with respect to  $\rho = PW_{50}$ , we obtain

$$\frac{\partial E(e_k^2)}{\partial \rho} = -2 \frac{\partial C^T}{\partial \rho} E(B_k r_k) + 2 \frac{\partial C^T}{\partial \rho} E(B_k B_k^T) C \quad (3.26)$$

$$= 2 \frac{\partial C^T}{\partial \rho} (R_b C - u) \quad (3.27)$$

Where  $R_b$  is the correlation matrix of  $B_k$ , and  $u$  denotes the cross-correlation of  $r_k$  and  $B_k$ . This derivative is equal to zero for the optimal value of  $\rho$ . If the channel is perfectly Lorentzian, this occurs when  $R_b C - u$  is zero, which corresponds to the unbiased minimum-mean-square-error (MMSE) solution. When the channel deviates from Lorentzian,  $R_b C - u$  will no longer be zero for the optimal value of  $\rho$ , which corresponds to a biased MMSE solution.

To obtain an expression for adaptive or on-line estimation of  $\rho$ , we drop the expectation in Equation (3.26) which then yields

$$\frac{\partial (e_k^2)}{\partial \rho} = -2 \left( \frac{\partial C^T}{\partial \rho} B_k \right) e_k \quad (3.28)$$

This expression represents the gradient of the square error function with respect to  $\rho$ .

To follow the real (optimal) value of  $PW_{50}$ , the value of  $\rho$  should be updated in the opposite direction of the gradient according to the following equation [Hayes, 1996]



$$\rho(k+1) = \rho(k) + \beta \left( \frac{\partial C^T}{\partial \rho} B_k \right) e_k \quad (3.29)$$

where  $\beta$  is the step size. The update process of the value  $\rho$  continues until it converges to the optimal value. This adaptive updating algorithm is called the least mean square (LMS) algorithm [Hayes, 1996]. For the updating process to be convergent, the selection of the step size  $\beta$  must be within a certain range. This is left to be investigated in the experimental study section.

The above adaptive estimation scheme originates from the mean-square-error strategy. This problem, however, could also be formulated in terms of maximum likelihood (ML) estimation of the unknown  $PW_{50}$  parameter. Assuming the noise is additive white Gaussian (AWG) and with  $PW_{50}$  as the only parameter, a likelihood function is defined as

$$P(r | \rho) = \frac{1}{(2\pi\sigma_n^2)^{N/2}} \exp \left( -\frac{1}{2\sigma_n^2} \sum_{k=0}^{N-1} (r(k) - x(k, \rho))^2 \right) \quad (3.30)$$

where  $N$  is the number of observation made,  $\sigma_n^2$  is the noise variance, and  $x(k, \rho)$  shows the explicit dependence of the readback signal on the unknown parameter. With  $C$  denoting the transition response and  $x(k, \rho) = C^T B_k$ , the first and second order derivatives of the logarithm of this function with respect to  $\rho$  are given by

$$\frac{\partial \ln P(r | \rho)}{\partial \rho} = \frac{1}{\sigma_n^2} \sum_{k=0}^{N-1} (r(k) - x(k, \rho)) \frac{\partial C^T}{\partial \rho} B_k \quad (3.31)$$

$$\frac{\partial^2 \ln P(r | \rho)}{\partial \rho^2} = \frac{1}{\sigma_n^2} \sum_{k=0}^{N-1} \left\{ (r(k) - x(k, \rho)) \frac{\partial^2 C^T}{\partial \rho^2} B_k - \left( \frac{\partial C^T}{\partial \rho} B_k \right)^2 \right\} \quad (3.32)$$

The ML estimate is found by setting the derivative of the likelihood function (Equation (3.31)) equal to zero. The solution to this equation can be obtained by using numerical

methods such as the Newton-Raphson algorithm [Kay, 1993], which will not be further investigated here.

### 3.4 Thermal Signal Detection Method

Thermal signal detection is another head-disk spacing measurement method proposed in recent years. It is intended to be used for the measurement of disk topography or dynamic flying height by detecting and processing the readback signal from a magnetoresistive (MR) head in a hard disk drive [Abraham, 1996; Smith, 1999; Sundaram et al., 1999]. Changes in flying height or head-disk spacing modulate both the envelope of the readback signal and its mean value. To clarify the statement, we introduce two nomenclatures: magnetic spacing and thermal spacing, although both of them refer to the flying height or head-disk spacing. While the envelope is related to the magnetic spacing, the mean value is a function of the thermal spacing. The thermal spacing signal is the result of Joule heating whereby some of the thermal energy generated in the MR head dissipates into the air film between the head and disk. Changes in head flying height alter the localised heat transfer and hence the temperature and resistance of the MR head. Abraham (1996) has shown that the MR head voltage resulting from thermal spacing can be approximated as:

$$e_{thermal}(t) = C_0 + C_1 \beta I^3 R^2 d(t) \quad (3.33)$$

where  $e_{thermal}$  is the MR voltage due to its temperature,  $t$  is time,  $C_0$  and  $C_1$  are constants that depend on the geometry and thermal properties of the MR element and adjacent shields,  $\beta$  is the temperature coefficient of resistance for the MR material,  $I$  and  $R$  are the MR current and electrical resistance respectively, and  $d$  is the head disk

spacing or flying height. From (3.33), we note that the flying height can be determined from the measured thermal signal. However, most disk drives use an arm-mounted electronic module circuitry (AEM) which is used to amplify the head output signal and usually includes a high pass filter. The filter provides the necessary AC coupling for the read channel but also distorts the thermal signal. This filter can be generally represented by a first order approximation as:

$$H_{AEM}(s) = K_{AEM} \frac{s}{s + a} \quad (3.34)$$

where  $K_{AEM}$  is the gain of the AEM at recording frequencies, and  $a$  is the cut-off frequency of the high pass filter. The AEM output signal is thus the convolution of  $e_{thermal}$  and the impulse response of the filter which is given by:

$$e_{AEM}(t) = K_{AEM} \int_{-\infty}^{+\infty} e_{thermal}(t - \tau) [\delta(\tau) - a \exp(-a\tau)] d\tau \quad (3.35)$$

The transfer function for an inverse filter that will correct for the AEM filter is:

$$H_{INV}(s) = \frac{1}{K_{AEM}} \frac{s + a}{s + b} \quad (3.36)$$

where  $b$  is a suitably chosen pole so that the inverse filter can be easily realized as an analogue circuit if desired, whereas the flying height variation component we are interested in can still be restored. If the AEM output voltage is sampled with a fixed sampling time interval, the true thermal signal of the MR head can be estimated by applying the matched z-transform to (3.36) and using the resulting infinite impulse response (IIR) digital filter to process the sampled sequence  $e_{AEM}(n)$ . It should be noted that although an inverse filter can partly correct this distortion, it is impossible for some low frequency components to be restored completely. Therefore, in that case, the

thermal detection method is suitable only for the measurement of spacing variation above a certain changing rate.

# **Chapter 4 Hard Disk Drive Operation Failure and Head Disk Spacing Variation Suppression**

Some background introduction has been given in Section 1.6. In this chapter, analyses are carried out first to reveal the reasons of hard disk drive operation failure under vibration conditions. Then an active flying height control method is proposed to suppress the head disk spacing variation under vibration conditions. Experimental study and simulation are performed in section 5.3 and 5.4.

## **4.1 Analysis of Hard Disk Drive Operation Failure under Vibration Conditions**

Analyses will be performed from two aspects, firstly from the mechanics of the head suspension arm, the rotating disk, and the aerodynamics of the head-slider's air-bearing, secondly from the characteristics of the head position servo control mechanism.

### **4.1.1 Related research within the Lab**

Some research has been performed within the laboratory with regard to the characterisation of disk drive operation under hostile conditions [Tunstall et al., 2000].

Firstly, finite element analysis software was used to model the resonant characteristics of the disk itself. Secondly, a test rig has been constructed to allow the hard disk drive to be vibrated at accelerations of up to 50g [Jenkins et al., 1999]. A personal computer is used to control the sweeps of the vibration and acceleration that the disk drive receives. When the disk drive is being vibrated, the computer can write and read data to and from it, and monitor the time taken for the data to be correctly transferred. As the amplitude of the vibration increases (with fixed vibration frequency), the disk drive's data transfer rate slows down, eventually leading to a completely failure of data transfer. Thirdly, piezo materials were used to construct micro sensors to characterise the resonance properties of the disk platter and suspension arm. To measure the bending of the suspension arm, a thin (28  $\mu\text{m}$ ) sheet of poly vinylidene fluoride (PVdF) was bonded to the suspension arm to measure the average strain. Another PVdF sensor was used to measure the disk's displacement. The sensor used was a cantilever that only introduces subtle changes to the system, with one end rigidly bonded to the drive's chassis in a manner that pre-tensions the cantilever against the disk. Any movement of the disk would therefore bend the cantilever from its static position. To record the signals from the sensors, they were connected to a 12-bit data acquisition board that is capable of sampling the signal at up to 200 kHz. Some experimental results can be found in [Tunstall et al., 2000].

#### **4.1.2 Analysis on head-disk spacing variation**

The Mathcad simulation software used for this section is listed in section 7.1.2. In this section, a theoretical model is developed for head disk spacing variation under vibration conditions.

In a hard disk drive, the head slider is mounted through a flexure or a gimbal to the load beam, which is mounted to the arm of the rotary or linear servo actuator. To analyze the head disk spacing variation under vibration conditions, the displacements of head slider and disk need to be first derived. The head suspension and disk assembly is shown in Figure 4-1.

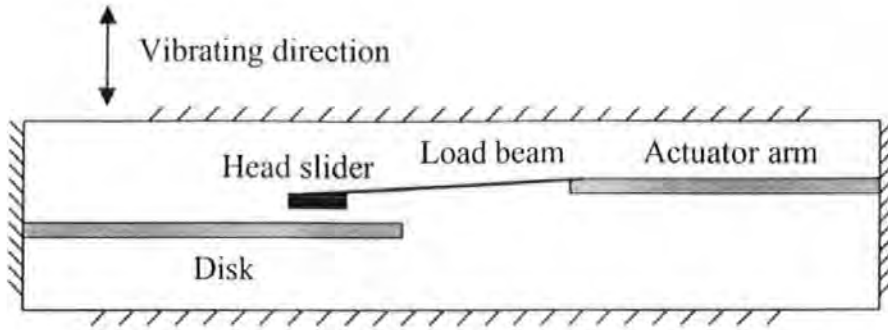


Figure 4-1 Head suspension and disk assembly in a hard disk drive.

To make the discussion simple, we assume both the actuator arm and the load beam have only one vibration mode respectively. The following derivation is made based on the theory of vibration [Shabana, 1996].

The hard disk drive is assumed to be vibrated vertically with a frequency of  $\omega$ . The actuator arm is forced to vibrate and the end displacement of the actuator arm (i.e., the end connected with the load beam) relative to the disk drive base can be derived as

$$d_A = Y_0 \beta_A \cdot \sin(\omega t - \psi_A) \quad (4.1)$$

where  $Y_0$  is the vibration amplitude of the hard disk drive,  $\psi_A$  is the phase angle given as

$$\psi_A = \tan^{-1} \left( \frac{2\xi_A \omega / \omega_A}{1 - (\omega / \omega_A)^2} \right) \quad (4.2)$$

$\omega_A$  and  $\xi_A$  are the natural frequency and damping factor of the actuator arm respectively, and  $\beta_A$  is the magnification factor given by

$$\beta_A = \frac{1}{\sqrt{\left(1 - (\omega / \omega_A)^2\right)^2 + (2\xi_A \omega / \omega_A)^2}} \quad (4.3)$$

The displacement of the head slider relative to the end of the actuator arm (i.e., the end connected with the load beam) can thus be approximated by:

$$d_{SA} = Y_0 \beta_A \beta_L \cdot \sin(\omega t - \psi_A - \psi_L) \quad (4.4)$$

where the phase angle  $\psi_L$  is given as

$$\psi_L = \tan^{-1} \left( \frac{2\xi_L \omega / \omega_L}{1 - (\omega / \omega_L)^2} \right) \quad (4.5)$$

the magnification factor  $\beta_L$  is given by

$$\beta_L = \frac{1}{\sqrt{\left(1 - (\omega / \omega_L)^2\right)^2 + (2\xi_L \omega / \omega_L)^2}} \quad (4.6)$$

$\omega_L$  is the natural frequency of the load beam with the effect of air bearing considered, and  $\xi_L$  is its damping factor. The displacement of the head slider relative to the disk drive base can therefore be derived as:

$$\begin{aligned} d_{SI} &= d_A + d_{SA} \\ &= Y_0 \cdot \beta_A \cdot \sqrt{(1 + \beta_L \cos \psi_L)^2 + (\beta_L \sin \psi_L)^2} \cdot \sin(\omega t - \psi_A - \psi_{AL}) \end{aligned} \quad (4.7)$$

where the phase angle  $\psi_{AL}$  is given by

$$\psi_{AL} = \tan^{-1} \left( \frac{\beta_L \sin \psi_L}{1 + \beta_L \cos \psi_L} \right) \quad (4.8)$$

Similarly, we assume the disk platter has only one vibration mode as well. In the same vibration, the displacement of the disk platter relative to the disk drive base can be written as

$$d_D = Y_0 \beta_D \cdot \sin(\omega t - \psi_D) \quad (4.9)$$

where the phase angle  $\psi_D$  is given by



$$\psi_D = \tan^{-1} \left( \frac{2\xi_D \omega / \omega_D}{1 - (\omega / \omega_D)^2} \right) \quad (4.10)$$

$\omega_D$  and  $\xi_D$  are the natural frequency and damping factor of the disk platter respectively with the effect of air bearing considered, and the magnification factor  $\beta_D$  is given as

$$\beta_D = \frac{1}{\sqrt{(1 - (\omega / \omega_D)^2)^2 + (2\xi_D \omega / \omega_D)^2}} \quad (4.11)$$

The disk vibration will act on the head slider and produce an additional displacement via the air bearing. The induced slider displacement relative to the disk platter can thus be approximated as

$$d_{SD} = Y_0 \beta_D \beta_L \cdot \sin(\omega t - \psi_D - \psi_L) \quad (4.12)$$

The induced displacement of the head slider relative to the disk drive base can be thus derived as

$$\begin{aligned} d_{S2} &= d_D + d_{SD} \\ &= Y_0 \cdot \beta_D \cdot \sqrt{(1 + \beta_L \cos \psi_L)^2 + (\beta_L \sin \psi_L)^2} \cdot \sin(\omega t - \psi_D - \psi_{DL}) \end{aligned} \quad (4.13)$$

where the phase angle  $\psi_{DL}$  is given by

$$\psi_{DL} = \psi_{AL} = \tan^{-1} \left( \frac{\beta_L \sin \psi_L}{1 + \beta_L \cos \psi_L} \right) \quad (4.14)$$

The total displacement of the slider relative to the disk drive base can thus be derived as:

$$\begin{aligned} d_S &= d_{S1} + d_{S2} \\ &= Y_0 \sqrt{(1 + \beta_L \cos \psi_L)^2 + (\beta_L \sin \psi_L)^2} \cdot \\ &\quad \sqrt{(\beta_A \cos \psi_A + \beta_D \cos \psi_D)^2 + (\beta_A \sin \psi_A + \beta_D \sin \psi_D)^2} \cdot \\ &\quad \sin(\omega t - \psi_{AL} - \psi_{AD}) \end{aligned} \quad (4.15)$$

where the phase angle  $\psi_{AD}$  is given by

$$\psi_{AD} = \tan^{-1} \left( \frac{\beta_A \sin \psi_A + \beta_D \sin \psi_D}{\beta_A \cos \psi_A + \beta_D \cos \psi_D} \right) \quad (4.16)$$

Since the mass and stiffness of the disk are far bigger than those of the head slider suspension, the displacement of the disk induced by the slider vibration can be neglected. So the displacement of the head slider relative to the disk, i.e. the head disk spacing variation can be approximated as

$$d = d_S - d_D \quad (4.17)$$

The amplitude of  $d$  can be derived to be:

$$A_d = Y_0 \sqrt{A_1^2 + A_2^2} \quad (4.18)$$

where  $A_1 = \delta \cos(\psi_{AL} + \psi_{AD}) - \beta_D \cos \psi_D$ ,

$A_2 = \delta \sin(\psi_{AL} + \psi_{AD}) - \beta_D \sin \psi_D$ , and

$$\delta = \sqrt{(1 + \beta_L \cos \psi_L)^2 + (\beta_L \sin \psi_L)^2} \cdot \sqrt{(\beta_A \cos \psi_A + \beta_D \cos \psi_D)^2 + (\beta_A \sin \psi_A + \beta_D \sin \psi_D)^2}$$

From equation (4.18), the frequency response of the amplitude of the head-disk spacing variation is plotted in Figure 4-2, where the natural frequencies of disk, load beam, and actuator arm are 700Hz, 1000Hz, and 2300Hz respectively, all the damping factors are chosen to be 0.02 (Note these are typical parameter values from previous experimental measurement.)

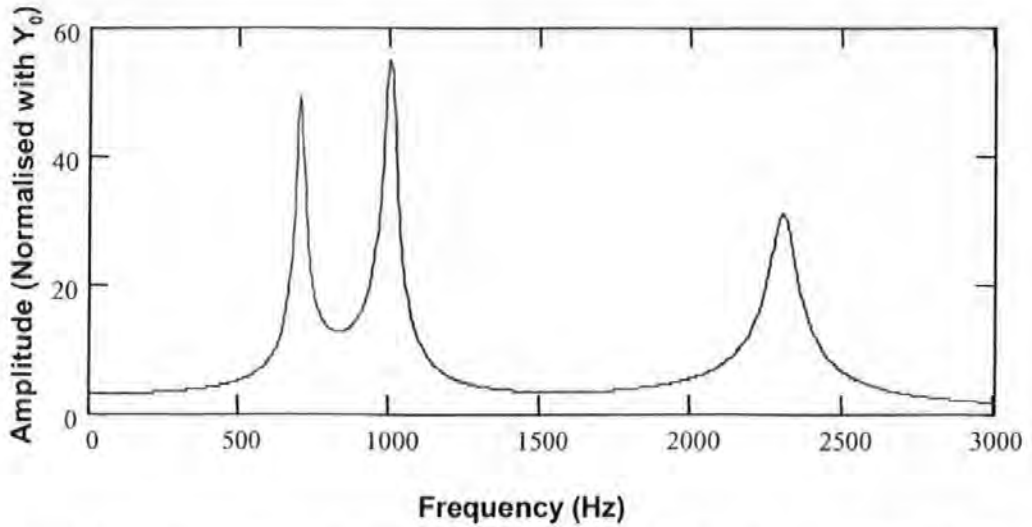


Figure 4-2 Frequency response of the amplitude of head disk spacing variation.

From simulation result, it can be seen that all the vibration modes will induce large amplitude of head disk spacing variation, which will result in data read/write failure under vibration conditions.

#### 4.1.3 Head position servo control mechanism.

It has been known that disk vibration will also produce head position error or track misregistration (TMR) [Srikrishna & Kasetty, 2000]. The block diagram of the servo control loop of a hard disk drive is shown in Figure 4-3, where  $G_C(s)$  is the controller transfer function,  $G_p(s)$  is the mechanical plant (including the actuator) transfer function,  $R$  is the reference position input,  $Y$  is the position output,  $PES$  is the position error signal,  $N_T(s)$  is the torque disturbance,  $N_E(s)$  is the electrical noise, and  $N_D(s)$  is the disk vibration disturbance.

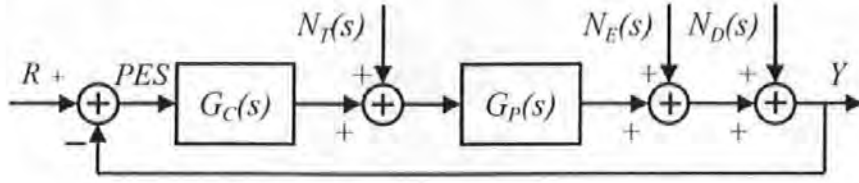


Figure 4-3 Block diagram of head position servo loop.

We do not discuss torque disturbance  $N_T(s)$  and electrical noise  $N_E(s)$  here. What we are interested in is the amplitude of the position error signal (PES) resulted from the disk vibration disturbance  $N_D(s)$ . From Figure 4-3, we have:

$$\frac{PES(s)}{N_D(s)} = S(s) = -\frac{1}{1 + G_C(s)G_P(s)} \quad (4.10)$$

where  $S(s)$  is the sensitivity function of the servo loop. Its frequency response has the general shape as shown in Figure 4-4 (which is generated by simulation described in section 7.1.2.2).

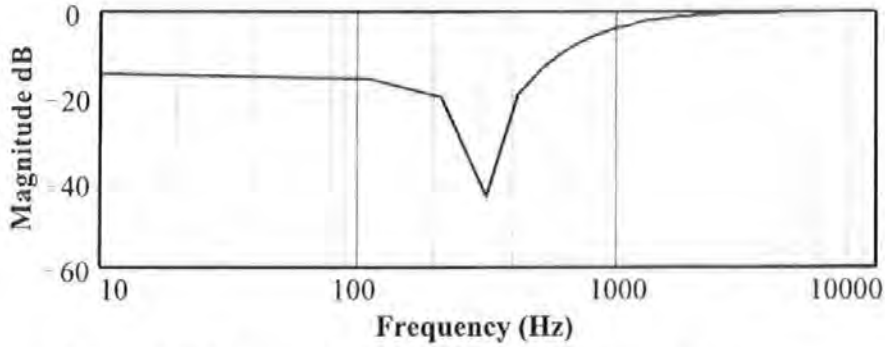


Figure 4-4 Frequency response of the sensitivity function.

The frequency response of the sensitivity function reflects the disturbance suppression performance of the servo control loop. It is apparent that the wider the servo loop bandwidth, the higher its disturbance suppression capability is. When the disturbance frequency is higher than the bandwidth, the servo loop loses its suppression ability for such frequency. It should be mentioned that if the vibration direction is absolutely

vertical to the disk surface, the vibration induced TMR should have less effect on disk read/write failure than the vibration induced head-disk spacing variation.

Experimental study and result analysis are performed in Section 5.3.

#### **4.1.4 Summary**

Analytical models are developed for head disk assembly and head position servo control mechanisms to analyze the operation failure of hard disk drives under vibration conditions. Theoretical and experimental results show that all the vibration modes of the head disk assembly will induce larger amplitude of head disk spacing variation and tend to result in read/write failure under vibration conditions. The TMR resulted from disk vibration can be suppressed by the servo control loop to some extent when the vibration frequency is within its bandwidth. When the frequency is beyond the bandwidth, the servo loop loses its capability. Therefore, under vibration conditions, the read/write process in a hard disk drive will tend to become failure more likely around the vibration modes of the head disk assembly. Vibrations above a certain frequency, say, the servo loop bandwidth, also have the tendency to result in operation failure because of the weakening of the suppression ability of the servo loop.

## **4.2 Head Disk Spacing Variation Suppression via Active Flying Height Control**

### **4.2.1 Introduction**

With the flying height getting lower and lower, it becomes more important to keep the head-disk spacing constant during disk operation. This is because the flying height variation will cause modulation of the readback signal due to the spacing loss [Wallace, 1951] and increase the bit-error-rate of the read channel. Drives operating under shock and vibration conditions have a high possibility of undesirable head disk contact, which will deteriorate the tribological performance of the head disk interface and its reliability. Therefore, active flying height control is highly desirable. Because of the difficulty of real time detection of the flying height variation in a real operated hard disk drive, very little research has been reported in this area. [Gao et al., 2000] investigated the active actuation and control of a miniaturised suspension structure in HDDs to reduce head-disk friction/wear and suppress induced vibrations. However, since the displacement of the head suspension arm is used for the feedback control signal, their investigation falls into the active vibration control of the suspension arm itself, not the control of head disk spacing variation.

#### **4.2.2 Research on micro actuators within the Lab**

Significant research work has been carried out with regard to the development of micro actuators and their applications to hard disk drives [Jenkins et al. 1999]. The main applications involve fine data tracking and head flying height control. In this laboratory, three possible routes have been identified to develop actuators for these applications [Jenkins et al. 1999]: bonded piezoelectric actuators, embedded piezoelectric actuators, and composite piezoelectric arms.

#### **4.2.2.1 Bonded piezoelectric actuators**

Piezoelectric bulk ceramic element such as lead zirconate titanate (PZT) can be attached close to the root of the load beam suspension arm to either move the arm up or down, or suppress induced motion of the arm at resonant frequencies [Cunningham et al., 1995]. When operated in this way, the actuator should be as thin as possible, but of comparable thickness to that of the cantilever. This is because of the two main reasons: one is to optimise the cantilever actuation [Cunningham et al., 1997]; the other is to prevent the actuator from affecting the cantilever's dynamic characteristics. This technique has been used previously for micro-positioning and active vibration control [Jenkins et al., 1997]. Another route involving bonded actuators is the use of composite piezoelectric materials. It is possible to make a piezoelectric thick film by combining piezoelectric powder and epoxy resin [Clegg et al., 1997]. However, films produced in this method have a much lower piezoelectric activity compared to bulk ceramics. And due to the flexibility of the film, it is difficult to couple this activity adequately to the underlying structure. In order to circumvent this problem, glass fibre and/or carbon fibre have been used to reinforce composite films [Chilumbu et al., 1999]. These films offer much improved rigidity, compared to standard composites, resulting in increased effective bending moments of the arm.

#### **4.2.2.2 Embedded piezoelectric actuators**

A simple method to form a micro actuator is to embed piezoelectric stacks into the head suspension system. The piezoelectric stacks are embedded at the end of the aluminium frame arm, while the current stainless steel load beam remains unchanged. On stack is

embedded such that when actuated, it produces motion of the arm in x-y plane, i.e., for fine tracking. The other stack is embedded such that it produces motion in z-axis. As both piezoelectric stacks are embedded at the end of the aluminium frame, resonance effects within the aluminium arm do not affect the performance of the piezoelectric stacks.

#### **4.2.2.3 Composite piezoelectric arms**

The idea is that the whole load suspension arm is fabricated from carbon and glass fibre, with PZT distributed within the composite framework to make it active. The composite arm would be used for the head flying height control, while the current aluminium frame would have a piezoelectric stack embedded to produce fine motion for data tracking. However, the fabrication of such composite arms is time consuming and requires several stages of intricate work, and thus may be unattractive for commercial adoption in current disk drive mass producing factories.

#### **4.2.3 Real time active flying height variation control**

In this section, a real time active control method is presented to suppress the flying height or head-disk spacing variation, in which thermal signal detection method is used for real time detection of the flying height variation. In Section 3.4, we discussed the thermal signal flying height variation detection method, where we have known that most disk drives use arm-mounted electronic module circuitry (AEM) to amplify the



head output signal and this usually includes a high pass filter. This filter can generally be represented by a first order approximation as:

$$H_{AEM}(s) = K_{AEM} \frac{s}{s + a} \quad (4.11)$$

where  $K_{AEM}$  is the gain of the AEM at recording frequencies,  $a$  is the cut-off frequency of the high pass filter.

The adjustment of the head suspension arm can be accomplished in a number of ways in real applications [Jenkins et al., 1999]. We can either use embedded piezoelectric actuators [Chilumbu et al., 2000] or bonded piezo films to the suspension arm [Gao & Swei, 2000]. In the case a piezo film is used, the film is bonded to one side of the suspension arm (beam), as is shown in Figure 4-5.

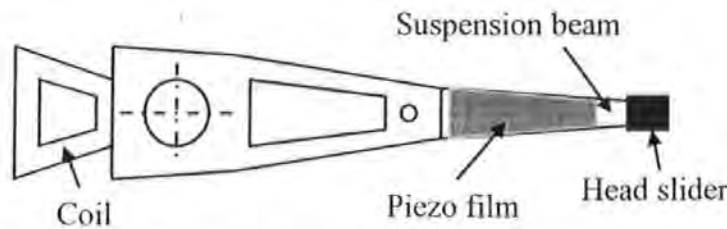


Figure 4-5 Head assembly in HDDs with bonded piezo film on the suspension arm.

When a voltage  $V$  is applied to the piezo film, a steady state displacement at the slider end will be produced as:

$$d = K_1 V \quad (4.12)$$

where  $K_1$  is a constant. In a working HDD where the disk is rotating at a constant speed, the displacement dynamics will be determined only by the characteristics of the suspension arm (beam) and the aerodynamics of the slider's air bearing. As the response of the piezo film actuator itself has a very wide bandwidth, its dynamic mode can be neglected here. Therefore, the dynamic relationship between the voltage applied to the piezo film and the displacement resulted can be simplified as:

$$\frac{d(s)}{V(s)} = G(s) = K \frac{\omega_{sn}^2}{s^2 + 2\xi_s \omega_{sn} s + \omega_{sn}^2} \frac{\omega_{an}^2}{s^2 + 2\xi_a \omega_{an} s + \omega_{an}^2} \quad (4.13)$$

where  $\omega_{sn}$  and  $\xi_s$  are the natural frequency and damping ratio of the suspension beam,  $\omega_{an}$  and  $\xi_a$  are the natural frequency and damping ratio of the slider's air bearing,  $K$  is a constant.  $\omega_{an}$  (a few tens of kilohertz) is usually much larger than  $\omega_{sn}$  (a few kilohertz). In the case we only consider vibrations below one kilohertz, the model can be further simplified as:

$$G(s) = K \frac{\omega_{sn}^2}{s^2 + 2\xi_s \omega_{sn} s + \omega_{sn}^2} \quad (4.14)$$

Now, the flying height variation suppression mechanism can be shown in Figure 4-6.

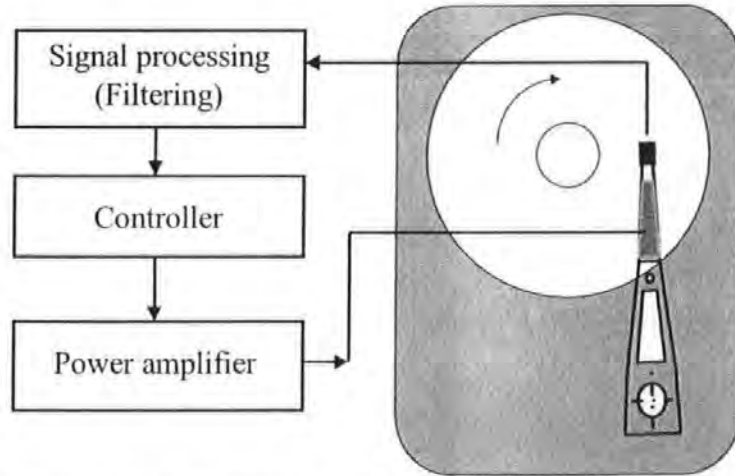


Figure 4-6 Flying height variation suppression mechanism

The block diagram of the closed-loop control system for flying height variation control is shown in Figure 4-7.

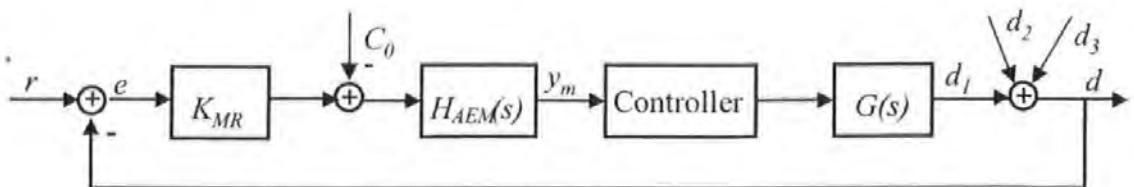


Figure 4-7 Block diagram of closed-loop control system

In the diagram,  $r$  is the reference input,  $e$  is the error between the reference input and the head-disk spacing signals  $K_{MR} = C_1 \beta I^3 R^2$  consists of parameters from equation (3.33),  $C_0$  is the constant shown in equation (3.33) in section 3.4,  $y_m$  is the output of the measurement point,  $d_1$  is the displacement output of the piezo film actuator,  $d_2$  is the disk spinning resulted head-disk spacing or flying height which can be treated as a constant,  $d_3$  is the vibration resulted head-disk spacing whose effect on the total spacing is intended to be suppressed here, and  $d$  is the total head-disk spacing.

The single pole of the high-pass filter is usually around  $a = 325000$ . Typical parameters for the suspension and slider's air bearing are given in the plant transfer function as:

$$G(s) = K \frac{902500}{s^2 + 32.3s + 902500} \cdot \frac{2025000000}{s^2 + 5220s + 2025000000} \quad (4.15)$$

The values of the constant parameter  $K_{MR}$ ,  $K_{AEM}$  and  $K$  do not need to be known at this stage. They are to be considered and compensated in the following controller design procedure.

The problem now becomes designing a servo control system to suppress the effect of vibrational disturbances on the head-disk spacing. For a good servo control system, the following performance is usually desired:

- a) good static performance that means zero or small static error;
- b) good dynamic performance that means fast response or wide bandwidth but low overshoot;
- c) good robustness that means system performance is invariant to or less affected by parameter variations and disturbances.

For this of our particular problem here, from the engineering point of view, a conventional controller that is easy to be designed and implemented will be practical and good enough. If we use a proportional-integral (PI) compensator to compensate the

high-pass filter  $H_{AEM}(s)$ , a proportional-integral-differential (PID) and two lead compensators to compensate the two second-order vibrational modes of the plant, the transfer function of the controller becomes:

$$G_C(s) = \frac{s + z_1}{s} \frac{s + z_2}{s + p_2} \frac{s + z_3}{s + p_3} K_{PID} \frac{(s + 1/T_d)(s + 1/T_i)}{s} \quad (4.16)$$

The selection of controller parameters values, simulation experiments, and result analysis are performed in Section 5.4.

#### 4.2.4 Summary

A novel active flying height control method is proposed to suppress the flying height or head-disk spacing variation in hard disk drives under vibration conditions. Real-time spacing variation signals derived from the readback signal of MR or GMR read/write heads are used for feedback control. Simulation results show that this active flying height control can effectively suppress the head-disk spacing variation, therefore the performance and reliability of the HDDs can be well improved when working in vibration conditions.

# Chapter 5 Experimental Study

## 5.1 Experimental Equipment

### 5.1.1 Electrodynamic shaker

The test facility has been constructed by previous researchers to allow the hard disk drive to be vibrated over a 10kHz bandwidth at accelerations of up to 50g (where g is the unit for acceleration due to gravity,  $9.81\text{ms}^{-2}$ ) [Tunstall, 2002], which is depicted in Figure 5-1.

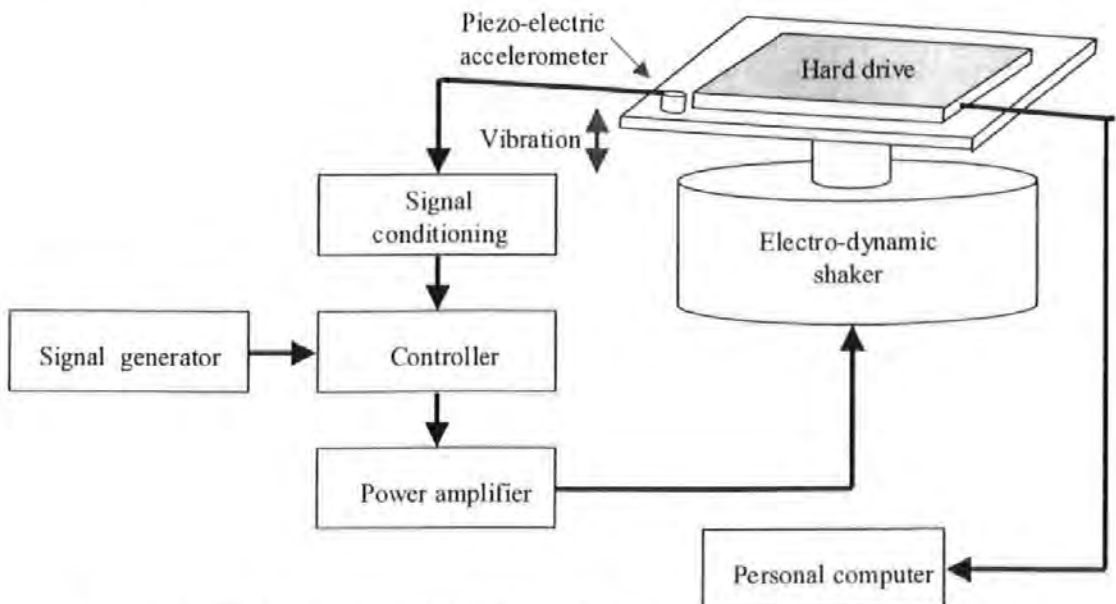


Figure 5-1 Block diagram of the electrodynamic shaker and its control system

The hard disk drive is rigidly clamped to an aluminium plate and is vibrated by an electro-dynamic shaker, Environmental Equipments Ltd type 1501. The axis of vibration is arranged to be through the spindle of the drive so as to simulate, closely, a drive mounted in a desktop PC experiencing vibration. A piezo-electric accelerometer sensor mounted to the plate (see Figure 5-2) monitors vibrations experienced by the disk drive, and provides a feedback signal to the control system.

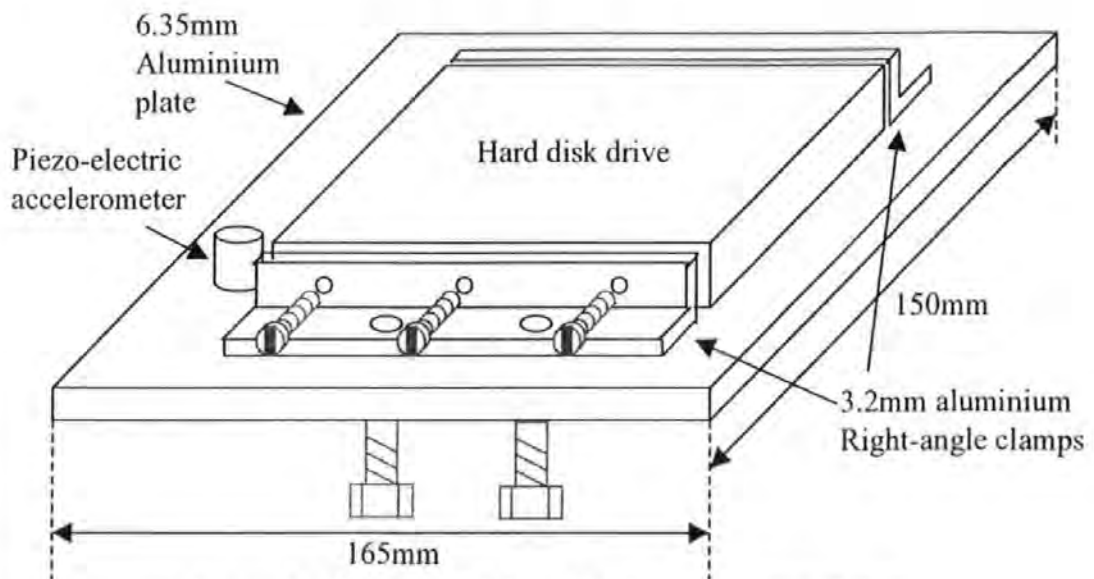


Figure 5-2 Mounting plate of the electrodynamic shaker

It is therefore critical to ensure that the disk drive is solidly mounted to the plate, and in turn the plate to the shaker. It is also extremely important for meaningful results that vibrations detected by the accelerometer match closely with those experienced by the drive. These have been done by several improvements in the design of plate and mountings [Tunstall, 2002].

### 5.1.2 Shaker control system

A block diagram of the system used to test hard disk drives under vibration is shown in Figure 5-1. The whole apparatus is located in a laminar air flow bench, the Lamarflo from Laminar Flow Systems Ltd, which provides a filtered air source with positive pressure. This ensures that the local environment is free of contaminants that could potentially damage any drive operating without its lid. A personal computer (PC) is used to control the sweeps of vibration and acceleration that the drive receives, but this function is not needed in the experiments performed for my research.

When the drive is vibrated, the control PC is able to transfer data with it, while simultaneously monitoring the time taken for the data to be correctly transferred. Software developed by Jepson [Jepson, 1997], enables the control PC to transfer a file comprising solely of '1's, '0's, or a pseudo random file to the drive under test. The software also has the ability to allow the selection of the data transfer direction. The performance of the drive can be assessed by either reading directly from the drive, or written to the drive. In the case of the latter, the data must then be read back to confirm that the data was correctly written. As will be shown in the experiments, and can be easily understood, the transfer rate of a drive is found to be dependent on the frequency and acceleration at which it is vibrated. As the magnitude of vibration increases the drive's transfer rate slows down, eventually leading to total data transfer failure. This is the result of the error-correction system becoming progressively defeated, and calling for increasingly more track re-reads.

The Environmental Equipments Ltd 1531 power oscillator is used as a final stage amplifier that is capable of providing a driving source for the shaker with frequencies of up to 10 kHz and sinusoidal accelerations of up to 50g. The power amplifier can accept an external input or provide sinusoidal waveforms by itself.

Software written by Tunstall [Tunstall, 2002] using the basic input/output (BIOS) commands, controls which sector and track is read or written with which head. It

enables the head to be positioned at different circumferential points on the disk of the drive to be tested.

### 5.1.3 Digital storage oscilloscopes

A Lecroy LT344 Waverunner Digital Oscilloscope is used. Its main specification data is listed below:

- Number of channels: 4
- Frequency range: DC to 500MHz
- Sample rate: 500MS/s max sampling rate
- Memory depth: 250kpts per channel
- Others: Flat panel TFT-LCD colour display with VGA, GPIB, RS-232-C, Built-in 3.5 inch floppy disk drive, Centronics.

### 5.1.4 FIR filter

In this chapter, lowpass and bandpass digital filters will be used to extract useful signals from the raw signals obtained from experiments. The general form of the difference equation for a linear, time-invariant, digital filter is [Shenoi, 2006]:

$$y(n) = \sum_{k=0}^M b_k x(n-k) - \sum_{k=1}^N a_k y(n-k)$$

The above equation represents an IIR filter.

The difference equation describing a FIR filter is given by:



$$y(n) = \sum_{k=0}^M b_k x(n-k)$$

$$= b_0 x(n) + b_1 x(n-1) + \dots + b_M x(n-M)$$

The FIR filters have the following features:

- The FIR filters are always stable because there is no feedback from past outputs.
- The FIR filters can be designed easily to meet the required magnitude response in such a way that it achieves a constant group delay. Group delay is defined as  $\tau = -(d\theta/d\omega)$ , where  $\theta$  is the phase response of the filter. The phase response of a filter with a constant group delay is therefore a linear function of frequency. It transmits all frequencies with the same amount of delay, which means that there will be no phase distortion and the input signal will be delayed by a constant when it is transmitted to the output.
- The samples of the unit impulse response of an FIR filter are the coefficients of the difference equation describing it.
- The higher of the order of FIR filter (i.e., the bigger the  $M$  in the equation is), the closer it is to the ideal filter.

The process of deriving filter coefficients that satisfies a given specifications is called filter design. Computer-aided design tools are widely available for designing digital filters. In this work, Matlab is used.

## 5.2 Real Time Head Disk Spacing Measurement

### 5.2.1 Amplitude of readback signal measurement method

Experiments are made to evaluate the amplitude detection method. The experiments are carried out by mounting a commercial hard disk drive on the electro-dynamic shaker [see Section 5.1]. Readback signals under vibration conditions are sampled and stored by a digital storage oscilloscope [see Section 5.1.3]. Figure 5-3 shows the readback signal from the hard disk drive that is vibrated vertically at a frequency of 5.8 kHz by the shaker. From measurement we know the recording frequency  $f$  of the hard disk drive is 12.8 MHz. Here in this experiment, the sampling rate of the digital oscilloscope is selected as 50 MHz. Note that the selection of the sampling rate of the oscilloscope  $f_s$  depends on the vibration frequency  $f_t$  under testing, and has little to do with the recording frequency for the purpose of this experiment. As the maximum number of samples  $N_s$  of a stored data file by the oscilloscope is 50000 and we set the parameter to this value all the time, the sampling rate is also determined by the number of modulation cycles  $N_{cycle}$  that is needed for the reliable detection of the amplitude of the readback signal. Therefore, we use

$$f_s = \frac{N_s \cdot f_t}{N_{cycle}} \quad (5.1)$$

Normally we need  $N_{cycle}$  larger than 5.

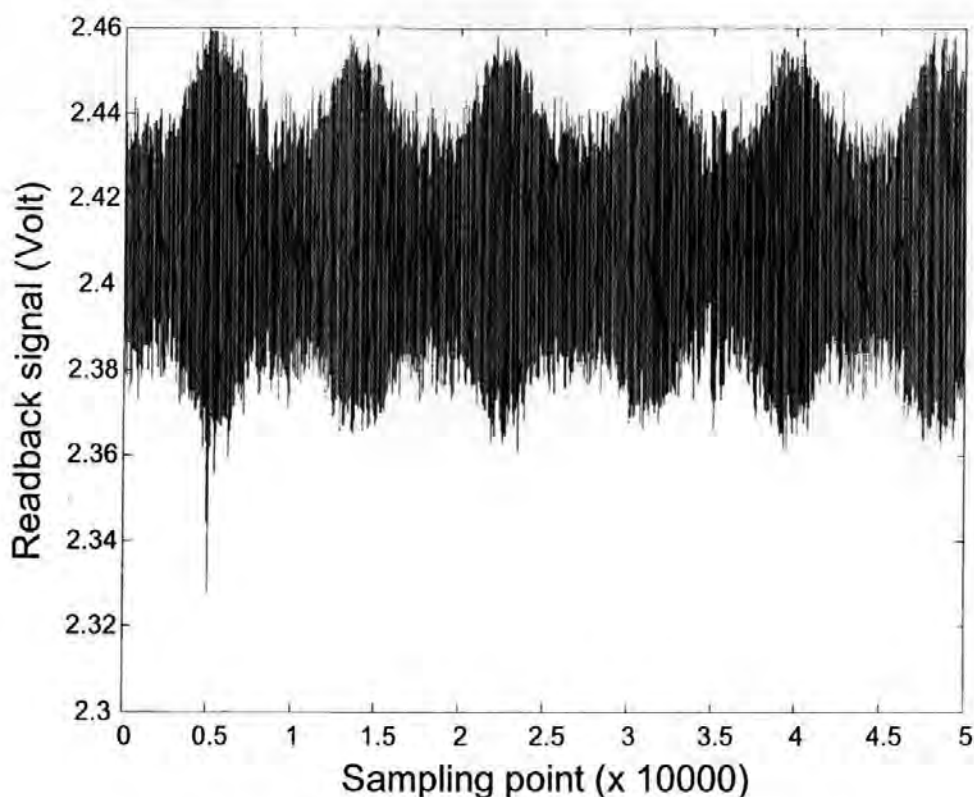


Figure 5-3 Readback signal at a vibration frequency of 5.8 kHz

The obtained readback signal is the spacing variation signal modulated by the high frequency recording signal. It can be noted that the readback signal stored by the digital oscilloscope has a constant DC offset which is caused by the setting of the oscilloscope. For the modulation amplitude of the readback signal (i.e., the envelope of the readback signal) to be read out conveniently, digital signal processing is applied to the recorded signal (see Section 7.1.3). First the readback signal data are processed by local area moving average to get rid of the DC component, and full-wave rectified, then followed by a linear phase low-pass FIR filter to get the envelope. The cut-off frequency of the low-pass filter should be selected high enough (e.g., 10 times the useful frequency, i.e., 10 times the vibration frequency in this case) so that all the useful signals will be attenuated by the same filter gain. The full-wave rectified signal of the readback under 5800 Hz vibration is shown in Figure 5-4.

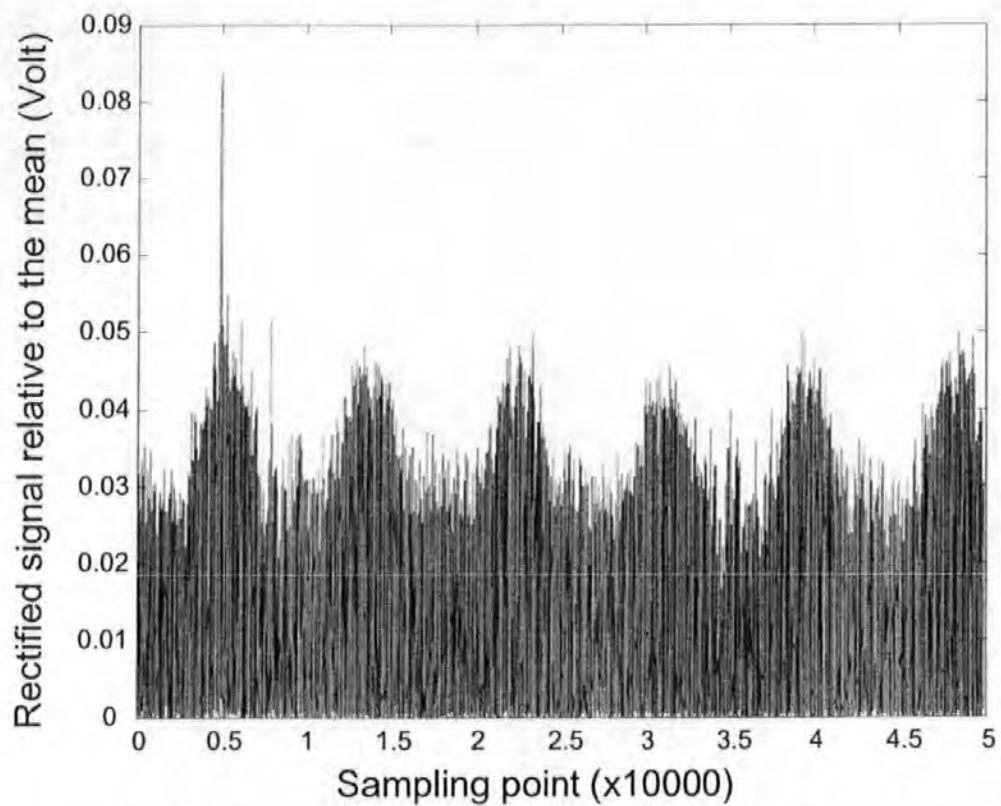


Figure 5-4 Fullwave rectified signal of the readback shown in Figure 5-3

Figure 5-5 shows the modulation amplitude of the readback signal extracted by a 60-order (i.e.,  $M=60$  for the FIR filter in Section 5.1.4) lowpass FIR filter with a cut-off frequency of 58 kHz.

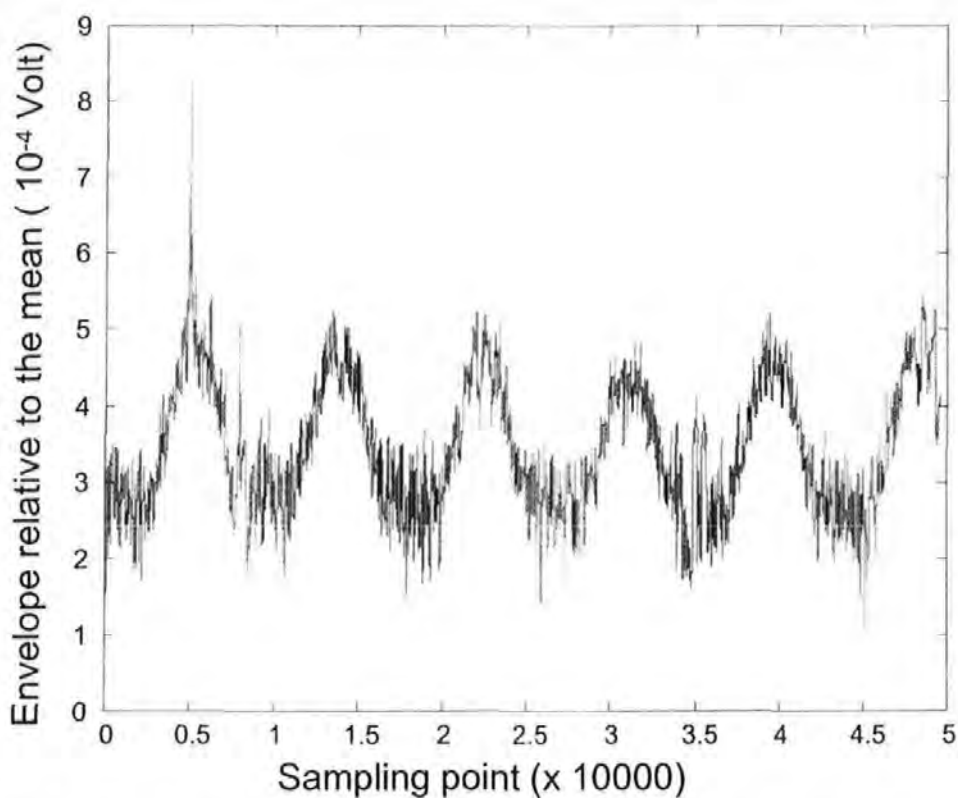


Figure 5-5 Extracted envelope of the readback signal under 5800 Hz vibration by a 60-order lowpass FIR filter

If desired, higher order FIR filter can be used to obtain improved quality amplitude envelope of the readback signal (note that the process time will be longer), which can be seen in Figure 5-6.

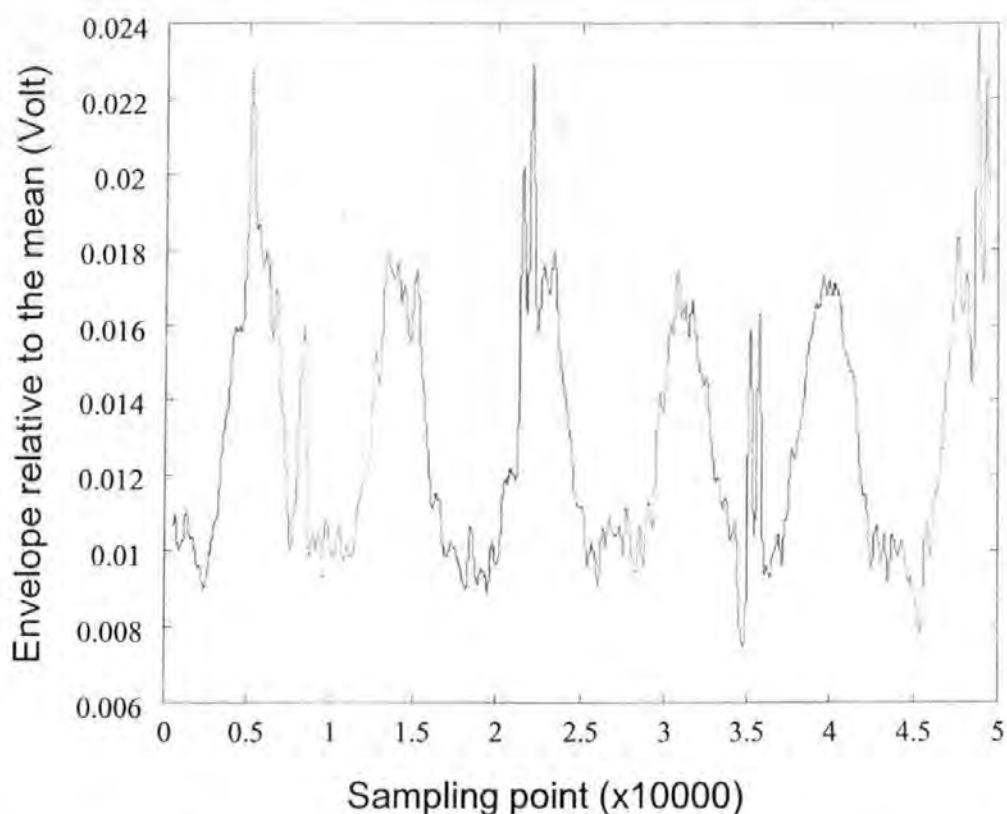


Figure 5-6 Extracted envelope of the readback signal under 5800 Hz vibration by a 500-order lowpass FIR filter

As has been stated earlier, the amplitude detection method can only provide a rough evaluation of the head-disk spacing variation, hence a simple signal processing should be good enough. Let's now calculate the head-disk spacing variation according to equation (3.7).

In the experiment, the disk rotation speed is  $n_r = 6000 \text{ r/m}$ , the recording frequency is  $f = 12.8 \text{ MHz}$ , and the read/write head position is  $r = 0.035 \text{ m}$ .

The tangential velocity of the head relative to the read point of the disk is:

$$v = n_r \cdot 2\pi r / 60 = 21.99 \text{ m/s}$$

From Figure 5-6, it can be read out that  $E_{\max}(d) = 18 \text{ mV}$ , and  $E_{\min}(d) = 10 \text{ mV}$ . From (3.7) the maximum head-disk spacing variation can be calculated as:

$$\Delta d_{\max} = -\frac{v}{2\pi f} \ln \frac{E_{\min}(d)}{E_{\max}(d)} = 160.7 \text{ nm}$$

### 5.2.2 PW50 of readback signal measurement method

Klaassen and van Peppen (1994) provided a method and circuitry, which can directly measure the pulse width from isolated read-back pulse signals. Zhu et al. (1998) also tried to provide a digital sampling technique to measure the  $PW_{50}$  of isolated readback pulse signals. It was claimed the method could be used under relatively low sampling rate. Some advanced Digital Storage Oscilloscopes/Disk Drive Analyzers (e.g. products of Lecroy and Tektronix) also provide the function of measuring the  $PW_{50}$  from isolated read-back pulse signals, which makes the measurement of  $PW_{50}$  much easier.

Let's have a look at how much a head-disk spacing variation will be resulted from a variation of  $PW_{50}$ .

Assuming the disk rotation speed is  $n_r = 6000 \text{ r/m}$  and the head position is at  $r = 0.035 \text{ m}$ , the tangential velocity of the head relative to the read point of the disk is  $v = n_r \cdot 2\pi r / 60 = 19.78 \text{ m/s}$ .

If the recording frequency is 25MHz, then the symbol period is  $T = 4 \times 10^{-8} \text{ s}$ .

If the variation of  $PW_{50}$  is  $\Delta PW_{50} = 0.4T = 1.6 \times 10^{-8} \text{ s}$ , from (3.13) the resulted spacing variation will be  $\Delta d = v \cdot \Delta PW_{50} / 2 = 176 \text{ nm}$ .

### 5.2.3 PW50 parameter estimation method for flying height determination

Both simulation and experiments are performed to study the effectiveness of the estimation method that is detailed in section 3.3.

### 5.2.3.1 Estimation using isotropic (1, -1) recorded sequences

In the simulations within this section, isotropic (1, -1) recorded bit sequences are used. The channel transition response is assumed to be a Lorentzian function with  $PW_{50} = 2T$ , where  $T$  is the symbol period. The initial estimate of  $PW_{50}$  is set to  $0.5T$ . The simulation software is presented in section 7.1.5.1

#### A. Readback signal with no noise

In this simulation, no noise is added to the readback channel. The readback signal is shown below in Figure 5-7.

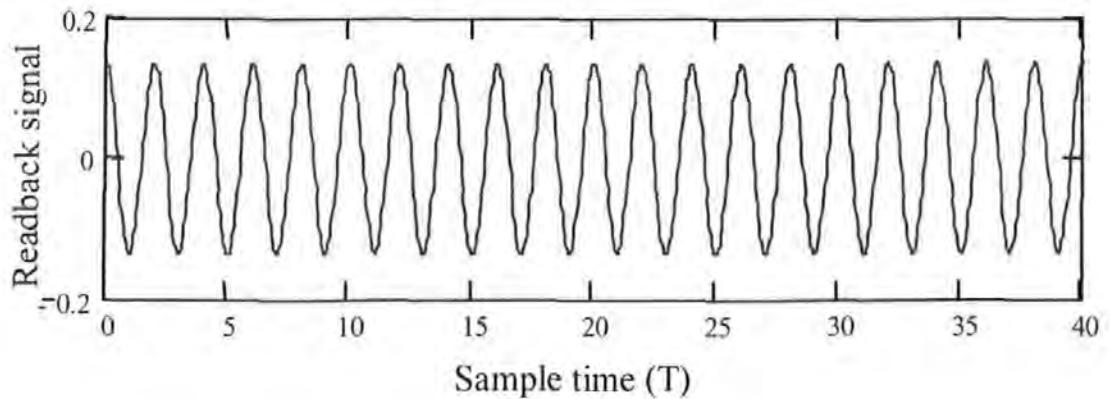


Figure 5-7 Readback signal with no added noise

With  $\beta = 0.20$ , the  $PW_{50}$  estimation process and result are shown below in Figure 5-8.



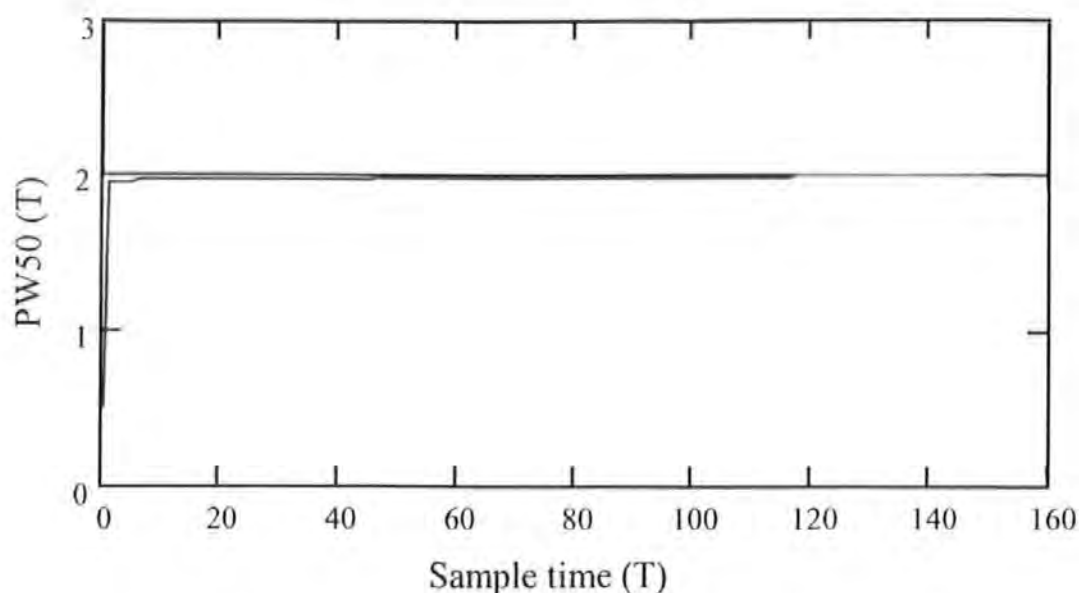


Figure 5-8 Estimation of  $PW_{50}$  from readback signal with no noise

It can be seen that the estimation converges to the real parameter value quickly.

### B. Readback signal with noises

In this simulation, heavy random noises are added to the readback channel with 5% of signal amplitude for the additive noise, and 25% of sample period (i.e., recording bit period) for pulse width jitter noise and position jitter (i.e., timing jitter) noise respectively. The readback signal is shown below in Figure 5-9.

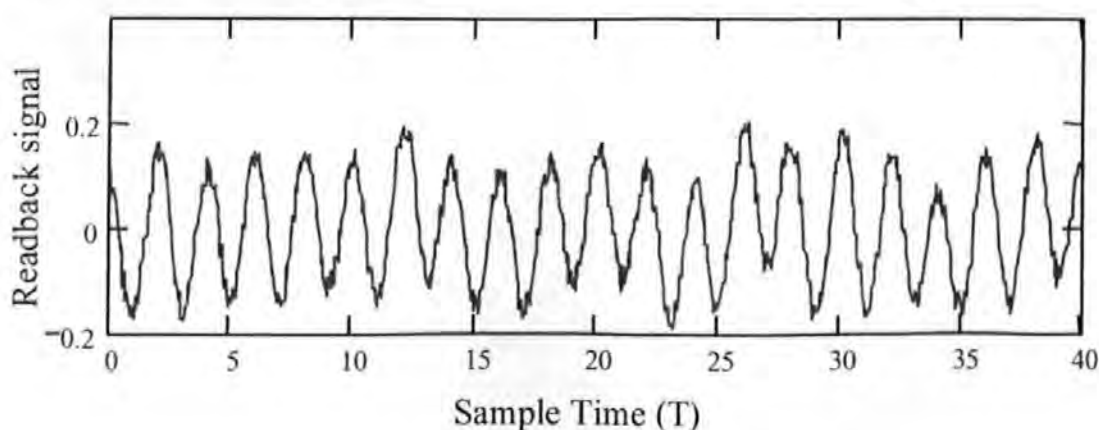


Figure 5-9 Readback signal with added noises

With  $\beta = 0.20$ , the  $PW_{50}$  estimation process and result are shown below in Figure 5-10.

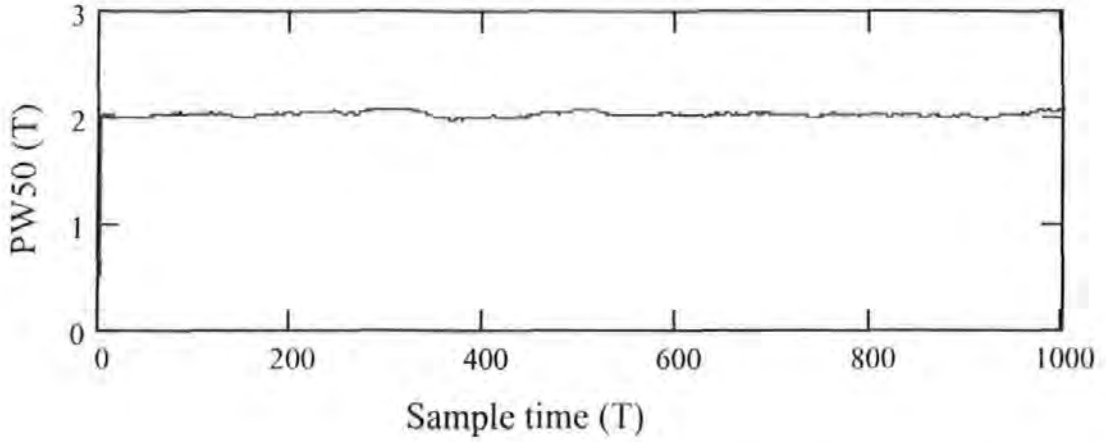


Figure 5-10 Estimation of  $PW_{50}$  from readback signal with noises

It can be seen that the estimation still converges to the real parameter value quickly.

### 5.2.3.2 Estimation using random bits recorded sequences

For the simulations within this section, random bits recorded sequences are used. The transition sequences are 5-bit Pseudo Random Binary Sequences (PRBS) of  $+1$  and  $-1$  [Hsia, 1977]. The channel transition response is assumed to be a Lorentzian function with  $PW_{50} = 2T$ , where  $T$  is the symbol period. The initial estimate of  $PW_{50}$  is set to  $0.5T$ . The simulation software is presented in section 7.1.5.2.

#### *A. Readback signal with no noise*

In this simulation, no noise is added to the readback channel. The readback signal is plotted below in Figure 5-11.

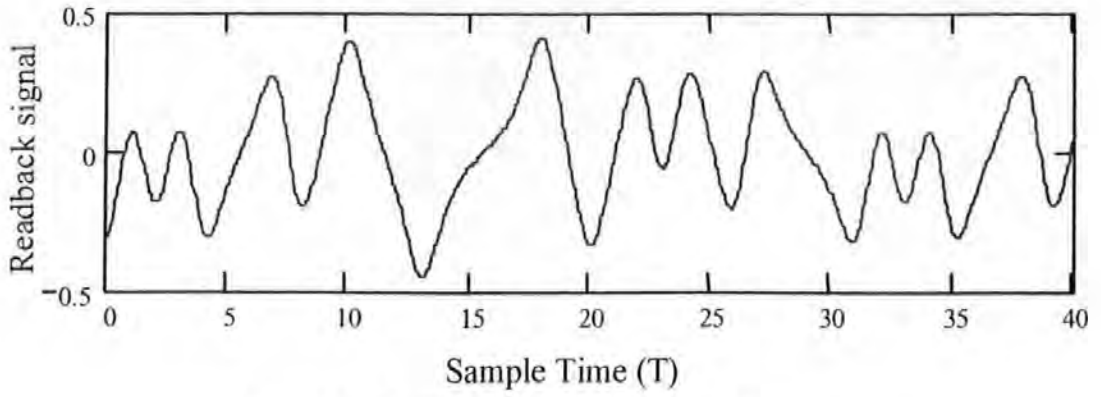


Figure 5-11 Readback signal with no added noise

With  $\beta = 0.25$ , the PW50 estimation process and result are shown below in Figure 5-12.

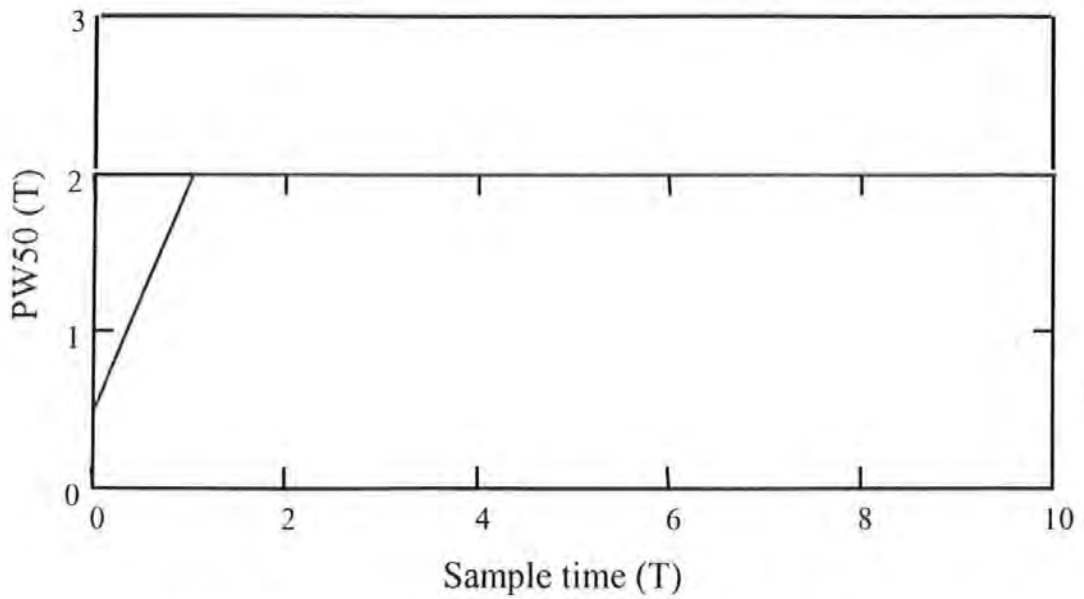


Figure 5-12 Estimation of  $PW_{50}$  from readback signal with no noise

It can be seen that the estimation converges to the real parameter value very quickly, quicker than that with isotropic (1, -1) input sequence case.

### ***B. Readback signal with noises***

In this simulation, heavy random noises are added to the readback channel with 5% of signal amplitude for the additive noise, and 25% of sample period (i.e., recording bit

period) for pulse width jitter noise and position jitter (i.e., timing jitter) noise respectively. The readback signal is shown below in Figure 5-13.

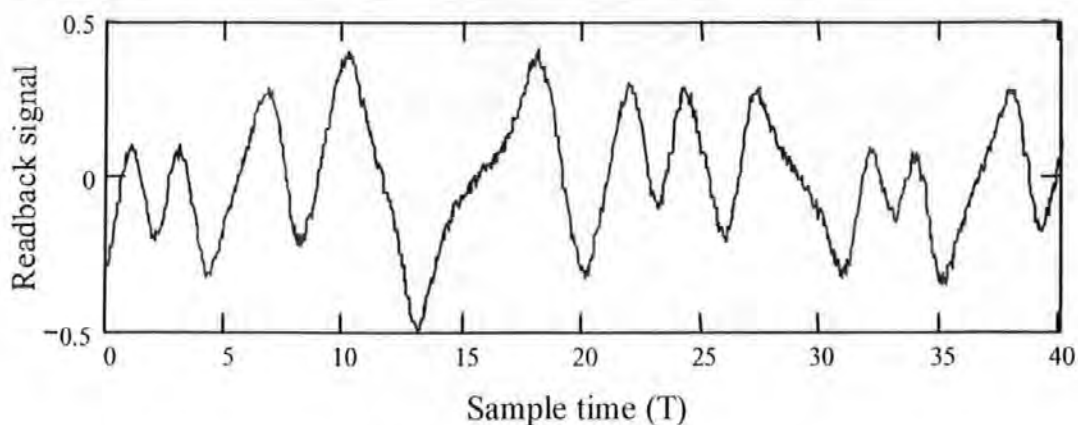


Figure 5-13 Readback signal with noises

With  $\beta = 0.25$ , the PW50 estimation process and result are shown below in Figure 5-14.

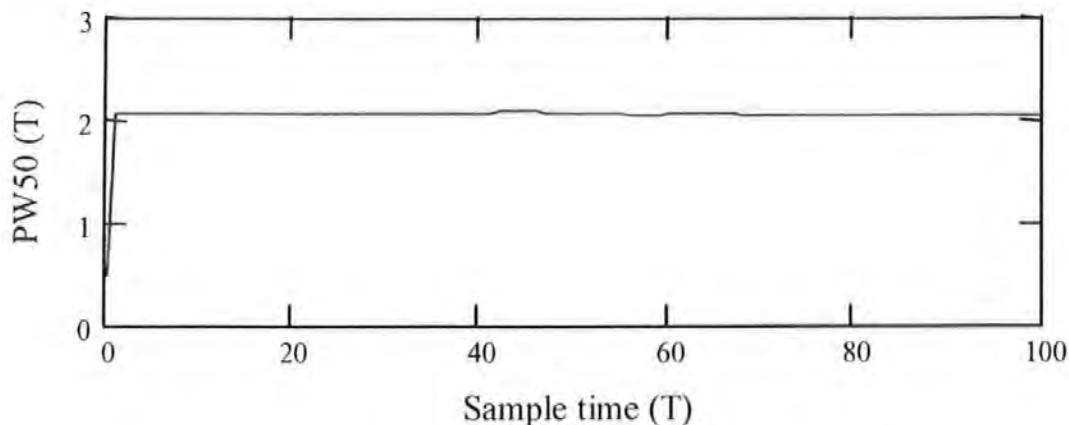


Figure 5-14 Estimation of  $PW_{50}$  from readback signal with noises

It can be seen that the estimation still converges to the real parameter value very quickly, quicker than that with isotropic (1, -1) input sequence case

### 5.2.3.3 Convergence and tracking properties of the parameter estimation method

In this section, we examine both the convergence and tracking properties of the estimation method with regard to the step size  $\beta$ . For the simulations in this section, recorded data bit sequences are read back from a hard disk drive with a bit-rate of 100Mb/s. Both random bit sequence and isotropic (1, -1) bit sequence are used for the study. The  $PW_{50}$  (or flying height) of the readback channel is made to vary in a 10 kHz sinusoidal waveform. Heavy random noises are added to the readback channel with 2.5% of signal amplitude for the additive noise, and 25% of sample period (i.e., recording bit period) for timing jitter noise respectively. A range of values of step size  $\beta$  in equation (3.12) has been used in the simulation to see the tracking property of the estimation algorithm. The simulation software is presented in section 7.1.5.3.

#### A. Using isotropic bit sequences

In this simulation, isotropic (1, -1) bit sequences are used in the estimation. With a range of different parameter values of step size  $\beta$  in equation (3.12), the real time estimation process and results are shown from Figure 5-15 to Figure 5-18.

With  $\beta = 0.2$ , and initial estimate of  $PW_{50} = 0.5$ , the estimation convergence and tracking process is shown below in Figure 5-15.

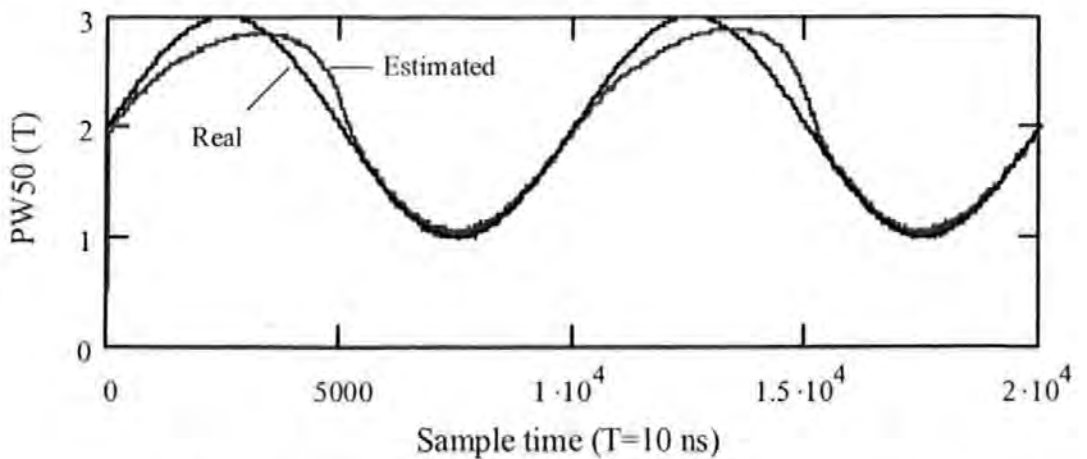


Figure 5-15  $PW_{50}$  estimation convergence and tracking process with  $\beta = 0.2$

With  $\beta = 0.5$ , and initial estimate of  $PW_{50} = 0.5$ , the estimation convergence and tracking process is shown below in Figure 5-16.

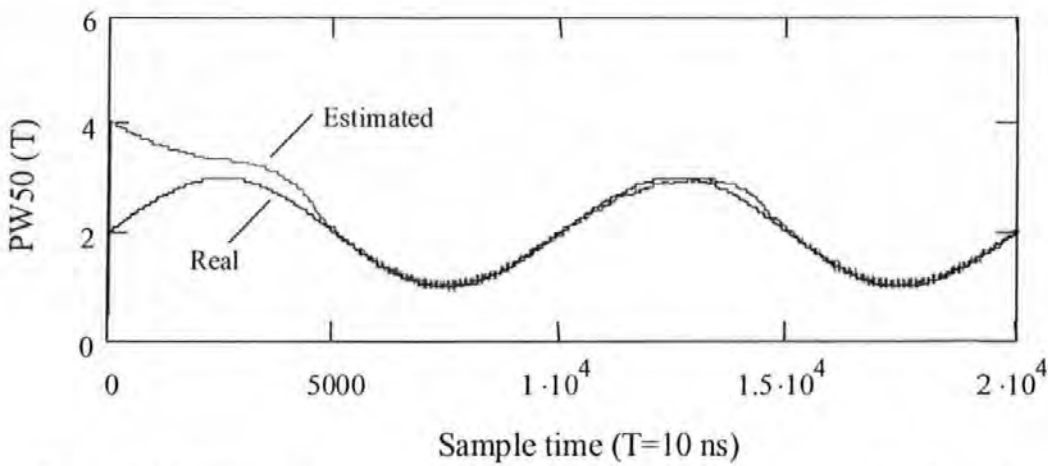


Figure 5-16 PW50 estimation convergence and tracking process with  $\beta = 0.5$

With  $\beta = 0.7$ , and initial estimate of  $PW_{50} = 0.5$ , the estimation convergence and tracking process is shown below in Figure 5-17.

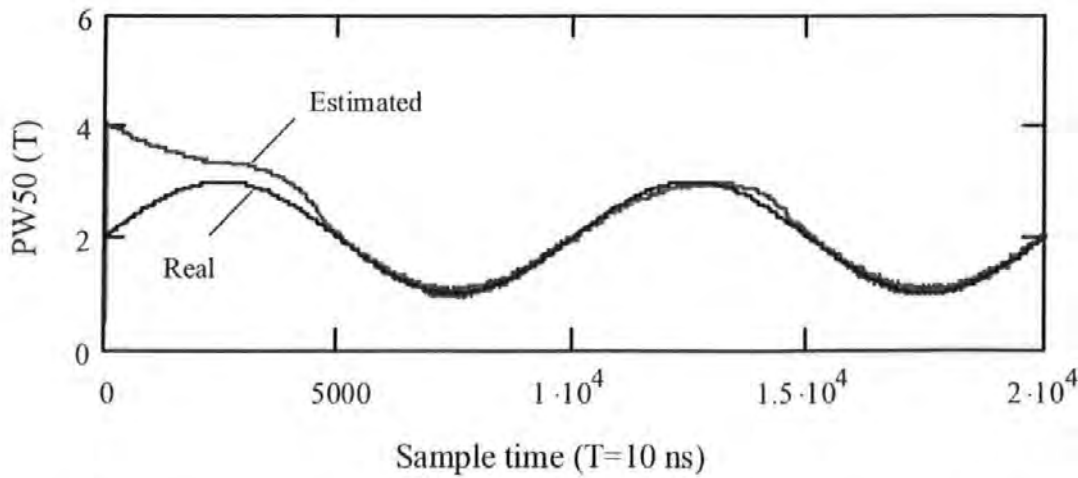


Figure 5-17 PW50 estimation convergence and tracking process with  $\beta = 0.7$

With  $\beta = 1.0$ , and initial estimate of  $PW_{50} = 0.5$ , the estimation process will not converge as shown below in Figure 5-18.

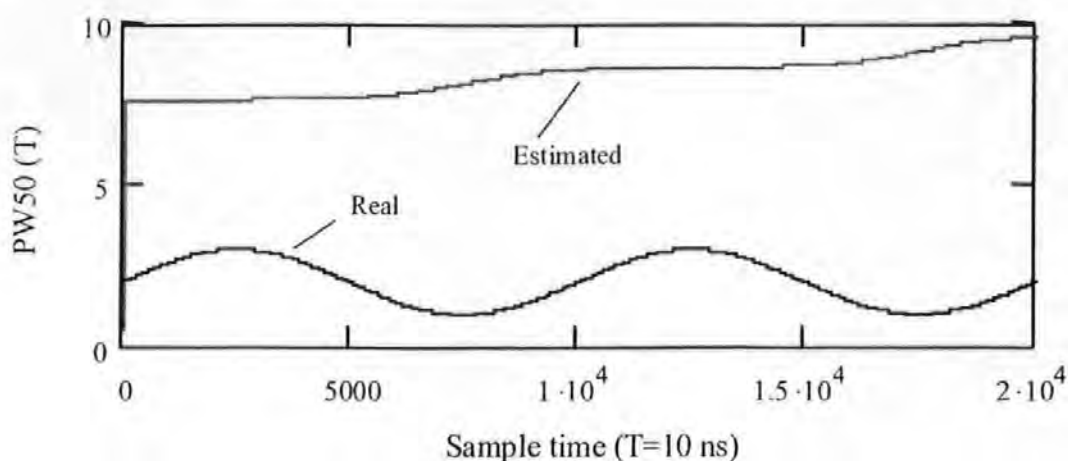


Figure 5-18 PW50 estimation convergence process with  $\beta = 1.0$

From the simulation results in this section, it can be seen that if the step size  $\beta$  is too small, the convergence is slow and there exist a large steady state estimation error. With  $\beta$  being increased, the convergence becomes quicker and the steady state estimation error becomes smaller. But with  $\beta$  being further increased, the convergence becomes slower again. If  $\beta$  is too big, the estimation will not converge. For a good estimation performance of both convergence and tracking, the step size  $\beta$  should be selected between 0.5 and 0.7.

### ***B. Using random bit sequences***

In this simulation, random recorded bit sequences are used in the estimation. The bit sequences are generated by a 5-bit Pseudo-Random Binary Sequence generator. With a range of different parameter values of step size  $\beta$  in equation (3.12), the real time estimation process and results are shown from Figure 5-19 to Figure 5-22.

With  $\beta = 0.2$ , and initial estimate of  $PW_{50} = 0.5$ , the estimation convergence and tracking process is shown below in Figure 5-19.

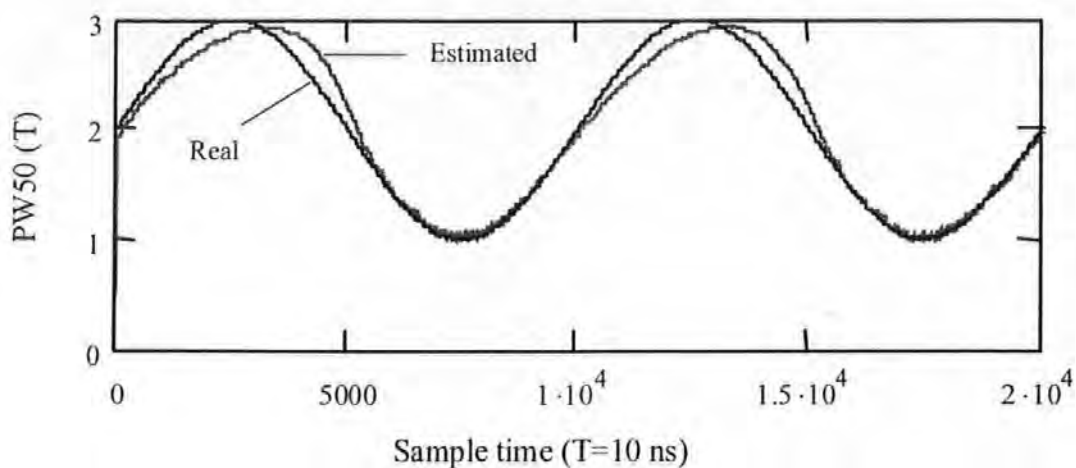


Figure 5-19 PW50 estimation convergence and tracking process with  $\beta = 0.2$

With  $\beta = 0.5$ , and initial estimate of  $PW_{50} = 0.5$ , the estimation convergence and tracking process is shown below in Figure 5-20.

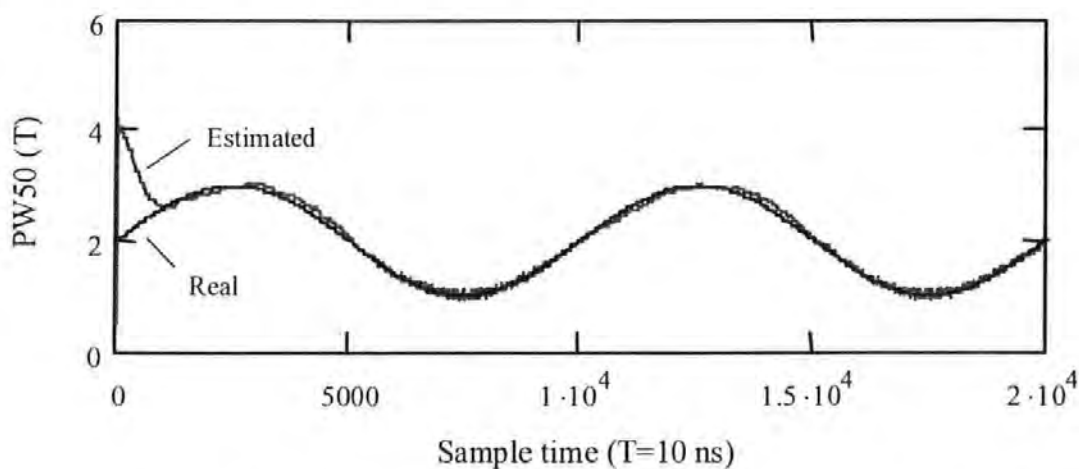


Figure 5-20 PW50 estimation convergence and tracking process with  $\beta = 0.5$

With  $\beta = 0.7$ , and the initial estimate  $PW_{50} = 0.5$ , the estimation convergence and tracking process is shown below in Figure 5-21.



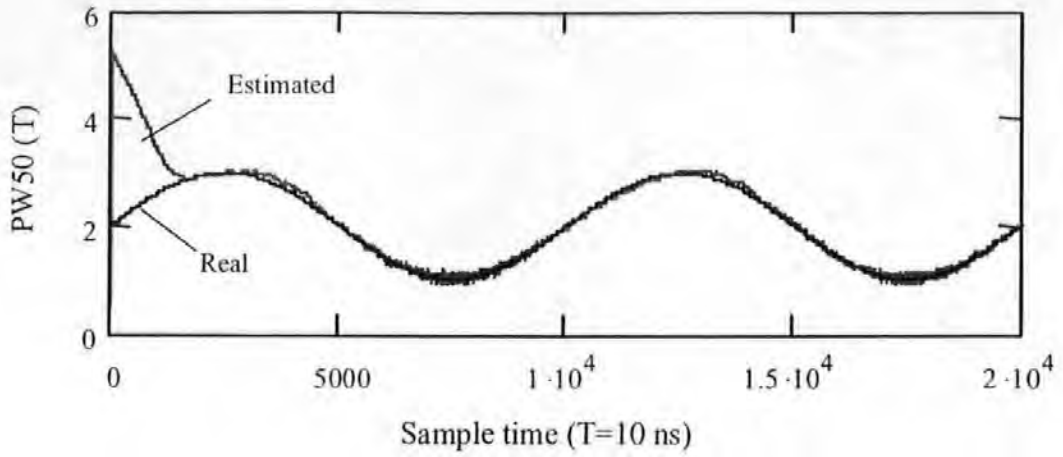


Figure 5-21 PW50 estimation convergence and tracking process with  $\beta = 0.7$

With  $\beta = 1.0$ , and the initial estimate  $PW_{50} = 0.5$ , the estimation convergence and tracking process is shown below in Figure 5-22.

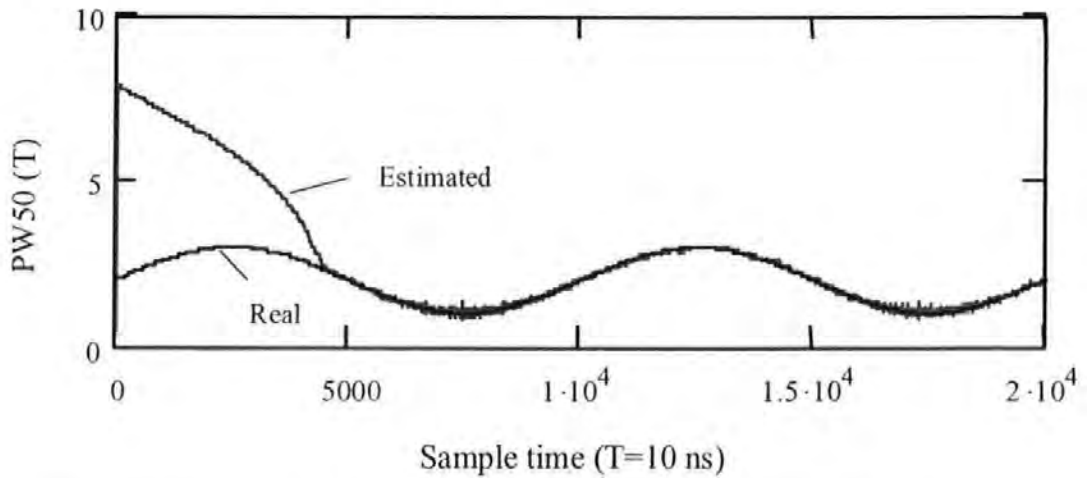


Figure 5-22 PW50 estimation convergence and tracking process with  $\beta = 1.0$

From the simulation results in this section, it can be seen that the selection rule of step size  $\beta$  summarised in the last section also holds here, with regard to the convergence and tracking performance of the estimation. One extra point is that with the same  $\beta$  value, the convergence and tracking performance with random bit sequence input in this section is better than that with isotropic bit sequence input in the last section. For a good

performance of both convergence and tracking, the step size  $\beta$  should still be selected between 0.5 and 0.7.

**5.2.3.4 PW50 estimation using readback signals of real hard disk drives**

In this section, estimation is made by using readback signal data from a real hard disk drive, which is a Quantum ProDrive LPS-170M hard disk drive. The readback signal is acquired with a sampling rate of 500MHz/s and saved by the Lecroy digital storage oscilloscope. Part of the readback signal is shown in Figure 5-23 using Mathcad.

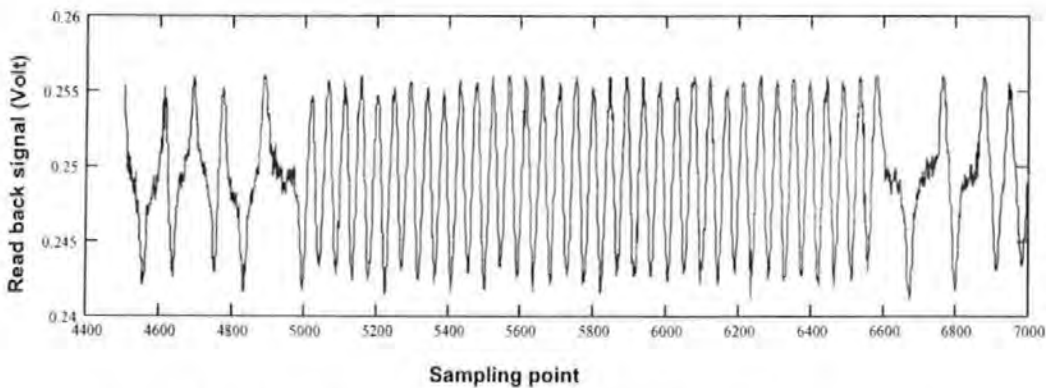


Figure 5-23 Part of readback signal from a real hard disk drive

The disk recording timing is derived within the estimation software itself. In the estimation algorithm, the recording bit rate of the hard disk drive is used as the estimation sample rate  $T$ . Details of the estimation software and estimation process are presented in Section 7.1.5.4. The estimation result is shown below in Figure 5-24.

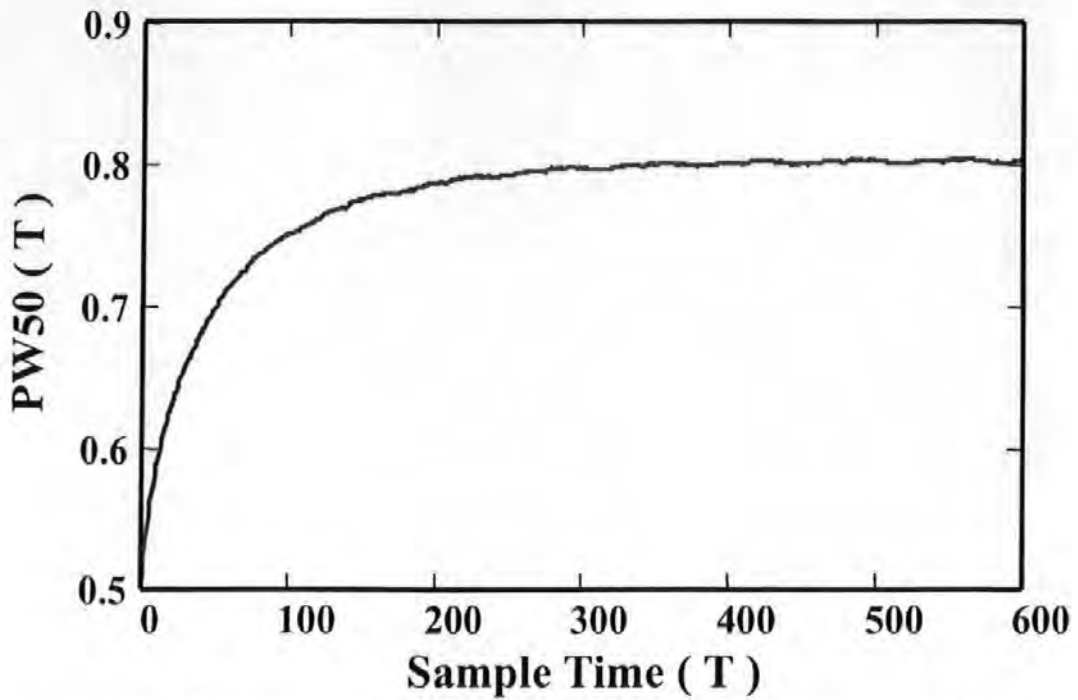


Figure 5-24 Estimation of  $PW_{50}$  using readback signals from a real hard disk.

### 5.2.3.5 Summary

From the simulation results of Section 5.2.3, it is found that for  $PW_{50}$  (or flying height) estimation, the recorded bit sequences are not restricted to just random bit sequences. With other types of input binary sequences, e.g., isotropic (1, -1) sequences, the estimation still converge to the correct  $PW_{50}$  value quickly. However, in regard to the convergence and tracking properties of the estimation process, using random bit sequences is superior to using isotropic (1, -1) sequences. This can be observed from the simulation results in section 5.2.3.3. Also from the simulation results in section 5.2.3.3, it is found that if the variation frequency of  $PW_{50}$  gets higher, the tracking error of its estimation will get bigger. According to the simulation result, for a hard disk drive with a recording bit-rate of 100MHz, the  $PW_{50}$  that can be accurately estimated should have a variation frequency less than 10 KHz.

The proposed parameter estimation method is effective to measure the  $PW_{50}$  so as to determine the flying height. Different from other  $PW_{50}$  measurement methods, this method is not restricted by the isolated readback pulse signal requirement. So it can be used to measure the flying height variation in real time in a normally operated hard disk drive, which may further provide a possibility for the measured flying height variation to be used for real time flying height control.

#### **5.2.4 Thermal signal detection method**

Since no hard disk drive with MR heads is currently available in the Lab for the vibration experiments, the following simulation method is used to demonstrate the thermal detection method. A sinusoidal thermal signal with frequency and phase the same as that of the testing vibration, is generated by the computer, which is then mixed with the readback signal obtained from the vibration experiment in section 5.2.1. The resulted readback signal is shown in Figure 5-25, which contains both the sinusoidal thermal signal component and an amplitude modulation.

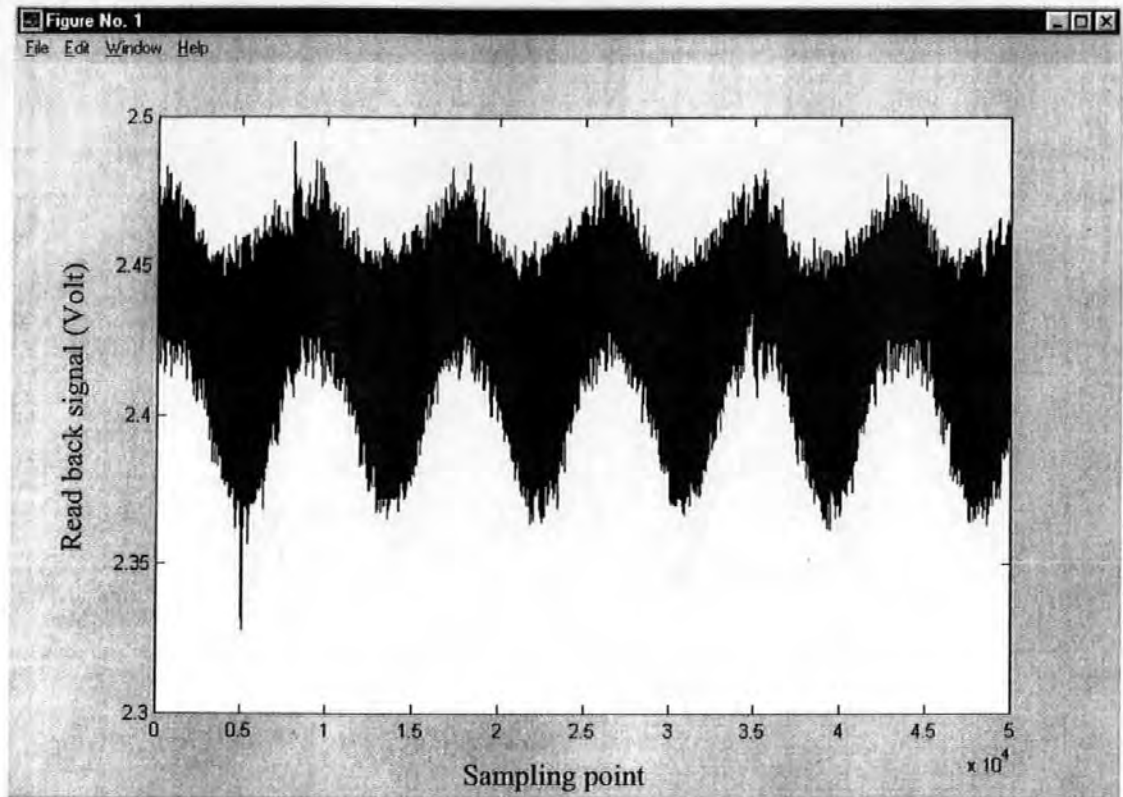


Figure 5-25 Readback signal of a disk drive with MR heads at a vibration frequency of 5.8kHz

To filter out the thermal signal, a 500-order linear phase band-pass FIR filter with cut-off frequencies of 200Hz and 11.6 kHz is applied to the combined readback signal (note that a 200-order FIR filter can also do the job with a bit heavier noise observed). The extracted thermal signal is shown in Figure 5-26, from which it can be seen that the signal is successfully restored.

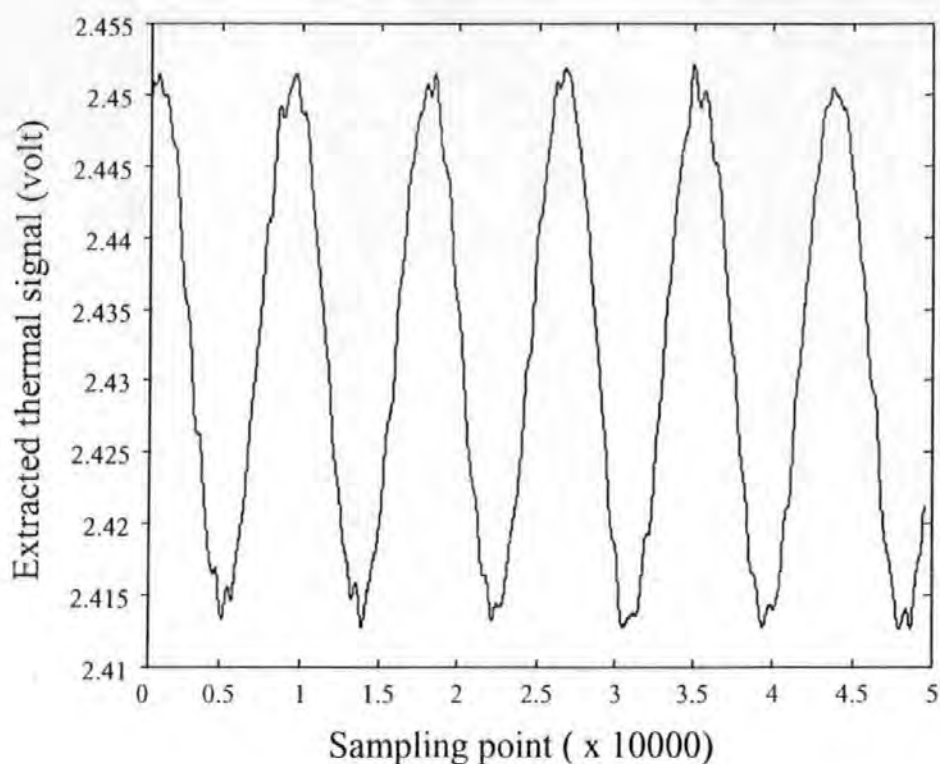


Figure 5-26 Extracted thermal signal by using signal processing

From (3.18), it can be seen that the spacing change and the thermal signal change have a linear relationship. The constant factor between the two needs to be calibrated before the real application. Thermal signal detection method is very promising for real-time head disk spacing variation detection, which can be used in the active flying height control, which has been detailed in Chapter 4.2.

### 5.3 Analysis of Hard Disk Drive Operation Failure under Vibration Conditions

In this section, a series of experiments were made to investigate the disk operation failure under vibration conditions. The experiments were carried out by mounting a commercial hard disk drive on the electro-dynamic shaker in the lab (see Section 5.1). Readback signals under a range of vibration frequencies were acquired and saved to

files by digital storage oscilloscope (see section 5.1.3). Figure 5-27 shows a typical plotted readback signal under the following condition: the vibration frequency is 4500Hz, the acceleration is 23.2g, the sampling frequency is 25MHz, and the number of samples is 50000.

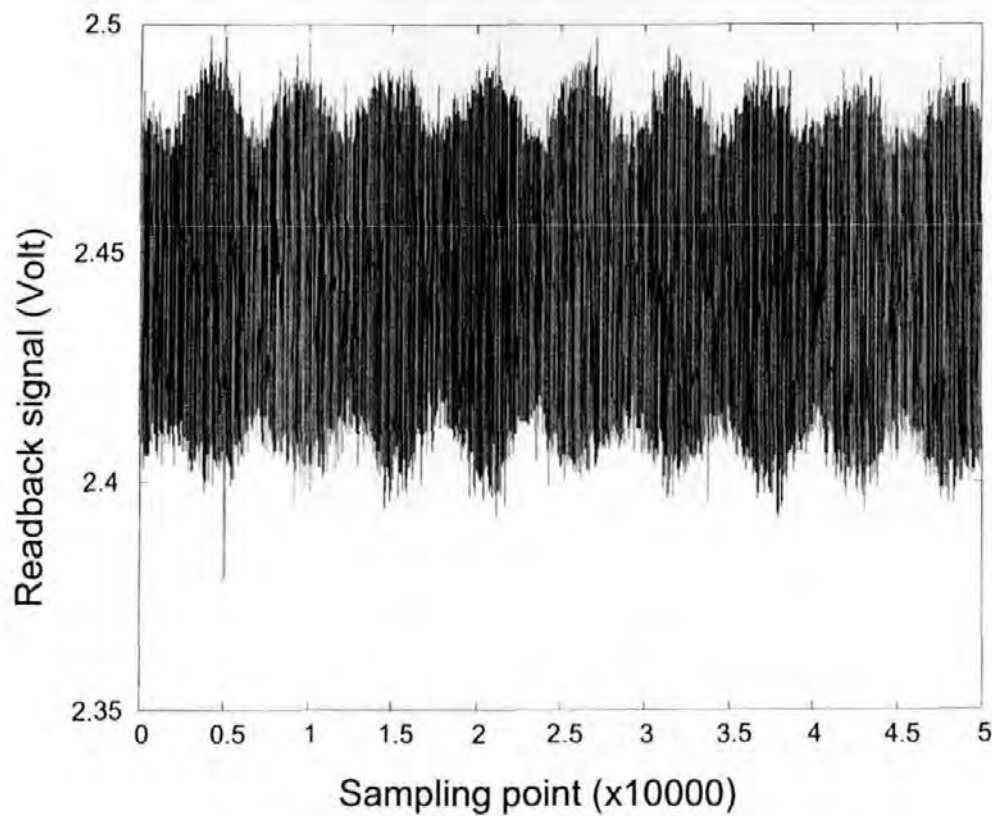


Figure 5-27 Readback signal under 4500Hz vibration

The readback signals under other vibration frequencies are plotted from Figure 7-1 to Figure 7-12 Appendices 7.2.

By applying the same signal processing method described in section 5.2.1 to the above readback signals, the extracted envelope of the 4500Hz vibration readback signal by using a 500-order lowpass FIR filter is shown below in Figure 5-28.

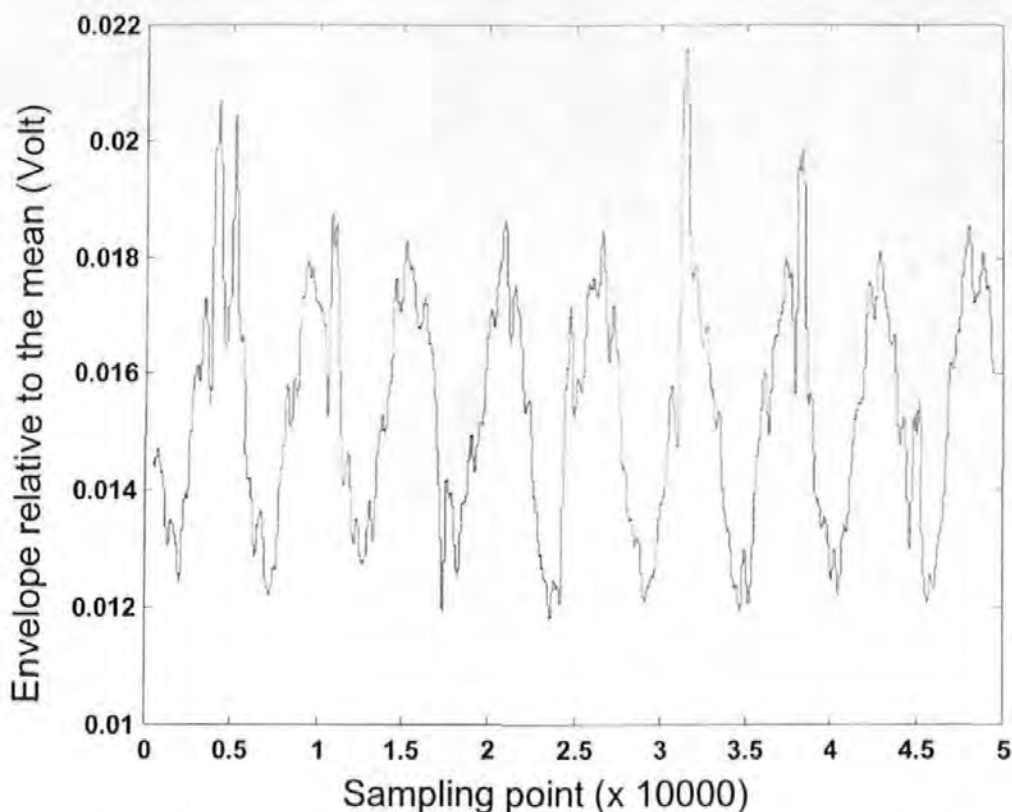


Figure 5-28 Extracted envelope of the readback signal under 4500Hz vibration

The extracted envelopes of the readback signals of the other vibration frequencies are plotted from Figure 7-13 to Figure 7-23.

If the vibration direction is absolutely vertical to the disk surface, the TMR caused by the vibration will be relatively small and have less effect on the modulation of the readback signal. In real vibration experiments, e.g., by using the electro-dynamic shaker in our lab, the vibration also contains quite a big horizontal component and the readback signal is in fact modulated by the combination of head disk spacing variation and TMR. However, we can still use the method described in section 3.1 to determine the spacing variation. This determined spacing variation can be referred to as the effective spacing variation, which contains also the contribution of TMR.

In all the experiments performed in this chapter, the disk rotation speed is  $n_r = 6000$  r/m, the recording frequency is  $f = 12.8$  MHz, and the read/write head



position is  $r = 0.035$  m. Using the same method as described in section 5.2.1, the maximum effective head-disk spacing variation under each vibration frequency can be determined according to (3.7) by:

$$\Delta d_{\max}(f_t) = -\frac{v}{2\pi f} \ln \frac{E_{\min}(f_t)}{E_{\max}(f_t)} \quad (5.2)$$

where  $f_t$  is the vibration frequency under testing.

As the vibration is sinusoidal, the amplitude of the disk drive vibration  $A_{\text{vibration}}$  is

$$A_{\text{vibration}}(f_t) = \frac{A_{\text{acc}}}{(2\pi f_t)^2} \quad (5.3)$$

where  $A_{\text{acc}}$  is the measured amplitude of the acceleration.

The frequency response of the head-disk spacing variation to the vibration amplitude of the disk drive with respect to the vibration frequency is

$$\frac{\Delta d_{\max}(f_t)}{A_{\text{vibration}}(f_t)} = \Delta d_{\max}(f_t) \cdot (2\pi f_t)^2 / A_{\text{acc}} \quad (5.4)$$

According to (5.4), the measured frequency response of the effective spacing variation is plotted in Figure 5-29.

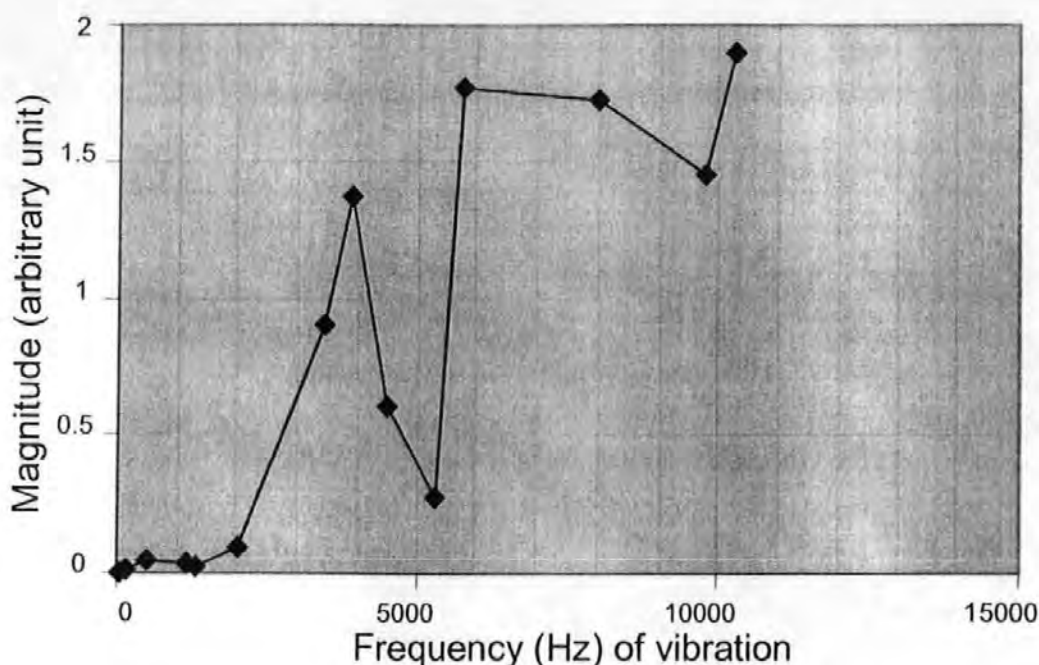


Figure 5-29 Frequency response of the effective head-disk spacing variation to the vibration amplitude of the disk

The plot in Figure 5-29 shows that, below 2KHz, vibrations around 500Hz and 1100Hz will result in read/write failure more easily (this should be caused by the large real spacing variation induced by vibration). Vibrations above 2 KHz are all detrimental to disk operation, depending on the vibration amplitude (the TMR caused by the vibration should contribute more to this due to the loss of tracking ability of the servo control loop subject to higher frequency disturbance). Results in [Tunstall et al., 2000] also demonstrated this point. The above explanation is made when only considering the vibration induced spacing variation and TMR. Other adverse factors mentioned in section 1.6 are not considered.

## 5.4 Active Flying Height Variation Control

We choose the parameters of the above controller as  $z_1 = 200000$ ,  $z_2 = z_3 = 22500$ ,  $p_2 = p_3 = 1125000$ ,  $T_d = 0.0005$ ,  $T_i = 0.01$ , and  $K_{MR}K_{PID}K_{AEM}K = 198$ . Note that we intentionally choose  $z_1$  as 200000 instead of 325000 to make partial compensation to see the system's robustness to parameter variation. The open loop frequency response of the servo control system is given by simulation as shown in Figure 5-30.

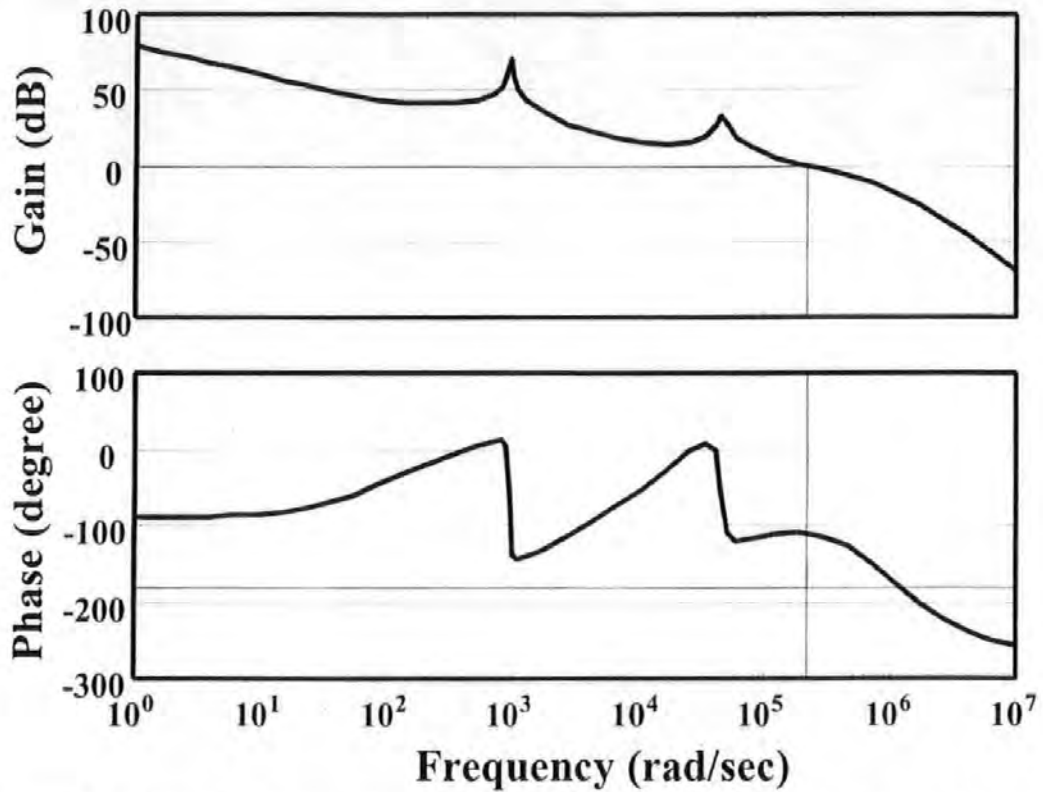


Figure 5-30 Open loop frequency response of the compensated servo control system.

The phase margin is about  $70^\circ$  at the gain crossover frequency of 219900 rad/sec. To help understand the performance of the system, the step response is given in Figure 5-31.

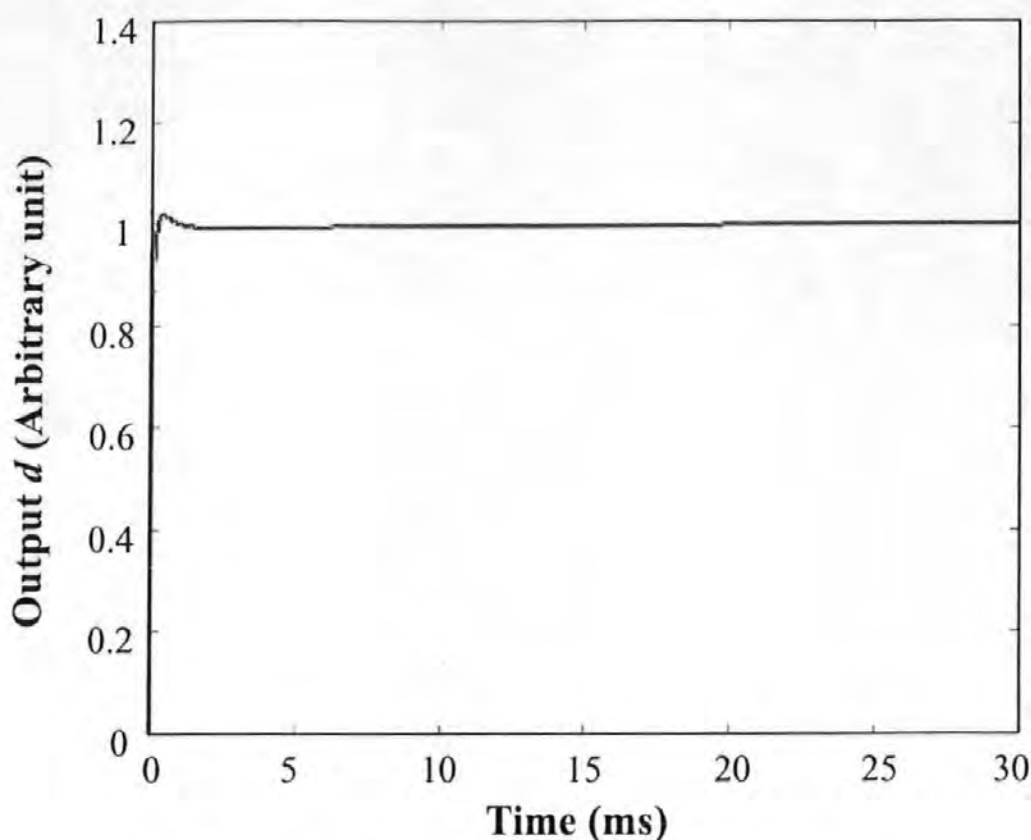


Figure 5-31 Step response of the servo control system.

To verify the flying height variation suppression ability of this servo control system, we have made a large number of simulation experiments. A series of sinusoidal signals from low to high frequencies are applied as the system's disturbance input. The resulted head-disk spacing outputs or suppressed spacing variations are given as shown from Figure 5-32 to Figure 5-35. For comparison purpose, the disturbance input  $d_3$  is also illustrated.

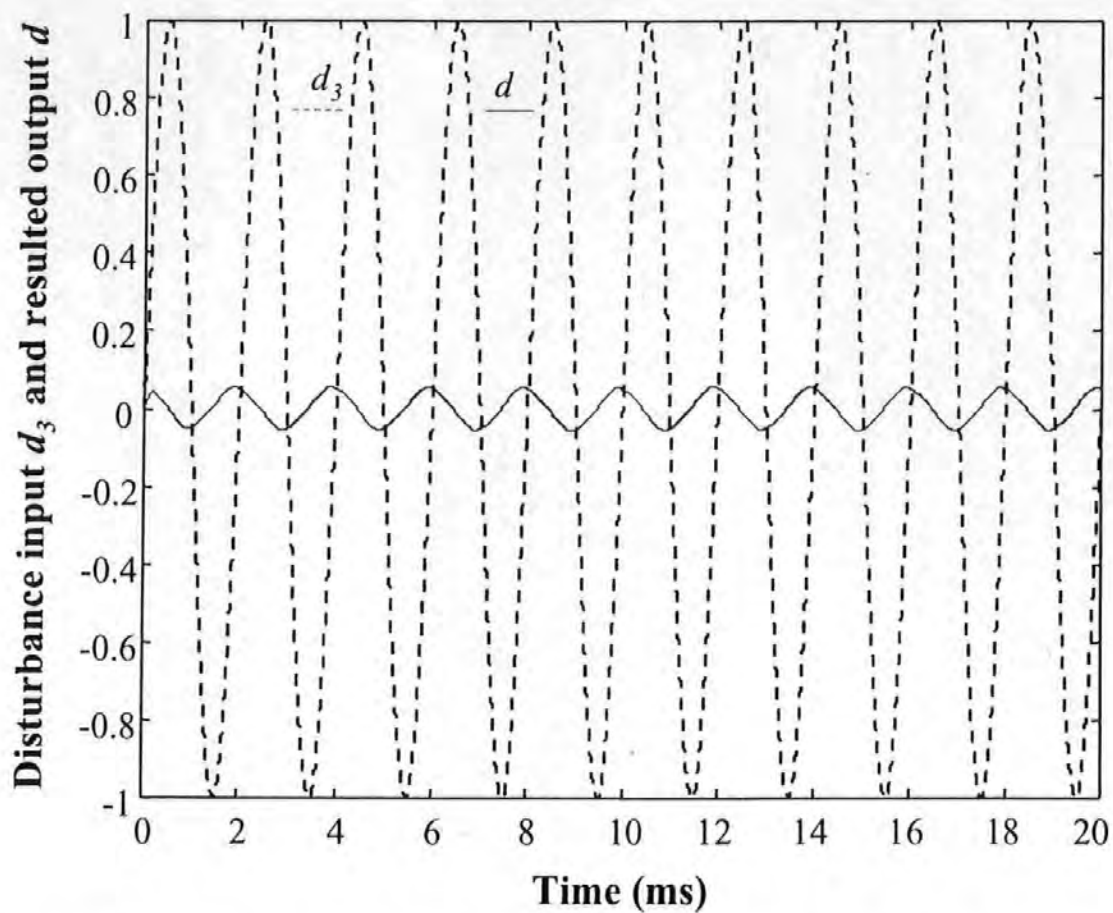


Figure 5-32 500Hz unit-amplitude sinusoidal disturbance input, and the resulted head-disk spacing variation.

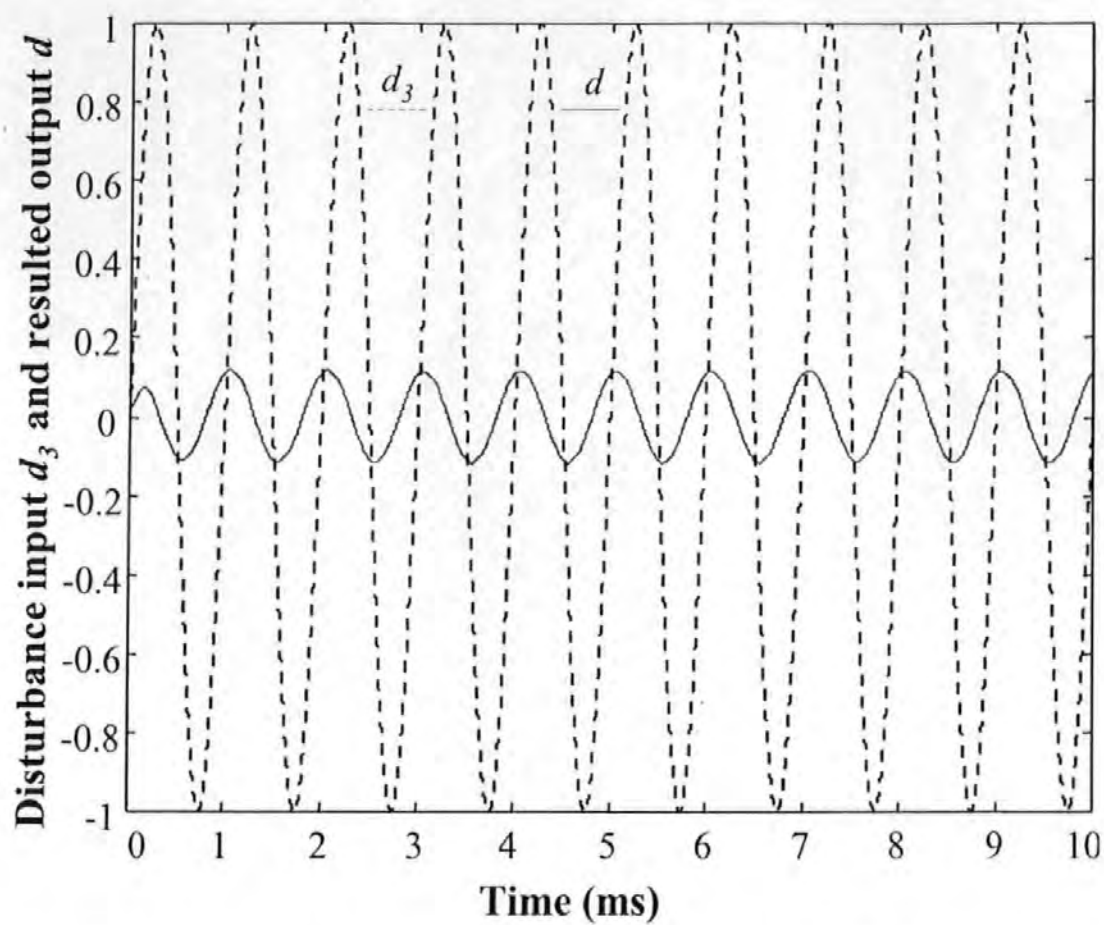


Figure 5-33 1000Hz unit-amplitude sinusoidal disturbance input, and the resulted head-disk spacing variation.

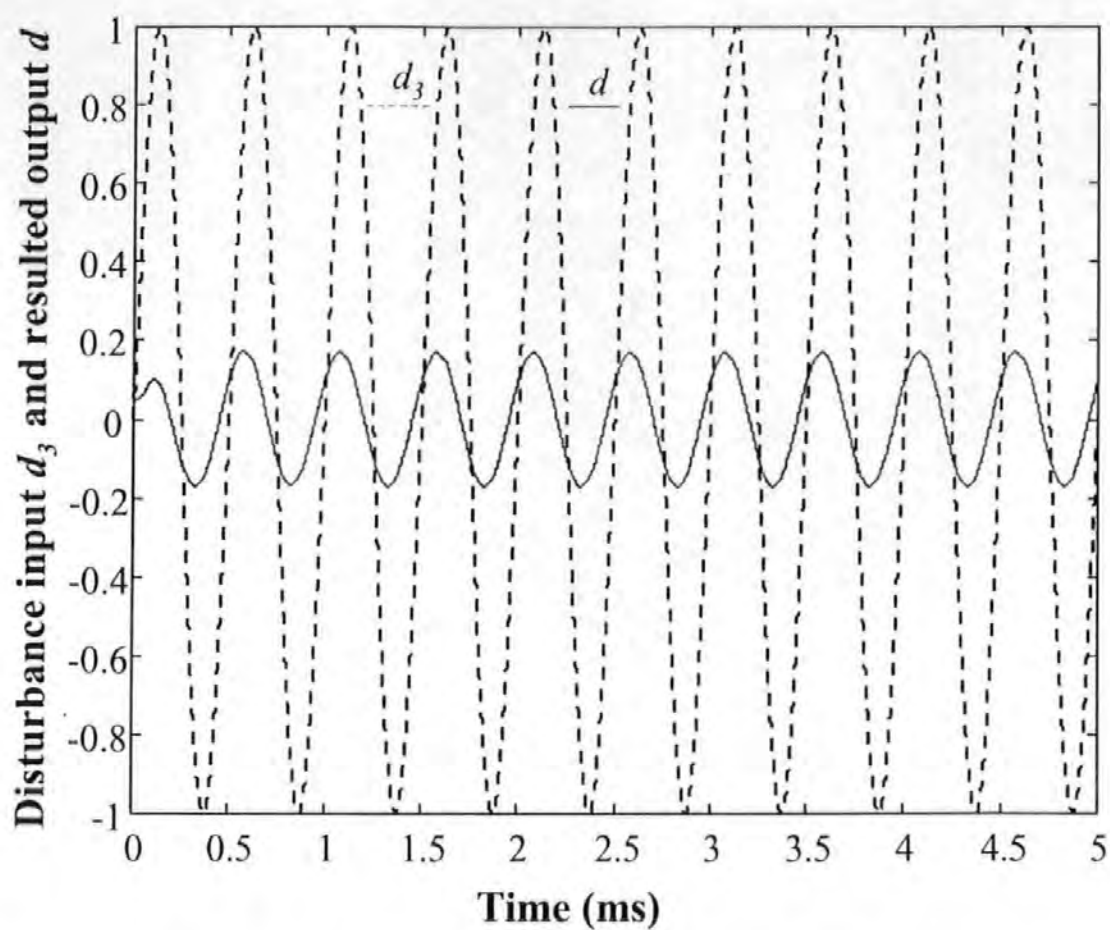


Figure 5-34 2000Hz unit-amplitude sinusoidal disturbance input, and the resulted head-disk spacing variation

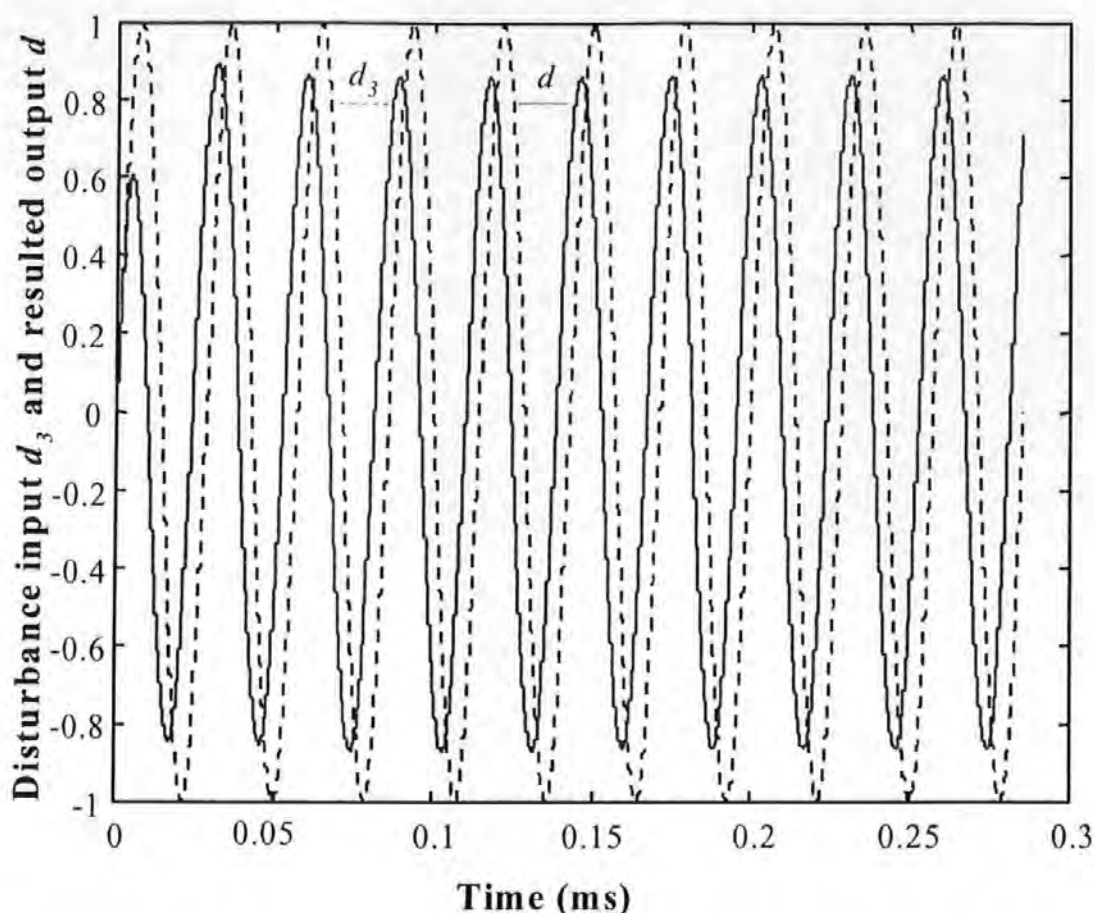


Figure 5-35 35000Hz unit-amplitude sinusoidal disturbance input, and the resulted head-disk spacing variation

From Figure 5-32 through to Figure 5-35, it can be seen that with the active flying height control in action, a 2000 Hz head disk spacing variation will be suppressed to about 17% of the amplitude without active control. It is apparent that variations with frequencies lower than 2000 Hz will be better suppressed. Although we have found that in the frequency band from 5000Hz to 9000Hz, the suppression results are even better than that at frequency of 2000Hz, which rests with the frequency response of the servo control system, generally speaking, With the increase of the variation frequency, the suppression effect will be gradually reduced, which depends on the bandwidth of the servo control system. The good news is that large head-disk spacing variations usually happen in the frequencies below 5000 Hz [Tunstall et al., 2000], which are caused by the vibration induced mechanical resonance. Another point we should make is that in



real applications, the benefit of even a 10% spacing variation suppression would be tremendous for the increase of the performance and reliability of the HDDs.

We should also note that at present, this method is only suitable for head-disk spacing variation/change suppression. It is not suitable for general flying height control since in that case,  $K_{MR}$  and  $H_{AEM}(s)$  need to be known accurately, for which, further work need to be carried out. This can be understood from the expression of the measurement point output:

$$\begin{aligned} y_m(s) &= ((r(s) - d(s))K_{MR} - C_0)H_{AEM}(s) \\ &= rK_{MR}H_{AEM}(s) - (C_0 + K_{MR}d(s))H_{AEM}(s) \end{aligned} \quad (5.5)$$

where the second term is the thermal signal measurement output. In the case of flying height variation suppression,  $r$  is constant, thus the first term will be zero since  $H_{AEM}(s)$  is a high pass filter. In the case of general flying height control,  $K_{MR}$  and  $H_{AEM}(s)$  need to be accurately known so as to generate the value of the first term.

# Chapter 6 Conclusions and Future Work

## 6.1 Conclusions

### 6.1.1 Real time head disk spacing measurement

Four readback signal detection methods (including the  $PW_{50}$  parameter estimation method) have been investigated in this thesis for real-time measurement of head disk spacing variation. Different from other  $PW_{50}$  measurement methods, the proposed  $PW_{50}$  parameter estimation method is not restricted by the requirement of isolated readback pulse signals. Thus it can be used for real-time spacing variation measurement in normally operated hard disk drives, which may further provide a possibility for the measured flying height variation to be used for real time flying height control. However, this method is more effective for low frequency spacing variation conditions. Thermal signal detection method, on the other hand, is more effective for high frequency spacing variation measurement. Therefore, by combining these two detection methods together, a spacing variation detection method for the whole frequency range could be constructed. The amplitude detection method gives a rough but simple way to study the head disk spacing change.

### **6.1.2 Analysis of hard disk drive operation failure under vibration conditions**

Analytical models are developed for head disk assembly and head position servo control mechanisms to analyze the operation failure of hard disk drives under vibration conditions. Theoretical and experimental results show that all the vibration modes of the head disk assembly will induce larger amplitude of head disk spacing variation and tend to result in read/write failure under vibration conditions. The TMR resulted from disk vibration can be suppressed by the servo control loop to some extent when the vibration frequency is within its bandwidth. When the frequency is beyond the bandwidth, the servo loop loses its capability. Therefore, under vibration conditions, the read/write process in a hard disk drive will tend to become failure more likely around the vibration modes of the head disk assembly. Vibrations above a certain frequency, say, the servo loop bandwidth, also have the tendency to result in operation failure because the weakening of the suppression ability of the servo loop.

### **6.1.3 Real time active flying height control**

A novel active flying height control method is proposed to suppress the flying height or head-disk spacing variation in hard disk drives under vibration conditions. Real-time spacing variation signals derived from the readback signal of MR or GMR read/write heads are used for feedback control. Simulation experimental results show that this active flying height control will effectively suppress the head-disk spacing variation, therefore the performance and reliability of the HDDs can be well improved when

working in vibration conditions. The method has a good potential to be applied to future ruggedized hard disk drives.

## **6.2 Future Work**

The following research work can be carried out by future researchers:

1. Build up a real flying height control system to suppress the head-disk spacing variation by applying the flying height detection methods and servo control method developed in this thesis. This system will serve as a demo for the applications to the future ruggedized hard disk drives.
2. Develop an adaptive equalisation and detection method to accommodate the flying height variation and minimise its adverse effect on the read channel performance. This can be done by using adaptive filter theory [Haykin, 1996]. Adaptive neural and fuzzy equalisation and detection methods can be developed, since their advantages have been shown to combat the transition noise, non-linear inter-symbol interference (ISI) and offtrack interference in high density disk drives [Lin & Juang, 1997; Nair & Moon, 1997; Choi et al., 1997; Obernosterer et al., 1997; Haykin, 1994; Gibson et al., 1989].

# Chapter 7 Appendices

## 7.1 Software Developed During This Research

The software routines are all written in Mathcad or Matlab.

### 7.1.1 Magnetic recording channel modelling and readback simulation software

The following Mathcad simulation software is used to study the characteristics of readback signal, and used in Chapter Chapter 3 as well.

#### 7.1.1.1 Readback from an isotropic (1,-1) recoded bit sequence

##### *A. Isolated read-back pulses*

When the recording bit density is very low, there will be no inter-symbol interference, and the readback pulses are isolated.

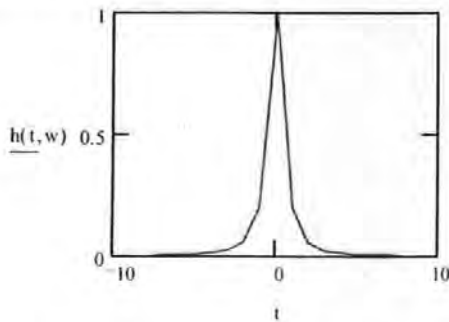
```
//*****  
/// Isolated read-back pulses  
//*****
```

```
Ah := 1.0  
w := 1.0 //Here w represents PW_50  
t := - 10·w, - 9·w, 10·w
```

```
//The transition response is
```

$$h(t, w) := \frac{1}{w} \cdot \frac{1}{1 + \frac{(2 \cdot t)^2}{w^2}}$$

//The following is a single isolated transition response



//Generate an isotropic 1, -1 input series:

$$b_0 := 1 \quad j := 0..1500$$

$$b_{j+1} := -b_j$$

//Obtain transition sequence of the above input series:

$$a_0 := 1 \quad i := 1..1500$$

$$a_i := \frac{(b_i - b_{i-1})}{2}$$

//a\_i is the transition series read back from the disk. We divide by 2 to make the series be 1,-1 as well .

//T is the recording bit period. When simulating isolated read-back pulses, T should be selected much larger than PW\_50 (e.g., 20 times PW\_50). In that case, there will be no inter-symbol interference in the readback signal.

$$T := 20$$

$$w := 0.05 T$$

//Storage density (or bit density) is w/T.

$$t := 0, 0.05 T..4 \cdot T$$

//Note: here the sample rate is 1/(0.05T)

//Generate timing jitter and PW\_50 variation noise

$$j := 0..1500$$

$$\Delta t_j := \text{rnd}(0.5 \cdot w) - 0.25 \cdot w$$

$$\Delta w_j := \text{rnd}(0.5 \cdot w) - 0.25 \cdot w$$

$$k := -50, -49..50$$

// Theoretically, k should be from -infinite to +infinite, but because h(t-kT) will be decreased to nearly zero when k>10PW\_50, so it is enough to choose k\_min<-(10PW\_50+t\_start), and k\_max>(10PW\_50+t\_end), where t\_start and t\_end are integers defined by the simulation range of t.

//The readback signal with all sorts of noises (including timing jitter and PW50 variation) can be written as:

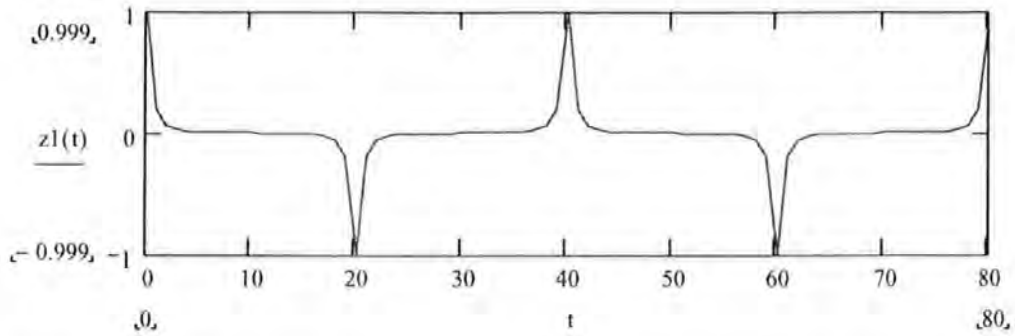
$$z(t) := \sum_k \left[ a_{k+50} \cdot h\left[t - k \cdot T - (\Delta t_{k+50}), w + (\Delta w_{k+50})\right] \right] + (\text{rnd}(0,1) \cdot A) - 0.05A$$

//Note: In the above expression,  $h(t-kT)$  is associated with  $a_{k+50}$ . We use this expression because the subscript can not be negative.

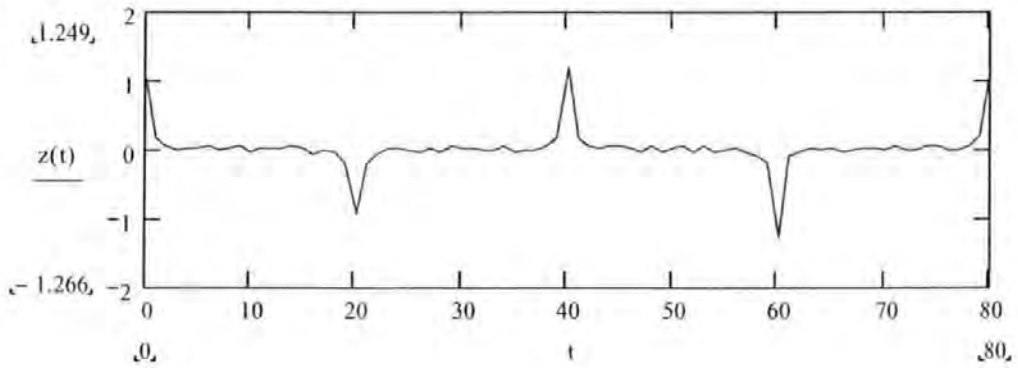
//If not considering any noise, the readback waveform is given by:

$$z_l(t) := \sum_k (a_{k+50} \cdot h(t - k \cdot T, w))$$

//Without any noise, the isolated readback pulses are plotted below:



//With all sorts of noises (including timing jitter and PW50 variation), the readback waveform is plotted as below:



## B. High density recording readback

When the recording bit density is high, there will be inter-symbol interference, i.e., the readback signals from the adjacent transitions will affect each other.

```
//*****
// Readback from high density recording of isotropic (1,-1) bit sequence
//*****
```

//T is the recording bit/symbol period. When recording density  $w/T$  gets high, there will be inter-symbol interference in the readback signal.

T := 1.0

```

w := 1/T
//Storage density (or bit density) is w/T.

t := 0, 0.05T..20T
//Note: here the sample rate is 1/(0.05T)

//Generate timing jitter and PW_50 variation noise:
j := 0..1500
Δtj := rnd(0.5 w) - 0.25 w
Δwj := rnd(0.5 w) - 0.25 w

k := 50..49..50
// Theoretically, k should be from -infinite to +infinite, but because h(t-kT) will be
//decreased to nearly zero when k>10PW_50, so it is enough to choose kmin<-
//(10PW_50+tstart), and kmax>(10PW_50+tend), where tstart and tend are
//integers defined by the simulation range of t.

//The readback signal with all sorts of noises (including timing jitter and PW50
variation) can be written as:

$$z(t) := \sum_k \left[ a_{k+50} \cdot h \left[ t - k \cdot T - (\Delta t_{k+50}), w + (\Delta w_{k+50}) \right] \right] + (md(0.1 \cdot A) - 0.05A)$$

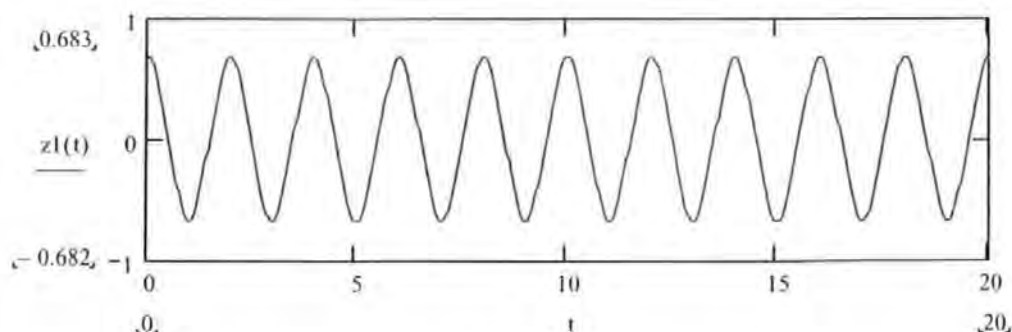
//Note: In the above expression, h(t-kT) corresponding to ak+50. We use this
//expression because the subscript can not be negative.

//If not considering any noise, the readback waveform is given by:

$$z1(t) := \sum_k (a_{k+50} \cdot h(t - k \cdot T, w))$$

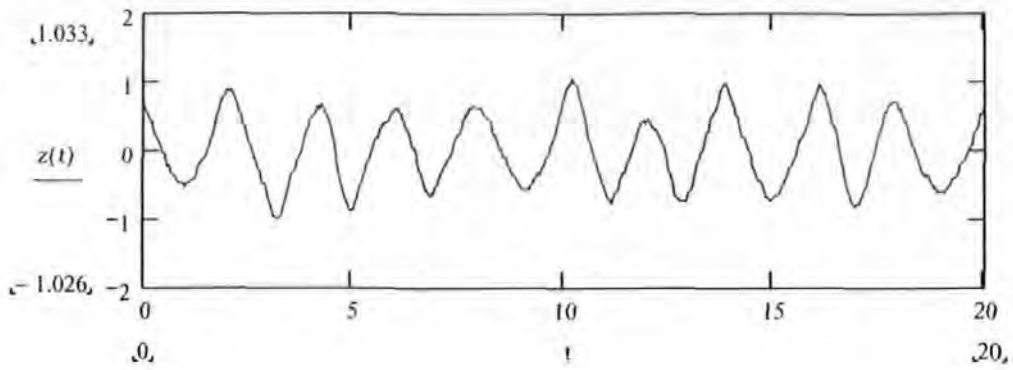

```

//Without any noise, the readback signal is plotted below:



//With all sorts of noises (including timing jitter and PW50 variation), the readback waveform is plotted as below:





### 7.1.1.2 Readback from a random bits recorded sequence

Here we simulate the cases when the recording bit density is high.

```

/*****
/// Readback from a recorded sequence of random bits
/*****

```

//The following part is used to generate a Pseudorandom Binary Sequences (random //data bits) being written on the disk. Note the value selection of a1 to a5. The theoretical basis is [Hsia, 1977]:

$$// \quad x(k+1) = \begin{pmatrix} a_1 & \cdots & a_n \\ 1 & 0 & \cdots & 0 & 0 \\ 0 & \cdots & 0 & 0 & 0 \\ 0 & \cdots & 0 & 1 & 0 \end{pmatrix} x(k)$$

$$// \quad y(k) = (0 \quad \cdots \quad 0 \quad 1)x(k)$$

// y(k) is the output. Modular 2 addition is used here for the add operation.

//Note that b\_m is the data bit sequence, a\_{m+1} = ((1-2\*b\_{m+1}) - (1-2\*b\_m))/2 is the //transition sequence (divided by 2 to make it a 1, 0, -1 series).

```

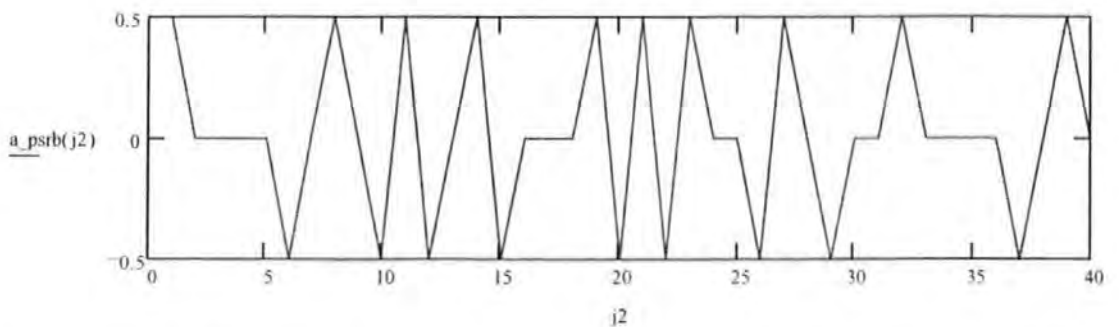
a :=
  m ← 0
  x1_0 ← 1
  x2_0 ← 1
  x3_0 ← 1
  x4_0 ← 1
  x5_0 ← 1
  a1 ← 0
  a2 ← 1
  a3 ← 0
  a4 ← 0
  a5 ← 1
  for j1 ∈ 0..1500
    x1_{m+1} ← if(if(if(if(a1·x1_m = a2·x2_m, 0, 1) = a3·x3_m, 0, 1) = a4·x4_m, 0, 1) = a5·x5_m, 0, 1)
    x2_{m+1} ← x1_m
    x3_{m+1} ← x2_m
    x4_{m+1} ← x3_m
    x5_{m+1} ← x4_m
    b_{m+1} ← x5_m
    a_{m+1} ←  $\frac{[(1 - 2 \cdot b_{m+1})] - [(1 - 2 \cdot b)_m]}{2}$ 
    m ← m + 1
  a

```

```

j2 = 1..40
a_psr(b(j2)) = a_{j2}

```



//T is the recording bit/symbol period. When recording density  $w/T$  gets high, there will be inter-symbol interference in the readback signal.

T := 1.0

w := 1·T

//Storage density (or bit density) is  $w/T$ .

$t := 0, 0.05T..40 \cdot T$

//Note: here the sample rate is  $1/(0.05T)$

//Generate timing jitter and PW\_50 variation noise:

$j := 0..2000$

$\Delta t_j := \text{rnd}(0.5 \cdot w) - 0.25 \cdot w$

$\Delta w_j := \text{rnd}(0.5 \cdot w) - 0.25 \cdot w$

$k = 50..-49..50$

// Theoretically,  $k$  should be from  $-\infty$  to  $+\infty$ , but because  $h(t-kT)$  will be decreased to nearly zero when  $k > 10PW_{50}$ , so it is enough to choose  $k_{\min} < (10PW_{50} + t_{\text{start}})$ , and  $k_{\max} > (10PW_{50} + t_{\text{end}})$ , where  $t_{\text{start}}$  and  $t_{\text{end}}$  are integers defined by the simulation range of  $t$ .

//The readback signal with all sorts of noises (including timing jitter and PW50 variation) can be written as:

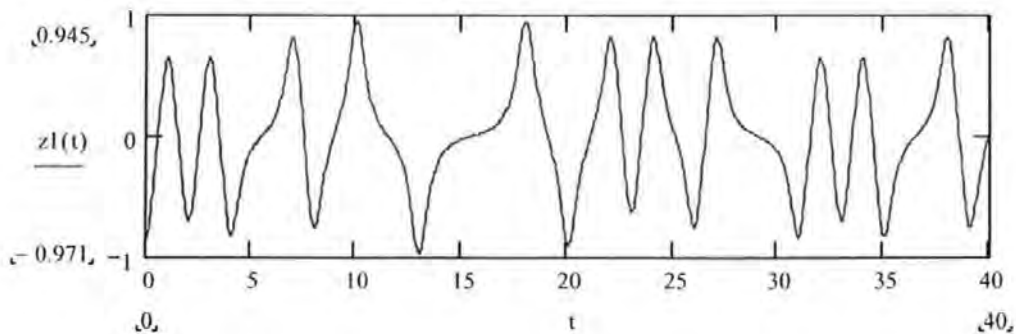
$$z(t) := \sum_k \left[ a_{k+50} \cdot h\left[t - k \cdot T - (\Delta t_{k+50}), w + (\Delta w_{k+50})\right] \right] + (\text{rnd}(0.1 \cdot A) - 0.05A)$$

//Note: In the above expression,  $h(t-kT)$  corresponding to  $a_{k+50}$ . We use this expression because the subscript can not be negative.

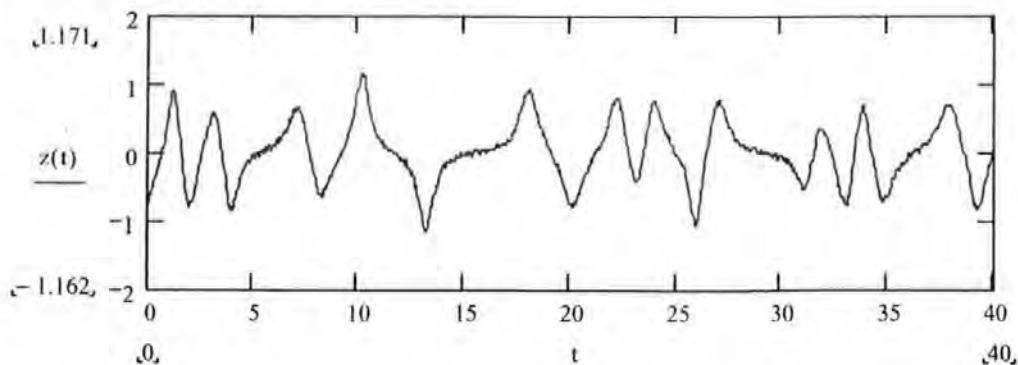
//If not considering any noise, the readback waveform is given by:

$$z1(t) = \sum_k (a_{k+50} \cdot h(t - k \cdot T, w))$$

//Without any noise, the readback signal is plotted below:



//With all sorts of noises (including timing jitter and PW50 variation), the readback waveform is plotted below:



## **7.1.2 Hard disk drive vibration analysis software**

### **7.1.2.1 Analysis of head-disk spacing variation**

The following Mathcad simulation software is used in section 4.1.2.

Simulation of the frequency response of the suspension arm, load beam, and disk under vibration conditions.

$$w := 1, 5, \dots, 3000 \quad // \text{frequency range of simulation (Hz)}$$

$$w_a := 2300 \quad // \text{natural frequency of the suspension arm}$$

$$w_l := 1000 \quad // \text{natural frequency of the load beam with the action of air bearing}$$

$$w_d := 700 \quad // \text{natural frequency of the disk.}$$

$$r_a(w) := \frac{w}{w_a} \quad r_l(w) := \frac{w}{w_l} \quad r_d(w) := \frac{w}{w_d}$$

$$\xi_a := 0.02 \quad \xi_l := 0.02 \quad \xi_d := 0.02 \quad // \text{damping factors}$$

$$\beta_a(w) := \frac{1}{\sqrt{(1 - r_a(w))^2 + (2 \cdot r_a(w) \cdot \xi_a)^2}} \quad \beta_l(w) := \frac{1}{\sqrt{(1 - r_l(w))^2 + (2 \cdot r_l(w) \cdot \xi_l)^2}}$$

$$\beta_d(w) := \frac{1}{\sqrt{(1 - r_d(w))^2 + (2 \cdot r_d(w) \cdot \xi_d)^2}}$$

$$\psi_a(w) := \text{atan}\left(\frac{2 \cdot r_a(w) \cdot \xi_a}{1 - r_a(w)^2}\right) \quad \psi_l(w) := \text{atan}\left(\frac{2 \cdot r_l(w) \cdot \xi_l}{1 - r_l(w)^2}\right)$$

$$\psi_d(w) := \text{atan}\left(\frac{2 \cdot r_d(w) \cdot \xi_d}{1 - r_d(w)^2}\right)$$

$$\sigma_l(w) := \sqrt{(1 - \beta_l(w) \cdot \cos(\psi_l(w)))^2 + (\beta_l(w) \cdot \sin(\psi_l(w)))^2}$$

$$\sigma_{AD_1}(w) := (\beta_a(w) \cdot \cos(\psi_a(w)) + \beta_d(w) \cdot \cos(\psi_d(w)))^2$$

$$\sigma_{AD_2}(w) := (\beta_a(w) \cdot \sin(\psi_a(w)) + \beta_d(w) \cdot \sin(\psi_d(w)))^2$$

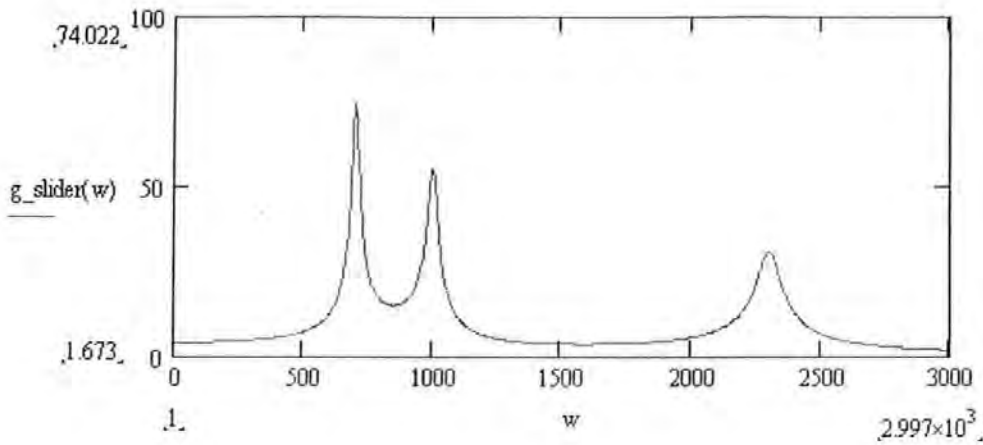
$$\sigma_{AD}(w) := \sqrt{\sigma_{AD_1}(w) + \sigma_{AD_2}(w)}$$

$$\sigma_{AD}(w) := \sqrt{\sigma_{AD\_1}(w) + \sigma_{AD\_2}(w)}$$

//From equation (3.15), the amplitude of the total/combined displacement of the slider relative to the disk drive base is:

$$g\_slider(w) := \sigma\_L(w) \cdot \sigma\_AD(w)$$

//The amplitude frequency response is shown in the following figure:



$$\psi\_AL(w) := \text{atan}\left(\frac{\beta\_l(w) \cdot \sin(\psi\_l(w))}{1 + \beta\_l(w) \cdot \cos(\psi\_l(w))}\right)$$

$$\psi\_AD(w) := \text{atan}\left(\frac{\beta\_a(w) \cdot \sin(\psi\_a(w)) + \beta\_d(w) \cdot \sin(\psi\_d(w))}{\beta\_a(w) \cdot \cos(\psi\_a(w)) + \beta\_d(w) \cdot \cos(\psi\_d(w))}\right)$$

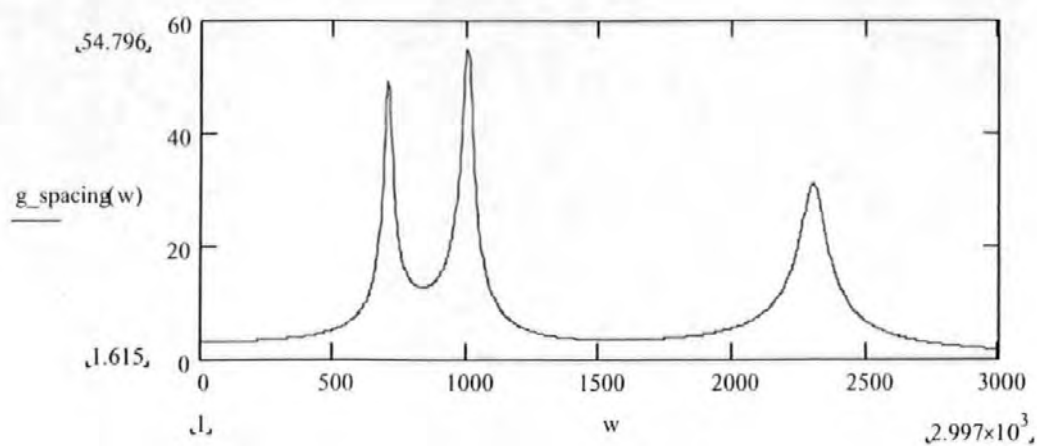
$$g\_spacing\_1(w) := (g\_slider(w) \cdot \cos(\psi\_AL(w) + \psi\_AD(w)) - \beta\_d(w) \cdot \cos(\psi\_d(w)))^2$$

$$g\_spacing\_2(w) := (g\_slider(w) \cdot \sin(\psi\_AL(w) + \psi\_AD(w)) - \beta\_d(w) \cdot \sin(\psi\_d(w)))^2$$

//From equation (3.18), the amplitude frequency response of the slider displacement relative to the disk (i.e. head disk spacing variation) is:

$$g\_spacing(w) := \sqrt{g\_spacing\_1(w) + g\_spacing\_2(w)}$$

//The amplitude frequency response of the head disk spacing is shown in the following figure:



### 7.1.2.2 Head position servo control

The following Mathcad simulation software is used in section 4.1.3.

//Disk head position servo control simulation

$w := 1, 11 \dots 10000$  //angular frequency range of simulation (radian/second)

$s(w) := i \cdot w$

$G_p(w) := \frac{0.05}{0.01 \cdot s(w)^2 + 0.004 \cdot s(w) + 10}$  //transfer function of the controlled object

//The magnitude and phase of the frequency response of the controlled object are:

$\text{mag}_s(w) := 20 \cdot \log \left( \sqrt{\text{Re}(G_p(w))^2 + \text{Im}(G_p(w))^2} \right)$

$\text{phase}_s(w) := \arg(G_p(w)) \cdot \frac{180}{\pi}$

$K := 2.6424 \cdot 10^6$

$G_c(w) := K \cdot \frac{s(w) + 32.5}{s(w) + 100000}$  //Transfer function of the servo controller

$H(w) := G_c(w) \cdot G_p(w)$

$G_{\text{cls}}(w) := \frac{G_c(w) \cdot G_p(w)}{1 + G_c(w) \cdot G_p(w)}$  //The closed loop transfer function of the control system

//The magnitude and phase of the frequency response of the closed loop system are:

$\text{mag}_{\text{lg\_cls}}(w) := 20 \cdot \log \left( \sqrt{\text{Re}(G_{\text{cls}}(w))^2 + \text{Im}(G_{\text{cls}}(w))^2} \right)$

$\text{mag}_{\text{cls}}(w) := \sqrt{\text{Re}(G_{\text{cls}}(w))^2 + \text{Im}(G_{\text{cls}}(w))^2}$

$\text{phase}_{\text{cls}}(w) := \arg(G_{\text{cls}}(w)) \cdot \frac{180}{\pi}$

$G_{\text{e}_r}(w) := \frac{1}{1 + G_c(w) \cdot G_p(w)}$  //The sensitivity function of the servo loop

//The magnitude and phase of the frequency response of the sensitivity function are:

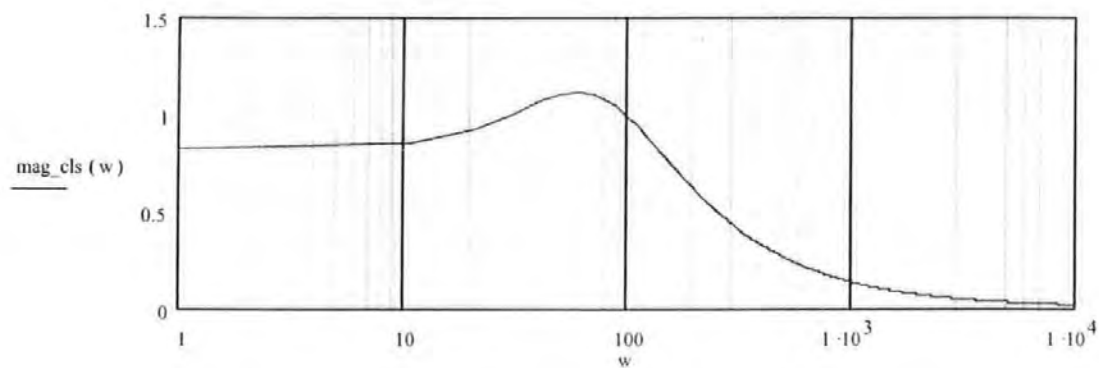


$$\text{mag\_lg\_e\_r}(w) := 20 \cdot \log \left( \sqrt{\text{Re}(\text{Ge}_r(w))^2 + \text{Im}(\text{Ge}_r(w))^2} \right)$$

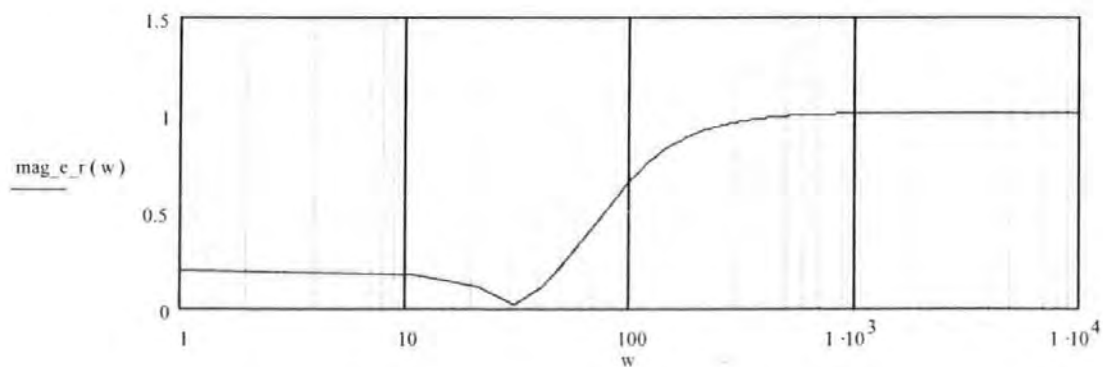
$$\text{mag\_e\_r}(w) := \sqrt{\text{Re}(\text{Ge}_r(w))^2 + \text{Im}(\text{Ge}_r(w))^2}$$

$$\text{phase\_e\_r}(w) := \arg(\text{Ge}_r(w)) \cdot \frac{180}{\pi}$$

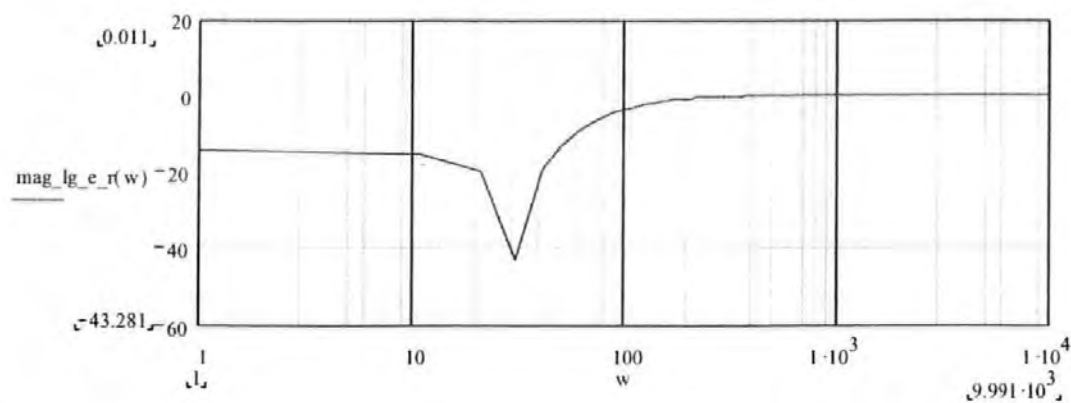
//The magnitude frequency response of the closed loop servo system is plotted below:



//The magnitude frequency response of the sensitivity function of the servo system is plotted below:



//The magnitude frequency response of the sensitivity function of the servo system is plotted below:



### 7.1.3 Readback signal processing software

The following signal processing routine written in Matlab is used in section 5.2.1 and 5.3.

```
%-----  
%Digital signal processing for readback signal under  
%shaking condition:  
%   The readback signal data first pass through local  
%   averaging to get rid of the DC component; then pass  
%   through full wave rectification. The rectified signal  
%   then go through the lowpass FIR filter for the  
%   envelope of the readback signal to be obtained.  
%-----  
clc;  
clear;  
  
%-----  
%Open the readback signal data file saved by the digital  
%oscilloscope. For this data file, the condition of the  
%experiment can be known from the file name: vibration  
%frequency is 2040Hz, acceleration is 31.2g, sampling  
%frequency is 10MHz.  
%The number of samples in a readback data file has been  
%always set to 50000.  
%-----  
fid=fopen('a2040H10M31p2g.dat','r');  
  
%-----  
%We take the first 25000 samples to be processed, which is  
%equivalent to  $25000 \times f_t / f_s = 5.1$  modulation cycles. We can  
%use the whole 50000 samples but the processing time becomes  
%longer.  
%-----  
v=fscanf(fid, '%f', 25000);  
f_s=10*1000000; %Sampling frequency  
f_t=2040;      %Vibration testing frequency  
num=25000; %Number of samples to be processing (maximum  
           %50000)  
  
%-----  
%Set the parameter for local averaging. It can be seen from  
%the following that  $(2 \times \text{num\_local} + 1)$  samples are used for  
%local averaging.  
%-----  
num_local=100;  
nsamp=num-2*num_local; %This is the actual number of  
                        %samples to be processed
```

```

%-----
%Local averaging and full wave rectification. After local
%averaging, the DC component of the readback signal is
%eliminated.
%-----
for n=1+num_local:num-num_local
    local_average=0;
    for n1=n-num_local:n+num_local
        local_average=local_average+v(n1);
    end
    local_average=local_average/(2*num_local+1);
    if v(n)>=local_average
        v_rect(n-num_local)=v(n)-local_average;
        %So v_rect is actually acted from the 101st sample.
    else
        v_rect(n-num_local)=local_average-v(n);
    end
end
end

m=2*250; %m is the order of the lowpass FIR digital filter

%Get the (m+1) coefficients of the lowpass FIR filter
B=firl(m, 10*f_t/f_s) %Set the cut-off frequency of the
                        %lowpass filter to 10 times the
                        %vibration frequency.

x=zeros(length(B),1);
for k = 1:num-m-1
    [x,y(k)]=arma(v_rect(k),B',x,0,m); %This function is
                                        %listed next in the following.
end
plot((501:num-501),y(501:num-501));

```

The following function is from [Schilling, 2000]

```
function [x,y] = arma (u,theta,x,n,m)
```

```
%-----
%Usage:      [x,y] = arma (u,theta,x,n,m)
%
```

```
%Description: Compute the output of an auto-regressive
               moving-average (ARMA) model having the
               following transfer function:
```

$$\frac{Y(z)}{U(z)} = \frac{\theta(n+1) + \dots + \theta(n+m+1)z^{(-m)}}{1 + \theta(1)z^{(-1)} + \dots + \theta(n)z^{(-n)}}$$

```
%Inputs:      u      = system input
%              theta = (n+m+1) by 1 vector of system
%                  parameters:
%                  [a1,...,an,b0,...,bm]'
```

```

% x      = (n+m+1) by 1 vector containing
%          system state:
%          [-y(k-1), ..., -y(k-n), u(k), u(k-
%          1), ..., u(k-m)]'
% n      = number of past outputs used (n >= 0)
% m      = number of past inputs used (m >= 0)
%
% Outputs: x      = (n+m+1) \times 1 vector containing
%                  updated system state with
%                  x(n+1) = 0.
%          y      = the system output.
% -----

```

```

% Initialize
chkvec (theta,2,'arma');
chkvec (x,3,'arma');
m = args (m,0,m,4,'arma');
n = args (n,0,n,5,'arma');
y = 0;
r = n + m + 1;

```

```

% Compute y

x(n+1) = u;
for i = 1 : r
    y = y + theta(i)*x(i);
end

```

```

% Update

for i = r : -1 : 2
    x(i) = x(i-1);
end
if n > 0
    x(1) = -y;
end
x(n+1) = 0;
% -----

```

## 7.1.4 Thermal signal simulation and processing software

The following Matlab routine is used in section 5.2.4.

```

% -----
% Thermal signal simulation and processing:
% Generate a sinusoidal thermal signal with a frequency

```

```

% the same as that of the vibration testing;
% Mix the thermal signal with the readback signal from the
% vibration testing;
% Signal processing to extract the thermal signal from the
% the mixed readback signal under vibration conditions
%-----
clc;
clear;
fs=50*1000000; %sampling frequency
%load a5800H50M19p2g.dat; %readback data
%v_r(1:50000)=a5800H50M19p2g(1:50000);
fid=fopen('a5800H50M19p2g.dat','r');
v_r=fscanf(fid, '%f', 50000);
ft=5800; %Vibration frequency under testing

%-----
%Generate the thermal signal with a frequency equal to the
%vibration frequency under testing. I.e., a parameter of
%fs/ft=8620 is used in the following sinusoidal wave
%generator. A phase parameter is added so that the wave has
the same phase as that of the vibration (600 is used here).
%-----
for i=1:50000
    v_cos(i)=0.02*(1+cos((2*3.14/8620)*(i-600)));
end

%Mix the thermal signal with the read back signal from the
%vibration testing.
v=v_r+v_cos';

num=50000;
%Signal processing starts.
plot(v)
%pause

m=2*250; %using a 500-order FIR filter

%Generate the parameters of the bandpass FIR filter
B=fir1(m,[200/fs 2*ft/fs])

%Filtering the mixed readback signal
x=zeros(length(B),1);
for k = 1:num-m-1
    [x,y(k)]=arma(v(k),B',x,0,m);
end

%Plot the processed signal
y1(1:num-2m)=y(m:num-m-1);
plot(y1)
%plot(y)

```

## 7.1.5 PW50 parameter estimation software

The following Mathcad software is used in Section 5.2.3.

### 7.1.5.1 Estimation using an isotropic (1, -1) recorded sequence

```

//*****
/// PW50 parameter estimation using an isotropic (1, -1) recorded sequence
//*****
w := 1.0 //Here w represents PW_50
Ah := 1.0
t := -10·w, -9·w.. 10·w

//The transition response is

$$h(t, w) = \frac{1}{w} \cdot \frac{1}{1 + \frac{(2 \cdot t)^2}{w^2}}$$


$$\frac{d}{dw} h(t, w) = \left[ \frac{1}{w^2 \cdot \left( 1 + 4 \cdot \frac{t^2}{w^2} \right)} \right] + \left[ \frac{8}{w^4 \cdot \left( 1 + 4 \cdot \frac{t^2}{w^2} \right)^2} \right] \cdot t^2$$

//Generate an isotropic 1, -1 input series:
b0 := 1      j := 0..1500
bj+1 := -bj

//Obtain transition sequence of the above input series:
a0 := 1      i := 1..1500

$$a_i := \frac{(b_i - b_{i-1})}{2}$$

//ai is the transition series read back from the disk. We divide by 2 to make the series
//be 1,-1 as well .

//T is the recording bit period. When simulating isolated read-back pulses, T should be
//selected much larger than PW_50 (e.g., 20 times PW_50). In that case, there will be no
//inter-symbol interference in the readback signal.
T := 20
w := 0.05 T
//Storage density (or bit density) is w/T.

t := 0, 0.05 T.. 4·T
//Note: here the sample rate is 1/(0.05T)

```

//Generate timing jitter and PW\_50 variation noise

j := 0..1500

$\Delta t_j := \text{rnd}(0.25T) - 0.125T$

$\Delta w_j := \text{rnd}(0.25T) - 0.125T$

k = -50..49..50

// Theoretically, k should be from -infinite to +infinite, but because  $h(t-kT)$  will be //decreased to nearly zero when  $k > 10PW\_50$ , so it is enough to choose  $k\_min < -(10PW\_50 + t\_start)$ , and  $k\_max > (10PW\_50 + t\_end)$ , where  $t\_start$  and  $t\_end$  are //integers defined by the simulation range of t.

//The readback signal with all sorts of noises (including timing jitter and PW50 variation) can be written as:

$$x(t) := \sum_k \left[ a_{k+50} \cdot h\left[t - k \cdot T - (\Delta t_{k+50}), w + (\Delta w_{k+50})\right] \right] + (\text{rnd}(0.1 \cdot A) - 0.05A)$$

//Note: In the above expression,  $h(t-kT)$  is associated with  $a_{k+50}$ . We use this //expression because the subscript can not be negative.

//Following is the PW50 parameter estimation. From the following simulation, we //found that when  $\beta=0.20$ , the estimation process is very quick; when  $\beta$  is smaller, the //convergence speed gets slow; when  $\beta$  is bigger, the estimation has overshoot so the //actual convergence speed is also getting slow.

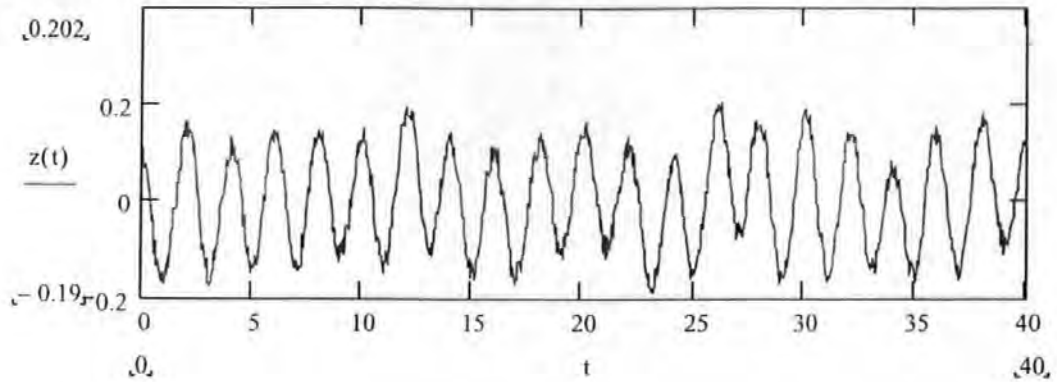
L := 11 · w

k := 0, 1..1500

$a\_shift_k := a_k$

```
Pw := Pw_0 ← 0.5T
β ← 0.20
w ← 2.0T
k1 ← 0
for k2 ∈ 0..1000
  r_k1 ← r_l_k1 ← 0
  for m ∈ -L..L
    r_l_k1 ← r_l_k1 + a_shift_k1-m+L ·  $\left[ \frac{1}{w} \cdot \frac{1}{1 + \frac{2 \cdot (m + \Delta t_{k1-m+L})^2}{[w + (\Delta w_{k1-m+L})]^2}} \right] + (\text{rnd}(0.05A) - 0.025A)$ 
  x_k1 ← x_l_k1 ← 0
  for m ∈ -L..L
    x_l_k1 ← x_l_k1 + a_shift_k1-m+L ·  $\left[ \frac{1}{Pw_{k1}} \cdot \frac{1}{1 + \frac{(2 \cdot m)^2}{(Pw_{k1})^2}} \right]$ 
  e_k1 ← r_k1 - x_k1
  Pw_k1+1 ← Pw_k1 + β · e_k1 ·  $\left[ \begin{array}{l} x_{dl\_k1} \leftarrow 0 \\ \text{for } m \in -L..L \\ x_{dl\_k1} \leftarrow x_{dl\_k1} + a\_shift_{k1-m+L} \cdot \left[ \frac{-1}{\left( \frac{Pw_{k1}}{(Pw_{k1})^2} \right) \left[ 1 + 4 \cdot \frac{m^2}{(Pw_{k1})^2} \right]} + \frac{8}{\left( \frac{Pw_{k1}}{(Pw_{k1})^4} \right) \left[ 1 + 4 \cdot \frac{m^2}{(Pw_{k1})^2} \right]^2} \cdot m^2 \right] \end{array} \right]$ 
  k1 ← k1 + 1
Pw
```

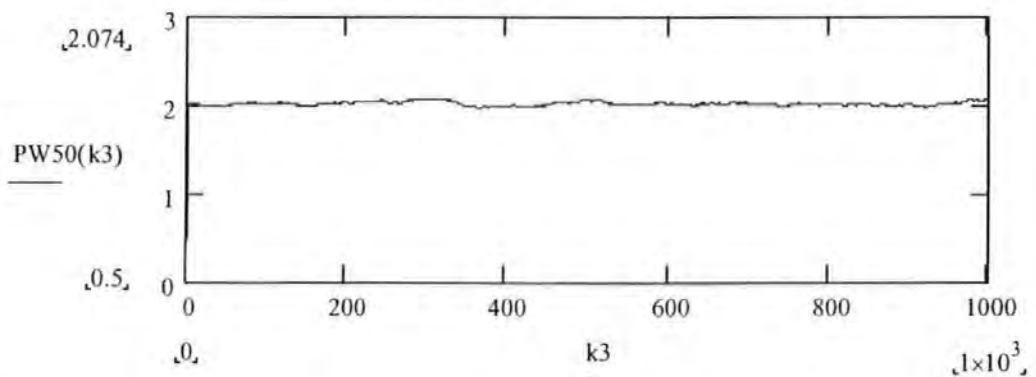
//The simulated readback signal is shown below:



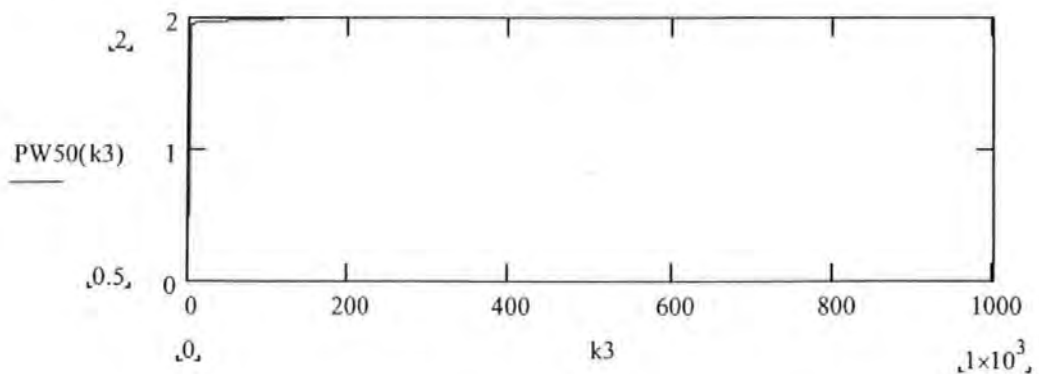
k3 := 0..1000

PW50(k3) := Pw<sub>k3</sub>

//The PW50 estimation process is shown below:



//If there is no noise in the readback signal, the PW50 estimation process is shown below:



### 7.1.5.2 Estimation using a random bits recorded sequence

```
//*****
/// PW50 parameter estimation using a random bits recorded sequence
//*****
```



//This software routine is the same as that listed in Section 5.2.3.2 except the input bit  
 //sequence used for the estimation, which is a random bit sequence. Thus here we only  
 //list the different parts of the routine.

//The following part is used to generate a Pseudorandom Binary Sequences (random  
 //data bits) being written on the disk. Note the value selection of a1 to a5. The  
 //theoretical basis is:

$$// x(k+1) = \begin{pmatrix} a_1 & \cdots & a_n \\ 1 & 0 & \cdots & 0 & 0 \\ 0 & \cdots & 0 & 0 & 0 \\ 0 & \cdots & 0 & 1 & 0 \end{pmatrix} x(k)$$

// y(k) = (0 ... 0 1)x(k), y(k) is output.

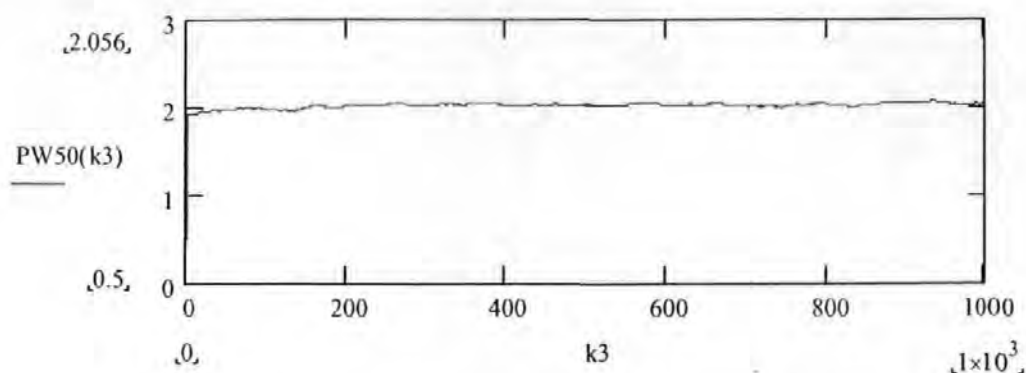
```

a := | m ← 0
      | x1_0 ← 1
      | x2_0 ← 1
      | x3_0 ← 1
      | x4_0 ← 1
      | x5_0 ← 1
      | a1 ← 0
      | a2 ← 1
      | a3 ← 0
      | a4 ← 0
      | a5 ← 1
      | for j1 ∈ 0..1500
      |   | x1_{m+1} ← if( if( if( a1·x1_m = a2·x2_m, 0, 1 ) = a3·x3_m, 0, 1 ) = a4·x4_m, 0, 1 ) = a5·x5_m, 0, 1 )
      |   | x2_{m+1} ← x1_m
      |   | x3_{m+1} ← x2_m
      |   | x4_{m+1} ← x3_m
      |   | x5_{m+1} ← x4_m
      |   | b_{m+1} ← x5_m
      |   | a_{m+1} ← (b_{m+1} - b_m) / 2
      |   | m ← m + 1
a

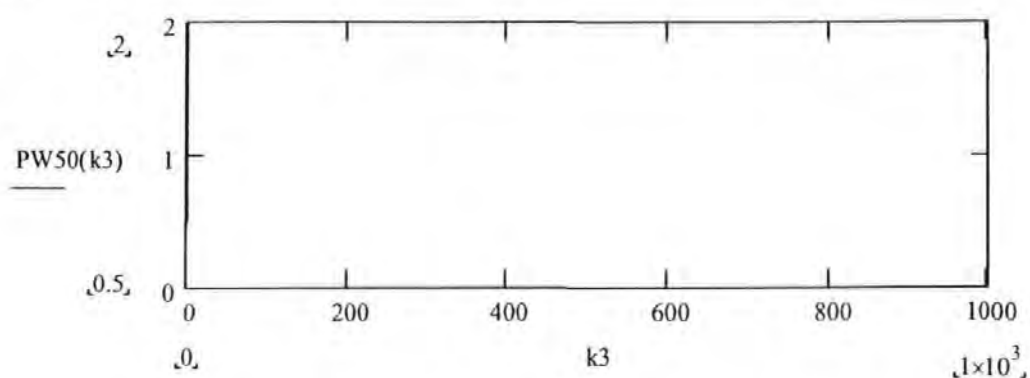
```

//Note: b\_m is the written magnetic cells and a\_m is the transition sequence.

//The PW50 estimation process is shown below:



//If there is no noise in the readback signal, the PW50 estimation process is shown  
//below:



### 7.1.5.3 Tracking property of the parameter estimation method

This software routine is used to study the tracking property of the parameter estimation method.

```
//*****+
// Estimation with varying PW50 parameter
//*****
//The transition response is
```

$$h(t, w) = \frac{1}{w} \cdot \frac{1}{1 + \frac{(2 \cdot t)^2}{w^2}}$$

$$\frac{d}{dw} h(t, w) = \frac{-1}{\left[ w^2 \cdot \left( 1 + 4 \cdot \frac{t^2}{w^2} \right) \right]} + \frac{8}{\left[ w^4 \cdot \left( 1 + 4 \cdot \frac{t^2}{w^2} \right)^2 \right]} \cdot t^2$$

//The following part is used to generate a Pseudorandom Binary Sequences (random  
//data bits) being written on the disk. Note that b\_m is the data bit sequence,

//a<sub>m+1</sub> = ((1-2\*b<sub>m+1</sub>) - (1-2\*b<sub>m</sub>))/2 is the transition sequence (divided by 2 to make  
//it a 1, 0, -1 series).

```

a :=
  m ← 0
  x10 ← 1
  x20 ← 1
  x30 ← 1
  x40 ← 1
  x50 ← 1
  a1 ← 0
  a2 ← 1
  a3 ← 0
  a4 ← 0
  a5 ← 1
  for j1 ∈ 0..20100
    x1m+1 ← if(if(if(if(a1·x1m = a2·x2m, 0, 1) = a3·x3m, 0, 1) = a4·x4m, 0, 1) = a5·x5m, 0, 1)
    x2m+1 ← x1m
    x3m+1 ← x2m
    x4m+1 ← x3m
    x5m+1 ← x4m
    bm+1 ← x5m
    am+1 ←  $\frac{(1 - 2 \cdot b_{m+1}) - (1 - 2 \cdot b_m)}{2}$ 
    m ← m + 1
  a

```

//T is the recording bit/symbol period. When recording density w/T gets high, there will  
//be inter-symbol interference in the readback signal.

T := 1.0

w := 2.0·T

//Storage density (or bit density) is w/T.

t := 0, 0.05T..40·T

//Note: here the sample rate is 1/(0.05T)

//Generate timing jitter and PW<sub>50</sub> variation noise:

j := 0..20100

Δt<sub>j</sub> := md(0.25T) - 0.125T

Δw<sub>j</sub> := md(0.25T) - 0.125T

k := -50, -49..50

// Theoretically, k should be from -infinite to +infinite, but because h(t-kT) will be  
//decreased to nearly zero when k>10PW<sub>50</sub>, so it is enough to choose k<sub>min</sub><-

//(10PW\_50+t\_start), and k\_max>( 10PW\_50+t\_end), where t\_start and t\_end are //integers defined by the simulation range of t.

//The readback signal with all sorts of noises (including timing jitter and PW50 variation) can be written as:

$$z(t) := \sum_k \left[ a_{k+50} \cdot h[t - k \cdot T - (\Delta t_{k+50}), w + (\Delta w_{k+50})] \right] + (\text{rnd}(0.025 A) - 0.0125)$$

//Note: In the above expression, h(t-kT) corresponding to a\_k+50. We use this //expression because the subscript can not be negative.

w := 2.0.T

L := 11.w

k := 0, 1., 20100

a\_shift\_k := a\_k

//In the following, the PWM50 parameter varies in sinusoidal waveform at a frequency //of 0.0001\*bit-rate (Hz).

$$\begin{aligned} & \text{Pw} := \left[ \begin{array}{l} \text{Pw}_0 \leftarrow 2.0.T \\ \beta \leftarrow 0.20 \\ k1 \leftarrow 0 \\ k\_sam \leftarrow 1 \\ \text{for } k2 \in 0..20000 \\ \quad \left[ \begin{array}{l} r_{k1} \leftarrow r_{k1} \leftarrow 0 \\ \text{for } m \in \text{ceil}(k1 \cdot k\_sam - 0.5) - L.. \text{ceil}(k1 \cdot k\_sam + 0.5) + L \\ \quad r_{k1} \leftarrow r_{k1} + a\_shift_{m+L} \left[ \frac{1}{w + 1.0 \sin \left[ 2.3.14159(m+L) \frac{1}{10000} \right]} + \frac{1}{\left[ w + 1.0 \sin \left[ 2.3.14159(m+L) \frac{1}{10000} \right] \right]^2} \right] + (\text{rnd}(0.025) - 0.0125) \\ x_{k1} \leftarrow x_{k1} \leftarrow 0 \\ \text{for } m \in \text{ceil}(k1 \cdot k\_sam - 0.5) - L.. \text{ceil}(k1 \cdot k\_sam + 0.5) + L \\ \quad x_{k1} \leftarrow x_{k1} + a\_shift_{m+L} \left[ \frac{1}{\text{Pw}_{k1}} \frac{1}{1 + \frac{12 \cdot (k\_sam \cdot k1 - m)^2}{(\text{Pw}_{k1})^2}} \right] \\ e_{k1} \leftarrow r_{k1} - x_{k1} \\ \text{Pw}_{k1+1} \leftarrow \text{Pw}_{k1} + \beta \cdot e_{k1} \left[ \begin{array}{l} x_{d1} \leftarrow x_{d1} \leftarrow 0 \\ \text{for } m \in \text{ceil}(k1 \cdot k\_sam - 0.5) - L.. \text{ceil}(k1 \cdot k\_sam + 0.5) + L \\ \quad x_{d1} \leftarrow x_{d1} + a\_shift_{m+L} \left[ \frac{-1}{\left( \text{Pw}_{k1} \right)^2 \left[ 1 + 4 \frac{(k\_sam \cdot k1 - m)^2}{(\text{Pw}_{k1})^2} \right]} + \frac{8}{\left( \text{Pw}_{k1} \right)^4 \left[ 1 + 4 \frac{(k\_sam \cdot k1 - m)^2}{(\text{Pw}_{k1})^2} \right]^2} \right] (k\_sam \cdot k1 - m)^2 \end{array} \right] \\ k1 \leftarrow k1 + 1 \end{array} \right] \\ \text{Pw} \end{array} \right. \end{aligned}$$

#### 7.1.5.4 PW50 estimation using readback signal of real hard disk drives

\*\*\*\*\*  
// This is the mathcad software routine that is used to estimate the PW50  
// parameter from the readback signal of real hard disk drives.  
\*\*\*\*\*

//"outest\_50k\_1.prn" is a data file obtained by using the Lecroy oscilloscope from a  
//Quantum\_ProDrive LPS-170M hard drive. The sample rate is 500MHz/s.

//In the estimation algorithm, the recording bit rate of the hard drive is used as the  
 //sample rate. Timing is determined offline within the software routine..

```
A := READPRN("outest_50k_1.prn" )
```

```
K := last(A<0>)
```

```
A := submatrix(A,2,K,0,1)
```

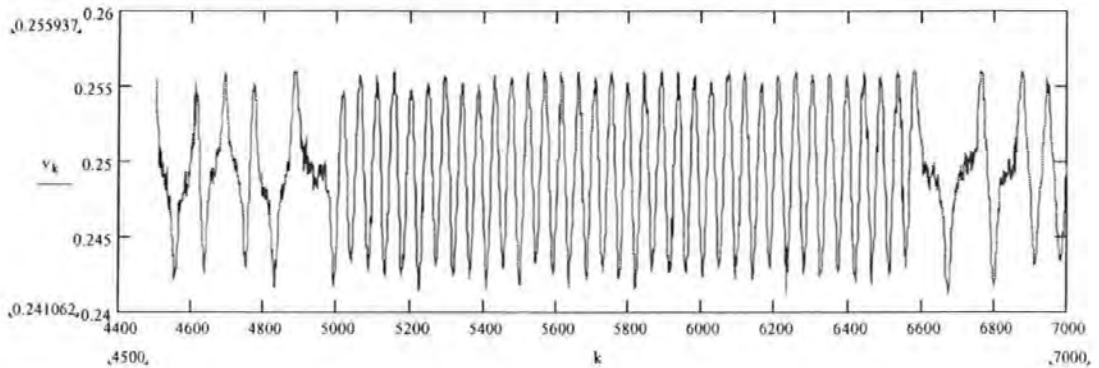
```
t := A<1>
```

```
v := A<1>
```

```
K := last(t)
```

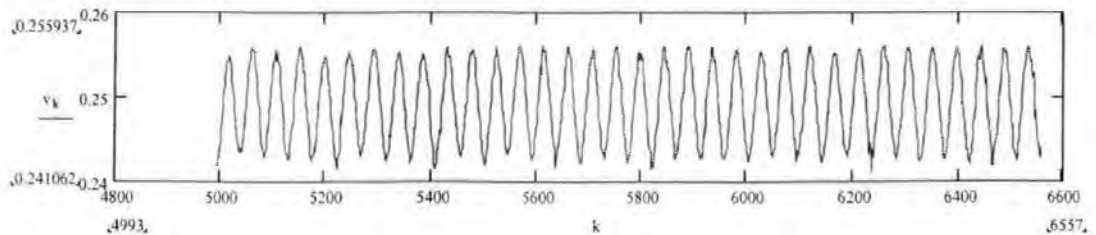
//Part of the readback signal is shown below:

```
k := 4500,4500 + 1..7000
```



//The following part of the readback signal will be used for the estimation of PW50.  
 //This is because the timing can be determined much easier, and this part of the signal  
 //will be used repeatedly for the estimation.

```
k := 4993..6557
```



//From above, we can see that the recording bit-period is about  $(6557-4993)/34/2=23$   
 //times the sampling period of the oscilloscope, i.e. the bit-rate is  $f_b=500/23 \text{ MHz} =$   
 //21.74 MHz

//Get the average value of this part of signal:

```

v_average := | v_average ← 0.0
               | for k2 ∈ 4993..6556
               |   v_average ← v_average + v_k2
               | v_average ←  $\frac{v\_average}{6557 - 4993}$ 

```

v\_average = 0.2491369853

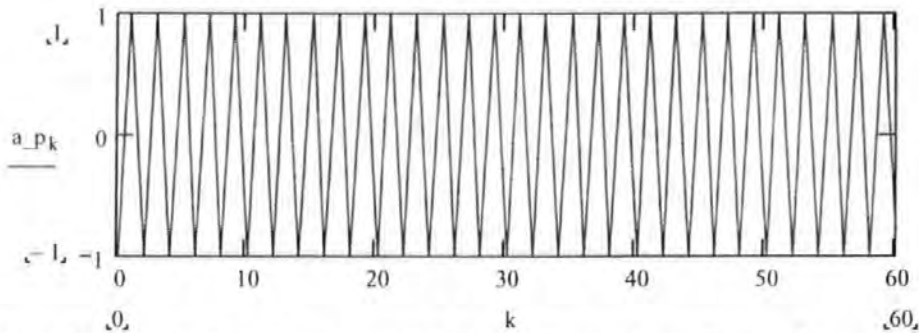
//The following part is used to see how good the timing is. Note that the timing accuracy  
//can not be better than the sampling period of the ocsilloscope, i.e., 2 ns.

```

a_p := | for k1 ∈ 4993,5016..46000
        |   k ←  $\frac{k1 - 4993}{23}$ 
        |   a_pk ← | 1 if v_k1 - v_average > 0.002
                    | -1 if v_k1 - v_average < 0.002
                    | 0 otherwise
        | a_p

```

k := 0..60



//From the above plot, it can be seen that the timing is pretty good.

//Therefore the same timing is used for the readback signal r\_r in the following:

```

r_r := | for k1 ∈ 4993,5016..46000
        |   k ←  $\frac{k1 - 4993}{23}$ 
        |   r_rk ← v_k1
        | r_r

```

//The following r\_amp is the average amplitude of the above part of the readback signal  
// (66 transitions).

```

r_amp := | r_amp ← 0.0
          | for k1 ∈ 4993,4993 + 46..6557 - 46
          |   r_amp ← r_amp + (v_k1+23 - v_k1)
          | r_amp ←  $\frac{r\_amp}{\left(\frac{6557 - 46 - 4993}{46}\right) \cdot 2}$ 

```

$$r\_amp = 0.0064980758 \quad \frac{6557 - 46 - 4993}{46} = 33$$

//The following r\_p\_average is the average value of the above timing sampled readback  
//signal (68 transitions).

$$v\_p\_average := \begin{cases} v\_p\_average \leftarrow 0.0 \\ \text{for } k1 \in 4993, 4993 + 23..6557 - 23 \\ \quad v\_p\_average \leftarrow v\_p\_average + v_{k1} \\ \quad v\_p\_average \leftarrow \frac{v\_p\_average}{68} \end{cases} \quad \frac{6557 - 23 - 4993}{23} = 67$$

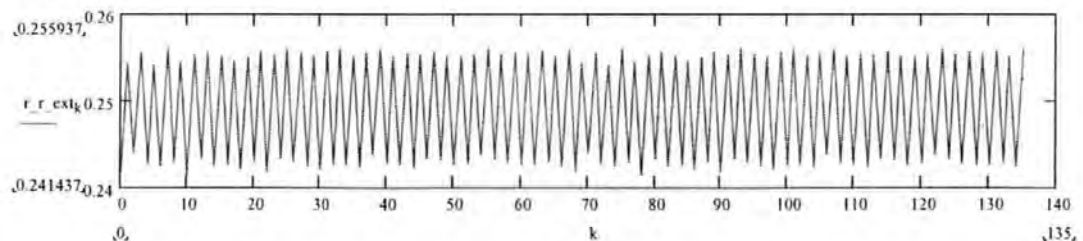
$$v\_p\_average = 0.2490072206$$

//The following is making periodical extension to the readback signal of the 68-  
//transition sequence in order to be used in the PW50 estimation.

$$r\_r\_ext := \begin{cases} \text{for } k2 \in 0..99 \\ \quad \begin{cases} \text{for } k1 \in 4993, 5016..6557 - 23 \\ \quad k \leftarrow \frac{k1 - 4993}{23} + 68 \cdot k2 \\ \quad r\_r\_ext_k \leftarrow v_{k1} \end{cases} \\ \quad r\_r\_ext \end{cases}$$

//From the following plot, it can be seen that the above periodical extension action is  
//correct. Part of the extended readback signal is displayed below:

$$k := 0, 1..2 \cdot 68 - 1$$



//From the above readback signal, the transition sequence has been known as the  
//following:

$$a1_0 := -1 \quad i := 0..10000$$

$$a1_{i+1} := -a1_i$$

//Note the value of parameter L should be selected big enough, usually  $L > 10 \cdot PW50$ .

$$L := 20$$

$$k := 0..10000$$

$$a_k := a1_k$$

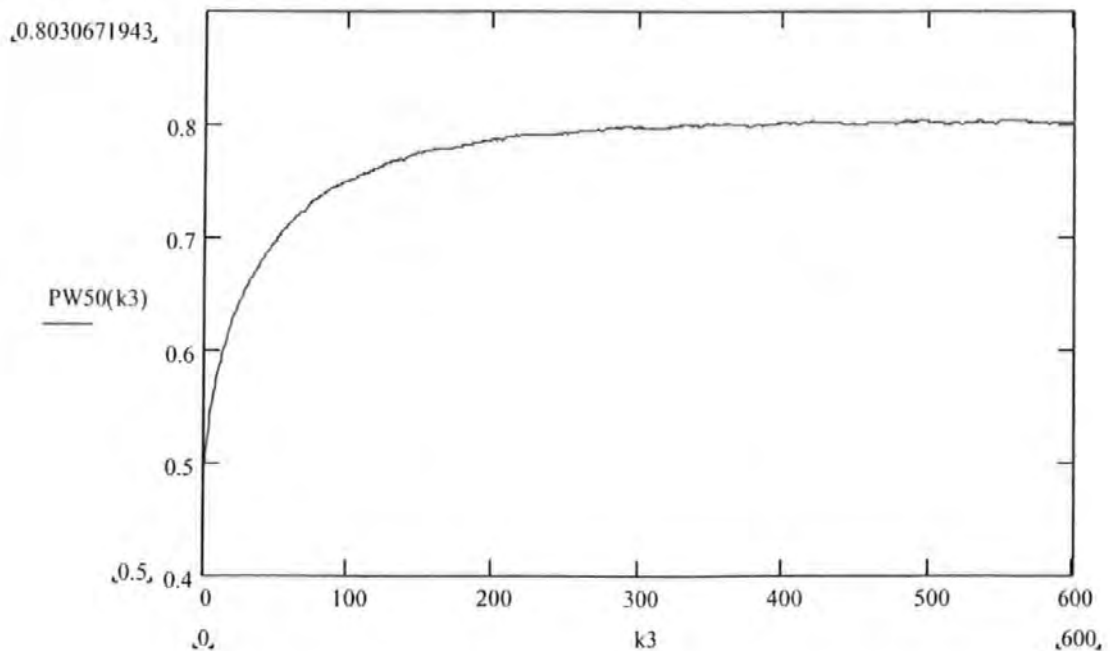
//For the PW50 estimation algorithm to be performed, the amplitude of the isolated  
 //readback signal needs to be known. This is a fixed value for a given hard disk drive.  
 //assembly. For the disk drive used in the experiment, this has been measured to be:  
 r\_amp := 0.0065

//The PW50 estimation is performed below:

```
Pw := | Pw_0 ← 0.5·T
      | β ← 0.5
      | k1 ← 0
      | for k2 ∈ 0..2000
      |   r_k1 ← r_ext_k1 - v_p_average
      |   x_k1 ← | x_l_k1 ← 0
      |           | for m ∈ -L..L
      |             | x_l_k1 ← x_l_k1 + r_amp·a_k1-m+L ·  $\left[ \frac{1}{Pw_{k1}} \cdot \frac{1}{1 + \frac{(2·m)^2}{(Pw_{k1})^2}} \right]$ 
      |           |
      |           | e_k1 ← r_k1 - x_k1
      |           | Pw_{k1+1} ← Pw_{k1} + β·e_k1
      |           |   | xdl_k1 ← 0
      |           |   | for m ∈ -L..L
      |           |   | xdl_k1 ← xdl_k1 + a_k1-m+L ·  $\left[ \frac{-1}{(Pw_{k1})^2 \cdot \left[ 1 + 4 \cdot \frac{m^2}{(Pw_{k1})^2} \right]} + \frac{8}{(Pw_{k1})^4 \cdot \left[ 1 + 4 \cdot \frac{m^2}{(Pw_{k1})^2} \right]^2} \cdot m^2 \right]$ 
      |           |
      |           | k1 ← k1 + 1
      | Pw
```

PW50(k3) := Pw\_k3

//The PW50 estimation process and result are shown in the plot below:





## 7.1.6 Flying height control simulation software

The following flying height control simulation software written in Matlab is used in Section 5.4.

```
%-----
%PID control of flying height (variation).
%A PI compensator here is used to compensate the highpass
%filter, and the compensation is designed to be not full to
%reflect the robustness of the controller. Another two lead
%compensators are used to compensate the second vibration
%mode (the first mode is compensated by the PID
%controller).
%-----
echo off
clc
clf
echo on
pause % Strike any key to continue.

% Assume the plant has two vibration mode, one from the
% suspension arm, another from the slider's air bearing.
% The third term is the highpass filter of the AEM.
% The transfer function of the plant now becomes:
%
%          b1          b2          s
%  H(s) = -----  -----  -----
%          s^2 + a1s + b1  s^2 + a2s + b2  s + a
%
%
%
a1 = 2*0.017*950; b1 = 902500;
num1 = b1;
den1 = [1 a1 b1];
H1 = tf(num1,den1);
pause % Press any key to continue ...
a2 = 2*0.058*45000; b2 = 2025000000;
num2 = b2;
den2 = [1 a2 b2];
H2 = tf(num2,den2);

%Single pole of the highpass filter a = 325000, tolerance
%may be as large as 125000
H3 = zpk(0,-325000,1)

%We use an inverse filter to try to compensate this
%highpass filter, and assume we failed to make a full
%compensation by using the following lag compensator:
%
%          s + 200000
%compensator G1 = -----
```

```

%                                     s
G1 = zpk(-200000,0,1)

% We use another two lead compensators:
%
%      s + b3
% G2 = -----
%      s + 20*b3
%      s + b4
% G3 = -----
%      s + 20*b4

b3 = 0.5*45000;
b4 = 10*45000;
G2 = zpk(-b3,-50*b3,1); %if 50 is changed to a bigger
                        %value, theoretically the result
                        %would be even better.

G3 = zpk(-b3,-50*b3,1);
H=H1*H2*H3*G1*G2*G3;

%                                     K                                     1
%PID controller:PID=---(Tds + 1)(s + ---)
%                                     s                                     Ti
%We set Ti = 20*Td

% s=zpk('s'); this doesn't work for Ver5.1, so has to be
% changed as below:
s=zpk(0,[],1);
K=1.0; Td=0.0005; Ti=20*Td;
PID=K/s*(Td*s+1.0)*(s+1.0/Ti);

olloop = H * PID;

% Lets see how the frequency response has changed.
% The open-loop response with the compensator is the solid
% line:
bode(H,'--',olloop,'-')

pause % Press any key to continue ...
clc

% Now let's try the root locus again with our compensator
rlocus(olloop); sgrid, set(gca,'xlim',[-10000 1],'ylim',[-
10000,10000]);

pause % Press any key and then choose a point on the plot

[k,poles] = rlocfind(olloop);

echo off
fprintf('\n');
disp(['You chose gain: ',num2str(k)]),

```

```

fprintf('\n');
disp('Yielding closed-loop poles at:')
echo on
damp(poles);

% Let's form the closed-loop system so that we can analyze
% the design.
k = 3.9591*100000;

cloop = feedback(k*olloop,1);

% These eigenvalues should match the ones you choose.

% Closed loop eigenvalues
damp(cloop)

pause % Press any key to continue ...

% Plot the closed-loop step response
% step(cloop), to see any part of the step response, we use
% the following instruction:
step(cloop,0:0.00001:0.03);

pause % Press any key after the plot ...

clc

% Let's now look at the robustness of the control system.
% The most common classical robustness criteria are the gain
% margin and phase margin. Use the function MARGIN to
% compute these margins.

% First form the unity-feedback open loop by connecting our
% designed system with the gain k selected in the above.
% k = 3.9591*100000;
olk = k*olloop;

% Compute the gain margin Gm, phase margin Pm (in degrees),
% and the corresponding crossover frequencies Wcg and Wcp
% (in radians/sec.):
[Gm,Pm,Wcg,Wcp] = margin(olk);
Margins = [Gm Wcg Pm Wcp]

% The gain margin in dB is:
20*log10(Gm)

% Plot Bode plot with margins
margin(olk),
pause % Press any key after the plot ...

% Now we check the tracking property of the system.

```

```

%Plot disturbance input curve and piezo film actuator
%output curve to compare the difference (this is not
%necessary now).
f=1000;
t=0:0.001/f:4/f; r=sin(2*3.14159*f*t);
[y,t1]=lsim(cloop,r,t);
plot(t,r,t1,y);
pause;

%Now, let's see the head-disk spacing output (or variation)
%in response to a sine wave disturbance input in the
%feedback servo control system.
disturb_sys = feedback(1,olk);

% For a 1000Hz disturbance signal:
t=0:0.001/f:20/f; r=sin(2*3.14159*f*t);
[e,t1]=lsim(disturb_sys,r,t);

%the error curve is:
plot(t,r,t1,e);

echo on

pause % Press any key to continue ...

% For a 2000Hz disturbance signal:
f=2000;
t=0:0.001/f:20/f; r=sin(2*3.14159*f*t);
[e,t1]=lsim(disturb_sys,r,t);

%the error curve is:
plot(t,r,t1,e);

echo on

pause % Press any key to continue ...

% For a 5000Hz disturbance signal:
f=5000;
t=0:0.001/f:20/f; r=sin(2*3.14159*f*t);
[e,t1]=lsim(disturb_sys,r,t);

%the error curve is:
plot(t,r,t1,e);

echo on

pause % Press any key to continue ...

% For a 500Hz disturbance signal:
f=500;

```

```
t=0:0.001/f:20/f; r=sin(2*3.14159*f*t);  
[e,t1]=lsim(disturb_sys,r,t);
```

```
%the error curve is:  
plot(t,r,t1,e);
```

```
echo on
```

```
pause % Press any key to continue ...
```

```
% Please take down the value of k:  
% We have known k=3.9591*100000, 3.3264*100000, etc. are  
ok.  
clc  
k = k  
olk = k* oloop
```

```
echo off
```

# 7.2 Readback Signals and Under Different Vibration Frequencies

Figure 7-1 shows the plotted readback signal under the following condition: the vibration frequency is 10300Hz, the acceleration is 20g, the sampling frequency is 50MHz, and the number of samples is 50000.

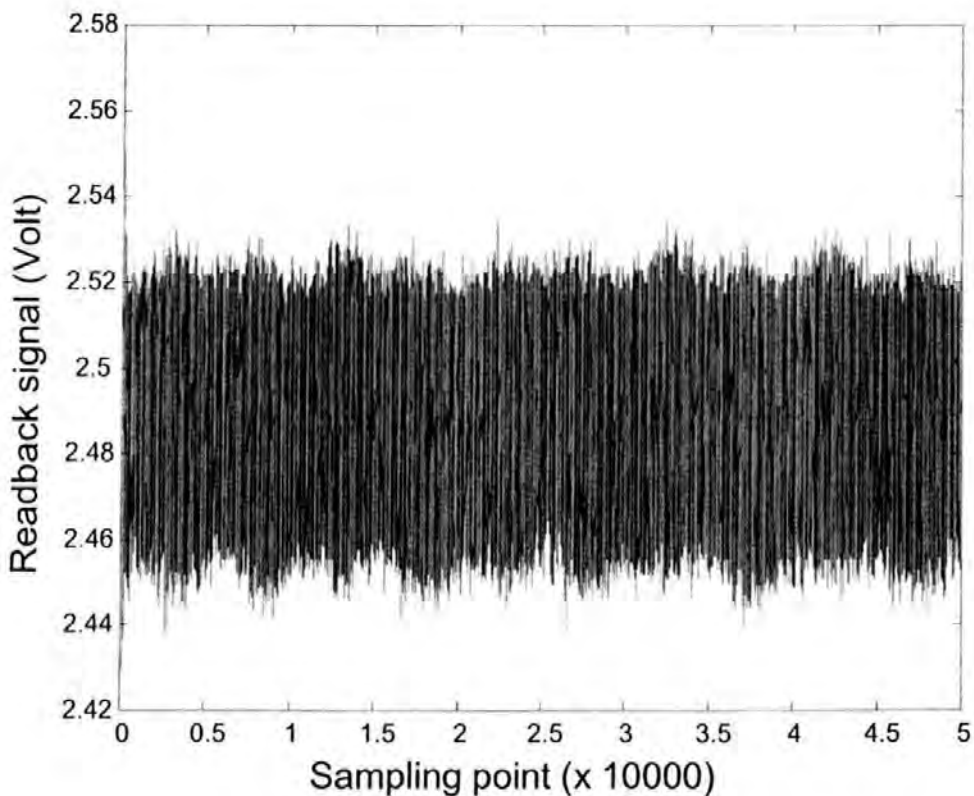


Figure 7-1 Readback signal under 10300Hz vibration.

Figure 7-2 shows the plotted readback signal under the following condition: the vibration frequency is 9800Hz, the acceleration is 23.6g, the sampling frequency is 50MHz, and the number of samples is 50000.

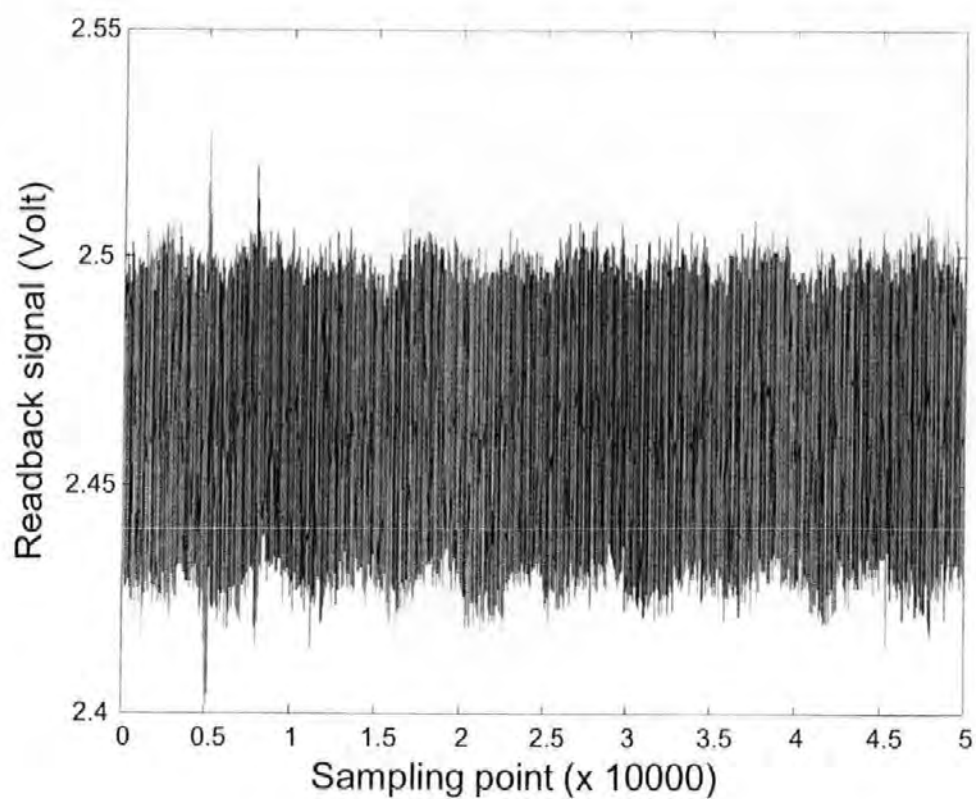


Figure 7-2 Readback signal under 9800Hz vibration

Figure 7-3 shows the plotted readback signal under the following condition: the vibration frequency is 8030Hz, the acceleration is 17.2g, the sampling frequency is 50MHz, and the number of samples is 50000.

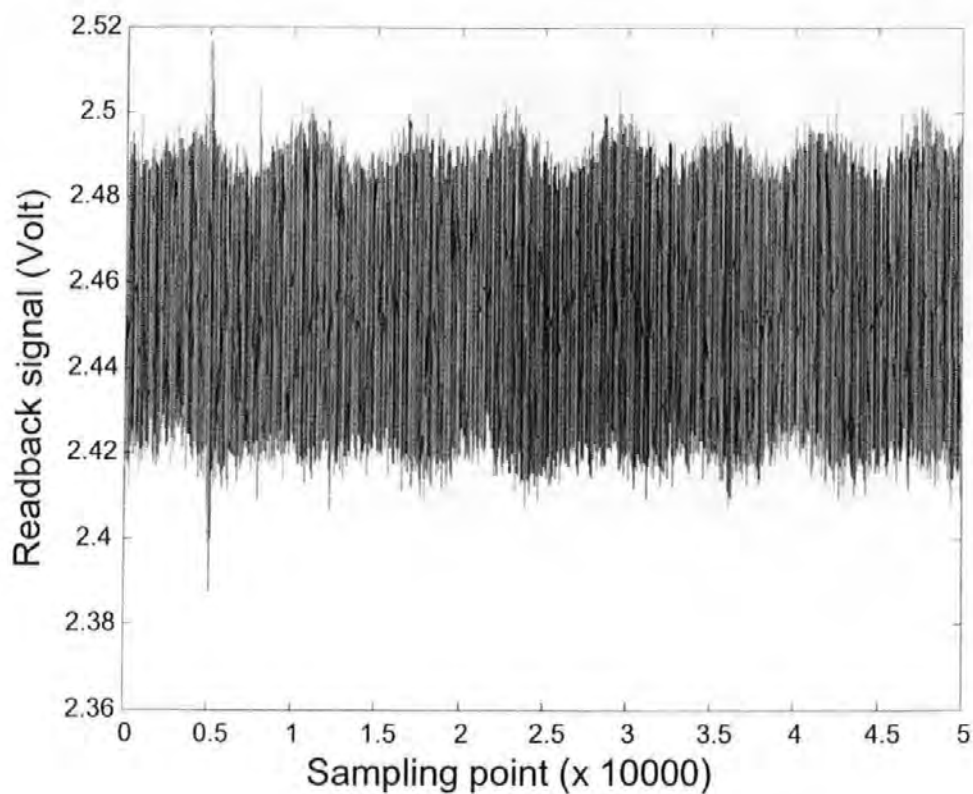


Figure 7-3 Readback signal under 8030Hz vibration

Figure 7-4 shows the plotted readback signal under the following condition: the vibration frequency is 5800Hz, the acceleration is 19.2g, the sampling frequency is 50MHz, and the number of samples is 50000.



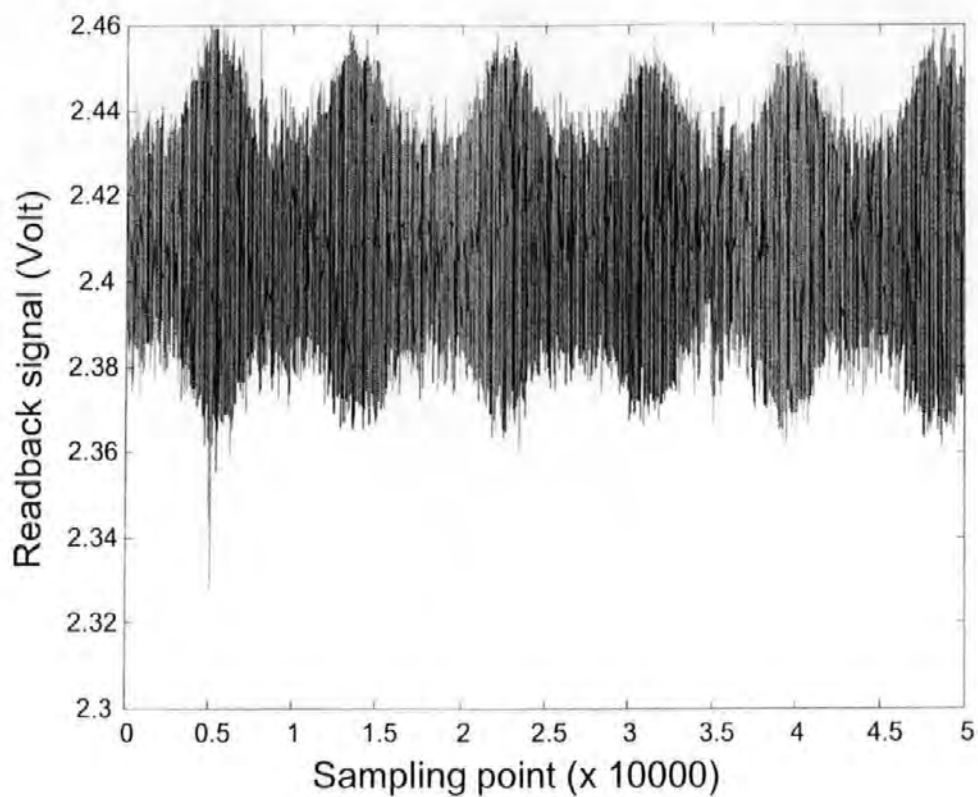


Figure 7-4 Readback signal under 5800Hz vibration

Figure 7-5 shows the plotted readback signal under the following condition: the vibration frequency is 5300Hz, the acceleration is 85.6g, the sample frequency is 50MHz, and the number of samples is 50000.

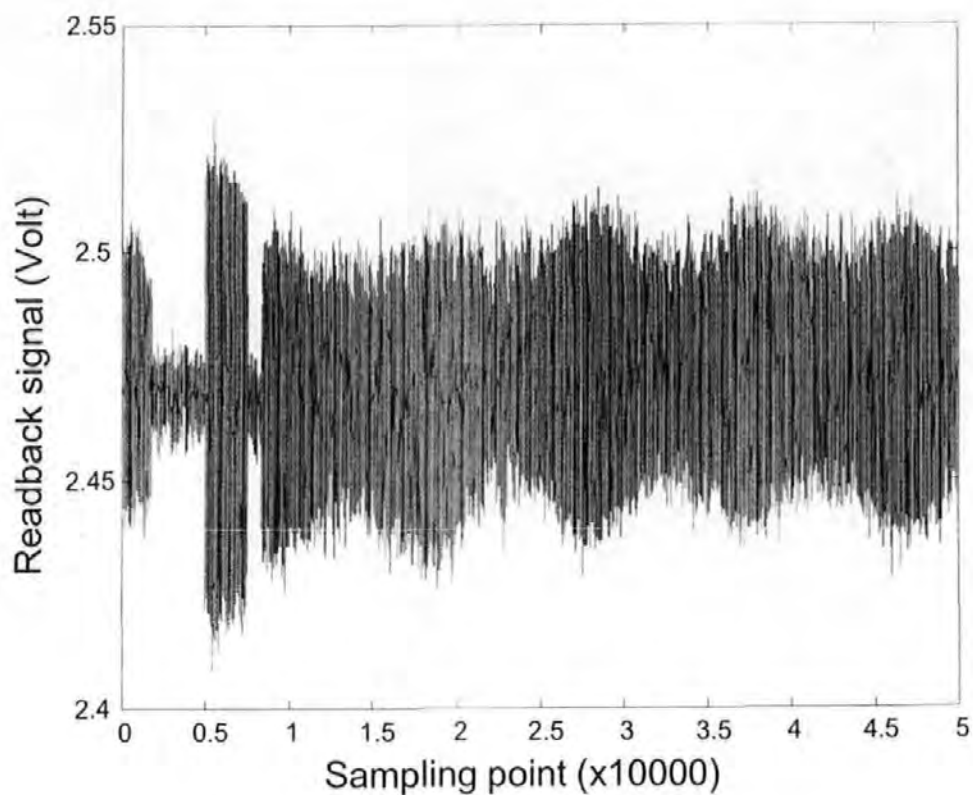


Figure 7-5 Readback signal under 5300Hz vibration

Figure 7-6 shows the plotted readback signal under the following condition: the vibration frequency is 3900Hz, the acceleration is 9.2g, the sampling frequency is 25MHz, and the number of samples is 50000.

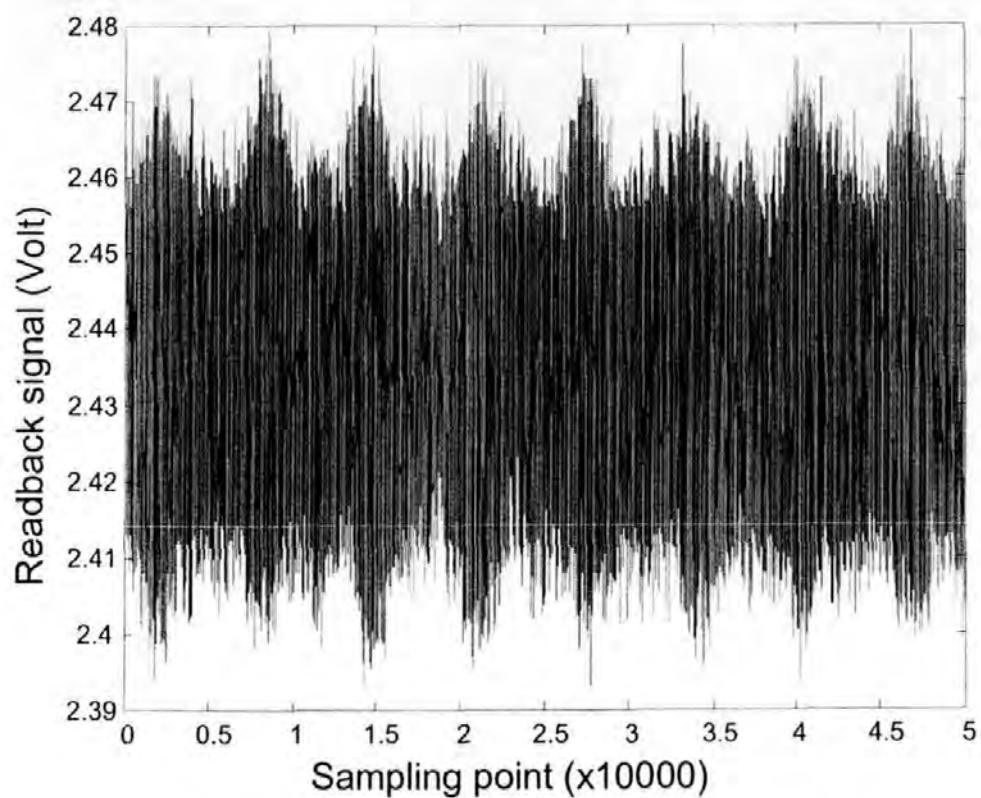


Figure 7-6 Readback signal under 3900Hz vibration

Figure 7-7 shows the plotted readback signal under the following condition: the vibration frequency is 3440Hz, the acceleration is 11.6g, the sampling frequency is 50MHz, and the number of samples is 50000.

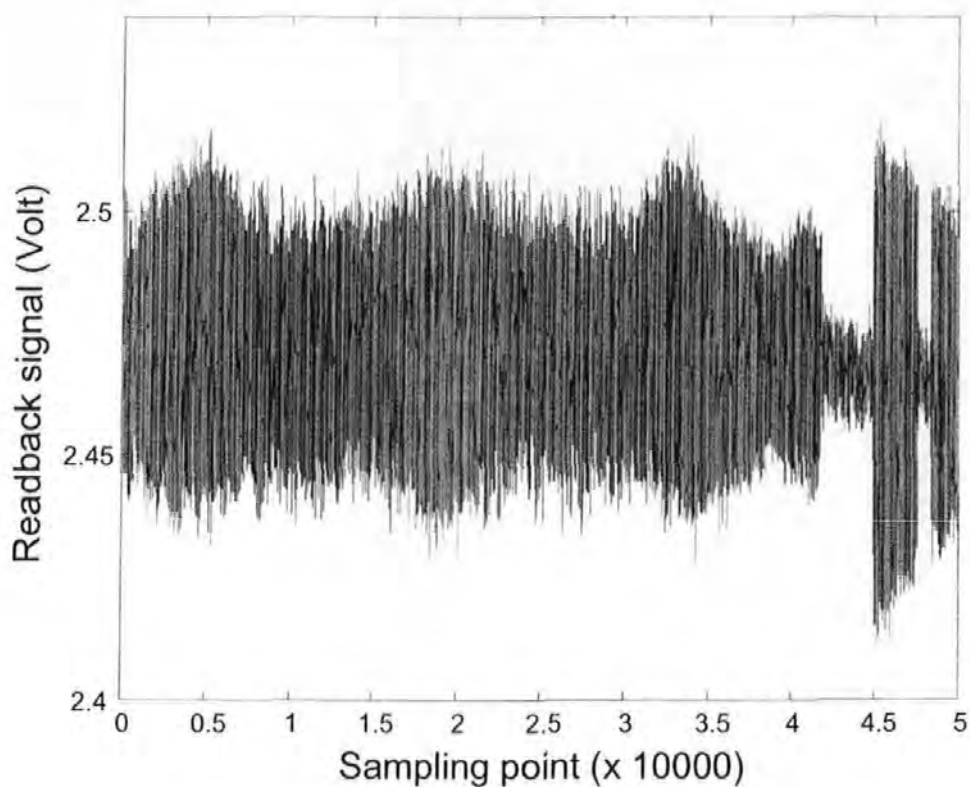


Figure 7-7 Readback signal under 3440Hz vibration

Figure 7-8 shows the plotted readback signal under the following condition: the vibration frequency is 1300Hz, the acceleration is 19g, the sampling frequency is 10MHz, and the number of samples is 50000.

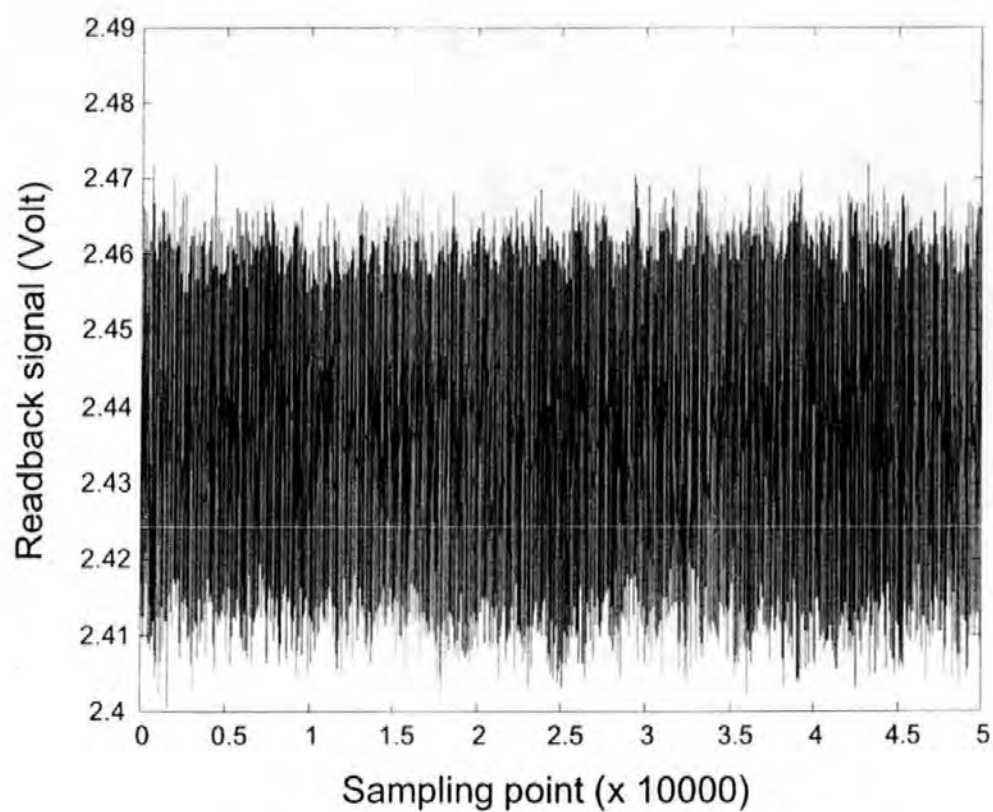


Figure 7-8 Readback signal under 1300Hz vibration

Figure 7-9 shows the plotted readback signal under the following condition: the vibration frequency is 1180Hz, the acceleration is 61.2g, the sampling frequency is 10MHz, and the number of samples is 50000.

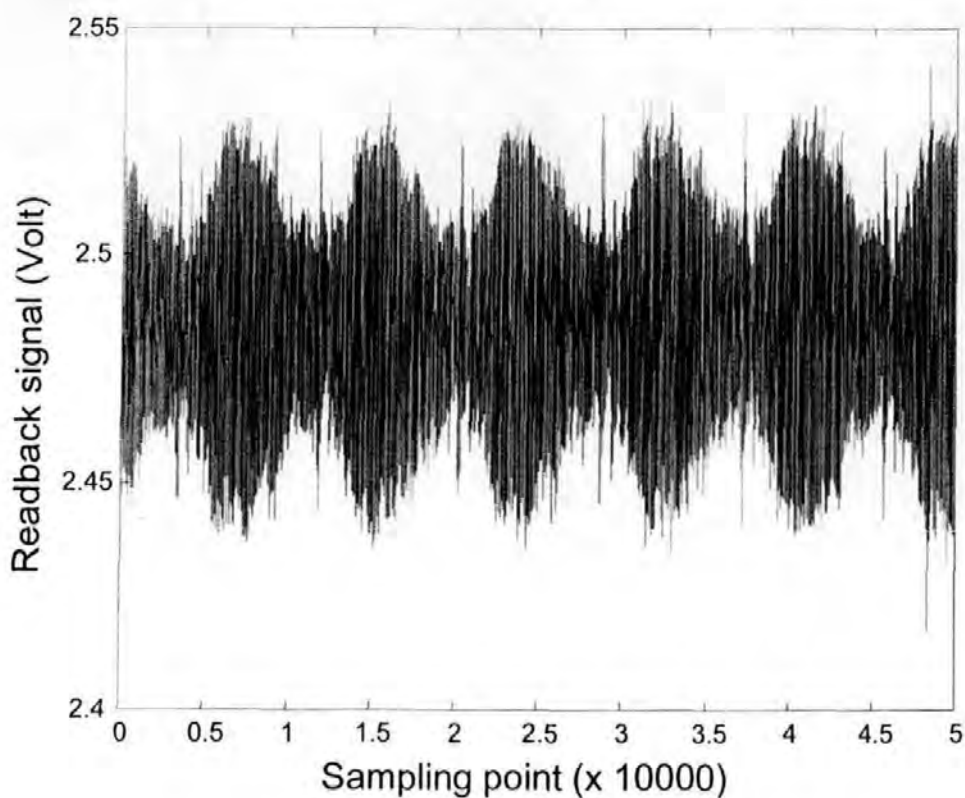


Figure 7-9 Readback signal under 1180Hz vibration

Figure 7-10 shows the plotted readback signal under the following condition: the vibration frequency is 523Hz, the acceleration is 5.3g, the sampling frequency is 5MHz, and the number of samples is 50000.

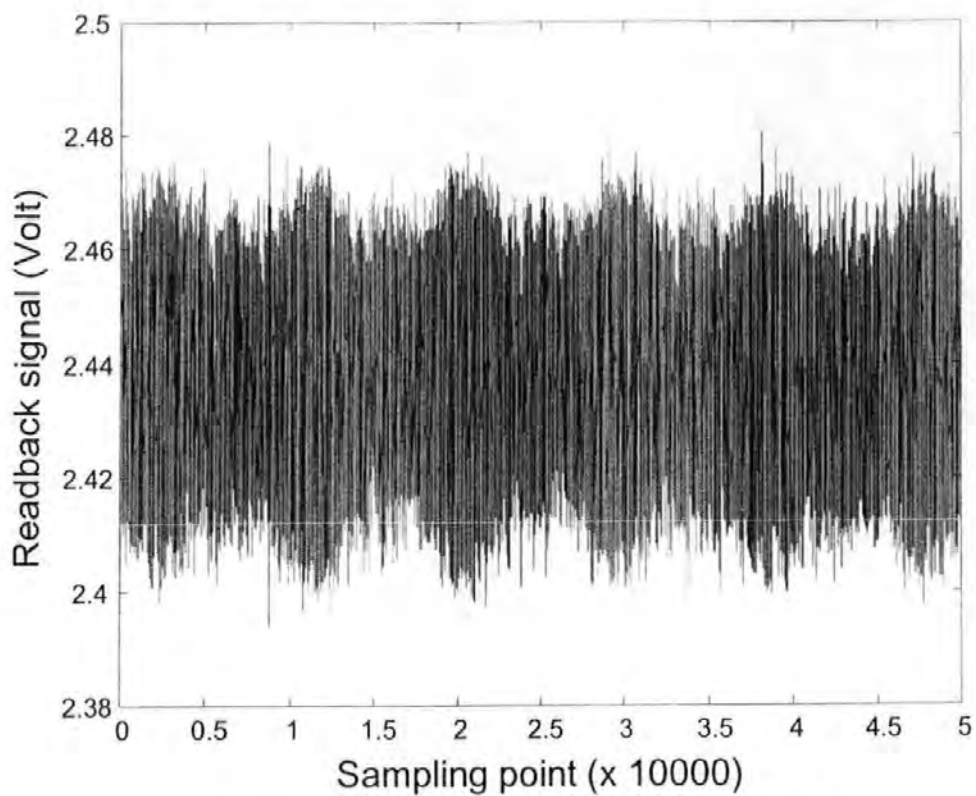


Figure 7-10 Readback signal under 523Hz vibration

Figure 7-11 shows the plotted readback signal under the following condition: the vibration frequency is 160Hz, the acceleration is 3.4g, the sampling frequency is 1MHz, and the number of samples is 50000.

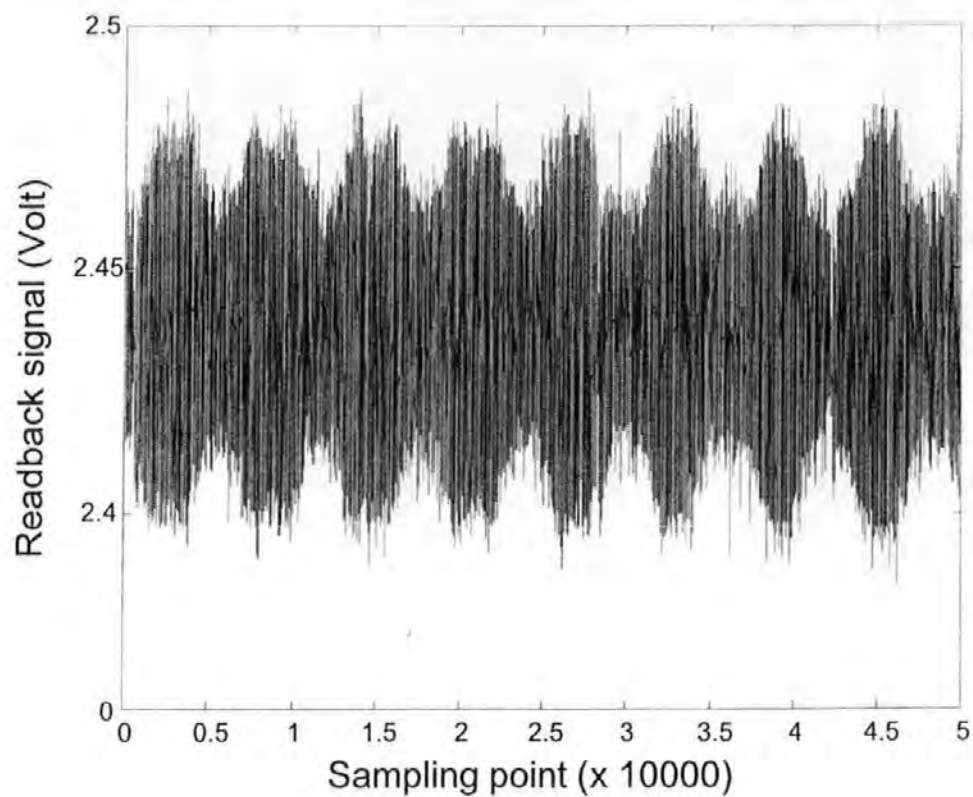


Figure 7-11 Readback signal under 160Hz vibration

Figure 7-12 shows the plotted readback signal under the following condition: the vibration frequency is 45Hz, the acceleration is 3.9g, the sampling frequency is 500kHz, and the number of samples is 50000.



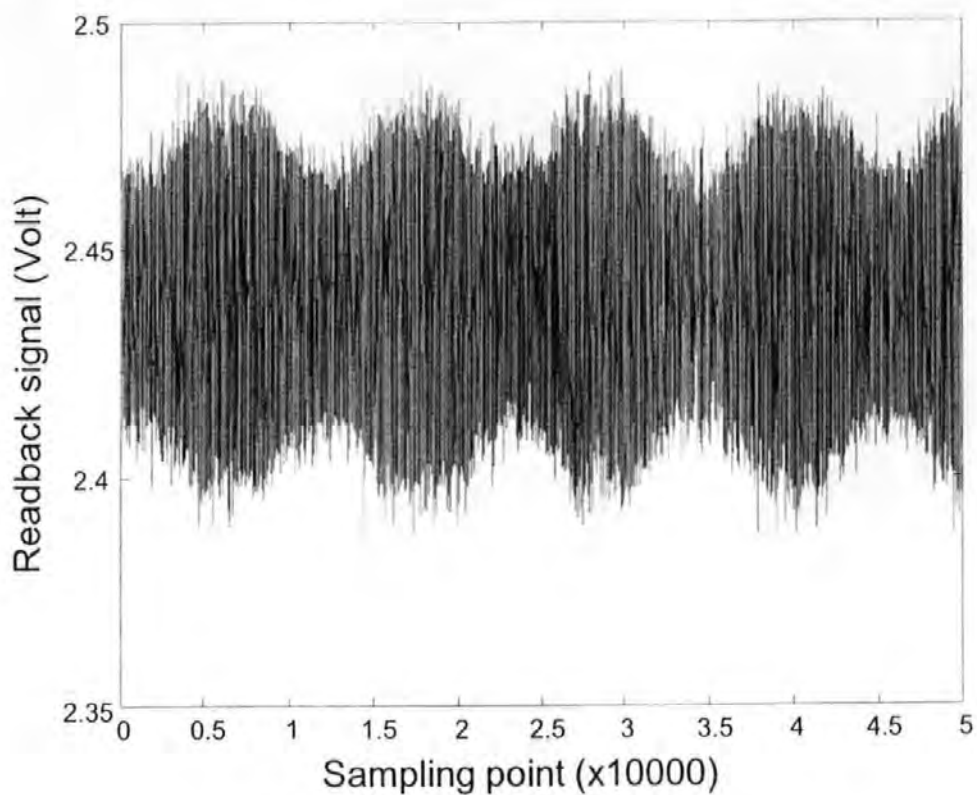


Figure 7-12 Readback signal under 45Hz vibration

By applying the same signal processing method described in section 5.2.1 to the above readback signals, the extracted envelopes of the readback signals by using a 500-order lowpass FIR filter are plotted in the figures below from Figure 7-13 to Figure 7-23.

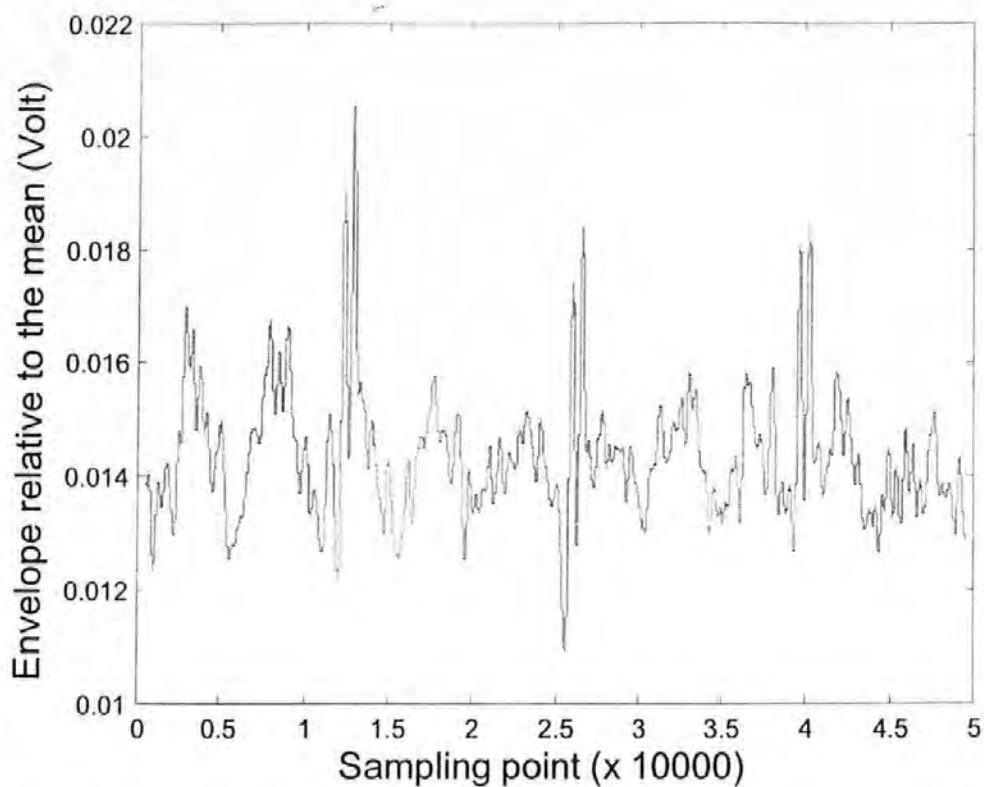


Figure 7-13 Extracted envelope of the readback signal under 10300Hz vibration

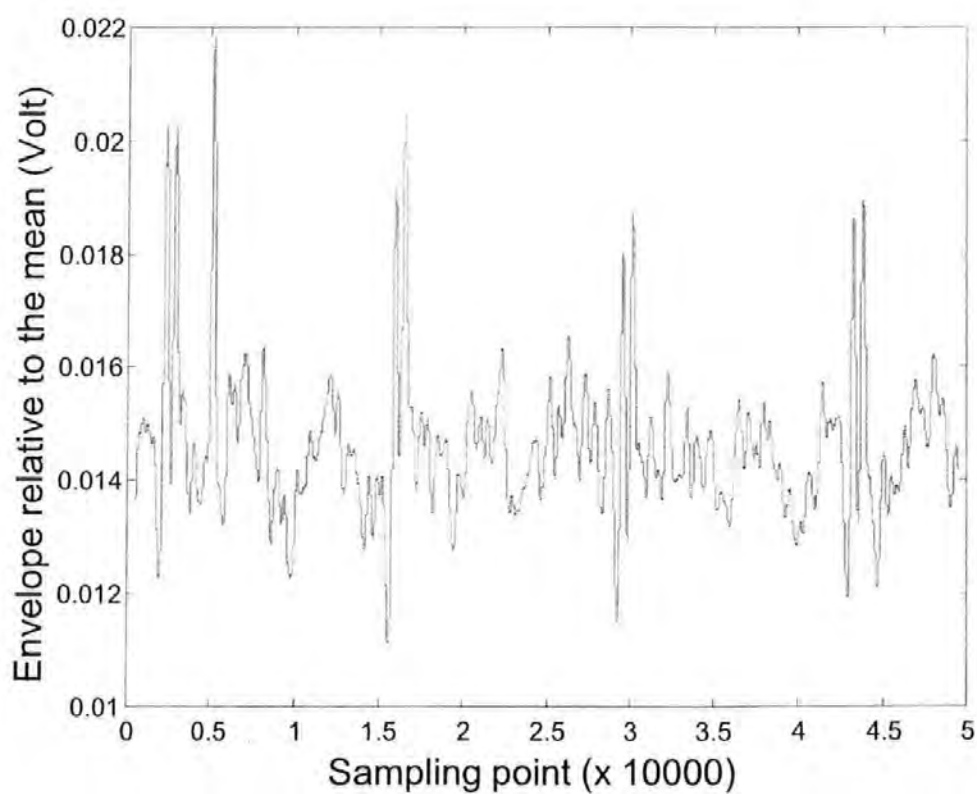


Figure 7-14 Extracted envelope of the readback signal under 9800Hz vibration

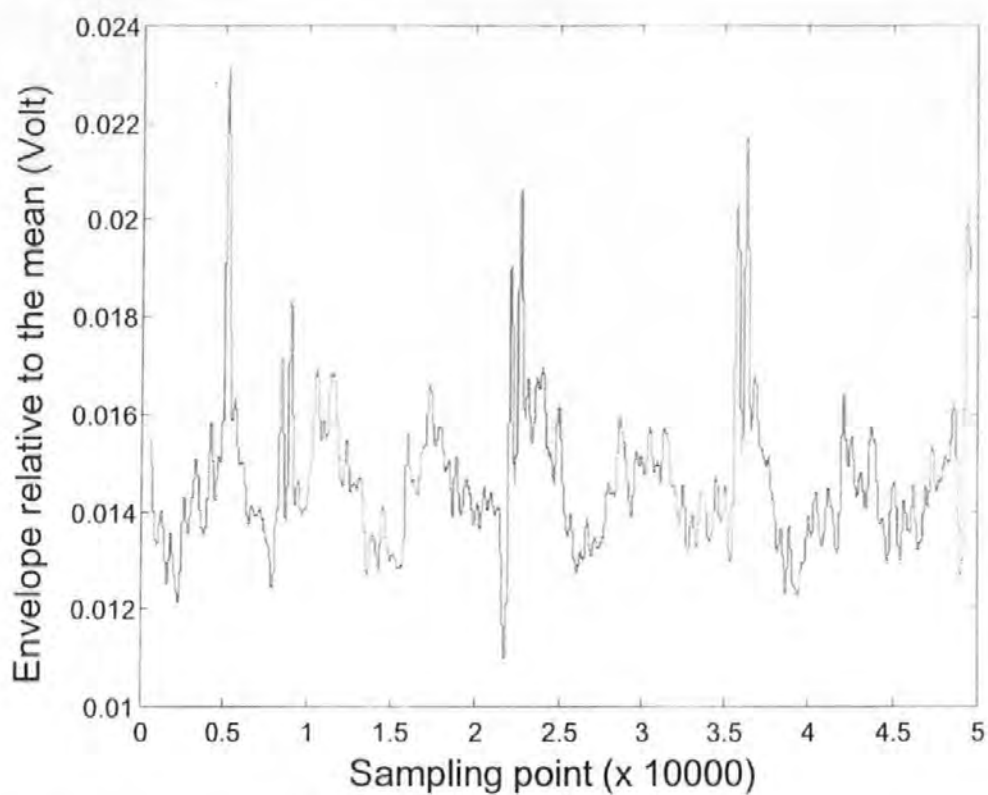


Figure 7-15 Extracted envelope of the readback signal under 8030Hz vibration

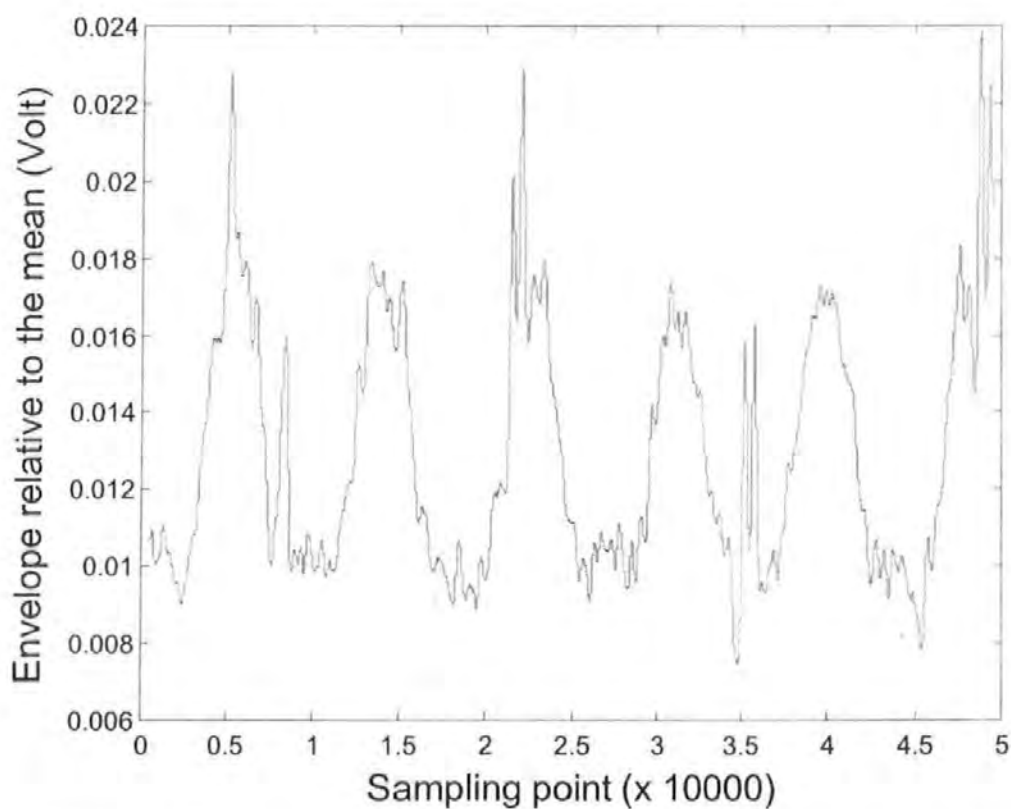


Figure 7-16 Extracted envelope of the readback signal under 5800Hz vibration

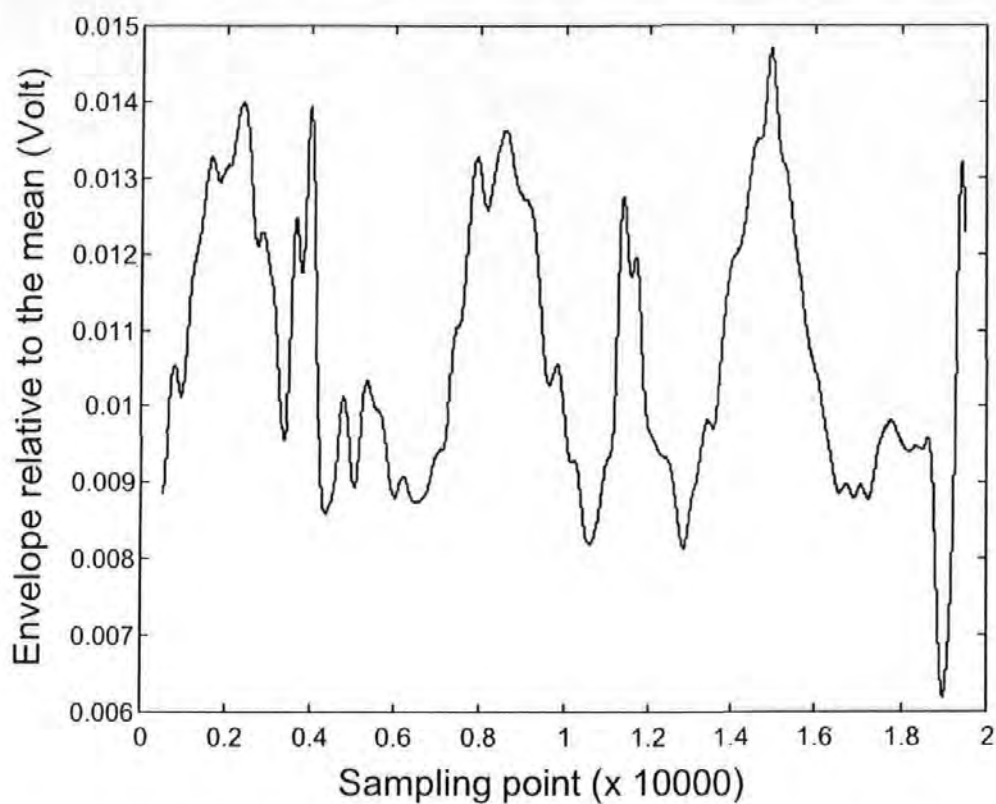


Figure 7-17 Extracted envelope of the readback signal under 3900Hz vibration

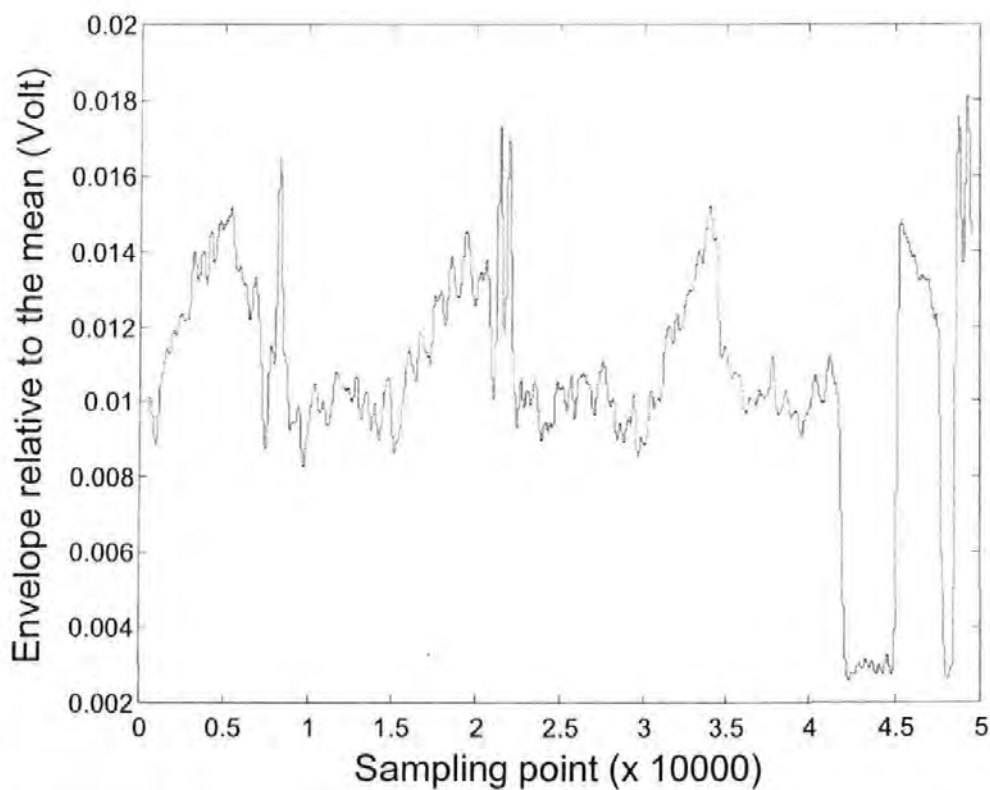


Figure 7-18 Extracted envelope of the readback signal under 3440Hz vibration

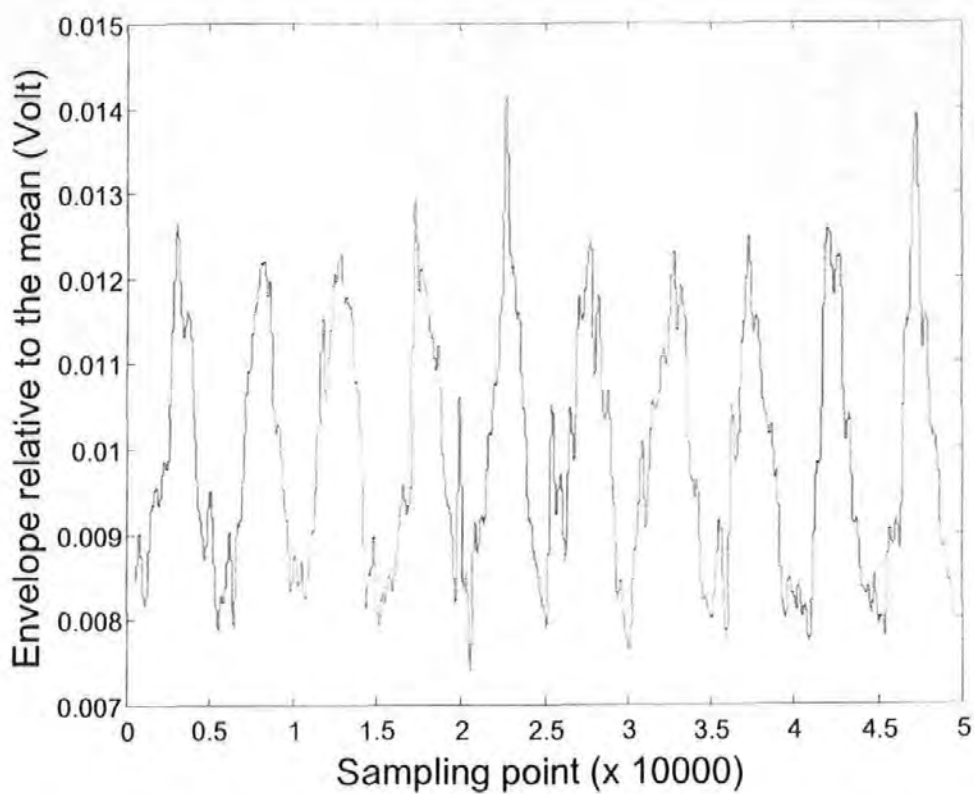


Figure 7-19 Extracted envelope of the readback signal under 2400Hz vibration

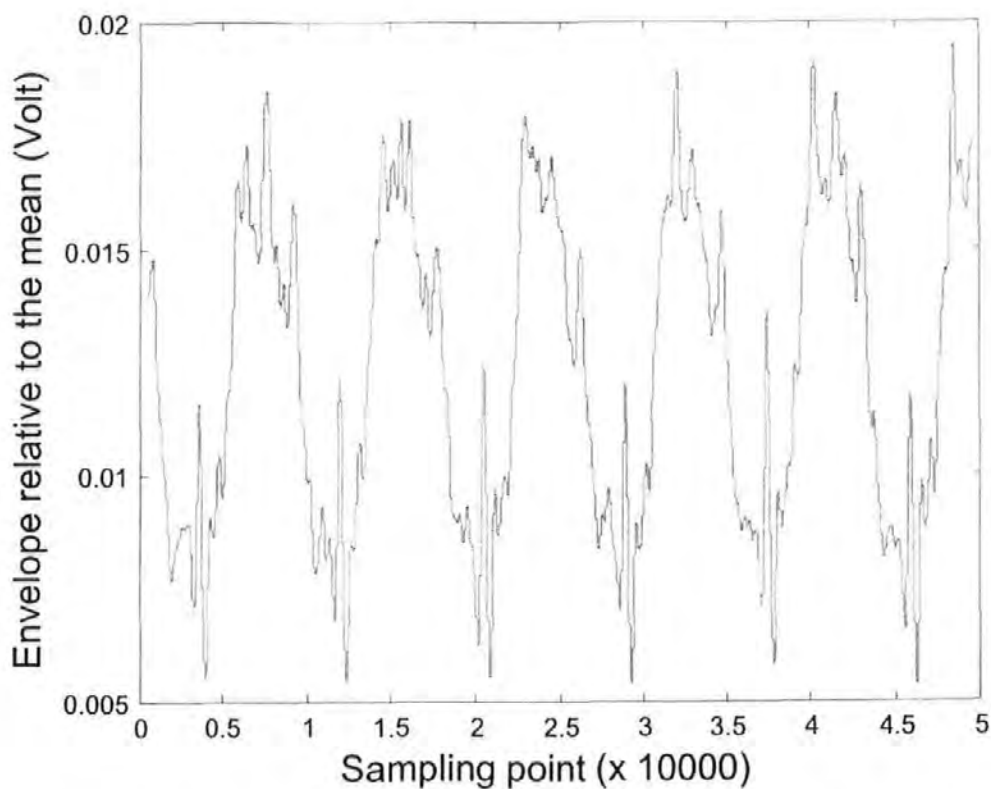


Figure 7-20 Extracted envelope of the readback signal under 1180Hz vibration

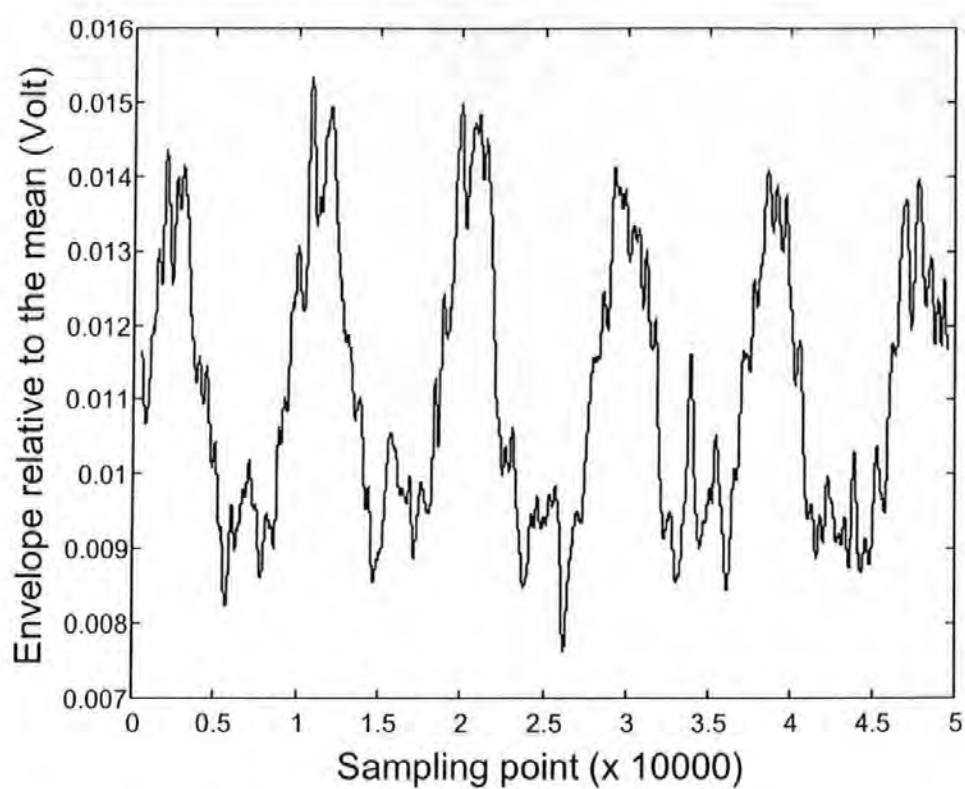


Figure 7-21 Extracted envelope of the readback signal under 523Hz vibration

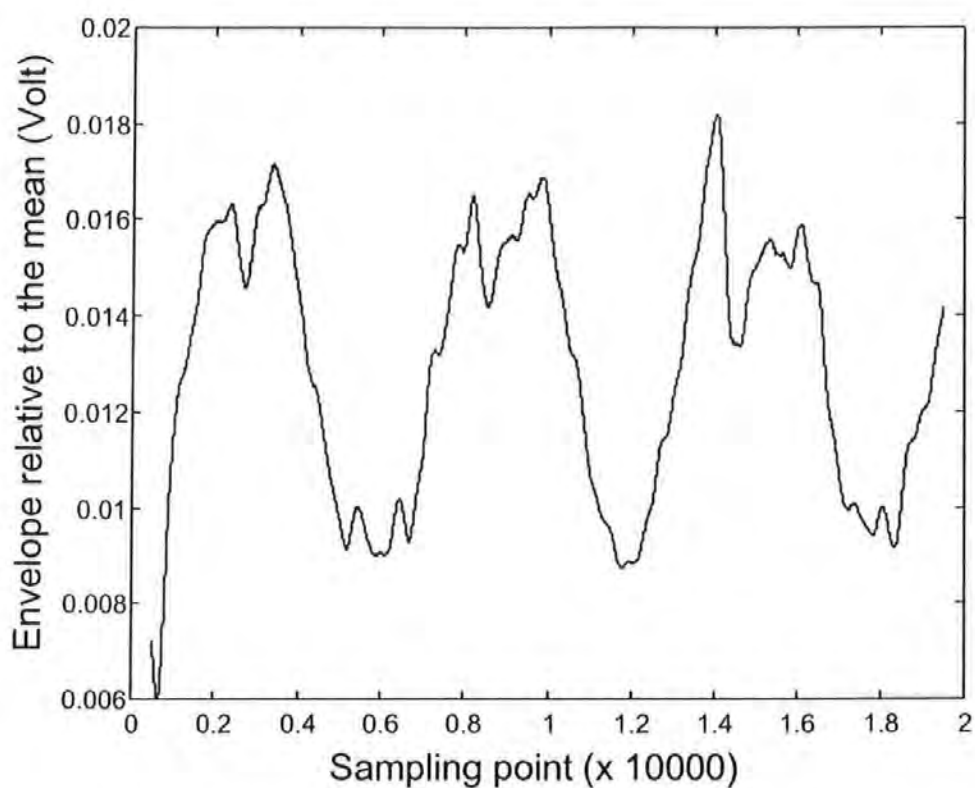


Figure 7-22 Extracted envelope of the readback signal under 160Hz vibration

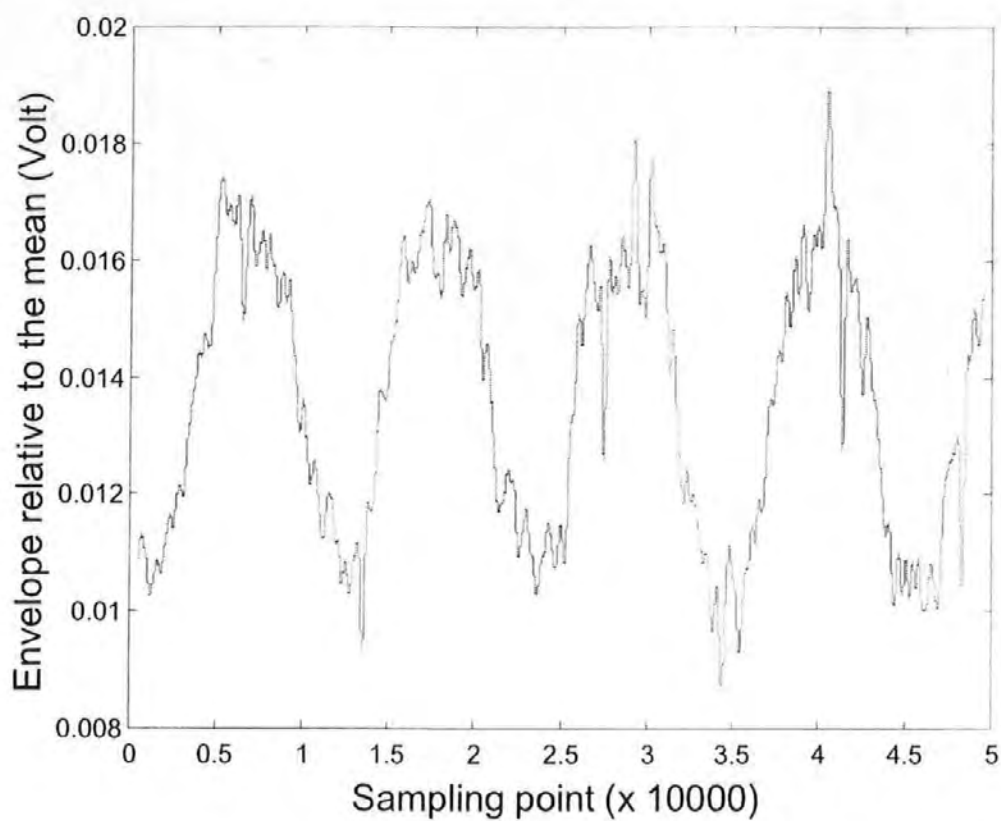


Figure 7-23 Extracted envelope of the readback signal under 45Hz vibration

# References

- [1] [Abraham, 1996] Abraham D. W., Praino A. P., Re M. E., and Wickramasinghe H. K., "Method and apparatus for detecting asperities on magnetic disk using thermal proximity imaging," U.S. patent 5527110, June 18, 1996.
- [2] [Abramovitch et al., 1998] Abramovitch D., Hurst T., and Henze D., "An overview of the PES Pareto method for decomposing baseline noise source in hard disk position error signals," IEEE Transactions on Magnetics, Vol.34, No.1, pp.17-23, 1998.
- [3] [Allen & Bogy, 1998] Allen A. M. and Bogy D. B., "Effects of shock on the head-disk interface," IEEE Transactions on Magnetics, Vol.32, No.5, pp.3717-3719, 1998.
- [4] [Archard & Kirk, 1961] Archard J. F., and Kirk M. T., "Lubrication at point contacts," Proc. Roy. Soc. (London) A261, 532-550, 1961.
- [5] [Aruga et al., 1986] Aruga K., Mizoshita Y., Yamada T., and Yaneoka S., "Spacing fluctuation of flying head sliders in track accessing (forced vibration analysis using finite element method)," Tribology and Mechanics of Magnetic Storage System, vol.3, (B. Bhushan, and N. S. Eiss, eds.), pp.79-86, SP-21, ASLE, Park Ridge, Illinois, 1986.
- [6] [Azzam & Bashara, 1987] Azzam R. M. A. and Bashara N. M., Ellipsometry and Polarized Light, North-Holland, 1987.
- [7] [Heo & Shen, 1999] Heo B., and Shen Y., "Taming disk and spindle rocking by damped laminated disks – an experimental study," IEEE Transactions on Magnetics, Vol.35, No.5, pp.2304-2306, 1999.
- [8] [Best, 1987] Best G. L., "Comparison of optical and capacitive measurements of slider dynamics," IEEE Transactions on Magnetics, Vol.23, pp.3453-3455, 1987.
- [9] [Best et al., 1986] Best G. L., Horne D. E., Chiou A., and Sussner H., "Precise optical measurement of slider dynamics," IEEE Transactions on Magnetics, Vol.22, pp.1017-1019, 1986.
- [10] [Bhushan, 1996] Bhushan Bharat, Tribology and Mechanics of Magnetic Storage Devices, 2nd edition, Springer, 1996.
- [11] [Bittner & Shen, 1999] Bittner H. and Shen I. Y., "Taming disk/spindle vibrations through aerodynamic bearings and acoustically tuned-mass dampers," IEEE Transactions on Magnetics, Vol.35, No.2, pp.827-832, 1999.



- [12] [Bogy & Talke, 1985] Bogy D. B., and Talke F. E., "Laser Doppler interferometry on magnetic recording systems," IEEE Transactions on Magnetics, Vol.21, pp.1332-1337, 1984.
- [13] [Born & Wolf, 1989] Born M. and Wolf E., Principle of optics, Pergamon Press, Oxford, 1989.
- [14] [Bouchard et al., 1984] Bouchard G., Miu D. K., Bogy D. B., and Talke F. E., "On the dynamics of Winchester and 3370-type sliders used in magnetic recording disk files," in Tribology and Mechanics of Magnetic Storage Systems, Vol.1 (B. Bhushan et al., eds.), pp.85-89, SP-16, ASLE, Park Ridge, Illinois, 1984.
- [15] [Bouchard et al., 1985] Bouchard G., Bogy D. B., and Talke F. E., "An experimental comparison of the head/disk interface dynamics in 5- and 8-inch disk drives," IBM J. Res. Develop. Vol.29, pp.316-323, 1985.
- [16] [Briggs & Herkart, 1971] Briggs G. R., and Herkart P. G., "Unshielded capacitor probe technique for determining disk file ceramic slider flying characteristics," IEEE Transactions on Magnetics, Vol.7, pp.428-, 1971.
- [17] [Briggs & Talke, 1989] Briggs C. A. and Talke F. E., "An investigation of the IBM 3380 K slider using laser doppler interferometry," IEEE Transactions on Magnetics, Vol.25, No.5, pp.3707-3709, 1989.
- [18] [Cameron & Gohar, 1966] Cameron A., and Gohar R., "Theoretical and experimental studies of the oil film in lubricated point contacts," Proc. Roy. Soc. (London) A291, 520-536, 1966.
- [19] [Cha et al., 1996] Cha Ellis, Chiang Chisin, Enguero Jorge, Lee Jerry J. K., "Effect of temperature and altitude on flying height," IEEE Transactions on Magnetics, Vol.32, No.5, Pt.1, pp 3729-3731, Sep., 1996.
- [20] [Chilumbu et al., 1999] Chilumbu C., Jenkins D. F. L., and Clegg W. W., Presented at Euroceramics VI, Montreux, Switzerland, Proceedings Electroceramics VI, 1999.
- [21] [Chilumbu et al., 2000] Chilumbu C., Clegg W., Jenkins D., and Robinson P., "A novel 2-dimensional suspension arm for flying height control and high-bandwidth track following in advanced hard disk drives," IMTC/2000, Baltimore, USA, May 2000.
- [22] [Choi et al., 1997] Choi S., Ong S., You C., Hong D., and Cho J., "Performance of neural equalizers on partial erasure model" IEEE Transactions on Magnetics, Vol.33, No.5 Pt1, pp.2788-2790, 1997.
- [23] [Clegg et al., 1997] Clegg W. W., Jenkins D. F. L., and Cunningham M. J., Sensors and Actuators A, Vol.A58, pp.173-177, 1997.
- [24] [Clegg et al., 2001] Clegg W., Liu X., Liu B., and Li A., "Normal incidence polarization interferometry flying height testing," IEEE Transactions on Magnetics, vol. 37, no. 4I, pp.1941-1943, 2001.

- [25] [Crook, 1958] Crook A. W., "the lubrication of rollers," Pro. Roy. Soc. (London), Phil. Trans. A250, 387-409, 1958.
- [26] [Crook, 1961] Crook A. W., "Elastohydrodynamic lubrication of rollers," Nature 190, 1182-1183, 1961.
- [27] [Cunningham et al., 1995] Cunningham M. J., Jenkins D. F. L., Clegg W. W., and Bakush M. M., Sensors and Actuators A – Micromechanics, Vol.A50, pp.147-150, 1995.
- [28] [Cunningham et al., 1997] Cunningham M. J., Jenkins D. F. L., and Bakush M. M., IEE Proceedings A – Science, Measurement and Technology, Vol.144, pp.45-48, 1997.
- [29] [de Groot 1996] de Groot Peter, "Optical gap measuring apparatus and method," U.S. patent 5557399, September 1996.
- [30] [de Groot et al., 1996a] de Groot P.; Deck L.; Sobbitsky J.; Biegen J. "Polarization interferometer for measuring the flying height of magnetic read-write heads," Optics Letters Vol.21, No.6, pp.441-443, March, 1996.
- [31] [de Groot et al., 1996b] de Groot P. D., Deck L., Soobitsky J., Biegen J., "Optical flying-height testing of magnetic read-write heads," Proceedings of the SPIE, Vol.2782, pp.47-57, 1996.
- [32] [de Groot, 1998a] de Groot Peter, "Determining the optical constants of read-write sliders during flying height testing," Applied. Optics, Vol.37, pp.5116-5125, 1998.
- [33] [Dennis, 1997] Dennis N., "Wideband passive mechanical mounting systems for disk drives on boats in rough seas," IEEE Oceans, pp.1488-1495, 1997.
- [34] [Eaton & Baldwinson, 1997] Eaton R., and Baldwinson M., "Imaging of media lubricant spacing contributions by readback signal analysis," IEEE Transactions on Magnetism Vol.33, No.1, pp.974-977, 1997.
- [35] [Edwards, 1999] Edwards J. R., "Finite element analysis of the shock response and head slap behaviour of a hard disk drive," IEEE Transactions on Magnetism Vol.35, No.2, pp.863-867, 1999.
- [36] [Ehrlich & Curran, 1999] Ehrlich. R and Curran R., "Major HDD TMR sources and projected scaling with TPI," IEEE Transactions on Magnetism Vol.35, No.2, pp.885-891, 1999.
- [37] [Erickson & Lauer, 1997] Erickson T. E. and Lauer J. P., "Multiplexed laser interferometer for non-dispersed spectrum detection in a dynamic flying height tester," US Patent, No.5673110, Sep.30, 1997.
- [38] [Feliss & Talke, 1977] "Capacitance probe study of rotating head/tape interface," IBM J. Res. Develop. Vol.21, pp.289-293, 1977.

- [39] [Fleisher & Lin, 1974] Fleisher J. M. and Lin C., "Infrared laser interferometer for measuring air-bearing separation," IBM Journal of Research and Development, Vol.18, No.6, pp.529-533, 1974.
- [40] [Foored et al., 1969-1970] Foored C. A., Wedevan L. D., Westlake F. J., and Cameron A., "Optical elastohydrodynamics," Proc. Inst. Mech. Engrs., 184, Part I, 1969-1970.
- [41] [Fossorier, 1996] Fossorier M. P. C., "Performance evaluation of decision feedback equalization for the Lorentzian channel", IEEE Transactions on Magnetism, Vol.32, No.2, pp.309-315, 1996.
- [42] [Fridge & Miller, 1986] Fridge D. A. and Miller K. A., U.S. Patent, No.4593368, June 3, 1986.
- [43] Fukuzawa Tadashi, Hisano Teiji, Watabe Hiroshi, "Glass disk distortion effect in an optical flying height tester," IEEE Transactions on Magnetism, Vol.32, No.5, Pt.1, pp.3690-3692, Sep., 1996.
- [44] [Fukuzawa et al, 1996] Fukuzawa T., Hisano T., Morita T. and Ikarugi K., "Method and apparatus for measuring flying height of a magnetic head above a disk surface at three wavelength," U.S. Patent, No. 5502565, Mar., 1996.
- [45] [Gao & Swei, 2000] Gao P and Swei S, "Active actuation and control of a miniaturized suspension structure in hard-disk drives using a polyvinylidene-fluoride actuator and sensor," Measurement Science and Technology, Vol.11, No.2, pp.89-94, 2000.
- [46] [Gibson et al., 1989] Gibson G. J., Siu S., and Cowan C. F N., "Multi-layer perceptron structures applied to adaptive equalizers for data communications", IEEE Proceedings ICASSP, Glasgow, Scotland, May 1989, pp. 1183-1186.
- [47] [Guo, et al., 1999] Guo L., Lee H. S., Hudson A., and Chen S. "A Comprehensive time domain simulation tool for hard disk drive TPI prediction and mechanical/servo enhancement," IEEE Transactions on Magnetism, Vol.35, No.2, pp.879-884, 1999.
- [48] [Hariharan, 1985] Hariharan P., Optical Interferometry, Academic Press, Orlando, Florida, 1985.
- [49] [Harrison et al., 1999] Harrison J, Altshuler K, and Huynh C, "An explanation of the observed frequency domain behaviour of head-disk interface resonances in the proximity recording regime," IEEE Transactions on Magnetism, Vol. 35, pp.933-938, 1999.
- [50] [Hayes, 1996] Hayes M., Statistical Digital Signal Processing and Modeling, John Wiley & Sons, Inc, 1996.
- [51] [Haykin, 1996] Haykin S., Adaptive Filter Theory, Third Edition, Prentice-Hall International, Inc, 1996.

- [52] [Haykin, 1994] Haykin S., *Neural Networks, A Comprehensive Foundation*, Macmillan College Publishing Company, 866 Third Ave., New York, NY 10022, USA, 1994.
- [53] [Hegde et al., 1990] Hegde S. G., Scranton R. A., and Yarmchuk E. J., "Capacitive measurement and control of the flying height of a recording slider," U.S. Patent, No.4931887, June 5, 1990.
- [54] [Hendriks, 1988] Hendriks F., "A design tool for steady gas bearings using finite elements," *Tribology and Mechanics of Magnetic Storage System*, vol.5, (B. Bhushan and N. S. Eiss, eds.), pp.124-129, SP-25, ASLE, Park Ridge, Illinois, 1988.
- [55] [Hoagland & Monson, 1991] Hoagland A. S., and Monson J. E., *Digital Magnetic Recording*, 2nd edition, John Wiley & Sons, Inc., 1991.
- [56] [Hsia, 1977] Hsia T. C., *System identification: least-squares methods*, Lexington Books, 1977.
- [57] [Hu & Bogy, 1997] Hu Y. And Bogy D. B., "Dynamic stability and spacing modulation of sub-25 nm fly height sliders," *Journal of Tribology*, Transactions of ASME, Vol.119, pp.646-652, 1997.
- [58] [Harrison, et al., 1999] Harrison J. C., Altshuler K. J., and Huynh C. M., "An explanation of observed frequency domain behaviour of head-disk interface resonance in the proximity recording regime," *IEEE Transactions on Magnetics*, vol. 35, pp.933-938, 1999.
- [59] [Immink, 1989] Immink K. A. S., "Coding techniques for the noisy magnetic recording channel: a state-of-the-art report," *IEEE Trans. on Comm.*, Vol.37, No.5, pp.413-419, May, 1989.
- [60] [Ishimaru, 1996] Ishimaru N., "Experimental studies of a head/disk interface subjected to impulse excitation during nonoperation," *Journal of Tribology*, Vol.118, pp.807-812, 1996.
- [61] [Jenkins et al., 1997] Jenkins D. F. L., Cunningham G., Velu G., and Remiens D., Presented at ISIF 1997, New Mexico, USA, *Integrated Ferroelectrics*, Vol.17, pp309-318, 1997.
- [62] [Jenkins et al., 1999] Jenkins D. F. L., Clegg W. W., Chilumbu C., and Tunstall G. A., "Actuators for tomorrows ruggedised hard disk drives," *Datatech ICG Publishing*, Vol.3, pp.71-75, 1999.
- [63] [Jenkins et al., 2001] Jenkins D. F. L., Chilumbu C., Tunstall G. A., Clegg W. W., Robinson P., "Multi-layer bulk PZT actuators for flying height control in ruggedised hard disk drives," *Proceedings of the 12<sup>th</sup> IEEE International Symposium on Applications of Ferroelectronics*, (ISAF 2000), Vol.1, pp.293-296, 2001.
- [64] [Jiang, 1992] Jiang Z., "Head disk interface subjected to impulsive excitation," prepr of Jpn, soc Mech Eng., No.920-67, pp.75-78, 1992.

- [65] [Jepson, 1997] Jepson S. D., The Development of a Computer-Controlled Environmental Test Rig," M.Sc. Dissertation, University of Manchester, 1997.
- [66] [Kay, 1993] Kay S., Fundamentals of Statistical Signal Processing: Estimation Theory, Englewood Cliffs, NJ., PTR., Prentice Hall, 1993.
- [67] [Klaassen & van Peppen, 1992] Klaassen K. B. and van Peppen J. C. L., "Method and circuitry for in-situ measurement of transducer and transducer magnetic instability," U.S. Patent, No.5130866, July 14, 1992.
- [68] [Klaassen & van Peppen, 1994] Klaassen K. B. and van Peppen J. C. L., "Slider-disk clearance measurements in magnetic disk drives using the readback transducer," IEEE Transactions on Instrumentation and Measurement, Vol.43, No.2, pp.121-126, 1994.
- [69] [Kouhei et al., 1995] Kouhei T., Yamada T., Kuroba Y., and Aruga K., "A study of head-disk interface shock resistance," IEEE Transactions on Magnetics, Vol.31, No.6, pp.3006-3008, 1995.
- [70] [Kumar et al., 1994] Kumar S., Khanna V., Sri-Jayantha M., "A study of the head disk interface shock failure mechanism," IEEE Transactions on Magnetics, Vol.30, No.6, pp.4155-4157, 1994.
- [71] [Kuo et al., 2000] Kuo D., Sundaram R., Thangaraj N., Ou-Yang J., and Shen I., "Mechanical performance of laminated discs," IEEE Transactions on Magnetics, Vol.36, pp.166-170, 2000.
- [72] [Lacey et al., 1992] Lacey, C., Adams, J. A., Ross, E. W., Cormier, A., "A new method for measuring flying height dynamically," Phase Metrics communication , 1992.
- [73] [Lacey et al, 1993] Lacey C., Shelor R., Cormier A., and Talke F. E., "Interferometric measurement of disk/slider spacing: the effect of phase shift on reflection," IEEE Transactions on Magnetics, Vol.29, No.6, 1993.
- [74] [Lacey & Ross, 1995] Lacey C., Ross E., "Method and apparatus to calibrate intensity and determine fringe order for interferometric measurement of small spacings," U.S. Patent, No. 5457534, 1995.
- [75] [Lee & Wu, 1995] Lee C. K., Wu T. W., "Differential laser interferometer for nanometer displacement measurements," AIAA Journal, Vol.33, No.9, pp.1675-1680, Sept., 1995.
- [76] [Li et al, 1996] Li Y., Menon A. K., Goglia P. "Evaluations of diamond-like-carbon film optical constants and their effects on flying height determination," Transactions of the ASME, Journal of Tribology, Vol.118, No.4, pp.767-773, Oct., 1996.
- [77] [Li & Menon, 1996] Li Y., Menon A. K., "Flying height measurement metrology for ultra-low spacing in rigid magnetic recording," IEEE Transactions on Magnetics, Vol.32, No.1, pp.129-134, Jan., 1996.

- [78] [Li, 1997] Li Y., "Flying height measurement on Al<sub>2</sub>O<sub>3</sub> film of a magnetic slider," *Journal of Tribology*, Vol.119, pp.681-686, 1997.
- [79] [Licht, 1968] Licht L., "An experimental study of self-acting foil bearings," *J. Lub. Tech., Trans. ASME*90, 199-220, 1968.
- [80] [Lin, 1973] Lin C., "Techniques for the measurement of air bearing separation - a review," *IEEE Transactions on Magnetics*, V9, 4, pp673-677, 1973.
- [81] [Lin & Juang, 1997] Lin C. T. and Juang C. F., "Adaptive neural fuzzy filter and its applications", *IEEE Transactions on Systems, Man, and Cybernetics, Part B: Cybernetics*, Vol. 27, no. 4, pp.635-656, 1997.
- [82] [Lin & Sullivan, 1972] Lin C., and Sullivan R. F., "An application of white light interferometry in thin film measurements," *IBM Journal of Research and Development*, Vol.16, No.3, pp.269-276, 1972.
- [83] [Liu et al., 1999] Liu B., Zhu Y., Li Y., Hua W., Leng Q., and Sheng G, "An experimental study of slider vibration in nanometer spaced head-disk interface," *IEEE Transactions on Magnetics*, Vol.35, No.5, pp.2463-2465, 1999.
- [84] [Liu et al., 2000] Liu X. Q., Clegg W. W., and Liu B., "Ultra low head disk spacing measurement using dual beam polarization interferometry," *Optics & Laser technology*, Vol.32, no.4, pp.287-291, 2000.
- [85] [Liu et al., 2005] Liu X. Q., Clegg W. W., and Liu B., "Polarisation Interferometry Flying Height Testing", *Optics and Laser Technology*, vol. 37, no.1 pp 21-27, 2005.
- [86] [Lue & Lacey, 1994] Lue K., Lacey C., Talke F.E. "Measurement of flying height with carbon overcoated sliders," *IEEE Transactions on Magnetics*, Vol.30, No.6, pp.4167-4169, Nov. 1994.
- [87] [Mallinson, 1993] Mallinson J. C., *The Foundations of Magnetic Recording*, 2nd edition, Academic press, 1993.
- [88] [McAllister, 1996] McAllister J. S., "The effect of disk platter resonances on track misregistration in 3.5 inch disk drives," *IEEE Transactions on Magnetics*, Vol.32, No.3, pp1762-1766, 1996.
- [89] [McAllister, 1997] McAllister J. S., "Characterisation of disk vibration on aluminium and alternate substrates," *IEEE Transactions on Magnetics*, Vol.33, No.1, pp.986-973, 1997.
- [90] [McMillan & Talke, 1994] McMillan T. C.; Talke F. E., "Ultra low flying height measurements using monochromatic and phase demodulated laser interferometry," *IEEE Transactions on Magnetics*, Vol.30, No.6, pp.4173-4175, Nov., 1994.
- [91] [Mee & Daniel, 1995] Mee C. Denis and Eric D. Daniel, *Magnetic Recording Technology*, 2nd edition, McGraw-Hill, 1995

- [92] [Millman, 1986] Millman S. E., Hoyt R. F., Horne D. E., and Beye B., "Motion pictures of in-situ air bearing dynamics," IEEE Transactions on Magnetics, Vol.22, pp1031-1033, 1986.
- [93] [Mitsuya & Ohkubo, 1987] Mitsuya Y., and Ohkubo T., "High knudsen number rarefaction effects in gas-lubricated slider bearings for computer flying heads," SME Journal of Tribology, Vol.109, No.2, pp.276-282, 1987.
- [94] [Miu et al., 1984] Miu D. K., Bouchard G., Bogy D.B., and Talke F. E. "Dynamic response of a winchester-type slider measured by laser doppler interferometry," IEEE Transactions on Magnetics, Vol.20, pp.927-929, 1984.
- [95] [Miu & Bogy, 1986-a] Miu D. K., and Bogy D. B., "Dynamics of gas-lubricated slider bearings in magnetic recording disk files - part I: experimental observation," ASME Journal of Tribology, Vol.108, No.4, pp.584-588. 1986.
- [96] [Miu & Bogy, 1986b] Miu D. K., and Bogy D. B., "Dynamics of gas-lubricated slider bearings in magnetic recording disk files - part II: Numerical Simulation," ASME Journal of Tribology, Vol.108, No.4, pp.589-593. 1986.
- [97] [Mizoshita et al., 1985] Mizoshita Y., Aruga K., and Yamada T., "Dynamic characteristics of a magnetic head slider," IEEE Transactions on Magnetics, Vol.21, pp.1509-1511, 1985.
- [98] [Moon & Carley, 1990] Moon J., and Carley L. R., "Performance comparison of detection methods in magnetic recording," IEEE Transactions on Magnetics, Vol.26, No.6, pp.3155-3172, Nov., 1990.
- [99] [Nair & Moon, 1997] Nair S. K. and Moon J., "A theoretical study of linear and nonlinear equalization in nonlinear magnetic storage channels" IEEE Transactions on Neural Networks, Vol.8, No.5, pp.1106-1118, 1997.
- [100] [Nigam, 1982] Nigam A., "A visible laser interferometer for air bearing separation measurement to submicron accuracy," ASME Journal of Lubrication Technology, Vol.104, No.1, pp.60-65, 1982.
- [101] [Novotny, 1997] Novotny V J, "Magnetic recording drive dynamics during seeking and parking," IEEE Transactions on Magnetics, Vol. 33, pp.3115-3117, 1997.
- [102] [Novotny & Hsiao, 1998] Novotny V. J. and Hsiao M. J., "Sensitive magnetic readback head-disk spacing measurements in recording drives," IEEE Transactions on Magnetics, Vol.34, No.4, pp1762-1764, 1998.
- [103] [Obernosterer et al., 1997] Obernosterer F., Oehme W. F., and Sutor A., "Application of a neural network for detection at strong nonlinear intersymbol interference", Transactions on Magnetics, Vol.33, No.5, pp.2794-2796, 1997.
- [104] [Ohkubo & Kishigami, 1988] Ohkubo T., and Kishigami J., "Accurate measurement of gas-lubricated slider bearing separation using visible laser interferometry," ASME Journal of Tribology, Vol.110, No. 1, pp. 148-155. 1988.

- [105] [Ohtsubo et al., 1987] Ohtsubo Y., Kawashima N., and Marumo H., "Measurement method for the spacing fluctuation of a head slider in a magnetic disk drive," IEEE Transactions on Magnetics, Vol.23, pp.3450-3452, 1987.
- [106] [Riener, 1988] Riener Timothy A., Goding Adrian C., and Talke Frank E., "Measurement of head/disk spacing modulation using a two channel fiber optic laser doppler vibrometer," IEEE Transactions on Magnetics, Vol.24, No.6, pp.2745-2747, 1988.
- [107] [Riener & Talke, 1988] Riener T. A., and Talke F. E., "Dynamics of magnetic recording sliders using laser doppler interferometry," Jour. of Precision Eng., Vol.10, No.3, pp.131-140, 1988.
- [108] [Sands & Cioffi, 1993] Sands N P., and Cioffi J M., "nonlinear channel models for digital magnetic recording", IEEE Transactions on Magnetics, Vol.29, no.6, pt2, pp.3996-3998, 1993.
- [109] [Schardt, 1998] Schardt B. C., Schrech E., and Sonnenfeld R., "Flying height measurement while seeking in hard disk drives," IEEE Transactions on Magnetics, Vol.34, No.4, pp.1765-1767, 1998.
- [110] [Schrek, 1994] Schrek E., "Magnetic-readback-mapping and its application to slider/disk interface damage due to shock impact," STLE Special Publication, SP-16, pp.5-10, 1994.
- [111] [Schilling, 2000] Schilling. R. J., Applied numerical methods for engineers: using MATLAB and C, Brooks/Cole, 2000.
- [112] [Shabana, 1996] Shabana A, Theory of Vibration – An Introduction, 2nd ed., Springer, 1996.
- [113] [Shafiee & Moon, 1996] Shafiee H. and Moon J., "Knowledge-based parameter estimation for identification and equalisation of storage channels," IEEE Transactions on Magnetics, Vol.32, No.4, pp.3274-3282, 1996.
- [114] [Shenoi, 2006] Shenoi B. A., Introduction To Digital Signal Processing And Filter Design, John Wiley & Sons, Inc., 2006.
- [115] [Shi et al., 1987] Shi W. K., Zhu L. Y., and Bogy D. B., "Use of readback signal modulation to measure head/disk spacing variations in magnetic disk files," IEEE Transactions on Magnetics, Vol.23, pp.233-240, 1987.
- [116] [Smith, 1999] Smith G., "Dynamic in-situ measurements of head-to-disk spacing," IEEE Transactions on Magnetics, Vol.35, No.5, pp.2346-2351, 1999.
- [117] [Sonnenfield, 1993] Sonnenfield R., "Capacitance methods in head-disk interface studies," IEEE Transactions on Magnetics Vol.29, No.2, pp.247-252, Nov., 1993.
- [118] [Srikrishna & Kasetty, 2000] Srikrishna P. and Kasetty K., "Prediction track misregistration (TMR) from disk vibration of alternate substrate materials," IEEE Transactions on Magnetics, Vol.36, No.1, pp.171-176. 2000.



- [119] [Staudenmann, 1998] Staudenmann M. "A new laser interferometer system for investigation of the dynamics at the head/disk interface," IEEE Transactions on Magnetism, Vol.34, No.4, pp.1696-1698, 1998.
- [120] Sommargren G., "Distance measuring interferometer and method of use," U.S. Patent, No.4,606,638, 1986.
- [121] Sommargren G., "Flying height and topography measuring interferometer," U.S. Patent, No.5,218,424, 1993.
- [122] [Sugawara et al., 1998] Sugawara T., Uehara Y., Oshima T., Takagi M., Shimoda K., and Mutoh H., "A nonlinear model for magnetic recording channel with an MR head", IEEE Transactions on Magnetism, Vol.34, No.1 Pt1, pp.57-62 1998.
- [123] [Sundaram et al., 1999] Sundaram R., Yao W., Ku R. C. and Kuo D., "Study of head/disk interface dynamics using a thermal asperity sensor," IEEE Transactions on Magnetism, Vol.35, No.5, pp.2481-2483, 1999.
- [124] [Suwa & Aruga] Suwa M. and Aruga K., "Evaluation system for residual vibration from HDD mounting mechanism," IEEE Transactions on Magnetism, Vol.35, No.2, pp.868-873, 1999.
- [125] [Tanaka et al., 1984] Tanaka K., Takeuchi Y., Terashima S., Odaka T., and Saitoh Y., "Measurements of transient motion of magnetic disk slider," IEEE Transactions on Magnetism, Vol.20, pp.924-926, 1984.
- [126] [Tsai et al., 1994] Tsai Youping, Nixon Hsiao-chu, Brian J., "Drive-level flying height measurements and altitude effects," IEEE Transactions on Magnetism, Vol.30, No.6, Pt.1, pp.4191-4193, Nov., 1994.
- [127] [Tunstall et al., 2000] Tunstall G., Clegg W., Jenkins D., and Chilumbu C., "Head-media interface instability under hostile operating conditions," IEEE IMTC-2000, Baltimore, USA, 2000.
- [128] [Tunstall, 2002] Tunstall G., Dynamic Characterisation of the Head-Media Interface in Hard Disk Drives Using Novel Sensor Systems, PhD thesis, 2002, University of Plymouth.
- [129] [Wallace, 1951] Wallace Jr. R. L., "The reproduction of magnetically recorded signals," The Bell System Technical Journal, 30, pp.1145-1173, 1951.
- [130] [Wang & Taratorin, 1999] Wang Shan X., and Taratorin, Alexander M., Magnetic Information Storage Technology, Academic press, 1999
- [131] [White 1984] White J. W., "Flying characteristics of the 3370-type slider on a 1/2-inch diskPart I: Static analysis," Tribology and Mechanics of Magnetic Storage System, vol.1, (B. Bhushan, et al., eds.), pp.72-76, SP-16, ASLE, Park Ridge, Illinois, 1984.

- [132] [White & Nigam, 1980] White J. W., and Nigam A., "A factored implicit scheme for the numerical solution of the Reynolds equation at very low spacing," J. Lub. Tech., Transactions on, ASME, vol.102, pp80-85, 1980.
- [133] [Yamada et al., 1986] Tamada T., Mizoshita Y., and Aruga K., "Spacing fluctuation of flying height head sliders in track accessing (measurement using optical interferometer)," Tribology and Mechanics of Magnetic Storage System, vol.3, (B. Bhushan and N. S. Eiss, eds.), pp.87-94, SP-21, ASLE, Park Ridge, Illinois, 1986.
- [134] [Yamaguchi et al., 1999] Yamaguchi T., Usui K., and Hirai H., "Modelling and TMR (track misregistration) budget design for head-positioning of high track-density disk drives," IEEE Transactions on Magnetics, Vol.35, No.2, pp.892-897, 1999.
- [135] [Zhu et al., 1998] Zhu J., Carr T., and Varsanofiev D., "A digital sampling technique for amplitude and pulse width measurement," IEEE Transactions on Magnetics, Vol.34, No.4, pp.2027-2029, 1998.

#### Selected Publications

1. Aimei Li, Xinqun Liu, Warwick Clegg, David Jenkins, and Donnelly T., "Real Time Method to Measure Head Disk Spacing Variation under Vibration Conditions", *IEEE Transactions on Instrumentation and Measurement*, vol. 52, no.3, pp.916-920, June, 2003.
2. Xinqun Liu; Aimei Li; Warwick Clegg, David Jenkins, and Paul Davey; "Head-disk spacing variation suppression via active flying height control", ", *IEEE Transactions on Instrumentation and Measurement*, vol. 51 no.5, pp.897-901, Oct., 2002.
3. Aimei Li, Xinqun Liu, Warwick Clegg, Glen Tunstall, and Paul Davey, "Analysis of hard disk drive operation failure under vibration conditions," presented at the *IEEE/AIP 8th Joint MMM-Intermag Conference*, San Antonio, Texas, January 7-11, 2001.

# Real-Time Method to Measure Head Disk Spacing Variation Under Vibration Conditions

Amel Li, Nanqun Liu, Warwick Clegg, *Senior Member, IEEE*, David F. L. Jenkins, and Terrence Donnelly

**Abstract**—Three readback signal detection methods are presented for real-time head disk spacing variation measurement under vibration conditions. The proposed  $PW_{50}$  parameter estimation method is not restricted by the isolated readback pulse signal requirement and, thus, can be used for spacing variation measurement in normally operated hard disk drives, especially for low-frequency variations. The thermal signal detection method, on the other side, is more effective for high-frequency spacing variation measurement. Amplitude detection gives a rough but simple way to study the head disk spacing change. Theoretical analysis and experimental results are given to illustrate the effectiveness of the methods.

**Index Terms**—Flying height, hard disk drive, head disk spacing variation, real-time measurement, vibration.

## I. INTRODUCTION

IN HARD disk drives, one of the most critical and effective parameters in increasing areal density is the flying height or spacing between the read-write head and the recording disk medium. Since 1990, flying height has been reduced from above 140 nm to under 20 nm for the leading-edge products of the magnetic recording industry. Although it is very desirable to reduce the head-disk spacing or flying height to increase the recording areal density, head disk contact is undesirable during disk operation since that will deteriorate the tribological performance of the head disk interface and its reliability. In vibration conditions, air bearing resonance will be produced in a hard disk drive. This resonance will cause head disk spacing or flying height fluctuation, which will induce modulation of the readback signals due to the spacing loss [1] so that increases the bit-error-rate of the read channel. Therefore, it is very important and necessary to make real time measurement of head disk spacing variation in working disk drives. This measurement will be used both for analysis of disk drive operation failure and real time flying height variation control. Optical interferometry has been the major means for the characterization of this parameter. However, in optical interferometry, a quartz or glass disk is often used in place of the real magnetic disk to measure the head-disk spacing. While this technique can be easily used to measure the flying height at the head component level, it is impossible to use it directly to measure the flying height on a sealed drive without any modification.

In this paper, three methods are presented for real-time measurement of head disk spacing variation under vibration conditions. They all use readback signals from hard disk drives to

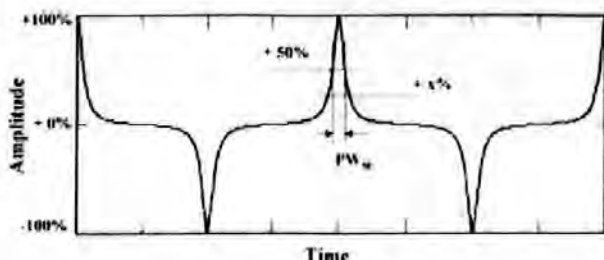


Fig. 1. Definition of  $PW_x$ , the pulse width at a slicing level of  $x\%$  ( $-100 \leq x \leq +100$ ).

derive the flying height variation. Theoretical analysis and experimental results are provided to illustrate the effectiveness of these methods.

## II. $PW_{50}$ PARAMETER ESTIMATION METHOD

### A. $PW_{50}$ and Flying Height

Below is a rational derivation of the relationship between the flying height change and the pulse width variation [2]. A readback signal is shown in Fig. 1, which is supposed to be read back from a series of isolated transitions written on the disk.

The shape of this waveform will be characterized by its pulse width  $PW_x$  at  $x$  percent ( $-100 \leq x \leq +100$ ) of the peak to base-line amplitude. The pulse length at  $x$  percent is represented by  $PL_x$  which is the length of the pulse projected along the track. For a disk rotating at a velocity  $v$  with respect to the head,  $PL_x = vPW_x$ . Wallace [1] demonstrated that the magnetic spacing loss can be represented by a noncausal (no phase shift) low-pass filter, whose cutoff frequency decreases with increasing flying height. For an increase  $\Delta d$  in the flying height  $d$ , this "spacing loss filter" has a transfer function  $H(\omega)$  given by

$$H(\omega) = \exp(-\Delta d |\omega| / v) = \exp(-2\pi \Delta d / \lambda) \quad (1)$$

where  $\lambda$  is the wavelength along the track of a sinusoidal signal at an angular frequency  $\omega$ . This filter is applied to the readback signal at flying height  $d$  to arrive at the signal at flying height  $d + \Delta d$ .

For pulses with Lorentzian shape, which is usually a close approximation of the readback signal shape, it is not difficult to calculate what happens to the pulse width for varying flying height. A Lorentzian readback pulse is given by

$$a(t) = \frac{a(0)}{1 + \left(\frac{2t}{PW_{50}}\right)^2} \quad (2)$$

Manuscript received May 27, 2001; revised February 26, 2003.

The authors are with the Centre for Research in Information Storage Technology, University of Plymouth, Devon, U.K. (e-mail: a.li-1@plymouth.ac.uk).  
Digital Object Identifier 10.1109/TIM.2003.814361

where  $c(0)$  is the peak amplitude. Its Fourier transform is

$$F_d(\omega) = \frac{\pi}{2} c(0) PW_{50} \exp(-|\omega| PW_{50} / 2). \quad (3)$$

Filtering the Lorentzian pulse of (2) by the spacing loss filter of (1) produces an output pulse whose Fourier transform  $F_{\hat{d}}(\omega)$  is equal to the product of  $F_d(\omega)$  and  $H(\omega)$

$$F_{\hat{d}}(\omega) = \frac{\pi}{2} c(0) PW_{50} \exp\left[-\left(\frac{PW_{50}}{2} + \frac{\Delta d}{v}\right) |\omega|\right]. \quad (4)$$

Transforming  $F_{\hat{d}}(\omega)$  back to the time domain gives out the Wallace spacing loss weighted pulse

$$c^f(x) = \frac{c^f(0)}{1 + \left(\frac{x}{PW_{50}^f}\right)^2} \quad (5)$$

which also has a Lorentzian shape. A Lorentzian pulse is obviously shape invariant under the Wallace head medium spacing loss.

The pulse width at half maximum value now becomes

$$PW_{50}^f = PW_{50} + 2 \frac{\Delta d}{v} \quad (6)$$

or

$$\Delta PW_{50}^f = PW_{50}^f - PW_{50} = 2 \frac{\Delta d}{v}. \quad (7)$$

From this, we conclude that a pulse width measurement yields an incremental measurement of flying height  $d$ .

#### B. Real-Time Parameter Estimation for $PW_{50}^f$

A similar method as described in [3] is used here. It is well known that the write/read process in digital magnetic recording is generally modeled as

$$s[j] = \sum_k a_k p[j - KT] + n[j] \quad (8)$$

where  $a_k \in \{-1, 1\}$  is the input sequence,  $p[j]$  is the effective channel impulse (or dibit) response,  $T$  is the symbol period, and  $n[j]$  is the additive noise [4], [5]. Equivalently, the readback signal can be written as

$$s[j] = \sum_k b_k h[j - KT] + n[j] \quad (9)$$

where  $h[j]$  is the step or transition response and  $b_k$  is the transition sequence given by

$$b_k = a_k - a_{k-1} - \dots - a_{k-L} \in \{-2, 0, 2\}. \quad (10)$$

The transition response is generally approximated by a Lorentzian function given as

$$h[j] = \frac{A_h}{PW_{50}} \frac{1}{1 + \left(\frac{j}{PW_{50}}\right)^2}. \quad (11)$$

For a given head-disk assembly,  $A_h$  is a constant, which must be known in order to use this estimation method. In real application or in calibration process, this constant can be determined from isolated readback signal pulses. In simulation, it can be selected as a reasonable value, and here we set it to 1. An equivalent discrete time model of the storage channel can be obtained by passing the readback signal through a matched-filter and a symbol-rate sampler. The schematic diagram of the resulting

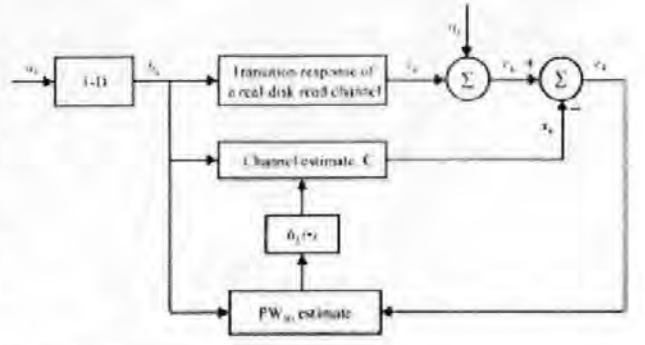


Fig. 2.  $PW_{50}$  estimation model

discrete time system is shown in Fig. 2, where the readback sample  $r_k$  is given by  $r_k = y_k + n_k$ , and  $n_k$  denote signal and noise samples, respectively.

The problem now becomes channel identification. As in all channel identification methods, it is assumed that linear superposition holds for the channel to be estimated. For a Lorentzian step response, since the transition response is a function of only one parameter, the channel identification reduces to estimation of the  $PW_{50}$  parameter, which is just what we need. We use the approach based on minimizing the error between  $r_k$  and the predicted channel output  $\hat{x}_k$ , with respect to the desired parameters.  $\hat{x}_k$  is given by

$$\hat{x}_k = \sum_{m=-L}^L b[k-m] c[m] = C^T B_k \quad (12)$$

where  $L$  is a integer which should be selected large enough so that  $c[L]$  is small enough to be neglected,  $B_k$  is a vector of length  $2L+1$  containing transition sequence, and  $C$  is a vector of length  $2L+1$  containing estimated step response coefficients which is given by

$$c[m] = \frac{1}{PW_{50}} \frac{1}{1 + \left(\frac{m}{PW_{50}}\right)^2}. \quad (13)$$

With  $PW_{50}$  as the only parameter to be estimated, the error function is defined as

$$e_k^2 = (r_k - C^T B_k)^2. \quad (14)$$

Taking the derivative of the expectation of the error function with respect to  $\rho = PW_{50}$ , we obtain

$$\frac{\partial E(e_k^2)}{\partial \rho} = -2 \frac{\partial C^T}{\partial \rho} E(B_k B_k^T) + 2 \frac{\partial C^T}{\partial \rho} E(B_k B_k^T) C. \quad (15)$$

This derivative is equal to zero for the optimal value of  $\rho$ . To obtain an expression for adaptive or on-line estimation of  $\rho$ , we drop the expectation in (15) which then yields

$$\frac{\partial E(e_k^2)}{\partial \rho} = -2 \left( \frac{\partial C^T}{\partial \rho} B_k \right) e_k. \quad (16)$$

This expression represents the gradient of the error function with respect to  $\rho$ . To follow the real (optimal) value of  $PW_{50}$ , the value of  $\rho$  should be changed in the opposite direction of the gradient according to the following equation

$$\rho[k+1] = \rho[k] + \beta \left( \frac{\partial C^T}{\partial \rho} B_k \right) e_k \quad (17)$$

where  $\Delta$  is the step size. The update process of the value  $\rho$  continues until it converges to the real value.

### III. AMPLITUDE DETECTION METHOD

It is well known that head disk spacing change can be expressed by Wallace spacing loss equation as [1]

$$\Delta d = d_0 = -\frac{\lambda}{2\pi} \ln \frac{E(d)}{E(d_0)} \quad (18)$$

where  $E(d_0)$  and  $E(d)$  are amplitudes of the readback signal at spacing of  $d_0$  and  $d$  respectively,  $\Delta d = d - d_0$  denotes the spacing change, and  $\lambda$  is the readback harmonic wavelength. Thus, the flying height variation can be determined by measuring the amplitude of the readback signal before and after the change. It must be stressed that (18) is not accurate for modern disk drives because of the assumptions being made in its derivation process. Therefore this method can only be used to qualitatively evaluate the head disk spacing change.

### IV. THERMAL SIGNAL DETECTION METHOD

The thermal signal flying height detection method was proposed in recent years for measurement of disk topography or dynamic flying height by using readback signals from a magnetoresistive (MR) or giant MR (GMR) head in a hard disk drive [6]–[9]. Changes in flying height or head-disk spacing modulate both the envelope of the readback signal and its mean value. Two nomenclatures, magnetic spacing and thermal spacing, are used here to clarify the statement, although both mean the same thing, flying height. The envelope relates to the magnetic spacing and the mean value is a function of thermal spacing. The thermal spacing signal is the result of Joule heating, whereby some of the thermal energy generated in the MR head dissipates into the air film between the head and disk. Changes in head flying height alter the heat transfer and hence the temperature and resistance of the MR head. Abraham [6] has shown that the MR head voltage resulting from thermal spacing can be approximated as

$$e_{\text{thermal}}(t) = C_0 + C_1 \delta I^2 R^2 \Delta d(t) \quad (19)$$

where  $e_{\text{thermal}}$  is the MR voltage due to its temperature,  $t$  is time,  $C_0$  and  $C_1$  are constants that depend on the geometry and thermal properties of the MR element and adjacent shields,  $\delta$  is the temperature coefficient of resistance for the MR material,  $I$  and  $R$  are the MR current and electrical resistance respectively, and  $\Delta d$  is the head disk spacing. From (19), it is seen that the flying height can be determined from the measured thermal signal. One thing needs to be noted is that many disk drives use an arm-mounted electronic module circuitry (AEM) which is used to amplify the head output signal and usually includes a high pass filter. The filter provides a necessary ac coupling for the read channel but also filters out the low frequency components and distorts the thermal signal. This filter can be generally represented by a first order approximation as

$$H_{\text{AEM}}(s) = K_{\text{AEM}} \frac{s}{s + \omega} \quad (20)$$

where  $K_{\text{AEM}}$  is the gain of the AEM at recording frequencies, and  $\omega$  is the cut-off frequency of the high pass filter. Although an inverse filter can partly correct this distortion, it is impossible

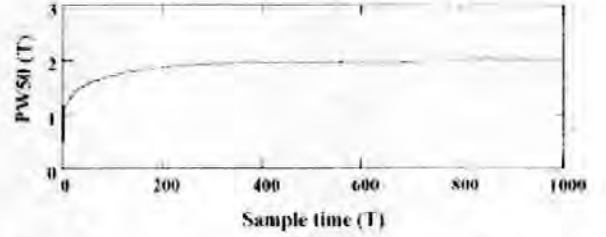


Fig. 3. Estimation of  $P^0 W_{70}$  from readback signals with noise.  $T$  is the symbol period.

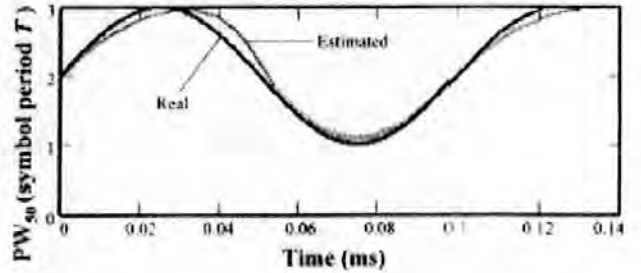


Fig. 4. On-line estimation of  $P^0 W_{70}$ ; the real value changes in a 10-kHz sinusoidal wave form.

for some low frequency components to be restored completely. Therefore in this case, the thermal detection method is suitable only for the measurement of spacing variation above a certain changing rate.

## V. EXPERIMENTAL RESULTS

### A. $P^0 W_{70}$ Parameter Estimation Method

A large number of simulations are made to evaluate this method. In the simulation, we found that the testing data sequence does not need to be restricted to random-like type, all-one data sequence can produce the same good result as well. The static performance of this estimation method is perfect, the  $P^0 W_{70}$  converges to its fixed real value within a few hundreds of symbol periods time without static error (or with very small negligible error). Even though heavy timing jitter noise and signal noise exist, the correct value can still be determined quickly. Fig. 3 gives a result in which the random timing jitter noise is 0.25  $T$  ( $T$  is the symbol period) and the random signal noise is 0.025  $A$  ( $A$  is the amplitude of the isolated readback signal). Now we evaluate the dynamic performance of the method. In the following simulation, a pseudo-random binary sequence data are read back from a hard disk drive with a bit-rate of 100 Mb/s. A 0.5  $T$  random timing jitter noise and a 0.05- $A$  random signal noise are added. The is made changing in a 10-kHz sinusoidal wave form. The on-line estimation result is shown in Fig. 4. From this result, it is seen that the maximum estimation error is 30% of the peak  $P^0 W_{70}$  change. From further simulation, we found the estimation error becomes larger when the  $P^0 W_{70}$  changes quicker (i.e., the estimator can not follow the real  $P^0 W_{70}$  change properly). In fact, the dynamic behavior of the estimator has close relationship with the bit-rate of the disk drive. The higher the bit-rate, the quicker the change that the estimator can well track and estimate. The sampling rate of the estimator is the bit-rate, over-sampling is not used. However,



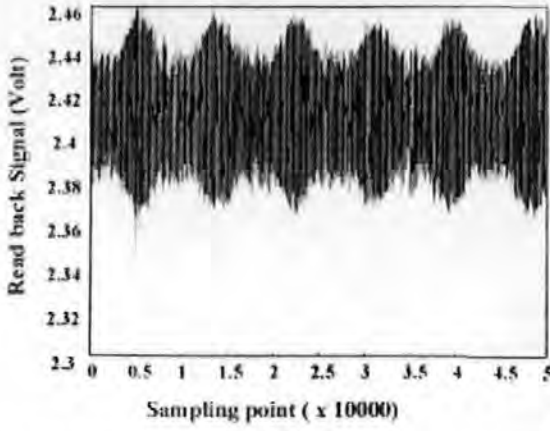


Fig. 5. Readback signal of a non-MR head at a vibration frequency of 5.8 kHz.

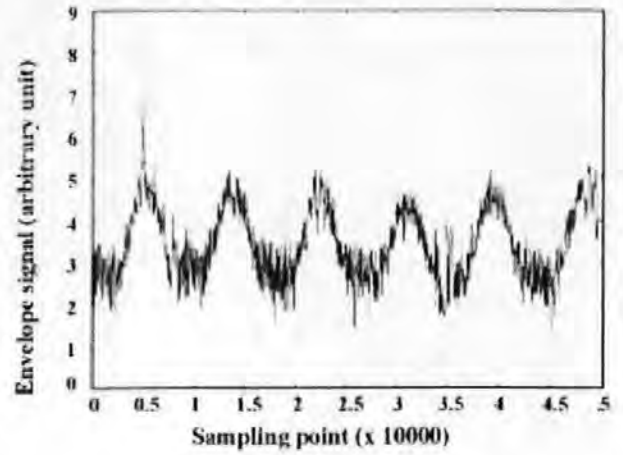


Fig. 6. Extracted envelope (or modulation) signal by using signal processing.

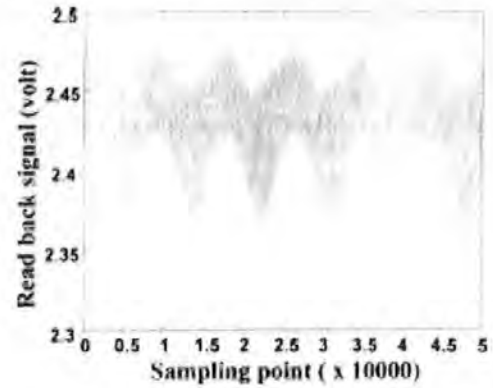


Fig. 7. Readback signal of a MR head at a vibration frequency of 5.8 kHz.

35 mm, and the bit-rate of the hard disk drive is 12.8 MHz, from (18) the maximum spacing variation can be calculated as 160 nm.

### C. Thermal Signal Detection Method

Since no hard disk drive with MR heads is currently available in the Lab for the vibration experiments, the following simulation method is used to demonstrate the thermal detection method. A sinusoidal thermal signal is generated by the computer, which is then mixed with the readback signal obtained from the vibration experiment in last subsection. The resulted readback signal is shown in Fig. 7, which contains both the sinusoidal thermal signal component and an amplitude modulation. The extraction of the amplitude envelope has been discussed in last subsection. To get the thermal signal out of it, a linear phase low-pass 501-tap FIR filter with cut-off frequency of 58 kHz is used to the combined readback signal (a 201-tap FIR filter can also do the job with a little bit heavier noise observed). The extracted thermal signal is shown in Fig. 8, from which it can be seen that the signal is successfully restored. From (19), it can be seen that the spacing change and the thermal signal change have a linear relationship. The constant factor between the two needs to be calibrated before the real application. Thermal detection method is very promising for real-time head disk spacing variation detection, which can be used in the active flying height control [10].

we do believe that over-sampling can improve the estimator's performance if it can be implemented in real application. As for the selection of step size  $\beta$  in (17), it is chosen as 0.95. Too small value of  $\beta$  results in a slow convergence speed. Too big value results in estimation overshoot, which also means a slow convergence speed. To have an idea of how much spacing variation will be resulted from a  $P/W_{20}$  change, an example is given here. Assume the bit-rate of the hard disk drive is 100 MHz which means a symbol period of  $T = 10^{-8}$  s, the radius at the head position is 35 mm, and the disk speed is 5400 r/m, then according to (7), a change of  $T = 10^{-8}$  s will result in a spacing variation of 99 nm.

### B. Amplitude Detection Method

Experiments are made to evaluate the amplitude detection method. The experiments are carried out by mounting a commercial hard disk drive on an electro-dynamic shaker (this disk drive uses non-MR heads therefore no thermal signal is observed). Read back signals under vibration conditions are sampled and stored by digital storage oscilloscope and post processed. Fig. 5 shows the readback signal from the hard disk drive that is vibrated vertically at a frequency of 5.8 kHz by the shaker. The sampling rate of the oscilloscope is selected as 50 MHz (after measurement we know the bit-rate of the hard disk drive is 12.8 MHz). Simple signal processing method is used to obtain the amplitude modulation envelope. First, the readback signal data are processed by local area moving average to get a full-wave rectified signal, then followed by a linear phase low-pass FIR filter to get the envelope. The cut-off frequency of the low-pass filter should be selected high enough (e.g., 10 times the useful frequency) so that all the useful signals will be attenuated by the same filter gain. Fig. 6 shows the amplitude signal extracted after the signal processing. The FIR filter used is a 61-tap low-pass filter with cut-off frequency of 58 kHz. If desired, the following means can be used to obtain better quality amplitude envelope signals: a) increase the sampling rate of the oscilloscope; b) increase the taps of the FIR filter. As stated earlier, the amplitude detection method can only provide a rough evaluation of spacing variation, simple signal processing should be fair enough. From Fig. 6, it can be seen that the maximum  $E_{\text{max}}(d)/E_{\text{min}}(d_0)$  is  $5/2.8 \approx 1.79$ . Since the disk speed is 6000 r/min, the radius at the head position is

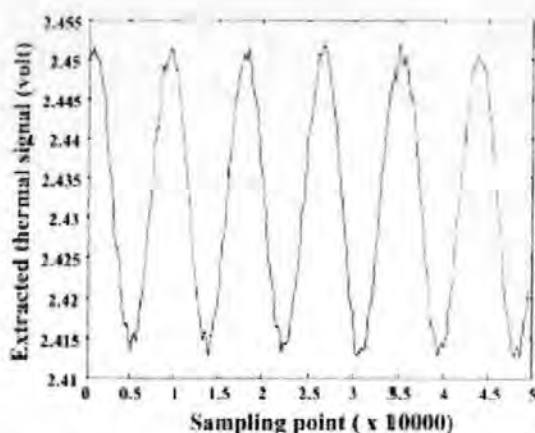


Fig. 8. Extracted thermal signal by using signal processing.

## VI. CONCLUSION

Three readback signal detection methods are discussed for real-time measurement of head disk spacing variation under vibration conditions. Different from other  $I^2W_{90}$  measurement methods, the proposed  $I^2W_{90}$  parameter estimation method is not restricted by the requirement of an isolated readback pulse signal. Thus, it can be used for real-time space variation measurement in normally operated hard disk drives. However, this method is more effective for low frequency spacing variation conditions. Thermal signal detection method, on the other side, is more effective for high frequency spacing variation measurement. Therefore, by combining these two detection methods together, a spacing variation detection method for the whole frequency range could be constructed, which has the potential of being used in the active flying height control [10]. The amplitude detection method gives a rough but simple way to study the head disk spacing change.

## REFERENCES

- [1] R. L. Wallace, Jr., "The reproduction of magnetically recorded signals," *Bell Syst. Tech. J.*, vol. 30, pp. 1145–1173, 1951.
- [2] K. B. Klaassen and J. C. L. van Peppen, "Slider-disk clearance measurements in magnetic disk drives using the readback transducer," *IEEE Trans. Instrum. Meas.*, vol. 43, pp. 121–126, Feb. 1994.
- [3] H. Shafiee and J. Moon, "Knowledge-based parameter estimation for identification and equalization of storage channels," *IEEE Trans. Magn.*, vol. 32, pp. 3274–3282, Nov. 1996.
- [4] J. Moon and L. R. Carley, "Performance comparison of detection methods in magnetic recording," *IEEE Trans. Magn.*, vol. 26, pp. 3155–3172, Nov. 1990.
- [5] K. Immler, "Coding techniques for the noisy magnetic recording channel: A state-of-the-art report," *IEEE Trans. Commun.*, vol. 37, pp. 413–419, May 1989.
- [6] D. W. Abraham, A. P. Pranno, M. E. Re, and H. K. Wickramasinghe, "Method and apparatus for detecting asperities on magnetic disk using thermal proximity imaging," U.S. Patent 5 527 110, June 18, 1996.
- [7] G. Smith, "Dynamic in-situ measurements of head-to-disk spacing," *IEEE Trans. Magn.*, vol. 35, pp. 2346–2351, Sept. 1999.
- [8] R. Sundaram, W. Yao, R. C. Ku, and D. Kuo, "Study of head disk interface dynamics using a thermal asperity sensor," *IEEE Trans. Magn.*, vol. 35, pp. 2481–2483, Sept. 1999.
- [9] Q. Leng, B. Liu, W. Zhang, A. Mydeen, and S. Hu, "Thump characterization with MR-GMR head as transducer," *IEEE Trans. Magn.*, vol. 36, pp. 2671–2673, Sept. 2000.
- [10] X. Liu, A. Li, W. Clegg, D. Jenkins, and P. Davey, "Head disk spacing vibration suppression via active flying height control," *IEEE Trans. Instrum. Meas.*, vol. 51, pp. 897–901, Oct. 2002.

**Amel Li** received the B.Eng. and M.Sc. degrees in electrical engineering from the Jilin University of Technology, China, in 1987 and 1995, respectively. She is currently pursuing the Ph.D. degree in information storage at the University of Plymouth, Devon, U.K. Her Ph.D. research work includes signal restoration and processing, head disk spacing characterization using electromagnetic transducers, recording channel coding, equalization, and detection, all for magnetic hard disk drives.

From 1987 until recently, she was an Electronics Engineer at a research institute in China, where she worked in the area of signal processing and digital communications.

**Xinqun Liu** received the B.Eng. and M.Eng. degree in electrical and control engineering from the Jilin University of Technology, China, in 1985 and 1988, respectively.

From 1988 to 1997, he was with the Changchun Institute of Optics and Fine Mechanics (one of the largest research institutes in China), Chinese Academy of Sciences, working in the area of micro-processor-based control system design, high precision speed and position servo control, analogue and computer control system design, and digital signal processing. In 1997, he joined the Center for Research in Information Storage Technology, University of Plymouth, Devon, U.K., as a Researcher, where he worked on building up computer controlled optical instruments to measure the head-disk spacing of the up-to-date hard-disk drives. During this period of time, he also gained interests in optical system design, magnetic recording channel technologies, such as coding, equalization, and detection, and servo control in hard-disk drives. Since 2000, he has been with Roke Manor Research, a top research center in the U.K. for communications and electronic sensors. His latest interests include DSP applications in 3G baseband systems, 3G radio link simulation, optical communications, and channel coding technologies.

Mr. Liu is a Senior Member of the Chinese Institute of Electronics.

**Warwick Clegg** (SM'94) received the degree in physics from Liverpool University, Liverpool, U.K., in the late 1960s, and the M.Sc. and Ph.D. degrees in magnetic data storage from Manchester University, U.K.

After many years at Manchester University, he moved to the University of Plymouth, Devon, U.K., where he is now Head of the Department of Communications and Electronic Engineering. His principal research interests continue to lie in the field of data storage, with increasing emphasis on characterization methods for advanced media and drives, including the development of novel scanning laser and scanning force probe instruments and techniques to visualize written data bits.

Prof. Clegg is a Member of the Institute of Physics and the Institution of Electrical Engineers.

**David F. L. Jenkins** received the B.Sc. degree in physics, the M.Sc. degree in lasers and their applications, and the Ph.D. degree in photothermal deflection spectroscopy from the Royal Military College of Science, U.K.

After receiving the Ph.D. degree, he became a post-doctoral Research Fellow at Coventry University, U.K., in 1990, working on magnetophoto-acoustic spectroscopy. From 1993 and 1997, he worked in the Information Storage Group, Division of Electrical Engineering, Manchester University, U.K., researching active vibration control of micro-mechanical structures. In 1997, he moved to the University of Plymouth, Devon, U.K., as Lecturer, and then as Senior Lecturer, in the Center for Research in Information Storage Technology, where he has continued his research into microactuators, microsensors, and optical instrumentation.

**Terence Donnelly** received the B.Sc. degree in electrical engineering from the University of Salford, U.K., after several years of experience in the electronics industry, in both in Europe and Canada. He received the M.Sc. and Ph.D. degrees from the University of Plymouth, Devon, U.K., in 1978 and 1989, respectively.

He was appointed to the lecturing staff of the University of Plymouth in 1976, where he is now Principal Lecturer and where his research interests include data recording and microprocessor systems.



# Head-Disk Spacing Variation Suppression via Active Flying Height Control

Xinqun Liu, Anei Li, Warwick Clegg, *Senior Member, IEEE*, David F. L. Jenkins, and Paul Davey, *Member, IEEE*

**Abstract**—A novel active flying height control method is proposed for the suppression of head-disk spacing variation in hard disk drives under shock or vibration conditions. The thermal signal detection method is used for real-time derivation of the spacing variation signal for feedback control. Design details of the servo control system are given. Simulation results are provided to demonstrate the effectiveness of the method.

**Index Terms**—Feedback control, flying height, hard disk drive, head-disk spacing, spacing variation suppression.

## I. INTRODUCTION

THE need for ever-greater storage capacity has resulted in the data-storage recording densities of magnetic hard disk drives (HDDs) growing at a rate of about 60% every year in the past decade. In order to support these developments, work has been undertaken in parallel to improve the heads, media, channel and electronics. However, one of the most critical and effective parameters in increasing areal density is the flying height or spacing between the read-write head and the recording disk medium. Since 1990, flying height has been reduced from above 140 nm to under 20 nm for the leading-edge products of the magnetic recording industry. It is expected that the head-disk spacing will reduce from the current value of 20–30 nm to a level of 5–10 nm, as the technology moves from the current 10 Gb/in<sup>2</sup> areal density to beyond 40 Gb/in<sup>2</sup> areal density of commercial hard disk drives by the year 2004 [1]. In such a low flying height condition, it becomes even more important to keep the head-disk spacing variation as small as possible during disk operation. This is because the flying height variation will cause modulation of the readback signal due to the spacing loss [2], thus increasing the bit-error-rate of the read channel. Especially in shock and vibration conditions, there is a high possibility of undesirable head-disk contact, which will deteriorate the tribological performance of the head-disk interface and its reliability. Therefore, active flying height control is highly desirable for suppression of this spacing variation. The reason why there are so few results and publications in this area is probably because of the difficulty of real-time detection of the flying height, or flying height variation in a real operating hard disk drive. Gao *et al.* investigated the active actuation and control of a miniaturized suspension structure in HDDs to reduce head-disk friction/wear and suppress induced vibrations [3]. However, since the displacement of the head suspension arm is used for the feed-

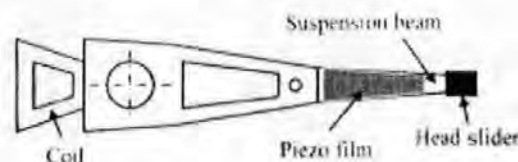


Fig. 1. Head assembly in HDDs with bonded piezo film on one side of the suspension beam.

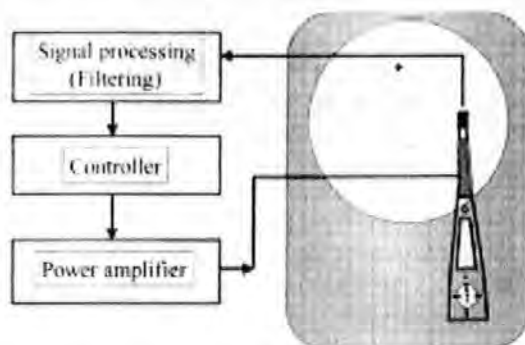


Fig. 2. Flying height variation suppression mechanism.

back control signal, their investigation falls into the active vibration control of the suspension arm itself, not the control of head-disk spacing variation.

In this paper, a real-time active control method is proposed to suppress the flying height or head-disk spacing variation, in which the thermal signal detection method is used for real-time flying height variation signal derivation. Simulation results are presented to demonstrate the effectiveness of the method.

## II. REAL-TIME HEAD-DISK SPACING VARIATION DETECTION USING THERMAL SIGNAL METHOD

The thermal signal flying height detection method was proposed in recent years. It was intended for the measurement of disk topography or dynamic flying height by detecting and processing the readback signal from a magneto-resistive (MR) or giant MR (GMR) head in a hard disk drive [4]–[6]. Changes in flying height or head-disk spacing modulate both the envelope of the readback signal and its mean value. To clarify the statement, we use two nomenclatures: magnetic spacing and thermal spacing, although both of them mean the flying height or head-disk spacing. While the envelope is related to the magnetic spacing, the mean value is a function of the thermal spacing. The thermal spacing signal is the result of Joule heating, whereby some of the thermal energy generated in the MR head dissipates into the air film between the head

Manuscript received May 29, 2001; revised August 5, 2002.

The authors are with the Centre for Research in Information Storage Technology, University of Plymouth, Devon, U.K. (e-mail: xinqun.liu@roke.co.uk, a.li-1@plymouth.ac.uk, URL: <http://er1.sec.plym.ac.uk>).

Digital Object Identifier 10.1109/11.1002.807790

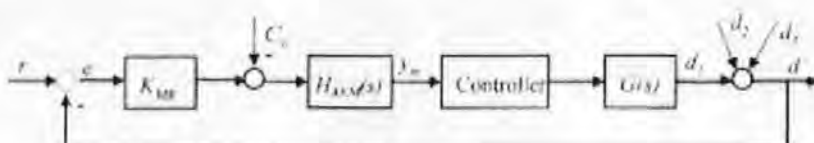


Fig. 3. Block diagram of closed-loop control system for flying height variation control

and disk. Changes in head flying height alter the heat transfer and hence the temperature and resistance of the MR head. Abraham [4] has shown that the MR head voltage resulting from the thermal spacing can be approximated as

$$e_{thermal}(t) = C_0 + C_1/I^2 R^2 d(t) = C_0 + K_{MH} \hat{d}(t) \quad (1)$$

where  $e_{thermal}$  is the MR voltage due to its temperature,  $t$  is time,  $C_0$  and  $C_1$  are constants that depend on the geometry and thermal properties of the MR element and adjacent shields,  $\beta$  is the temperature coefficient of resistance for the MR material,  $I$  and  $R$  are the MR current and electrical resistance, respectively, and  $d$  is the head-disk spacing or flying height. From (1), it can be noted that the flying height can be determined from the measured thermal signal. However, we must note that most disk drives use arm-mounted electronic module circuitry (AEM) to amplify the head output signal and usually include a high-pass filter. The filter provides the necessary ac coupling for the read channel, but also distorts the thermal signal. This filter can be generally represented by a first-order approximation as

$$H_{AEM}(s) = K_{AEM} \frac{s}{s + a} \quad (2)$$

where  $K_{AEM}$  is the gain of the AEM at recording frequencies and  $a$  is the cut-off frequency of the high-pass filter. The AEM output signal is thus the convolution of  $e_{thermal}$  and the impulse response of the filter that is given by

$$e_{AEM}(t) = K_{AEM} \int_{-\infty}^{+\infty} e_{thermal}(t - \tau) \delta(\tau) - a \exp(-a\tau) d\tau \quad (3)$$

### III. REAL-TIME ACTIVE FLYING HEIGHT VARIATION CONTROL

The adjustment of the head suspension arm can be accomplished in a few ways in real applications. We can either use embedded piezoelectric actuators [7] or bonded piezoelectric films to the suspension arm [3]. If a piezoelectric film is used, the film is bonded to one side of the suspension arm (beam) that is shown in Fig. 1.

When a voltage  $V$  is applied to the piezo film, a steady-state displacement at the slider end will be produced as

$$d_1 = KV \quad (4)$$

where  $K$  is a constant. In an operating HDD where the disk is rotating at a constant speed, the displacement dynamics will be determined both by the characteristics of the suspension arm (beam) and the aerodynamics of the slider's air bearing. As the response of the piezo film actuator itself has a very wide bandwidth, its dynamic mode can be neglected here. Therefore, the

dynamic relationship between the voltage applied to the piezo film and the displacement resulting can be simplified as

$$\frac{d_1(s)}{V(s)} = G(s) = K \frac{\omega_{ps}^2}{s^2 + 2\xi_s \omega_{ps} s + \omega_{ps}^2} \frac{\omega_{ab}^2}{s^2 + 2\xi_a \omega_{ab} s + \omega_{ab}^2} \quad (5)$$

where  $\omega_{ps}$  and  $\xi_s$  are the natural frequency and damping ratio of the suspension beam,  $\omega_{ab}$  and  $\xi_a$  are the natural frequency and damping ratio of the slider's air bearing and  $K$  is a constant.  $\omega_{ab}$  (a few tens of kilohertz) is usually much larger than  $\omega_{ps}$  (a few kilohertz). In the case that we only consider vibrations below one kilohertz, the model can be further simplified as

$$G(s) = K \frac{\omega_{ps}^2}{s^2 + 2\xi_s \omega_{ps} s + \omega_{ps}^2} \quad (6)$$

Now, the flying height variation suppression mechanism can be shown in Fig. 2.

The block diagram of the closed-loop control system is shown in Fig. 3. In the diagram,  $y_m$  is the output of the measurement point,  $d_1$  is the displacement output of the piezo film actuator,  $d_2$  is the disk spinning resulting head-disk spacing or flying height which can be treated as a constant,  $d_3$  is the vibration resulting head-disk spacing whose effect on the total spacing is intended to be suppressed here, and  $d$  is the total head-disk spacing. The single pole of the high-pass filter  $H_{AEM}(s)$  is usually around  $a = 325000$ . Typical parameters for the suspension and slider's air bearing are given in the plant transfer function as

$$G(s) = K \frac{902500}{s^2 + 32.3s + 902500} \frac{202500000}{s^2 + 5220s + 202500000} \quad (7)$$

The values of the constant parameters  $K_{MH}$ ,  $K_{AEM}$ , and  $K$  do not need to be known at this stage. They are to be considered and compensated in the following controller design procedure.

The problem now becomes designing a servo control system to suppress the effect of vibrational disturbances on the head-disk spacing. The flying height variation suppression is now equivalent to a servo control system tracking a reference varying input signal. Obviously, the purpose of this controller design is to make the closed-loop control system has a wide bandwidth. For a good servo control system, the following performance is usually desired: a) good static performance which means zero or small static error; b) good dynamic performance which means fast response or wide bandwidth but low overshoot; c) good robustness which means system performance is invariant to or less affected by parameter variations and disturbances. For this particular problem here, from the engineering point of view, an easy to be designed and implemented conventional controller will be practical and sufficient. If we use a proportional-integral (PI) compensator to compensate the high-pass filter  $H_{AEM}(s)$ , a proportional-integral-differential (PID) and two lead compensators

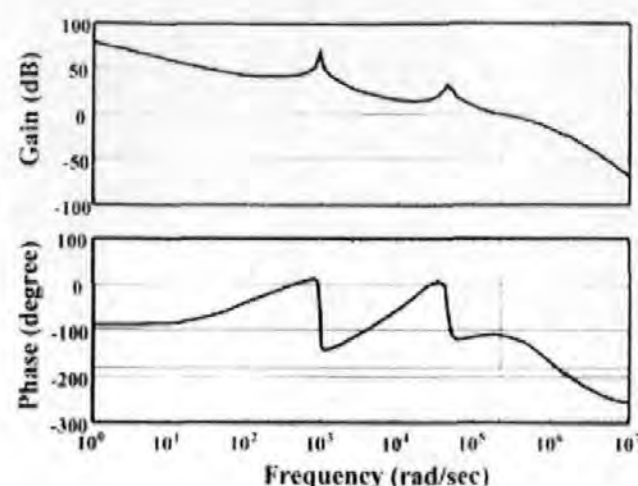


Fig. 4. Open-loop frequency response of the compensated servo control system.

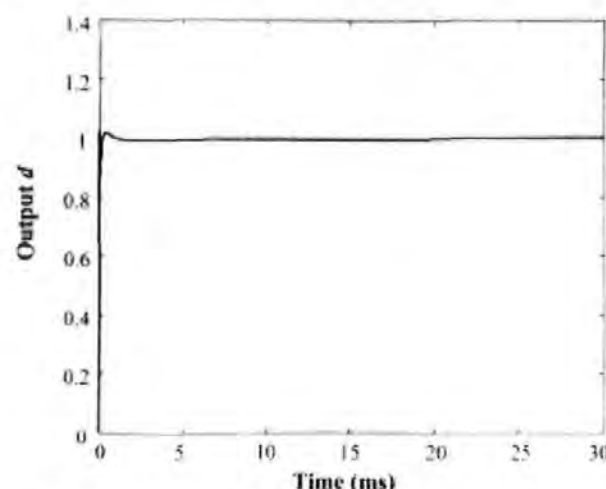


Fig. 5. Step response of the servo control system.

to compensate the two second-order vibrational modes of the plant, the transfer function of the controller becomes

$$G_C(s) = \frac{s + z_1}{s} \frac{s + z_2}{s + p_2} \frac{s + z_3}{s + p_3} K_{PID} \frac{(s + \frac{1}{T_d})}{s} \frac{(s + \frac{1}{T_i})}{s} \quad (8)$$

We choose the parameters of the above controller as  $z_1 = 200\,000$ ,  $z_2 = z_3 = 22\,500$ ,  $p_2 = p_3 = 1\,125\,000$ ,  $T_d = 0.0005$ ,  $T_i = 0.01$  and  $K_{MR}K_{PID}K_{LEM}K = 198$ . Note that we intentionally choose  $z_1$  as 200 000 instead of 325 000 to make partial compensation to see the system's robustness to parameter variation. The open-loop frequency response of the servo control system is given by simulation as shown in Fig. 4.

The phase margin is about  $70^\circ$  at the gain crossover frequency of 219 900 rad/s. To help understand the performance of the system, the step response is given in Fig. 5.

To verify the flying height variation suppression ability of this servo control system, we have made a large number of simulation experiments. A series of sinusoidal wave signals from low to high frequencies are applied as the system's referencedisturbance input. The resulting head-disk spacing outputs or suppressed spacing variations are given from Fig. 6 to Fig. 9. For

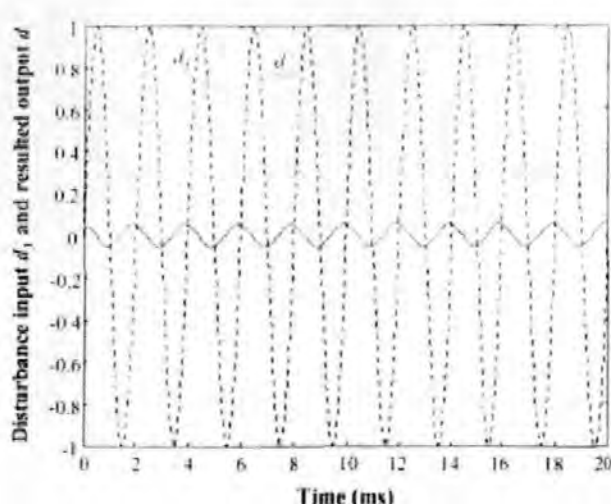


Fig. 6. 500-Hz unit-amplitude sinusoidal disturbance input and the resulting head-disk spacing variation.

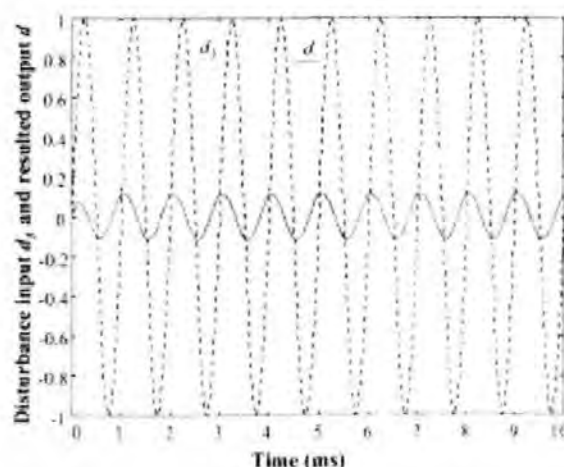


Fig. 7. 1000-Hz unit-amplitude sinusoidal disturbance input and the resulting head-disk spacing variation.

comparison purposes, the reference disturbance input  $d_0$  is also illustrated.

From Fig. 6 through Fig. 9, it can be seen that with the active flying height control in action, a 2000-Hz head-disk spacing variation will be suppressed to about 17% of the amplitude without active control. It is apparent that variations with frequencies lower than 2000 Hz will be better suppressed. We have found that in the frequency band from 5000 Hz to 9000 Hz, the suppression results are even better than those at the frequency of 2000 Hz, which results from the frequency response of the servo control system, generally speaking. With the increase of the variation frequency, the suppression effect will be gradually reduced, which depends on the bandwidth of the servo system. The good news is that large head-disk spacing variations usually happen in the frequencies below 5000 Hz [8], which are caused by the vibration-induced mechanical resonance. Another point we should make is that in real applications, the benefit of even a 10% spacing variation suppression would be tremendous for the increase of the performance and reliability of the HDDs.



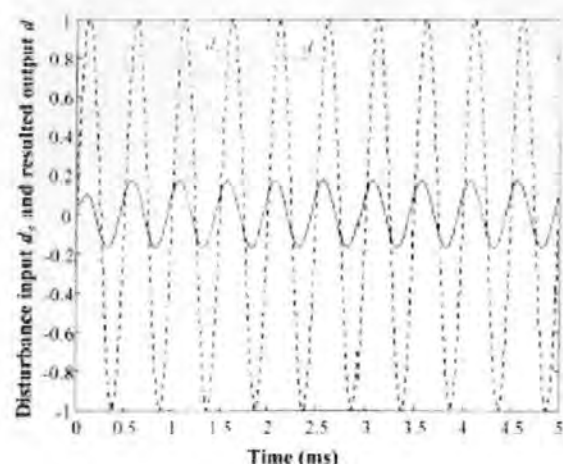


Fig. 8. 2000-Hz unit-amplitude sinusoidal disturbance input and the resulting head-disk spacing variation.

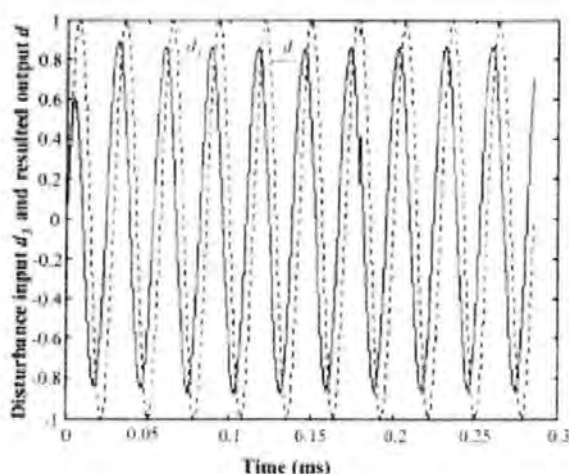


Fig. 9. 35000-Hz unit-amplitude sinusoidal disturbance input and the resulting head-disk spacing variation.

#### IV. CONCLUSION

A novel active flying height control method is proposed to suppress the flying height or head-disk spacing variation in hard disk drives under vibration conditions. Real-time spacing variation signals derived from the feedback signal of MR or GMR read/write heads are used for feedback control. Simulation experimental results show that this active flying height control will effectively suppress the head-disk spacing variation; therefore, the performance and reliability of the HDDs could be well improved when working in vibration conditions. The method has a good potential to be applied to future ruggedized hard disk drives.

#### REFERENCES

- [1] B. Liu, Y. Zhu, Y. Li, W. Hua, Q. Leng, and G. Sheng, "An experimental study of slider vibration in nanometer spaced head-disk interface," *IEEE Trans. Magn.*, vol. 35, pp. 2463–2465, Oct. 1999.
- [2] R. L. Wallace Jr., "The reproduction of magnetically recorded signals," *Bell Syst. Tech. J.*, vol. 30, pp. 1145–1173, 1951.
- [3] P. Gao and S. Swei, "Active actuation and control of a miniaturized suspension structure in hard-disk drives using a polyvinylidene-fluoride actuator and sensor," *Meas. Sci. Technol.*, vol. 11, no. 2, pp. 89–94, 2000.

- [4] D. W. Abraham, A. P. Pranno, M. F. Ke, and H. K. Wickramasinghe, "Method and Apparatus for Detecting Asperities on Magnetic Disk Using Thermal Proximity Imaging," U.S. patent 5527110, June 18, 1996.
- [5] G. Smith, "Dynamic in-situ measurements of head-to-disk spacing," *IEEE Trans. Magn.*, vol. 35, pp. 2346–2351, Oct. 1999.
- [6] R. Surdianu, W. Yao, R. C. Ku, and D. Kuo, "Study of head disk interface dynamics using a thermal asperity sensor," *IEEE Trans. Magn.*, vol. 35, pp. 2181–2183, Oct. 1999.
- [7] C. Chulambur, W. Clegg, D. Jenkins, and B. Robinson, "A novel 2-dimensional suspension arm for flying height control and high-bandwidth track following in advanced hard disk drives," in *Proc. IMTC*, Baltimore, MD, May 2000.
- [8] G. Tunstall, W. Clegg, D. Jenkins, and C. Chulambur, "Head-media interface instability under hostile operating conditions," in *Proc. IMTC*, Baltimore, MD, May 2000.



Xinqun Liu received the B.Eng. and M.Eng. degrees in electrical and control engineering from Jilin University of Technology, China, in 1985 and 1988, respectively.

From 1988 to 1997, he was with Changchun Institute of Optics and Fine Mechanics (one of the largest research institutes in China), Chinese Academy of Sciences, working in the area of mC/mP/DSP based control system design, high precision speed and position servo control, analog and computer control system design, and digital signal processing. In 1997, as a Researcher, he joined the Center for Research in Information Storage Technology, University of Plymouth, Plymouth, U.K., where he worked on building up computer controlled optical instruments to measure the head-disk spacing of the up-to-date hard-disk drives. During this period of time, he also gained interests in optical system design, magnetic recording channel technologies, such as coding, equalization, and detection, and servo control in hard-disk drives. Since 2000, he has been working for Roke Manor Research. His interests include DSP applications in 3G baseband system design, 3G radio link simulation, optical communications, and channel coding technologies.

Dr. Liu is a senior member of Chinese Institute of Electronics.



Aneli Li received the B.Eng. and M.Sc. degrees in electrical engineering from Jilin University of Technology, China, in 1987 and 1995, respectively. She is currently pursuing the Ph.D. degree in information storage at the University of Plymouth, Plymouth, U.K. Her Ph.D. research work includes signal restoration and processing, head-disk spacing characterization using electro-magnetic transducers, recording channel coding, equalization, and detection, all for magnetic hard disk drives.

Since 1987, she has been an Electronics Engineer at a research institute in China, working in the area of signal processing and digital communications.



Warwick Clegg (SM'94) received the degree in physics from Liverpool University, Liverpool, U.K., in the late 1960s, and then researched for the M.Sc. and Ph.D. degrees in the area of magnetic data storage at Manchester University, Manchester, U.K.

After many years at Manchester, he moved to the University of Plymouth, Plymouth, U.K., where he is now Head of the Department of Communication and Electronic Engineering. His principal research interests continue to lie in the field of data storage, with increasing emphasis on characterization methods for advanced media and drives, including the development of novel scanning laser and scanning force probe instruments and techniques to visualize written data bits.

Prof. Clegg is a Member of the Institute of Physics and the Institution of Electrical Engineers.



**David F. L. Jenkins** received the B.Sc. degree in physics, the M.Sc. degree in lasers and their applications, and the Ph.D. degree in photothermal deflection spectroscopy.

After completing his Ph.D. research at Royal Military College of Science, U.K., he became a post-doctoral Research Fellow at Coventry University, U.K., in 1990, working on magneto-photo-acoustic spectroscopy. Between 1993 and 1997, he worked in the Information Storage Group, Division of Electrical Engineering, Manchester University, Manchester, U.K., researching active vibration control of micro-mechanical structures. In 1997, he moved to the University of Plymouth, Plymouth, U.K., to take up the position of Lecturer and then Senior Lecturer, in the Center for Research in Information Storage Technology, where he has continued his research micro-actuators, micro-sensors, and optical instrumentation.



**Paul Davey** (M'00) received B.Eng. (Hons.) in electrical and electronic engineering and the Ph.D. degrees from the University of Plymouth, Plymouth, U.K., in 1988 and 1994, respectively.

Since 1994, he has worked as a Information Storage Consultant responsible for PRML, data channel evaluation, integration, and optimization for removable hard disk drive products for Myrica U.K. Ltd. and the development for portable measurement and quality control electronics for the Bank of England Printing Works. In 1997, he rejoined

the Centre for Research in Information Storage Technology, University of Plymouth, as a Research Fellow, continuing his research on two dimensional coding and detection. Since June 2000, he has been a Senior Lecturer in the Department of Communication and Electronic Engineering. His research interests include adaptive digital signal processing and multidimensional coding, parallel processing algorithms, embedded microprocessor applications, intelligent systems and internet technologies.